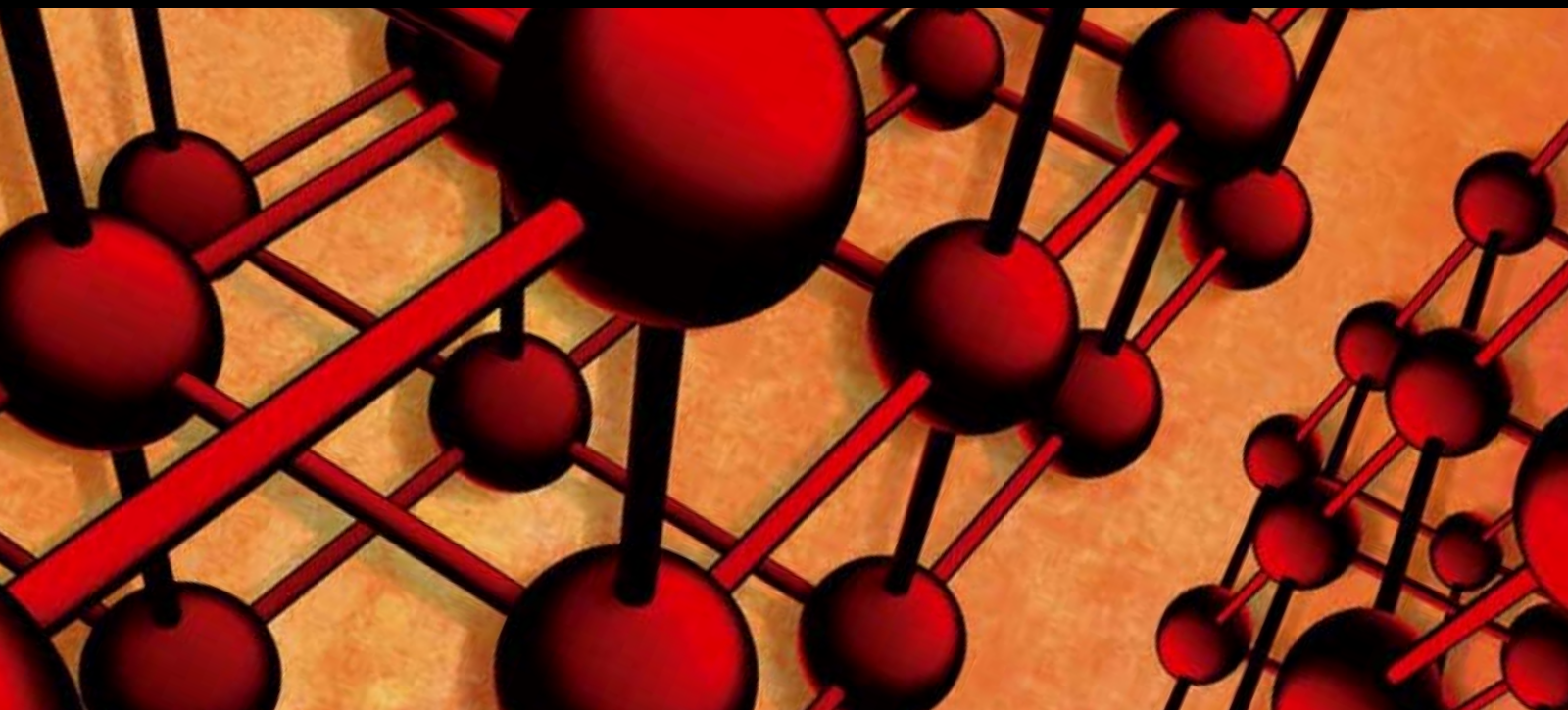


Microstructural Evolution in Materials during Thermal Processing

Guest Editors: Joseph K. L. Lai, Brian Ralph, Zhiwen Chen, and Kin Ho Lo





Microstructural Evolution in Materials during Thermal Processing

Advances in Materials Science and Engineering

Microstructural Evolution in Materials during Thermal Processing

Guest Editors: Joseph K. L. Lai, Brian Ralph, Zhiwen Chen, and Kin Ho Lo



Copyright © 2012 Hindawi Publishing Corporation. All rights reserved.

This is a special issue published in “Advances in Materials Science and Engineering.” All articles are open access articles distributed under the Creative Commons Attribution License, which permits unrestricted use, distribution, and reproduction in any medium, provided the original work is properly cited.

Editorial Board

Marcel Ausloos, Belgium
Robert S. Averbach, USA
V. P. S. Awana, India
Amit Bandyopadhyay, USA
Z. Barber, UK
Mark Blamire, UK
Susmita Bose, USA
Steve Bull, UK
David Cann, USA
Daolun Chen, Canada
Manish U. Chhowalla, USA
Paolo Colombo, Italy
Martin Crimp, USA
Jie Dai, Singapore
C. K. Das, India
Chris Davies, Australia
J. Paulo Davim, Portugal
Seshu Babu Desu, USA
Yong Ding, USA
Shi Xue Dou, Australia
Chunying Duan, China
Nadia El-Masry, USA
David Field, USA
Qiang Fu, China
John W. Gillespie, USA
Jeffrey T. Glass, USA
Zhennan Gu, China
Hiroki Habazaki, Japan
Richard Hennig, USA

Dachamir Hotza, Brazil
Chun-Hway Hsueh, USA
Rui Huang, USA
Shyh-Chin Huang, Taiwan
Jacques Huot, Canada
Hamlin Jennings, USA
William A. Jesser, USA
A. Jorio, Brazil
Kazuro Kageyama, Japan
S. Komarneni, USA
Prashant Kumta, USA
Pearl Lee-Sullivan, Canada
Pavel Lejcek, Czech Republic
Markku Leskela, Finland
Jun Li, Singapore
Jing Li, USA
Yuanhua Lin, China
Zhimin Liu, China
Meilin Liu, Georgia
Maria A. Loi, The Netherlands
Hai Lu, China
Yiu-Wing Mai, Australia
Peter Majewski, Australia
A.-S. H. Makhlof, Germany
R. S. Mishra, USA
S. Miyazaki, Japan
Paul Munroe, Australia
Korukonda L. Murty, USA
Luigi Nicolais, Italy

Tsutomu Ohzuku, Japan
Xiaoqing Pan, USA
Ganapathiraman Ramanath, USA
Raju V. Ramanujan, Singapore
Jainagesh A. Sekhar, USA
You Song, China
Charles C. Sorrell, Australia
Steven L. Suib, USA
Wen-Hua Sun, China
Sam-Shajing Sun, USA
Achim Trampert, Germany
An-Pang Tsai, Japan
Vladimir Tsukruk, USA
Krystyn Van Vliet, USA
Stan Veprek, Germany
Rui Vilar, Portugal
Lianzhou Wang, Australia
Kunpeng Wang, China
John Wang, Singapore
Jörg M. K. Wiezorek, USA
Aiguo Xu, China
Jenn-Ming Yang, USA
Yadong Yin, USA
Jihong Yu, China
Guan-Jun Zhang, China
Dao Hua Zhang, Singapore
Ming-Xing Zhang, Australia

Contents

Microstructural Evolution in Materials during Thermal Processing, Joseph K. L. Lai, Brian Ralph, Zhiwen Chen, and Kin Ho Lo
Volume 2012, Article ID 302478, 2 pages

Crystallisation Kinetics of a β -Spodumene-Based Glass Ceramic, Oscar Rubem Klegues Montedo, Dachamir Hotza, Antonio Pedro Novaes de Oliveira, Robert Meszaros, Nahum Travitzky, and Peter Greil
Volume 2012, Article ID 525428, 8 pages

Formation and Device Application of Ge Nanowire Heterostructures via Rapid Thermal Annealing, Jianshi Tang, Chiu-Yen Wang, Faxian Xiu, Yi Zhou, Lih-Juann Chen, and Kang L. Wang
Volume 2011, Article ID 316513, 16 pages

Thermal Effect on Structure of Silver in Ion-Exchanged Soda-Lime Glasses and Aluminum-Doped Zinc Oxide Films, Paul W. Wang, Yanfeng Jiang, Jin-Cherng Hsu, Yu-Yun Chen, Yung-Hsing Lin, and Huang-Lu Chen
Volume 2011, Article ID 987671, 7 pages

The Effects of Different Types of Fly Ash on the Compressive Strength Properties of Briquettes, Özlem Çelik Sola, Murat Yayla, Barış Sayın, and Cengiz Duran Atiş
Volume 2011, Article ID 430604, 6 pages

Crystallization Behavior and Microstructural Analysis of Strontium Rich $(\text{Pb}_x\text{Sr}_{1-x})\text{TiO}_3$ Glass Ceramics in Presence of La_2O_3 , C. R. Gautam, Devendra Kumar, and Om Parkash
Volume 2011, Article ID 747346, 9 pages

Crystallization Behavior and Microstructural Analysis of Lead-Rich $(\text{Pb}_x\text{Sr}_{1-x})\text{TiO}_3$ Glass Ceramics Containing 1 mole % La_2O_3 , C. R. Gautam, Devendra Kumar, and Om Parkash
Volume 2011, Article ID 402376, 11 pages

Powder Characterization and Electrochemical Properties of $\text{LiNi}_{0.5}\text{Mn}_{1.5}\text{O}_4$ Cathode Materials Produced by Large Spray Pyrolysis Using Flame Combustion, Shinsuke Akao, Motofumi Yamada, Takayuki Kodera, Kenichi Myoujin, and Takashi Ogihara
Volume 2011, Article ID 768143, 6 pages

Low-Temperature Strengths and Ductility of Various Tungsten Sheets, Yutaka Hiraoka and Hiroaki Kurishita
Volume 2011, Article ID 509457, 7 pages

Young's Modulus and Coefficient of Linear Thermal Expansion of ZnO Conductive and Transparent Ultra-Thin Films, Naoki Yamamoto, Hisao Makino, and Tetsuya Yamamoto
Volume 2011, Article ID 136127, 10 pages

TEM Study of High-Temperature Precipitation of Delta Phase in Inconel 718 Alloy, Moukrane Dehmas, Jacques Lacaze, Aliou Niang, and Bernard Viguiier
Volume 2011, Article ID 940634, 9 pages

γ' Precipitation and Growth Kinetics in Mechanically Alloyed Ni-Al, QingXin Tang, Shigeharu Ukai, Akinobu Minami, and Shigenari Hayashi
Volume 2011, Article ID 137387, 7 pages

Editorial

Microstructural Evolution in Materials during Thermal Processing

Joseph K. L. Lai,¹ Brian Ralph,² Zhiwen Chen,³ and Kin Ho Lo⁴

¹Department of Physics and Materials Science, City University of Hong Kong, Tat Chee Avenue, Kowloon, Hong Kong

²Brunel University, Kingston Lane, Uxbridge, UB8 3PH, UK

³School of Environmental and Chemical Engineering, Shanghai University, Shangda Road 99, P.O. Box 144, Shanghai 200444, China

⁴Department of Electromechanical Engineering, University of Macau, Avenida Padre Tomás Pereira, Taipa, Macau, China

Correspondence should be addressed to Joseph K. L. Lai, apjoelai@cityu.edu.hk

Received 16 October 2011; Accepted 16 October 2011

Copyright © 2012 Joseph K. L. Lai et al. This is an open access article distributed under the Creative Commons Attribution License, which permits unrestricted use, distribution, and reproduction in any medium, provided the original work is properly cited.

The study of materials science is mainly based on our understanding of the relationship between microstructure and materials properties. Factors such as temperature, stress, and environment can lead to microstructural evolution with a concomitant change in properties. It is the materials scientist's role to harness our knowledge on this relationship to produce materials with improved properties, or to predict the performance of existing materials under various service conditions.

Over the past two decades, there have been a burgeoning number of novel or improved materials. This development is accompanied by significant advances in techniques in materials characterization as well as increased sophistication in theoretical methods for the analysis of microstructures. The application of these new techniques and methodologies to study the microstructural evolution of novel materials offers tremendous opportunities for scientific advancement on many fronts, with the prospect of providing new solutions to problems which have hitherto remained intractable.

The papers published in this special issue encompass various materials systems: metals and alloys, glass ceramics, thin films, nanowire, and oxide powders for engineering applications.

The paper by Dehmas et al. reports an investigation on the precipitate phases in Inconel 718, an important alloy for high temperature applications such as turbine blades. Using transmission electron microscopy and X-ray diffraction, the authors were able to confirm the presence of rotation-ordered domains in δ plates and explain unexpected contrast by double diffraction due to overlapping phases.

The paper by Ukai et al. is also focused on Nickel-based super-alloy for high temperature turbine applications. This study has enhanced our understanding of the precipitation and growth kinetics of γ' and its characteristics in mechanically alloyed materials.

The paper by Hiraoka et al. reports the results of an investigation on the strength and ductility of tungsten sheets after various recrystallization treatments. Three-point bend tests were performed at temperatures between 290 and 500 K. Fracture surfaces were examined by scanning electron microscopy. The mechanical properties of tungsten and molybdenum were compared.

A glass ceramic material was studied by Montedo et al. in their paper. The material studied is a candidate material for applications such as laminated tapes for screen-printed electronic components. The crystallization kinetics was studied using differential thermal analysis and scanning electron microscopy.

Other two papers were written by the same team of authors. Two titanium oxide glass ceramic materials with La_2O_3 addition, one strontium rich and one lead rich, were studied. The crystallization behavior of these materials was investigated using differential thermal analysis and X-ray diffraction.

Microstructural evolution during rapid thermal annealing of Ge nanowires was investigated by Tang et al. in the seventh paper. Scanning electron microscopy and transmission electron microscopy were used to observe $\text{Ni}_2\text{Ge}/\text{Ge}/\text{Ni}_2\text{Ge}$ nanowire heterostructures. This work has

important implications for the future development of field effect transistors.

Wang et al. present their work on zinc oxide thin films in their paper. Two types of thin films were investigated: Ag ion-exchanged soda-lime glasses and aluminium-doped ZnO (AZO). Changes in chemical states and structural modification during and after heat treatment were explored. The results provide the basic information for determining the optimum heat treatment to grow silver quantum dots of various size and density in thin films.

Another interesting contribution on the subject of ZnO thin films appears in one of the papers. Japanese researchers from the Kochi University of Technology have developed a new technique for measuring the Young's modulus of ultra-thin films with thickness in the range of about 10 nm. The technique was applied to study the mechanical properties of Ga-doped ZnO thin films, a possible substitute material for indium-tin-oxide transparent electrodes.

Another paper deals with powder materials for Lithium ion battery applications. Akao et al. from the University of Fukui produced $\text{LiNi}_{0.5}\text{Mn}_{1.5}\text{O}_4$ cathode materials by flame combustion using a spray pyrolysis apparatus. X-ray diffraction revealed that, after calcination at 900°C , crystalline powders with polygonal morphology and narrow particle size distribution were obtained.

The paper by Sola et al. is concerned with a literally "down to earth" problem. For many years, scientists have been developing ways to make use of fly ash in order to turn it from an industrial waste with environmental and storage problems into a useful material. The most obvious solution to this conundrum is to use it as an additive in sintered briquettes in the construction industry. These authors have determined the effect of different types of fly ash on the compressive strength of sintered briquettes. They showed that sintered briquettes samples made with Tuncbilek fly ash had higher percentage of glassy phase and compressive strength.

Papers published in this special issue will be of interest to materials scientists and engineers who wish to extend their knowledge on the effect of thermal processing on a broad range of materials. We would like to take this opportunity to thank all the authors who have submitted their papers to this publication.

*Joseph K. L. Lai
Brian Ralph
Zhiwen Chen
Kin Ho Lo*

Research Article

Crystallisation Kinetics of a β -Spodumene-Based Glass Ceramic

Oscar Rubem Klegues Montedo,¹ Dachamir Hotza,²
Antonio Pedro Novaes de Oliveira,² Robert Meszaros,³
Nahum Travitzky,³ and Peter Greil³

¹Unidade Acadêmica de Ciências, Engenharias e Tecnologias (UNACET), Universidade do Extremo Sul Catarinense (UNESC), 88806-000 Criciúma, SC, Brazil

²Group of Ceramic and Glass Materials (CERMAT), Department of Mechanical Engineering (EMC), Federal University of Santa Catarina (UFSC), 88040-900 Florianópolis, SC, Brazil

³Department of Materials Science, Institute of Glass and Ceramics, University of Erlangen-Nuremberg, 91058 Erlangen, Germany

Correspondence should be addressed to Oscar Rubem Klegues Montedo, oscar.rkm@gmail.com

Received 25 February 2011; Revised 19 September 2011; Accepted 20 September 2011

Academic Editor: Joseph Lai

Copyright © 2012 Oscar Rubem Klegues Montedo et al. This is an open access article distributed under the Creative Commons Attribution License, which permits unrestricted use, distribution, and reproduction in any medium, provided the original work is properly cited.

LZSA ($\text{Li}_2\text{O}-\text{ZrO}_2-\text{SiO}_2-\text{Al}_2\text{O}_3$) glass ceramic system has shown high potential to obtain LTCC laminate tapes at low sintering temperature ($<1000^\circ\text{C}$) for several applications, such as screen-printed electronic components. Furthermore, LZSA glass ceramics offer interesting mechanical, chemical, and thermal properties, which make LZSA also a potential candidate for fabricating multilayered structures processed by Laminated Objects Manufacturing (LOM) technology. The crystallization kinetics of an LZSA glass ceramic with a composition of $16.9\text{Li}_2\text{O}\cdot 5.0\text{ZrO}_2\cdot 65.1\text{SiO}_2\cdot 8.6\text{Al}_2\text{O}_3$ was investigated using nonisothermal methods by differential thermal analysis and scanning electronic microscopy. Apparent activation energy for crystallization was found to be in the $274\text{--}292\text{ kJ}\cdot\text{mol}^{-1}$ range, and an Avrami parameter n of 1 was obtained that is compared very favorably with SEM observations.

1. Introduction

A considerable effort has been spent to obtain high-performance glass ceramics for several potential applications in the medical, automotive, and telecommunication fields [1]. Low-temperature cofired ceramics (LTCCs) have created good perspectives for those applications, with special attention to the glass ceramic materials [2, 3]. LZSA glass ceramics ($\text{Li}_2\text{O}-\text{ZrO}_2-\text{SiO}_2-\text{Al}_2\text{O}_3$) have been studied because of their beneficial thermal, mechanical, and thermal properties [4], among other interesting features. Moreover, laminated LZSA bodies crystallized at $850^\circ\text{C}/30\text{ min}$ have demonstrated to exhibit a low dielectric constant of 8.61 ± 0.84 at 1 MHz (room temperature) [5]. Furthermore, their relatively low temperatures of sintering [6] make β -spodumene-based glass ceramics (LZSA) a potential candidate for obtaining multilayered structures processed by LOM technology (Laminated Objects Manufacturing) [7]. However, the low

sintering temperature is also accomplished by low crystallization temperature in this system, especially for very fine powders and low heating rates. In order to control thermal treatment for obtaining optimized properties, it is necessary to determine the kinetics parameters of crystallization for this glass ceramic system.

Isothermal crystallization kinetics of glass ceramic systems commonly refers to the following well-established Johnson-Mehl-Avrami equation [8]:

$$-\ln(1-x) = kt^n, \quad (1)$$

where x is the volume fraction crystallized at a given temperature and time t , n is the Avrami parameter related to the nucleation and crystal growth mechanisms, and k is the reaction rate constant related to the apparent activation energy for crystallization, E_c . Nonisothermal conditions have been more largely widespread in the crystallization studies

TABLE 1: Chemical composition of LZSA parent glass.

Oxides	Glass composition, mol%
SiO ₂	65.1
Al ₂ O ₃	8.6
Na ₂ O	0.6
K ₂ O	0.4
Li ₂ O	16.9
CaO	0.6
MgO	2.0
ZrO ₂	5.0
BaO	0.2
ZnO	0.6

of amorphous materials [3, 9–15], despite the scepticism of Shaaban [16]. According to Shaaban [16], Kissinger plot and Ozawa plot cannot be directly used for crystallization of amorphous materials, because crystallization is advanced by the nucleation and crystal growth process instead of by n th order reaction. However, most of work reported in the literature used DTA or DSC to determine the kinetics parameters E_c and n . Measurements using dilatometer were also applied in some cases [17, 18].

Those methods, which assume that deflection from the baseline is proportional to the instantaneous reaction rate, require a uniform temperature of the sample independently of the heating rate. This is obtained employing small samples and low heating rates during heat treatments [9].

The aim of this work is to present the results of an investigation about the crystallization kinetics of a β -spodumene-(LiAl [Si₂O₆]) based LZSA glass ceramic composition by means of Nonisothermal method.

2. Material and Methods

2.1. Samples Preparation. A β -spodumene-based glass ceramic composition with interesting chemical, thermal, and electrical (dielectric constant) properties [4, 5] was selected and prepared from suitable amounts of Li₂CO₃, ZrSiO₄, SiO₂, and LiAl[Si₂O₆] (spodumene, Colorminas Colorificio e Mineraço, Cricima, Brazil). The powders were mixed and melted at $1550 \pm 3^\circ\text{C}$ for 2 h in a gas furnace using a mullite crucible. The melt was poured into deionized water and the quenched frit powder was remelted at $1550 \pm 2^\circ\text{C}$ for 2 h in an electric furnace (Nabertherm LHT 02/17 LBR, Nabertherm, Lilienthal, Germany) using an alumina crucible to finally obtain a homogeneous viscous liquid. Chemical analysis is shown in Table 1. A small amount of the obtained melt was poured into a graphite crucible, transferred to an annealing furnace (Linn High Therm LM 421.27, Linn High Therm, Eschenfelden, Germany) and held at 570°C for 1 h to obtain small monoliths ($50\text{ mm} \times 5\text{ mm} \times 4\text{ mm}$) that were used to determine the glass transition temperature (T_g) by beam-bending test (Beam-Bending Viscosimeter, Bhr Thermoanalyse VIS 401, Hllhorst, Germany) applying a constant heating rate of $10^\circ\text{C}\cdot\text{min}^{-1}$. Thermal expansion was measured with a horizontal dilatometer (DIL 402C,

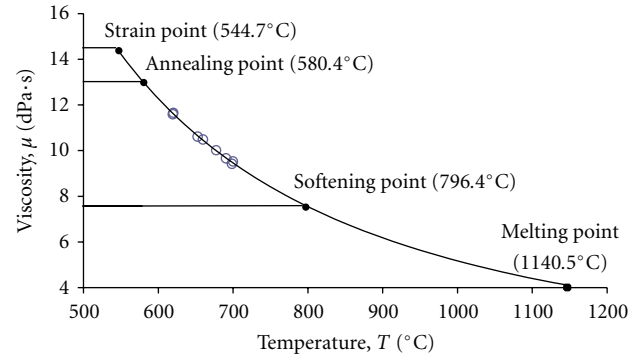


FIGURE 1: Viscosity of the selected glass in function to the temperature.

Netzsch, Selb, Germany) at the same heating rate. From the remaining glass frit a powder fraction of 0.5–0.7 mm was prepared and subsequently dry-milled in a porcelain ball mill for 3 h. The particle size was determined by laser granulometric analysis (Cilas 1064L particle size analyzer, Orleans, France). Theoretical densities of glass powder and glass ceramic obtained at different temperatures were measured by He pycnometry (AccuPyc 1330, Micromeritics, Norcross, GA; 5 measurements). Apparent geometric densities of the compacted bodies (40 MPa, $1.4\text{ g}\cdot\text{cm}^{-3}$ green density) were determined geometrically. Relative densities at several temperatures were calculated taking into account the ratio between apparent and theoretical densities of the heat-treated samples. Dielectric constant measurements were carried out according to DIN 53 482/VDE 0303 in a HP Dielectric Test Fixture (16451B, Hewlett Packard, Waldhausen, Germany) at room temperature applying a frequency of 1 MHz. The samples were discs of $20\text{ mm} \times 1.2\text{ mm}$ heat-treated at 850°C for 10 min.

2.2. Determination of the Predominant Crystallization Mechanism. The method of Thakur and Thiagarajan [19] was used to determine the nucleating efficiency, in which the variation in onset of crystallization, ΔT_x , with particle size was monitored in a differential scanning calorimeter (DSC 404C, Netzsch, Selb, Germany; alumina crucibles, dry air). A constant heating rate of $10^\circ\text{C}\cdot\text{min}^{-1}$ was applied to determine the predominant crystallization mechanism. Moreover, a small monolith sample ($5\text{ mm} \times 4\text{ mm} \times 4\text{ mm}$) was polishing to eliminate apparent surface defects and subsequently heat-treated at 875°C for 2 h ($10^\circ\text{C}\cdot\text{min}^{-1}$).

2.3. Identification of the Crystalline Phases Formed. High-temperature X-ray diffraction (HT-XRD) patterns were recorded (Siemens D500, Siemens AG, Mannheim, Germany) from powdered samples. Monochromated Cu K α 1 radiation was applied at a voltage of 30 kV and a current of 30 mA.

2.4. Crystallisation Kinetics Investigation. The onset of crystallization T_c was determined by differential thermal analysis

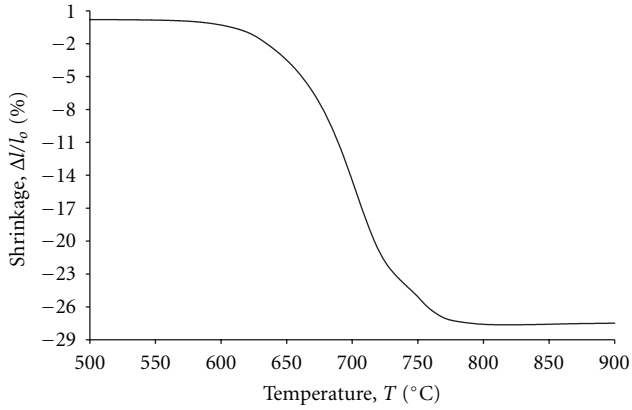


FIGURE 2: Linear shrinkage versus temperature of the selected glass.

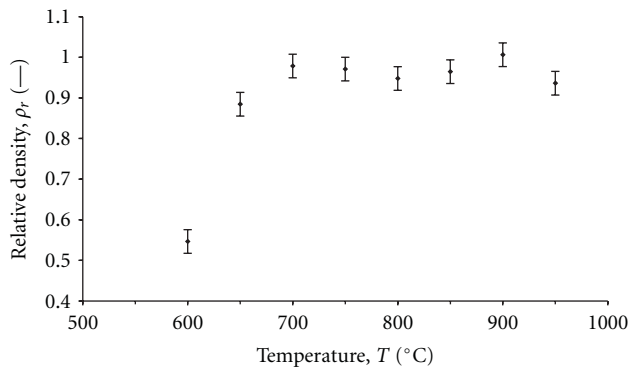


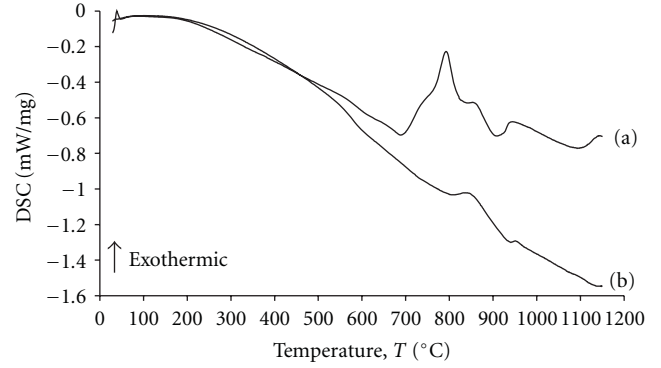
FIGURE 3: Relative density versus temperature of the selected glass.

TABLE 2: Properties of the investigated LZSA glass ceramic (sintered at 850°C for 10 min).

d_{50} , μm	2.34
ρ , $\text{g}\cdot\text{cm}^{-3}$	
Parent glass	2.622 ± 0.004
Glass ceramic	2.711 ± 0.003
α , $10^6\text{ }^\circ\text{C}^{-1}$	2.38
$\tan \delta$	0.029 ± 0.011
ϵ_r	9.97 ± 0.84
T_g , $^\circ\text{C}$	580
T_c , $^\circ\text{C}$	794
$T_c - T_g$, $^\circ\text{C}$	214

(DTA STA 429, Netzsch, Selb, Germany; alumina crucibles, dry air) at 5, 10, 15, and $20^\circ\text{C}\cdot\text{min}^{-1}$ heating rates.

2.5. Crystal Growth Investigation. Monoliths ($50\text{ mm} \times 5\text{ mm} \times 4\text{ mm}$) were prepared from the transparent glass samples. Some of them were cut in small pieces of $5\text{ mm} \times 4\text{ mm} \times 4\text{ mm}$ which were used for investigating the crystal growth under different heat treatment conditions in an electrically heated furnace (LM 421.27, Linn High Therm, Eschenfelden, Germany). Temperatures of 700, 750, 775, 800, 825, 850, 875, and 900°C and swelling times of 15,

FIGURE 4: DSC scans at $10^\circ\text{C}\cdot\text{min}^{-1}$ heating rate for different glass powders: (a) $2.34\ \mu\text{m}$ mean particle size; (b) $0.5\text{--}0.7\ \text{mm}$ size.

30, 60, and 120 min were applied. After heat treatment, each sample was transversally cut. Morphology, crystal formation, and crystalline growth from surface towards to the centre of the monoliths were analysed by scanning electronic microscopy (SEM, Philips XL 30, Eindhoven, The Netherlands).

2.6. Determination of the Activation Energy for Structural Relaxation. The activation energy for structural relaxation was determined for the investigated composition by means of the method of Moynihan et al. [20] Small monoliths ($20\text{ mm} \times 5\text{ mm} \times 4\text{ mm}$) were analyzed to determine the glass transition temperature (T_g) according to DIN 52324 (*Bestimmung der Transformationstemperatur*) with a horizontal dilatometer (DIL 402C, Netzsch, Selb, Germany; dry air). However, the last heating run to determine T_g was performed at 5, 10, 15, and $20^\circ\text{C}\cdot\text{min}^{-1}$ heating rates.

3. Results and Discussion

Some basic properties of the selected glass are summarized in Table 2. Taking into account this glass presents T_g of 580°C (Figure 1), determined by beam-bending test, and sintering in glasses occurs by viscous flow, densification would be expected to start around T_g . In fact, Figure 2 shows that sintering started at about 600°C and maximum shrinkage was achieved at $800\text{--}850^\circ\text{C}$. This result compares very favorably with relative density data, Figure 3. By means of optimized heat treatment (30 min at 700°C and 10 min at 850°C), a low-porosity (3.2%), low-CET ($2.38 \times 10^{-6}\text{ }^\circ\text{C}^{-1}$), and low-dielectric constant (9.97 ± 0.84) material was obtained.

3.1. Crystallization and Particle Size. According to previous work [4], very fine powders of β -spodumene-based glass ceramics show crystallization on the surface rather than in the bulk because of very high specific surface area. Figure 4 shows DSC of two LZSA glass powders differing in size: powder *a* is of small grain size ($d_{50} \sim 2.34\ \mu\text{m}$) and exhibits a pronounced exothermic peak centered at approximately 790°C indicating intensive crystallization of $\beta\text{-LiAl}[\text{Si}_2\text{O}_6]$

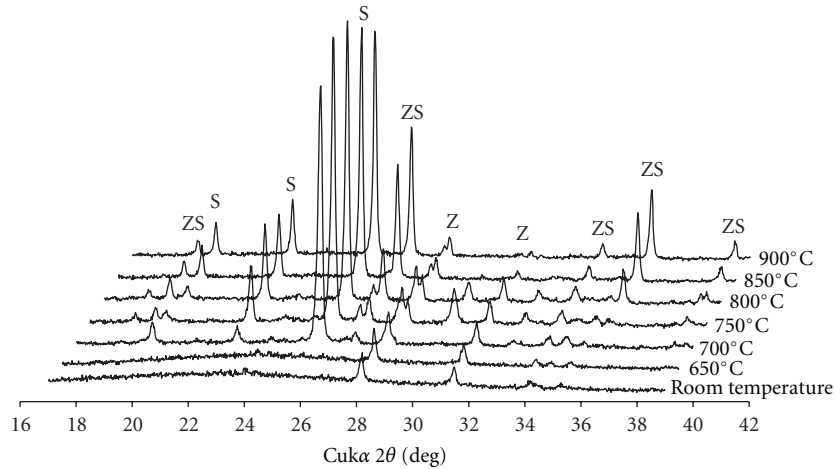


FIGURE 5: HT-XRD patterns recorded on a powdered sample in the specified temperatures: S: β -LiAl[Si₂O₆]-ss; ZS: ZrSiO₄; Z: ZrO₂.

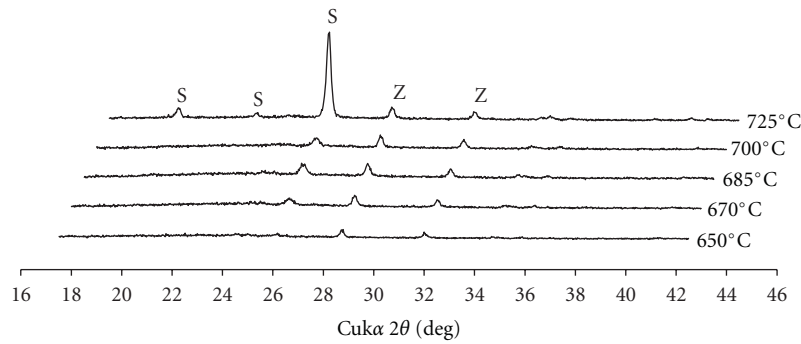


FIGURE 6: XRD patterns recorded of the samples after heat treatment for 10 min in the specified temperatures: S: β -LiAl[Si₂O₆]-ss; ZS: ZrSiO₄; Z: ZrO₂.

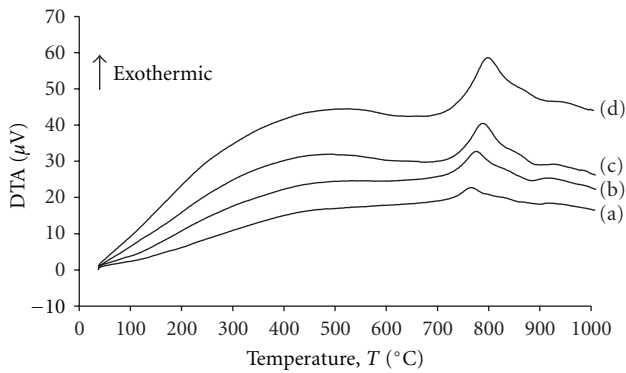


FIGURE 7: DTA scans at different heating rates of the selected glass: (a) 5°C·min⁻¹; (b) 10°C·min⁻¹; (c) 15°C·min⁻¹; (d) 20°C·min⁻¹.

during heating; powder *b* has a significantly larger particle size ($d_{50} \sim 500\text{--}700 \mu\text{m}$) and a small peak at approximately 840°C. Thus, with decreasing particle size, the temperature of the exothermic peak maximum was shifted to lower temperatures. From the magnitude of the peak temperature shift with the particle size, ΔT_x , it was concluded that surface crystallization should dominate over volume crystallization

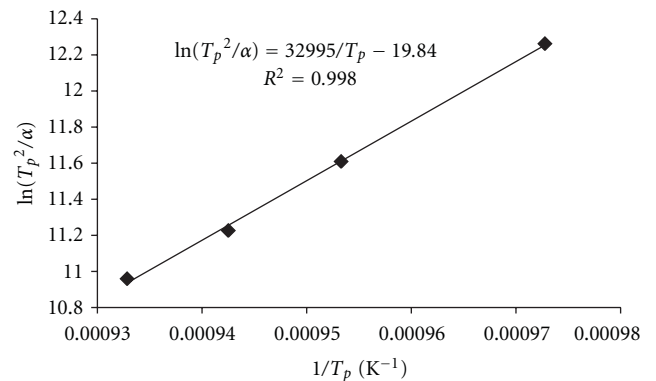


FIGURE 8: Apparent activation energy for crystallization plot for the selected glass based on (2) with $n = m = 1$.

when $\Delta T_x > 20^\circ\text{C}$ whereas volumetric crystallization was expected to prevail for $\Delta T_x < 10^\circ\text{C}$ [19]. Since for the LSZA glass $\Delta T_x \sim 50^\circ\text{C}$ for the two grain sizes studied surface crystallization is concluded to dominate devitrification which is in good agreement with previous work for similar glasses [4]. Thus, the results confirm a distinct particle size effect on the

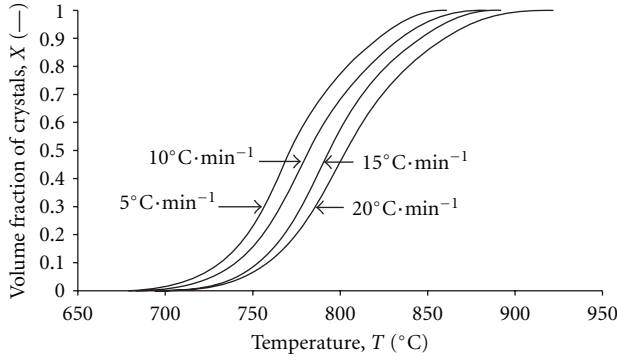


FIGURE 9: Measurement of the crystallization progress from normalization and integration of the DTA scans.

crystallization of β -LiAl[Si₂O₆] which for small particle sizes will be dominated mainly by surface crystallization. Hence, for larger particle size, crystallization rate will be slower and volumetric crystallization will increase at a given heating rate [14].

3.2. Crystalline Phase Composition. HT-XRD patterns recorded on a powdered sample in the temperature range of 650–950°C are shown in Figure 5. Additional powder samples were prepared and heat-treated at 650, 670, 685, 700, and 725°C for 10 min in order to obtain new XRD patterns as shown in Figure 6. At room temperature the material is essentially vitreous except for traces of zirconia (monoclinic ZrO₂, *m*-ZrO₂) (Figure 5). Due to the limited cooling rate and small solubility, precipitation of *m*-ZrO₂ may have occurred even during quenching. Crystallization of β -spodumene solid solution (Li₀₋₆Al₀₋₆Si₂₋₄O₆, ICDD card no. 21-503; LiAlSi₃O₈, ICDD card no. 15-27) was found to commence at approximately 670°C (Figure 6). A pronounced acceleration was observed at temperatures above 725°C. The peak maxima occurred at 800°C which coincides with the results of DTA measurements. Above 750°C zircon (ZrSiO₄, ICDD card no. 6-266) crystallized as the second major phase with maxima reached at 900°C (Figure 5).

3.3. Crystallization Kinetics. DTA and DSC have widely been used to evaluate Nonisothermal crystallization kinetics [14–16, 21–23]. Based on the variation in peak crystallization temperature (T_p) with heating rate ($\alpha = dT/dt$) the apparent activation energy for crystallization, E_c , was derived from Matusita and Sakka's [22] modification of the Kissinger [21] equation:

$$\ln\left(\frac{\alpha^n}{T_p^2}\right) = -\left(\frac{mE_c}{RT_p}\right) + C, \quad (2)$$

where n and m are numerical factors related to the crystallization mechanism [12], R is the gas constant, and C is a constant. For the case when crystallization is dominated by three-dimensional crystal growth, $n = m = 3$, and for predominantly surface crystallization, $n = m = 1$. A plot of

TABLE 3: Onset temperature for each heating rate investigated.

Heating rates	T_p (°C)
5°C·min ⁻¹	755
10°C·min ⁻¹	776
15°C·min ⁻¹	788
20°C·min ⁻¹	799

$\ln(T_p^2/\alpha^n)$ against $1/T_p$ should give a straight line with slope (E_c/R). The value of the Avrami parameter n was evaluated from a common method developed by Augis and Bennett [23]:

$$n = \frac{2.5RT_p^2}{E_c\Delta w}, \quad (3)$$

where Δw is the full width of the DTA exothermic peak at the half maximum and E_c was calculated from (2). Avrami parameter n was found to be in the range of 1.0 and 1.2 and can be adjusted to a value of 1, confirming that the glass shows crystallization by surface mechanism. Then, one can consider $n = m = 1$ [9], taking into account that crystallization at different heating rates occurs on a fixed number of nuclei, and (3) can be reduced to the Kissinger equation [20].

Typical DTA scans of glasses subjected to different heating rates from 5°C/min to 20°C/min are shown in Figure 7, while T_p values are summarized in Table 3. The peak temperature T_p of the exothermic peak associated with crystallization of β -spodumene_{ss} increased from 755°C to 799°C with increasing heating rate. However, the exothermic event related to zircon crystallization is not well defined, although it was clearly recorded in the XRD patterns.

Apparent activation energy for crystallization plot is given in Figure 8. The linearity of the curve obtained for these plots suggests that a fixed number of nuclei were achieved in the crystallization [24]. Taking $n = m = 1$ values of $E_c \sim 274$ kJ/mol and $n \sim 1.2$ were derived. Hu et al. [25] reported E_c values of 415 kJ·mol⁻¹ for crystallization of β -quartz_{ss} and β -spodumene crystalline phases, whilst Lee et al. [24] measured 285 kJ·mol⁻¹ for crystallization of β -eucryptite (β -LiAl[SiO₄]).

The area under the exothermic peak can provide information about the evolution of the crystallization process. Considering the area under the exothermic peak (DTA scan) for each temperature that is proportional to the volumetric fraction of crystals (X), the crystallization progress by DTA scans with different heating rates was also evaluated (Figure 9). For each heating rate, the curves assumed typical sigmoidal shape. Crystallization started at approximately 700°C independently on all the heating rate but finished at higher temperatures as the heating rate was increased. The incubation time (τ), that is, the time necessary for β -spodumene_{ss} crystalline phase development, increases with heating rate increasing. Thus, the improvement of densification could be achieved at 20°C·min⁻¹ heating rate.

3.4. Microstructure. Figure 10 shows SEM micrographs of the microstructures observed in the parent and crystallized

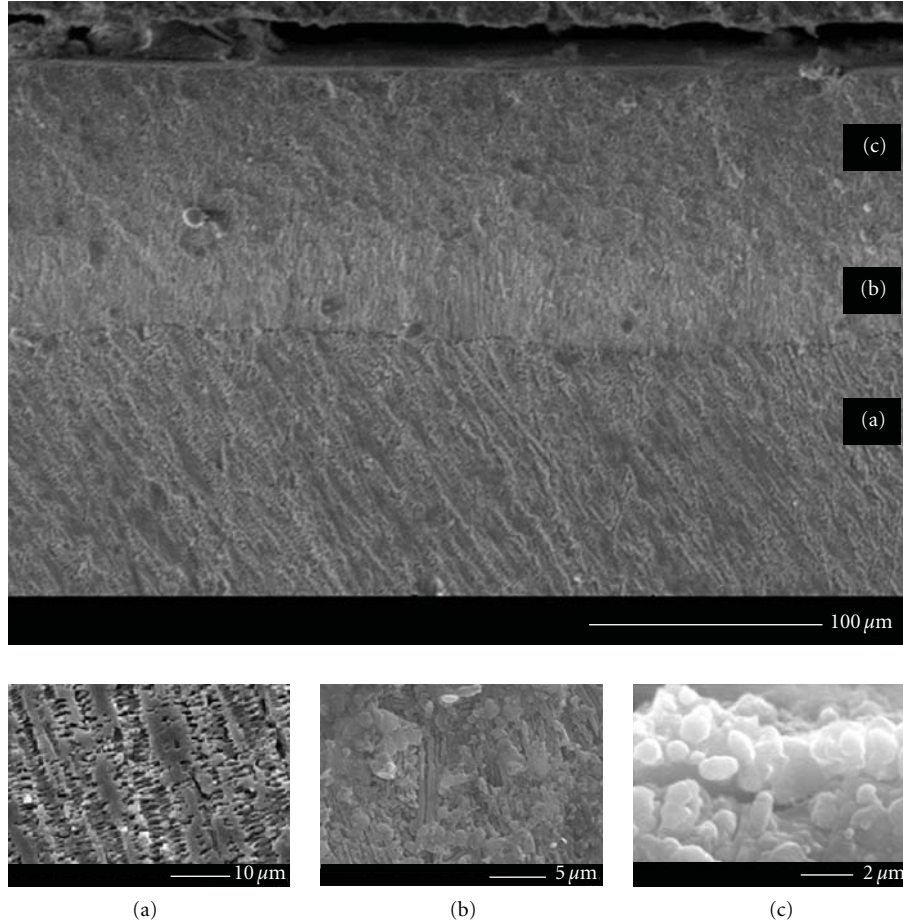


FIGURE 10: SEM image of β -spodumene-based glass ceramic monolith prepared at 875°C for 15 min: (a) parent glass; (b) first crystallization front; (c) second crystallization front.

LZSA glass ceramic. Distinct differences in morphology and distribution of crystalline precipitations are related to different stages of the crystallization process. At the beginning of the crystallization process, columnar crystals of β -spodumene_{ss} with a typical grain size of $\sim 4\mu\text{m}$ form that preferentially grow perpendicular from the surface (Figure 10(b)). This one-dimensional growth pattern is in agreement with Avrami parameter obtained ($n \sim 1.2$). With increasing crystallization time at 875°C, however, crystallites tend to form spherical particles with grain sizes of $1\mu\text{m}$ (Figure 10(c)). According to the DTA data and XRD patterns, the second front of crystalline growing should be related to the formation of zircon in the presence of β -spodumene_{ss}.

3.5. Determination of the Activation Energy of Structural Relaxation. The activation energy of structural relaxation, E_{relax} , can be related to the activation energy of viscous flow. The value for E_{relax} should give an indication of the sintering ability of a glass powder system [26]. The activation energy of structural relaxation was calculated according to the relation of Moynihan et al. [20]:

$$\ln \alpha = -\frac{E_{\text{relax}}}{RT_g} \quad (4)$$

Values of glass transition temperature, T_g , for the different heating rates were 589°C ($\alpha = 5^\circ\text{C}/\text{min}$), 600°C (10°C/min), and 607°C (15°C/min). The activation energy of structural relaxation derived from these data attained a value of $E_{\text{relax}} \sim 386\text{ kJ/mol}$ which significantly is higher than the activation energy for crystallization.

Regarding the powdered glass features (composition, mean particle size, and thermal properties), processing characteristics (temperatures and heating rates), and the final properties of the obtained glass ceramic, some properties were improved such as porosity, despite the small temperature range for sintering, and CTE. However, the control of crystallization (temperature and time) can be used to create a three-layered structure with specific thickness of each layer from glass monoliths. An internal, thinner layer mostly formed by crystals of β -spodumene_{ss} and an external, coarser layer formed by crystals of β -spodumene_{ss} and zircon could create residual stress in order to exhibit increased apparent fracture toughness and energy absorption.

4. Conclusions

Taking into account some interesting thermal and dielectric properties, a selected β -spodumene-based glass ceramic composition ($16.9\text{Li}_2\text{O}\cdot 5.0\text{ZrO}_2\cdot 65.1\text{SiO}_2\cdot 8.6\text{Al}_2\text{O}_3$) was used for crystallization kinetics investigation by means of Nonisothermal method. The crystallization mechanism was found to be predominantly surface crystallization when the particle size is small. Two crystallization fronts regarding the crystalline phases formed, β -spodumene_{ss} and zircon, were identified starting at approximately 670°C and 700°C, respectively. The morphology of the microstructures showed a columnar structure for the former and a globular for the second one. Apparent activation energy for crystallization E_c was found to be in the range 274 kJ/mol with an Avrami parameter n of 1 that is compared very favorably with SEM observations. At 850°C/10 min, a low-porosity (3.2%), low-CTE ($2.38 \times 10^{-6} \text{C}^{-1}$), low-dielectric constant (9.97 ± 0.84) material was obtained. Moreover, the dielectric loss at 1 MHz was <0.3%. A value of 386 kJ·mol⁻¹ was obtained for the activation energy of structural relaxation E_{relax} , in which its value is significantly higher than the activation energy for crystallization, hindering densification of material.

Acknowledgments

The authors are grateful to the Brazilian Foundation for the Coordination of Higher Education Graduate Training (CAPES), to the National Council of Scientific and Technological Development (CNPq), and to the German Foundation for Interchange (DAAD) for supporting this work.

References

- [1] R. R. Tummala, "Ceramic and glass ceramic packaging in the 1990s," *Journal of the American Ceramic Society*, vol. 74, pp. 895–908, 1991.
- [2] Y. Shimada, K. Utsumi, M. Suzuki, H. Takamizawa, M. Nitta, and T. Watari, "Low firing temperature multilayer glass ceramic substrate," *IEEE Transactions on Components, Hybrids, and Manufacturing Technology*, vol. 6, no. 4, pp. 382–388, 1983.
- [3] C. R. Chang and J. H. Jean, "Crystallization kinetics and mechanism of low-dielectric, low-temperature, cofirable CaO-B₂O₃-SiO₂ glass-ceramics," *Journal of the American Ceramic Society*, vol. 82, no. 7, pp. 1725–1732, 1999.
- [4] O. R. K. Montedo, F. M. Bertan, R. Piccoli, D. Hotza, A. N. Klein, and A. P. N. de Oliveira, "Low thermal expansion sintered LZSA glass-ceramics," *American Ceramic Society Bulletin*, vol. 87, no. 7, pp. 34–40, 2008.
- [5] C. M. Gomes, A. P. N. Oliveira, D. Hotza, N. Travitzky, and P. Greil, "LZSA glass-ceramic laminates: fabrication and mechanical properties," *Journal of Materials Processing Technology*, vol. 206, no. 1–3, pp. 194–201, 2008.
- [6] O. R. K. Montedo, F. J. Floriano, J. de Oliveira Filho, E. Angoletto, and A. M. Bernardin, "Sintering behavior of LZSA glass-ceramics," *Materials Research*, vol. 12, no. 2, pp. 197–200, 2009.
- [7] C. M. Gomes, C. R. Rambo, A. P. N. de Oliveira et al., "Colloidal processing of glass-ceramics for laminated object manufacturing," *Journal of the American Ceramic Society*, vol. 92, no. 6, pp. 1186–1191, 2009.
- [8] W. A. Johnson and R. F. Mehl, "Reaction kinetics in processes of nucleation and growth," *AIME Transactions*, vol. 135, pp. 416–442, 1939.
- [9] I. W. Donald and B. L. Metcalfe, "Thermal properties and crystallization kinetics of a sodium aluminophosphate based glass," *Journal of Non-Crystalline Solids*, vol. 348, pp. 118–122, 2004.
- [10] A. Marotta, A. Buri, and F. Branda, "Surface and bulk crystallization in non-isothermal devitrification of glasses," *Thermochimica Acta*, vol. 40, pp. 397–403, 1980.
- [11] F. Branda, "Nucleation and crystal growth in inorganic glass-forming systems: a DTA study," *Thermochimica Acta*, vol. 203, pp. 373–378, 1992.
- [12] I. W. Donald, "The crystallization kinetics of a glass based on the cordierite composition studied by DTA and DSC," *Journal of Materials Science*, vol. 30, no. 4, pp. 904–915, 1995.
- [13] A. P. N. de Oliveira, A. B. Corradi, L. Barbieri, C. Leonelli, and T. Manfredini, "The effect of the addition of ZrSiO₄ on the crystallization of 30Li₂O/70SiO₂ powdered glass," *Thermochimica Acta*, vol. 286, no. 2, pp. 375–386, 1996.
- [14] Y. Hu and C. L. Huang, "Crystallization kinetics of the LiNbO₃-SiO₂-Al₂O₃ glass," *Journal of Non-Crystalline Solids*, vol. 278, no. 1–3, pp. 170–177, 2000.
- [15] H. Shao, K. Liang, and F. Peng, "Crystallization kinetics of MgO-Al₂O₃-SiO₂ glass-ceramics," *Ceramics International*, vol. 30, no. 6, pp. 927–930, 2004.
- [16] E. R. Shaaban, "Non-isothermal crystallization kinetic studies on a ternary, Sb_{0.14}As_{0.38}Se_{0.48} chalcogenide semi-conducting glass," *Physica B*, vol. 373, no. 2, pp. 211–216, 2006.
- [17] M. S. Bapna and H. J. Mueller, "Thermodynamic characterization for devitrification of a micaceous dental glass-ceramic," *Journal of the American Ceramic Society*, vol. 82, no. 7, pp. 1771–1776, 1999.
- [18] B. Karmakar, P. Kundu, S. Jana, and R. N. Dwivedi, "Crystallization kinetics and mechanism of low-expansion lithium aluminosilicate glass-ceramics by dilatometry," *Journal of the American Ceramic Society*, vol. 85, no. 10, pp. 2572–2574, 2002.
- [19] R. K. Thakur and S. Thiagarajan, "Studies in catalyzed crystallization of glasses: a DTA method," *Glass and Ceramic Bulletin*, vol. 13, pp. 33–45, 1966.
- [20] C. T. Moynihan, A. J. Easteal, M. A. Debolt, and J. Tucker, "Dependence of the fictive temperature of glass on cooling rate," *Journal of the American Ceramic Society*, vol. 59, pp. 12–16, 1976.
- [21] H. E. Kissinger, "Variation of peak temperature with heating rate in differential thermal analysis," *Journal of Research of the National Bureau of Standards*, vol. 57, pp. 217–221, 1956.
- [22] T. Ozawa, "Kinetics of non-isothermal crystallization," *Polymer*, vol. 12, no. 3, pp. 150–158, 1971.
- [23] J. A. Augis and J. E. Bennett, "Calculation of the Avrami parameters for heterogeneous solid state reactions using a modification of the Kissinger method," *Journal of Thermal Analysis*, vol. 13, no. 2, pp. 283–292, 1978.
- [24] K. Lee, D. A. Hirschfeld, and J. J. Brown, "In situ whisker-reinforced β -eucryptite glass-ceramic: I, morphology and crystallization kinetics," *Journal of the American Ceramic Society*, vol. 79, no. 3, pp. 597–602, 1996.

- [25] A. M. Hu, M. Li, D. L. M. Dali, and K. M. Liang, "Crystallization and properties of a spodumene-willemite glass ceramic," *Thermochimica Acta*, vol. 437, no. 1-2, pp. 110–113, 2005.
- [26] E. M. Rabinovich, "Preparation of glass by sintering," *Journal of Materials Science*, vol. 20, no. 12, pp. 4259–4297, 1985.

Review Article

Formation and Device Application of Ge Nanowire Heterostructures via Rapid Thermal Annealing

Jianshi Tang,¹ Chiu-Yen Wang,² Faxian Xiu,^{1,3} Yi Zhou,¹ Lih-Juann Chen,² and Kang L. Wang¹

¹Device Research Laboratory, Department of Electrical Engineering, University of California, Los Angeles, CA 90095, USA

²Department of Materials Science and Engineering, National Tsing Hua University, Hsinchu 30013, Taiwan

³Department of Electrical and Computer Engineering, Iowa State University, Ames, IA 50014, USA

Correspondence should be addressed to Kang L. Wang, wang@ee.ucla.edu

Received 21 April 2011; Accepted 14 June 2011

Academic Editor: Joseph Lai

Copyright © 2011 Jianshi Tang et al. This is an open access article distributed under the Creative Commons Attribution License, which permits unrestricted use, distribution, and reproduction in any medium, provided the original work is properly cited.

We reviewed the formation of Ge nanowire heterostructure and its field-effect characteristics by a controlled reaction between a single-crystalline Ge nanowire and Ni contact pads using a facile rapid thermal annealing process. Scanning electron microscopy and transmission electron microscopy demonstrated a wide temperature range of 400~500°C to convert the Ge nanowire to a single-crystalline Ni₂Ge/Ge/Ni₂Ge nanowire heterostructure with atomically sharp interfaces. More importantly, we studied the effect of oxide confinement during the formation of nickel germanides in a Ge nanowire. In contrast to the formation of Ni₂Ge/Ge/Ni₂Ge nanowire heterostructures, a segment of high-quality epitaxial NiGe was formed between Ni₂Ge with the confinement of Al₂O₃ during annealing. A twisted epitaxial growth mode was observed in both two Ge nanowire heterostructures to accommodate the large lattice mismatch in the Ni_xGe/Ge interface. Moreover, we have demonstrated field-effect transistors using the nickel germanide regions as source/drain contacts to the Ge nanowire channel. Our Ge nanowire transistors have shown a high-performance *p*-type behavior with a high on/off ratio of 10⁵ and a field-effect hole mobility of 210 cm²/Vs, which showed a significant improvement compared with that from unreacted Ge nanowire transistors.

1. Introduction

As an important one-dimensional material, semiconductor nanowire has attracted enormous research interest for its unique electrical properties, which has promising applications as building blocks for nanoelectronics [1–5]. Since 2004, there have been a lot of efforts on studying the thermal diffusion of metal into a single-crystalline Si nanowire, in which a silicide/silicon/silicide nanowire heterostructure is formed by solid-state reactions between the Si nanowire and metal contacts. Many metals (contact pads or nanowires) have been studied as the diffusion source, such as Ni [6–8], Co [9], Pt [10], and Mn [11]. One of the salient features in this nanowire heterostructure is the atomically sharp interface between the Si nanowire and the formed silicide nanowire. Such clean interface may help to avoid Fermi-level pinning effect, which is commonly observed in conventional metal-semiconductor contacts [12]. Also, the nanowire

heterostructure can be easily used to fabricate nanowire field-effect transistors (FETs) using the formed silicide regions as the source/drain contacts to the Si nanowire channel [6, 7, 10]. The channel length can be well controlled by the annealing time and growth length of silicide, therefore, can be aggressively shrunk down to sub-50 nm [11]. Clearly, this process offers great advantages over modern high-cost and complex photolithography technology to fabricate short-channel transistors and may further facilitate the advance of scaled nanodevices.

Compared with Si nanowire, metal-Ge nanowire is a new system of interest, since Ge is an important complement to Si with even higher carrier mobilities for further device miniaturization compatible to the existing CMOS technology [1, 2]. For Ge, the atomically sharp interface is of particular interest to alleviate the Fermi-level pinning effect in the metal-Ge contact, since Ge has a high density of interface states due to native defects on the Ge surface [12].

Experimentally, Yamane et al. have demonstrated the epitaxial growth of high-quality Fe₃Si on Ge(111) substrate with an atomically controlled interface, which successfully depined the Fermi-level of Fe₃Si/Ge contact [19]. It is, therefore, highly desirable to achieve a metallic contact to Ge with a high-quality interface. On the other hand, many germanides, such as Mn₅Ge₃ and Ni₃Ge, exhibit ferromagnetism above room temperature [20, 21], and thus offer great advantages over silicides for future applications in spintronics, such as realizing spin injection into semiconductor from a ferromagnetic contact. Therefore, there is an increasing research interest on the metal-Ge nanowire system, such as Ni-Ge [13–15] and Cu-Ge [16–18]. For comparison, Table 1 briefly summarizes the literature report of Si and Ge nanowire heterostructures formed by solid-state reactions between a semiconductor nanowire and metal contacts. It is noted that the annealing temperature of metal-Ge nanowire system is usually lower than that of metal-Si nanowire system, which is partially due to a lower melting point of Ge than Si. The low-temperature process in metal-Ge nanowire systems is favorable to reduce the thermal budget in forming nanowire heterostructures toward future process integration.

In this paper, we will first discuss the formation of single-crystalline Ge nanowire heterostructure by the solid-state reaction between a Ge nanowire and Ni contact pads. By a comparative study of with or without an Al₂O₃ capping layer during annealing, we study the effect of oxide confinement in the growth of germanide in a Ge nanowire. A detailed transmission electron microscopy (TEM) analysis including the epitaxial relationships is presented in this section. In the second part of this paper, we will introduce electrical characterizations of Ge nanowire back-gate FETs fabricated using the Ge nanowire heterostructures. Specifically, the effect of Al₂O₃ capping layer on the device performance is studied in this section. Finally, we will discuss the possible research directions for future work on the Ge nanowire heterostructures, especially for promising applications in spintronics and further study on the growth dynamics.

2. Experimental Results

The growth of Ge nanowires can be accomplished by a variety of techniques. In this study, two popular methods were employed to synthesize single-crystalline Ge nanowire with $\langle 111 \rangle$ growth direction. One is the supercritical fluid-liquid-solid (SFLS) approach, in which Ge nanowires were produced in highly pressurized supercritical fluids enriched with organogermane precursors and metal nanocrystals as catalyst [22, 23]. The typical diameter of as-synthesized Ge nanowires is around 40–50 nm and the length could be more than 10 μm . The other approach is the vapor-liquid-solid (VLS) method, in which metal (such as Au) catalyzed Ge nanowires were grown on SiO₂/Si(100) substrates by means of chemical vapor deposition (CVD) using a gaseous Ge precursor GeH₄ [24]. The VLS-grown Ge nanowires are typically 70–80 nm in diameter and have lengths over 10 μm . The reported carrier mobility of VLS-grown Ge nanowires is higher than SFLS-synthesized Ge nanowires [13, 14], while

the latter method is claimed to provide a better control of the nanowire size and a higher product yield [23, 25]. In both two methods, Ge nanowires are not doped on purpose during growth, but unintentional doping usually occurs [26, 27].

To form Ni_xGe/Ge nanowire heterostructures, SFLS-synthesized Ge nanowires diluted in isopropyl alcohol (IPA) were dispersed onto a SiO₂/Si substrate. The top thermal SiO₂ was about 330 nm thick. The Si substrate was degenerately doped with a resistivity of $1\text{--}5 \times 10^{-3} \Omega\text{-cm}$, which served as a back gate for further device characterization. E-beam lithography (EBL) was used to define Ni contacts to Ge nanowires. Before e-beam evaporation of about 120 nm-thick Ni (with the purity of 99.995% and in vacuum at a pressure lower than 10^{-6} Torr), the sample was dipped into diluted hydrofluoric acid (HF) for 15 s to completely remove native oxide in the contact region. A field-emission scanning electron microscopy (JEOL JSM-6700 FESEM) was used to examine the sample morphology before and after the annealing process. Figures 1(a) and 1(b) show the device schematics before and after the thermal diffusion of Ni into the Ge nanowire. Figure 1(c) shows the SEM image of the as-fabricated Ge nanowire device showing a uniform contrast. Then the sample was annealed with rapid thermal annealing (RTA) in the ambient of N₂ to allow Ni thermal intrusion into Ge nanowire and subsequently form Ni_xGe/Ge heterostructures along the nanowire. In the previous study on the interfacial reactions of Ni thin film on Ge(111) substrate, the germanide phase formation sequence was found to be Ni₂Ge and NiGe at increasing temperatures in the range of 160°C to 600°C [28]. Various annealing temperatures ranging from 400°C to 700°C were used in this study to optimize the formation of nanowire heterostructures. It is found out that Ge nanowires were easily broken at a high annealing temperature ($>550^\circ\text{C}$) due to the significant reduction of the melting point for Ge nanowires compared with that of bulk Ge [29]. When the temperature decreased to 400°C–500°C, clear diffusion of Ni into the Ge nanowire was also observed and the formed germanide was identified to be Ni₂Ge (refer to the TEM analysis later). Figure 1(d) shows the SEM image of the Ge nanowire device upon RTA at 500°C for 60 s, in which clear contrast was observed between the Ge nanowire and the formed nickel germanide nanowire due to the conductivity difference. The remained Ge region was easily controlled down to 650 nm, and it can be further reduced to sub-100 nm [11, 16]. Similar contrast was also observed after RTA at 400°C for 40 s, as shown in Figure 1(e).

In order to identify the phase of the formed germanide and the epitaxial relationship of germanide-germanium interface, *in situ* TEM was used to study the formation process and reaction kinetics. To prepare the TEM sample, the single-crystalline Ge nanowires were dispersed on the TEM grid with a square opening of a Si₃N₄ thin film. The low-stress Si₃N₄ film was deposited by low-pressure chemical vapor deposition (LPCVD). The Si₃N₄ film was about 50 nm thick, which provided a reliable mechanical support for Ge nanowire devices during the fabrication process and at the same time to assure it is transparent to the electron

TABLE 1: Summary of Si and Ge nanowire heterostructures formed by solid-state reactions between a semiconductor nanowire and metal contacts.

Material system	Annealing condition ($^{\circ}\text{C}$)	Formed silicide/germanide	Metal diffusion source
Ni-Si [6]	550	NiSi	Ni contact pad
Ni-Si [7]	470	NiSi_x (not identified)	Ni contact pad
Ni-Si [8]	500–700	NiSi	Ni nanowire
	700	CoSi	Co nanodots
Co-Si [9]	800	Co_2Si	Co nanodots
Pt-Si [10]	520	PtSi	Pt contact pad
Mn-Si [11]	650	MnSi	Mn contact pad
Ni-Ge [13]	400–500	Ni_2Ge	Ni contact pad
Ni-Ge [14]	450 (capped with Al_2O_3)	$\text{Ni}_2\text{Ge}/\text{NiGe}$	Ni contact pad
Ni-Ge [15]	300–450	Ni_2Ge	Ni contact pad
Cu-Ge [16–18]	310	Cu_3Ge	Cu contact pad

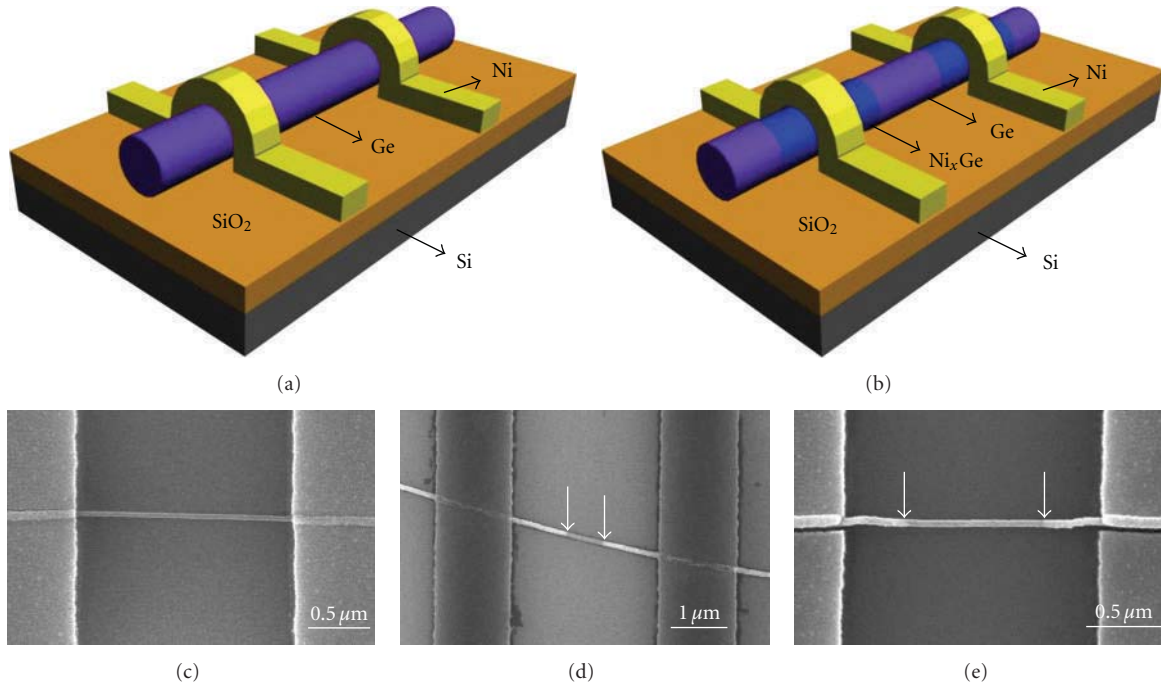


FIGURE 1: Formation of $\text{Ni}_2\text{Ge}/\text{Ge}/\text{Ni}_2\text{Ge}$ heterostructures. Schematic illustration showing (a) before and (b) after the diffusion process of Ni into the Ge nanowire forming a $\text{Ni}_2\text{Ge}/\text{Ge}/\text{Ni}_2\text{Ge}$ heterostructure. (c) SEM image of the Ge nanowire device with EBL defined Ni electrodes. (d) SEM image of the $\text{Ni}_2\text{Ge}/\text{Ge}/\text{Ni}_2\text{Ge}$ heterostructure after RTA at 500°C for 60 s in which the length of the Ge region was easily controlled to submicron range. The arrows indicate the growth tips of the Ni_2Ge nanowire. (e) SEM image of the $\text{Ni}_2\text{Ge}/\text{Ge}/\text{Ni}_2\text{Ge}$ heterostructure after RTA at 400°C for 40 s. The arrows indicate the growth tips of the Ni_2Ge nanowire. Reproduced from [13].

beam without interference with images of the nanowires. EBL-defined Ni pads were employed as the Ni diffusion source. A JEOL-2010 TEM (operated at 200 KV with a point-to-point resolution of 0.25 nm) attached with an energy dispersive spectrometer (EDS) was used to investigate the microstructures and to determine the compositions of the samples. To *in situ* observe the reactions of the Ni electrodes with Ge nanowires, the samples were heated inside TEM with a heating holder (Gatan 652 double tilt heating holder connected with a power supply to heat up the samples to the desired temperature) under a RTA mode with a pressure

below 10^{-6} Torr. Figures 2(a)–2(c) show high-resolution TEM (HRTEM) images of the formed $\text{Ni}_x\text{Ge}/\text{Ge}$ interface upon 500°C annealing. According to the lattice-resolved HRTEM analysis, the formed germanide was identified to be single-crystalline Ni_2Ge with an orthorhombic lattice structure and lattice constants $a = 0.511$ nm, $b = 0.383$ nm, and $c = 0.726$ nm (space group 62). It was observed that a large lattice mismatch of 56.3% at the $\text{Ni}_2\text{Ge}/\text{Ge}$ epitaxial interface could result in the segregation of nanoparticles (see Figure 4). In Figure 2(b), a clean and sharp interface between $\text{Ni}_2\text{Ge}/\text{Ge}$ was observed with an approximately 1 nm GeO_x

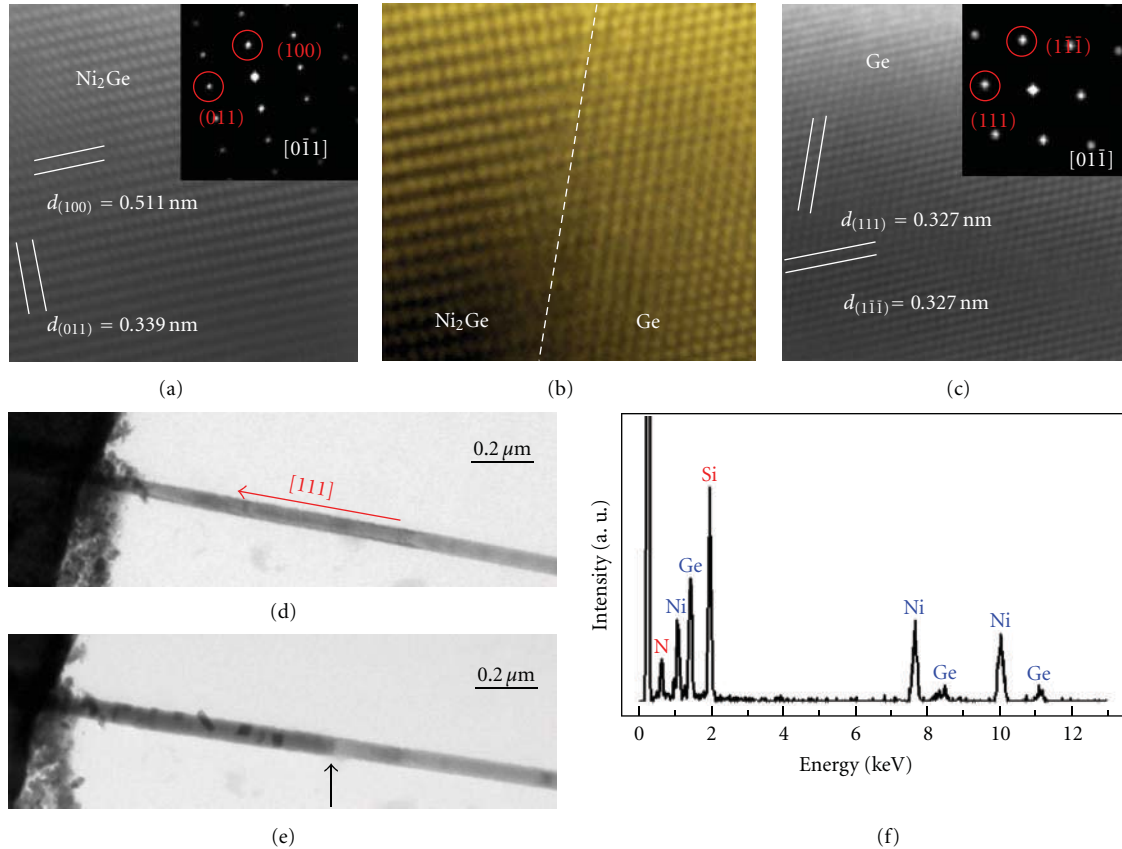


FIGURE 2: Epitaxial relationship at the Ni₂Ge/Ge interface. (a) Lattice-resolved TEM image of the formed Ni₂Ge nanowire. The inset shows the FFT pattern, confirming that the formed germanide phase is Ni₂Ge. (b) TEM image of Ni₂Ge/Ge heterostructure showing an atomically sharp interface. (c) Lattice-resolved TEM image of the unreacted Ge nanowire. The inset shows the FFT pattern. (d) Low magnification TEM image of the as-fabricated device with the Ni pad and the Ge nanowire. (e) Low magnification TEM image after annealing at 500°C. The arrow indicates the interface of the Ni₂Ge/Ge nanowire. (f) EDS of Ni₂Ge, showing a relative 2 : 1 concentration ratio of Ni and Ge atoms. Reproduced from [13].

shell surrounding both the Ge and Ni₂Ge regions. The insets in Figures 2(a) and 2(c) illustrate the fast Fourier transform (FFT) patterns of Ni₂Ge and Ge HRTEM images, respectively. The crystallographic epitaxial relationships between Ge and Ni₂Ge are shown to be Ge[011̄]/Ni₂Ge[011̄] and Ge(111̄)/Ni₂Ge(100), as we discussed. Figures 2(d) and 2(e) show the low-magnification TEM images of Ge NWs before and after annealing at 500°C, respectively. Figure 2(f) shows the EDS of the formed germanide nanowire region, showing that the ratio of Ni to Ge concentration is about 2 : 1, which further supports the fact that the formed germanide phase is Ni₂Ge. The signals of Si and N peaks are contributed from the Si₃N₄ window.

Real-time observation on the Ni₂Ge growth in a Ge nanowire was performed using *in situ* TEM video, which allows us to obtain lattice-resolved TEM images of the epitaxial interface in progression and thus to estimate the growth velocity. Figure 3(a) shows the relation of Ni₂Ge nanowire length versus the reaction time at 400 and 500°C, illustrating a potentially linear growth behavior of Ni₂Ge in the Ge nanowires, while the detailed growth mechanism requires further study. Figures 3(b), 3(c), 3(d), and 3(e)

show the *in situ* TEM images of the Ni₂Ge nanowire growth at 400 and 500°C, respectively. The growth length of the Ni₂Ge nanowire is 138.9 nm for 455 s at 400°C and 357.5 nm for 340 s at 500°C, respectively. Based on the data collected on more than three nanowires, the extracted growth velocities are about 0.31 nm/s at 400°C and 1.05 nm/s at 500°C, respectively. Using the Arrhenius plot [8], the activation energy of the Ni₂Ge growth in the Ge nanowire is estimated to be $0.55 \pm 0.05 \text{ eV/atom}$.

As mentioned above, due to a large lattice mismatch on the Ni₂Ge/Ge epitaxial interface, the resulting huge strain in the Ni₂Ge/Ge/Ni₂Ge nanowire heterostructure could lead to the segregation of Ni₂Ge nanoparticles on the Ni₂Ge nanowire after a long-time annealing. Figure 4(a) shows the TEM image of an as-fabricated Ge nanowire device with EBL-defined Ni pads at room temperature. Figures 4(b)–4(d) are a series of *in situ* TEM images of the Ge nanowire device upon 400°C, 450°C and 500°C sequential annealing, respectively. The time clocks shown at the lower-right corner in each TEM image were captured in the form of hour:minute:second. Volume expansion and segregation to form nanoparticles were clearly observed. Figure 4(e) shows a

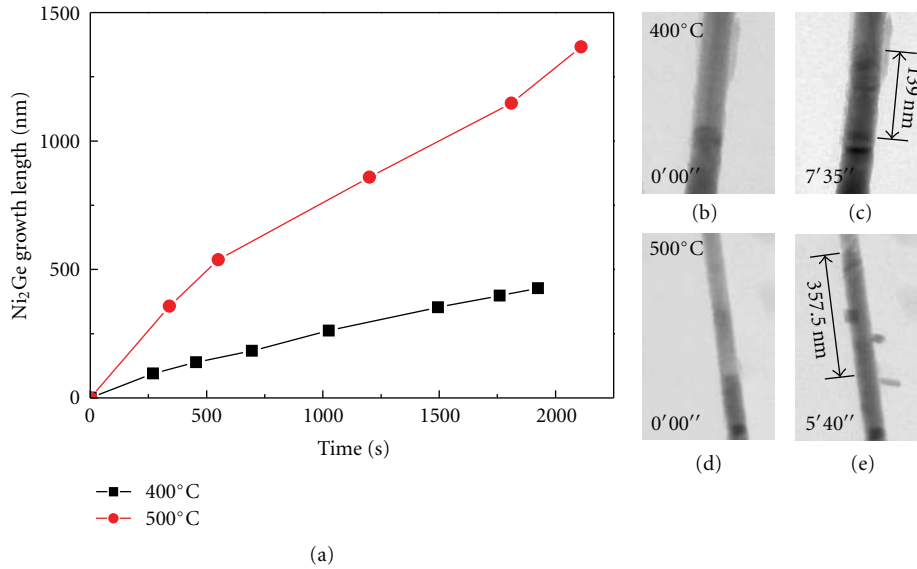


FIGURE 3: Kinetic analysis of the Ni₂Ge epitaxial growth within Ge nanowires. (a) Real-time record of the Ni₂Ge nanowire growth length versus the reaction time at 400 and 500°C, illustrating a potentially linear growth rate. (b)–(c) *In situ* TEM images of the Ni₂Ge growth within a Ge nanowire at 400°C annealing. The arrow indicates a corresponding length of 138.9 nm growth in 7 min 35 sec. (d)–(e) *In situ* TEM images of the Ni₂Ge growth within a Ge nanowire at 500°C annealing. The arrow indicates a corresponding length of 357.5 nm growth in 5 min 40 sec. Reproduced from [13].

TEM image of another Ge nanowire device annealed at 400°C for 30 min. The results in Figures 4(c)–4(e) clearly demonstrate that as a result of strain release, Ni₂Ge nanoparticles were formed and segregated on the Ni₂Ge nanowire as Ni diffused along the formed Ni₂Ge nanowire.

Similarly, the segregation of nanoparticles during annealing was also observed in the Ni-Si nanowire system as reported by Weber et al. [7]. For Si, a thin layer of high-quality native oxide is usually formed on the Si nanowire surface, while Ge does not have a stable native oxide. It is observed that the SiO₂ shell has a substantial confinement effect on the nickel silicide growth along with phase transformation in a Si nanowire [30]. We studied the effect of oxide confinement on the germanide growth in a Ge nanowire; an oxide layer, such as Al₂O₃, was deposited to cap the Ge nanowire device before the annealing process, as shown in the schematics of Figure 5(a). Figure 5(b) shows the SEM image of the as-fabricated Ge nanowire device showing uniform contrast. Prior to RTA, 20 nm thick Al₂O₃ was deposited on top by atomic layer deposition (ALD) at 250°C (Figure 5(c)). It was noticed that the diameter of the Ge nanowire was increased after the Al₂O₃ deposition since ALD provided a conformal coverage. After that the sample was then annealed with RTA in N₂ ambient to allow for the thermal intrusion of Ni into the Ge nanowire and subsequently form the Ni_xGe/Ge heterostructures along the nanowire. Clear diffusion of Ni into the Ge nanowire was observed in both SEM and TEM, and the formed germanide was analyzed in HRTEM, as to be explained further later. Figure 5(d) shows the SEM image of the Ni_xGe/Ge/Ni_xGe heterostructures after RTA

at 450°C for 20 s. Clear contrast was observed between the Ge nanowire and the formed nickel germanide nanowire, which is again attributed to the conductivity difference of the two. Figure 5(e) schematically illustrates the formation of Ni_xGe/Ge/Ni_xGe nanowire heterostructure with the Al₂O₃ confinement. The red line indicates the position where the device was cut with focused ion beam (FIB) to study the cross-sectional structure, as to be explained in Figure 6.

Figure 6(a) shows the low-magnification cross-sectional TEM image of the Ni_xGe/Ge nanowire heterostructure, which was cut with FIB from the Ge nanowire device fabricated on a SiO₂/Si wafer, as shown in Figure 5(e). Before FIB cutting, a 200 nm-thick Pt film was deposited on top to protect the Ni_xGe/Ge/Ni_xGe nanowire heterostructure from the ion beam bombardment. When preparing the cross-section of Ni_xGe for TEM analysis using FIB, we chose the position as close as to the Ni_xGe/Ge interface. It is noted that in the cross-sectional view, there were some nanoparticles segregated on the SiO₂ surface from the bottom of the formed nickel germanide, the region that was not confined by the Al₂O₃ capping layer. This result also explains the fact that we did not observe nanoparticles on the Al₂O₃ capped surface from the SEM image shown in Figure 5(d). Figure 6(b) shows the lattice-resolved HRTEM image of the interface between the formed NiGe nanowire and the segregated NiGe nanoparticle, which were both identified to be NiGe from the FFT pattern shown in the inset of Figure 6(b). NiGe has an orthorhombic lattice structure with lattice constants $a = 0.538$ nm, $b = 0.342$ nm, and $c = 0.581$ nm (space group 62). In order to further confirm the germanide phase, an EDS line scan was performed through

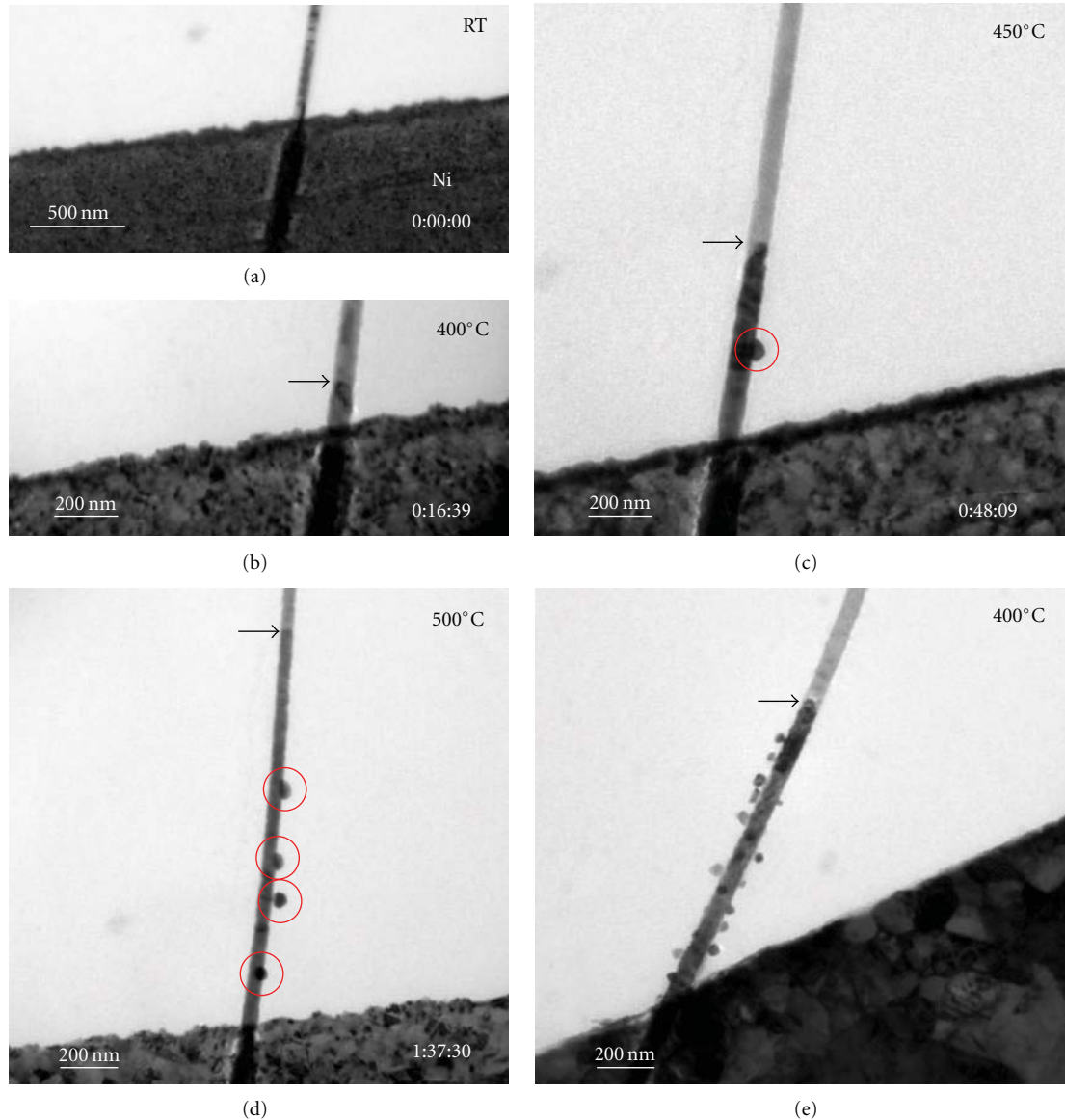


FIGURE 4: A series of *in situ* TEM images at various annealing temperatures: (a) room temperature; (b) 400°C; (c) 450°C; (d) 500°C. The arrows indicate the interface between the formed Ni_2Ge and the Ge nanowire. The red circles indicate Ni_2Ge nanoparticles segregated from the Ni_2Ge nanowire. (e) TEM image of the Ni electrode reacted with a Ge nanowire upon 400°C annealing for 30 min. Reproduced from [13].

the Al_2O_3 -capped Ni_xGe nanowire to determine the profiles of Ge, Ni, Al and O atoms, as shown in the cross-sectional TEM image in Figure 6(c) as well as the individual line-scan profile in Figures 6(d)–6(g). From Figures 6(d) and 6(e), the Ni/Ge ratio was estimated to be about 1 : 1, which further proved the NiGe phase.

To study the epitaxial relationships between Ni_xGe and Ge, the VLS-grown Ge nanowires were dispersed on the TEM grids with a square opening of a Si_3N_4 thin film, as described above. The sample preparation was similar to the process as explained above for the $\text{Ni}_2\text{Ge}/\text{Ge}/\text{Ni}_2\text{Ge}$ nanowire heterostructure. The only difference is that before the annealing process, an Al_2O_3 film was deposited by ALD

at 250°C to cap the device and confine the solid state reaction of germanidation during annealing. The Al_2O_3 -coated devices were then annealed both *in situ* (inside TEM) and *ex situ* (in RTA). Figure 7(a) shows the low-magnification TEM image of the Ni-Ge nanowire device capped with 10 nm Al_2O_3 after annealing at 450°C for 30 s. The enlarged TEM image in Figure 7(b) shows that there are clearly two interfaces in the $\text{Ni}_x\text{Ge}/\text{Ge}$ nanowire heterostructure. Figure 7(c) shows the EDS line-scan profile from the nanowire heterostructure. The line profile indicates two germanide phases in the formed Ni_xGe region, which corresponds to the two interfaces observed in the $\text{Ni}_x\text{Ge}/\text{Ge}$ heterostructure. The Ni/Ge ratio is about 1 : 1 in the small

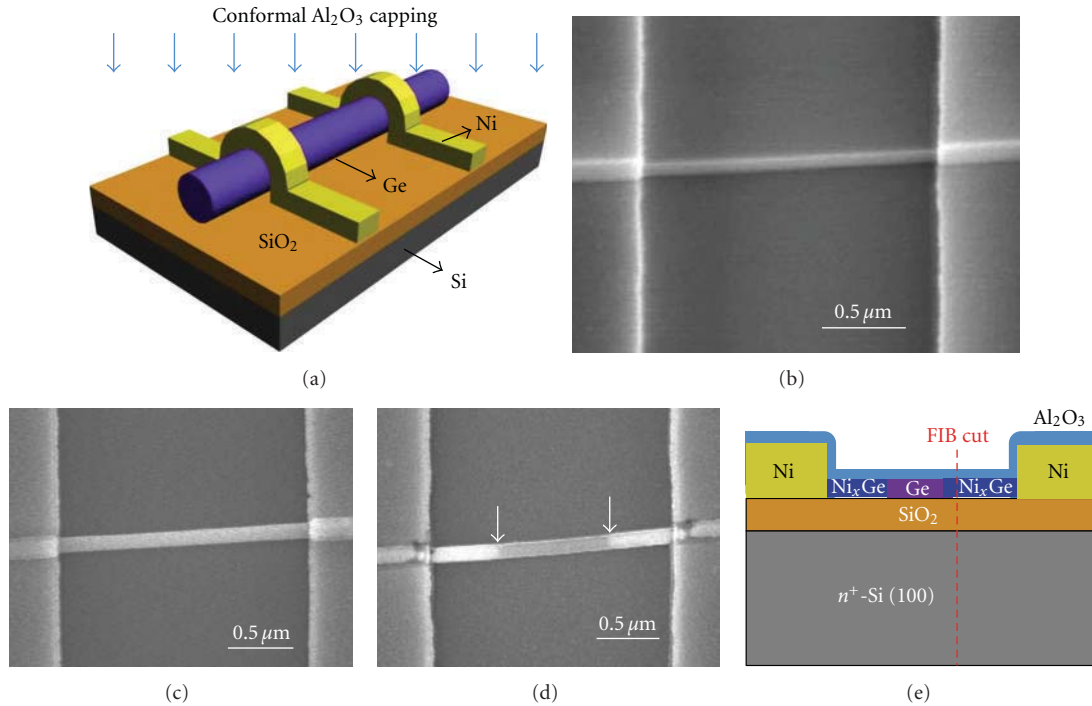


FIGURE 5: Formation of $\text{Ni}_x\text{Ge}/\text{Ge}/\text{Ni}_x\text{Ge}$ heterostructure with the Al_2O_3 confinement. (a) Schematic illustration of an Al_2O_3 conformal capping on the Ge nanowire device by ALD. (b) SEM image of the as-fabricated Ge nanowire device with EBL-defined Ni electrodes. (c) SEM image of the Ge nanowire device after a conformal capping of 20 nm thick Al_2O_3 . (d) SEM image of the $\text{Ni}_x\text{Ge}/\text{Ge}/\text{Ni}_x\text{Ge}$ heterostructure after RTA at 450°C for 20 s in which the length of the Ge region was easily controlled to be several hundred nanometers. The arrows indicate the growth tip of the Ni_xGe nanowire. (e) Schematic illustration showing the formation of $\text{Ni}_x\text{Ge}/\text{Ge}/\text{Ni}_x\text{Ge}$ nanowire heterostructure with the Al_2O_3 confinement. The red line indicates the position chosen for FIB to study the cross-sectional structure in Figure 6. Reproduced from [14].

germanide region close to the $\text{Ni}_x\text{Ge}/\text{Ge}$ interface, suggesting the formation of NiGe. This result is consistent with the line-scan profile in Figures 6(d) and 6(e). The length of the NiGe region can range from tens of nanometers to hundreds of nanometers in our experiments. On the other hand, the Ni/Ge ratio is about 2:1 in the other germanide region close to the Ni pad on the left, implying that the phase is Ni_2Ge . It is also worth noting that the almost constant concentration of Ge along the heterostructure suggests Ni is the dominant diffusion species in this system [28]. Figure 7(d) shows the lattice-resolved HRTEM image of the $\text{Ni}_x\text{Ge}/\text{Ge}$ heterostructure, clearly exhibiting two interfaces. The FFT patterns at the Ni_2Ge , NiGe, and Ge regions are shown in Figures 7(e)–7(g), which help further confirm the germanide phases. The crystallographic epitaxial relationships between the Ge/NiGe interface were determined to be $\text{Ge}[01\bar{1}]/\text{NiGe}[010]$ and $\text{Ge}(1\bar{1}\bar{1})/\text{NiGe}(001)$, while those for the $\text{Ni}_2\text{Ge}/\text{NiGe}$ interface were $\text{Ni}_2\text{Ge}[100]/\text{NiGe}[010]$ and $\text{Ni}_2\text{Ge}(011)/\text{NiGe}(001)$. It is worth noting that a large lattice mismatch of 77.7% observed at the NiGe/Ge epitaxial interface could result in the segregation of nanoparticles (see Figure 6). In contrast, the epitaxial relationships in the $\text{Ni}_2\text{Ge}/\text{Ge}/\text{Ni}_2\text{Ge}$ nanowire heterostructure formed without oxide confinement during annealing were found to be $\text{Ge}[01\bar{1}]/\text{Ni}_2\text{Ge}[0\bar{1}1]$ and $\text{Ge}(1\bar{1}\bar{1})/\text{Ni}_2\text{Ge}(100)$, as we discussed [13]. Therefore, the Al_2O_3 capping layer plays an

important role in confining the growth of germanides and also promoting the formation of NiGe to maintain high-quality epitaxial relationships between Ni_2Ge and Ge.

Figure 8 schematically illustrates the epitaxial relationships of the $\text{Ni}_2\text{Ge}/\text{Ge}$ interface in the $\text{Ni}_2\text{Ge}/\text{Ge}/\text{Ni}_2\text{Ge}$ nanowire heterostructure and the NiGe/Ge interface in the $\text{Ni}_2\text{Ge}/\text{NiGe}/\text{Ge}/\text{NiGe}/\text{Ni}_2\text{Ge}$ nanowire heterostructure. According to the epitaxial relationships in both cases, the nanowire growth direction (along the Ge [111] direction) is not perpendicular to the epitaxial planes (parallel to the Ge $(1\bar{1}\bar{1})$ plane). This “twisted” growth mode of nanowires is substantially different from that in the typical epitaxial growth of thin films, in which the growth direction is usually perpendicular to the epitaxial planes [31]. The presence of the oxide capping may alter the energy of the growth and thus change the twisted angle. Furthermore, it suggests that the twisting in nanowires may be used to accommodate substantially large lattice mismatches. This unique growth mode may be attributed to the fact in minimizing the total system energy in the presence of a large lattice mismatch in the interface. Further microscopic studies in simulation and experiment are required to understand the growth kinetics for this unique growth mode in one-dimensional systems.

The formed atomically sharp interface in the $\text{Ni}_x\text{Ge}/\text{Ge}/\text{Ni}_x\text{Ge}$ nanowire heterostructures (both with and without Al_2O_3 capping during annealing) can be used

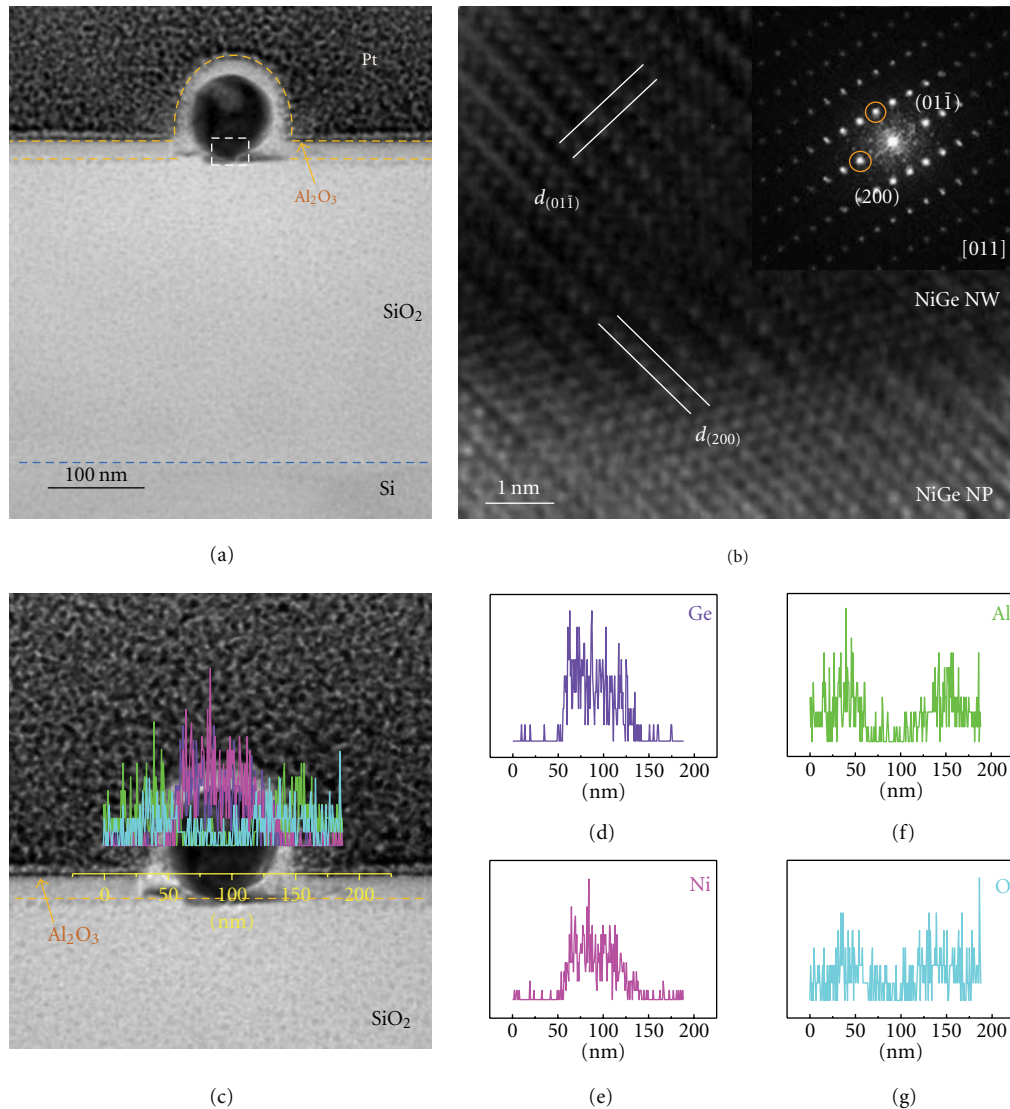


FIGURE 6: Cross-sectional TEM study of a Ni-Ge nanowire device on a SiO₂/Si substrate cut with FIB. (a) Low-magnification cross-sectional TEM image of the NiGe region. The 20 nm thick Al₂O₃ film provides a conformal capping on the device surface and germanide nanoparticles are clearly observed as they segregated underneath the nanowire, the region that is not covered by Al₂O₃. (b) Lattice-resolved HRTEM image of the interface between the formed NiGe nanowire (NW) and the segregated NiGe nanoparticle (NP), as indicated by the white rectangle in Figure 5(a). The inset shows the corresponding FFT pattern. The labeled lattice spacings for NiGe are: $d_{(01\bar{1})} = 0.295$ nm and $d_{(200)} = 0.269$ nm. (c) Cross-sectional TEM image with the line-scan profiles of Ge, Ni, Al and O atoms. (d)–(g) The individual line-scan profile of Ge, Ni, Al, and O atoms, respectively, The Ni/Ge ratio is about 1 : 1. Reproduced from [14].

to explore promising applications in nanoscale devices [6, 7, 10, 16]. As aforementioned, this Ni_xGe/Ge/Ni_xGe nanowire heterostructure can be easily used to fabricate Ge nanowire FETs, in which the germanide regions Ni_xGe can be used as source/drain contacts to the Ge nanowire channel. The channel length can be simply controlled by the annealing time and growth length of the germanide nanowire; therefore, it can be well controlled to sub-100 nm using a convenient RTA process. Clearly, this simple process has a great advantage over traditional complex and expensive photolithography technology in achieving short-channel transistors.

Back-gate FETs were fabricated on the SiO₂/Si substrate to study the electrical transport property of the Ni₂Ge/Ge/Ni₂Ge nanowire heterostructure. The Si substrate is degenerately doped to serve as a back gate. The device schematic is shown in Figure 9(a), and electrical measurements were performed using a probe station with a Keithley 4200 semiconductor parameter analyzer. For comparison, Figure 9(b) shows the logarithm plot of typical I_{ds} - V_{gs} curves for the Ge nanowire FET at various drain voltages before and after RTA. They both show a p-type transistor behavior, although we intended to grow undoped Ge nanowires. This is mainly due to the Fermi level pinning at the Ge nanowire

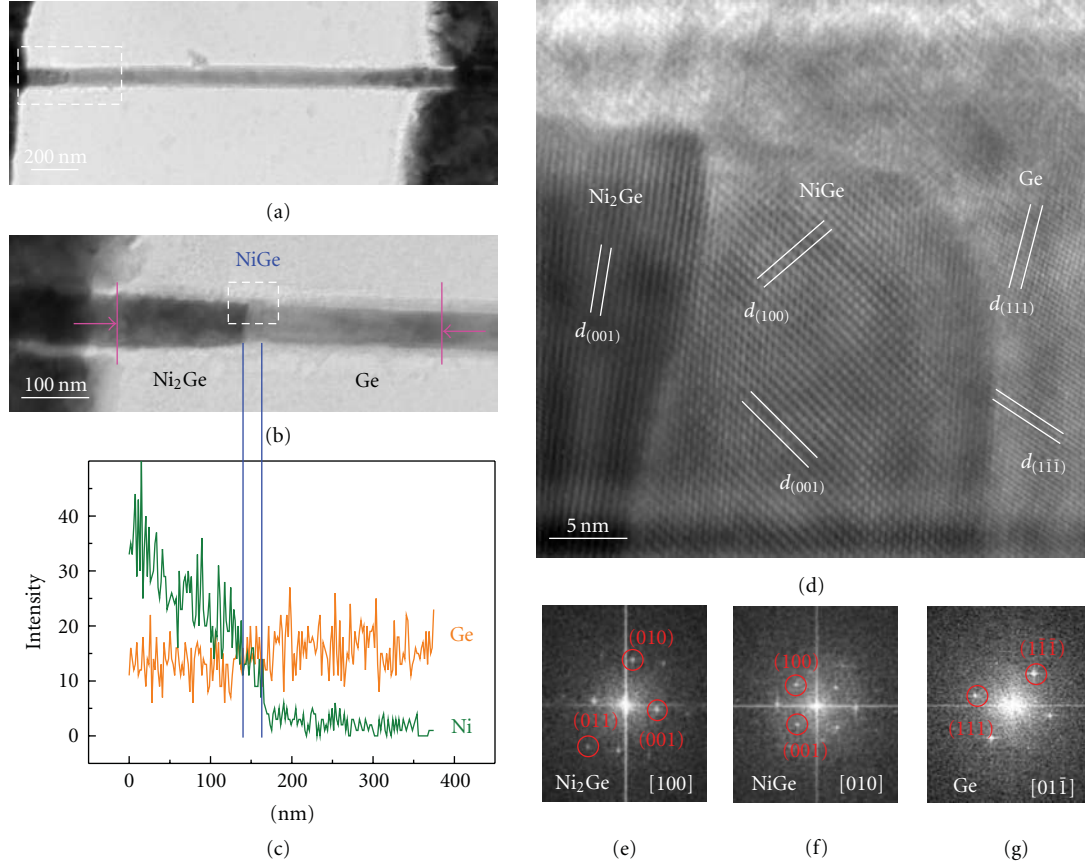


FIGURE 7: Plane-view TEM images of Ni-Ge nanowire devices on a TEM grid with a 50 nm thick Si_3N_4 window. (a) Low-magnification TEM image of a Ge nanowire reacted with 120 nm thick Ni pads upon 450°C RTA for 30 s. (b) Enlarged TEM image from the white rectangle in (a). These regions with different contrasts and compositions are labeled. (c) Corresponding EDS line-scan profiles of Ge and Ni across the region between two red lines in (b). (d) Lattice-resolved TEM image of the formed $\text{Ni}_x\text{Ge}/\text{Ge}$ nanowire heterostructure from the white rectangle in (b). The labeled lattice spacings are: $d_{(001)} = 0.5036$ nm for Ni_2Ge ; $d_{(100)} = 0.538$ nm and $d_{(001)} = 0.5811$ nm for NiGe ; $d_{(111)} = 0.3265$ nm and $d_{(1-1-1)} = 0.3265$ nm for Ge. (e)–(g) are the FFT patterns taken from the Ni_2Ge , NiGe , and Ge regions in (d), respectively. Reproduced from [14].

surface induced by Ge surface states, which tends to result in hole accumulation [26, 27]. The maximum current measured before RTA at $V_{\text{ds}} = 0.5$ V is about 30 nA, corresponding to a current density of 2.4×10^3 A/cm². The current density is relatively small due to a large Schottky barrier at the source/drain contacts before annealing. To extract the mobility, we first used the cylinder-on-plate model to estimate the gate capacitance coupling between the Ge nanowire and the back-gate oxide as

$$C_{\text{ox}} = \frac{2\pi\epsilon_{\text{ox}}\epsilon_0 L}{\cosh^{-1}((r + t_{\text{ox}})/r)}, \quad (1)$$

(see [32]) where $\epsilon_0 = 8.85 \times 10^{-14}$ F/cm is the vacuum dielectric constant, $\epsilon_{\text{ox}} = 3.9$ is the relative dielectric constant for SiO_2 , and $r = 20$ nm is the radius of the Ge nanowire. The Ge nanowire channel bis $L = 3$ μm , and the thickness of the back-gate dielectric is $t_{\text{ox}} = 330$ nm. Given the above parameters, the estimated gate capacitance is $C_{\text{ox}} = 1.83 \times 10^{-16}$ F. The field effect hole mobility can be extracted from

the $I_{\text{ds}}-V_{\text{gs}}$ curves using the transconductance (g_m) at a fixed drain bias V_{ds}

$$\mu = \frac{g_m L^2}{V_{\text{ds}} C_{\text{ox}}}. \quad (2)$$

Using the maximum transconductance extracted from the $I_{\text{ds}}-V_{\text{gs}}$ curves, the hole mobility obtained falls in the range of 3–8 cm²/Vs. This is consistent with previous reported values (less than 10 cm²/Vs) for SFLS-synthesized Ge nanowires [25].

After RTA at 400°C for 15 s, however, electrical transport measurements on the Ge nanowire device show much improved transistor characteristics, as shown in Figure 9(b). The gate bias was scanned from 0 V to –40 V, the latter of which corresponds to a maximum vertical gate electrical field of 1.21×10^6 V/cm. The $I_{\text{ds}}-V_{\text{gs}}$ curves show a p-type behavior with an on/off ratio larger than 10^3 . The maximum current measured at $V_{\text{ds}} = 0.5$ V is about 0.7 μA corresponding to a current density of 5.6×10^4 A/cm², which was more than 20 times larger after annealing, in

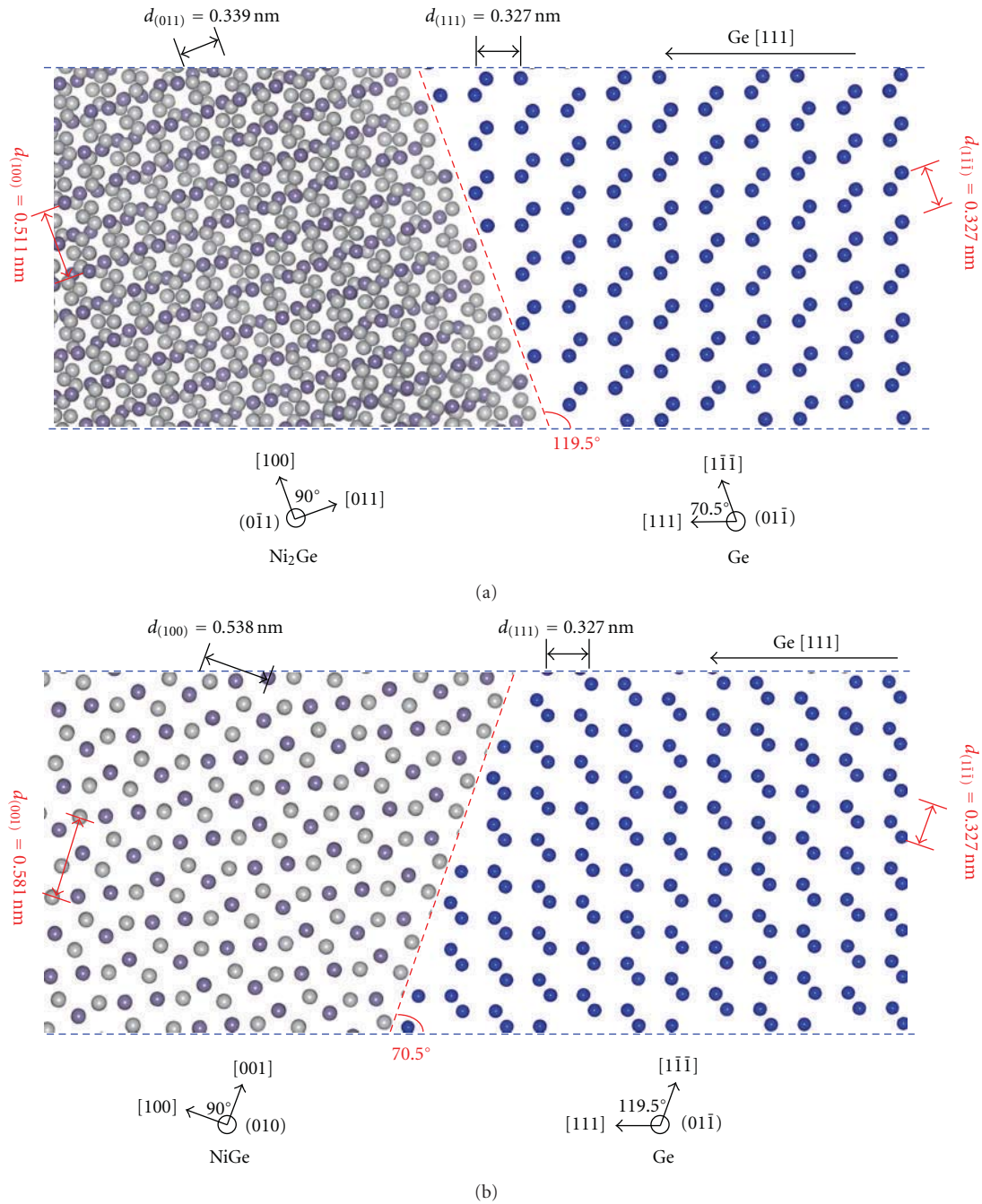


FIGURE 8: Schematic illustration of the epitaxial relationships of (a) the $\text{Ni}_2\text{Ge}/\text{Ge}$ interface in the $\text{Ni}_2\text{Ge}/\text{Ge}/\text{Ni}_2\text{Ge}$ nanowire heterostructure and (b) the NiGe/Ge interface in the $\text{Ni}_2\text{Ge}/\text{NiGe}/\text{Ge}/\text{NiGe}/\text{Ni}_2\text{Ge}$ nanowire heterostructure, respectively. Both of them show “twisted” but different growth modes. The grey and purple balls represent the Ni and Ge atoms in the Ni_xGe lattice, respectively, while the blue one represents the Ge atom in the Ge lattice. Reproduced from [14].

which the Ni_2Ge contact to the Ge nanowire channel was developed. The maximum transconductance extracted from $I_{ds}-V_{gs}$ curves at drain bias $V_{ds} = 0.1\text{ V}$ is 13.3 nS, giving rise to a field-effect hole mobility of $65.2\text{ cm}^2/\text{Vs}$. Although this mobility is still lower than the reported value from VLS-grown Ge nanowires [14, 16], it still shows about one order of magnitude improvement among SFLS-synthesized

Ge nanowires [25], and this increase may be attributed to the atomically sharp contact of Ni_2Ge to the Ge nanowire.

Similarly, the $\text{Ni}_2\text{Ge}/\text{NiGe}/\text{Ge}/\text{NiGe}/\text{Ni}_2\text{Ge}$ nanowire heterostructures formed with Al_2O_3 capping during annealing can also be used to fabricate Ge nanowire FETs. To further improve the transistor performance, VLS-grown nanowires were used in this study because of their higher

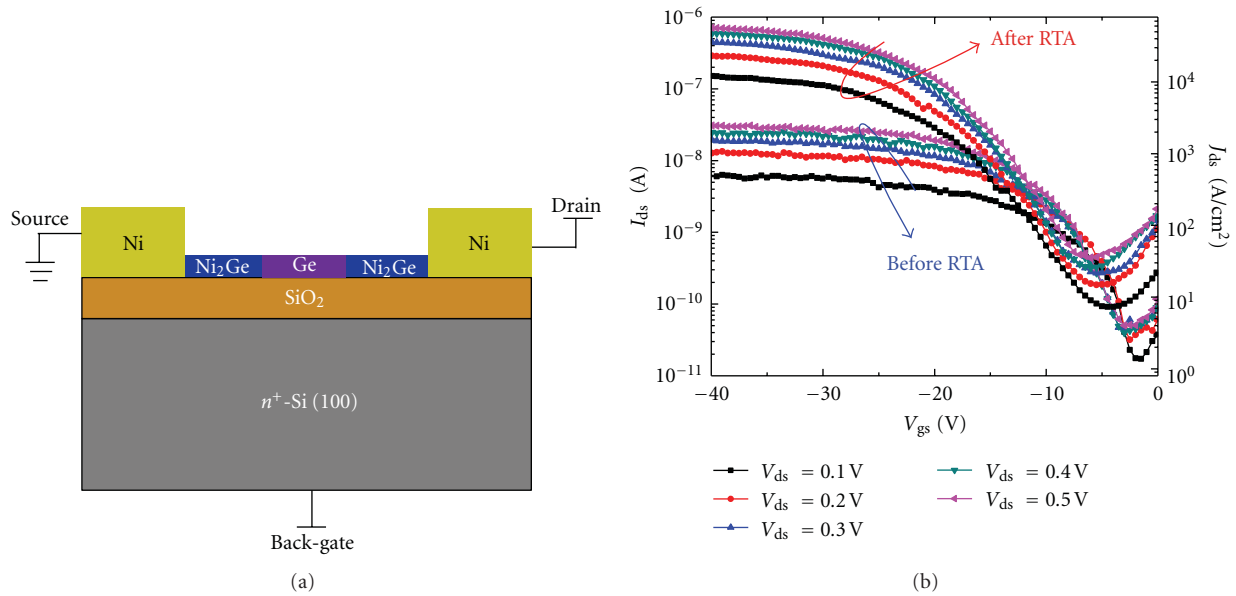


FIGURE 9: Electrical characterization of Ge nanowire back-gate FETs (without Al_2O_3 capping during annealing) at 300 K. (a) Schematic illustration of a Ge nanowire back-gate FET. (b) $I_{\text{ds}}-V_{\text{gs}}$ curves of the back-gate Ge nanowire transistor before and after RTA, both showing a p-type MOSFET behavior. The transistor performance was significantly improved after RTA, in which the Ni_2Ge source/drain contacts were formed. Reproduced from [13].

carrier mobility. Back-gate nanowire FETs were fabricated on the SiO_2/Si substrate similarly as shown in Figure 10(a). Figure 10(b) shows the typical $I_{\text{ds}}-V_{\text{gs}}$ curves of a back-gate Ge nanowire FET after RTA at 450°C for 20 s, in which the on/off ratio is as high as 10^5 . The maximum transconductance is obtained to be about $0.168 \mu\text{S}$ at $V_{\text{ds}} = 0.1 \text{ V}$, which gives rise to a normalized transconductance of $2.4 \mu\text{S}/\mu\text{m}$, assuming the effective channel length is equal to the nanowire diameter (70 nm) [10]. The extracted hole mobility in our experiments is typically in the range of $150\text{--}210 \text{ cm}^2/\text{Vs}$. Compared with SFLS-synthesized Ge nanowires, the significant improvement in the transistor performance here could be attributed to a better crystalline quality of VLS-grown Ge nanowires. Figure 10(c) shows the typical $I_{\text{ds}}-V_{\text{ds}}$ curves of a back-gate Ge nanowire FET at various gate voltages.

As explained above, the Al_2O_3 capping layer helps confine the growth of germanide in a Ge nanowire during thermal annealing. More importantly, it is of interest to study the effect of the Al_2O_3 capping layer on the device performance. In the previous study on the metal contacts to Ge substrate through a thin layer of Al_2O_3 tunneling oxide by Zhou et al., it is found that Al_2O_3 helps terminate the dangling bonds and passivate the Ge surface, therefore, alleviate Fermi level pinning effect [12]. In this study, dual sweepings of gate bias in the $I_{\text{ds}}-V_{\text{gs}}$ curves were performed to investigate the charge trapping due to the Al_2O_3 capping layer on passivating the Ge nanowire surface. Figure 10(d) shows the $I_{\text{ds}}-V_{\text{gs}}$ curves under various conditions: before Al_2O_3 deposition (both in air and in vacuum) and after Al_2O_3 deposition at 250°C . The gate bias was swept from $+40 \text{ V}$ to -40 V then back to $+40 \text{ V}$ in steps of 0.5 V at a fixed drain bias of $V_{\text{ds}} =$

20 mV . The $I_{\text{ds}}-V_{\text{gs}}$ curve measured in air before annealing shows the biggest hysteresis, which is mainly due to the absorption of molecules from the ambient and the charge trapping on the Ge surface [26, 33]. The measured reduced hysteresis in a vacuum (less than 10^{-5} Torr), however, rules out the contribution from the ambient. Also, measurements in the vacuum help reduce scatterings from the molecules absorbed on the Ge surface as carriers transport along the Ge nanowire channel, which will reduce the resistance of Ge nanowires. Furthermore, the hysteresis was significantly reduced after the Al_2O_3 deposition, which unambiguously demonstrates the passivation effect of the Al_2O_3 layer on the Ge nanowire surface [12]. Besides, the Al_2O_3 passivation could again reduce scatterings for carriers transport along the Ge nanowire channel and thus further reduce the resistance of Ge nanowires. The small hysteresis present after Al_2O_3 passivation, however, may arise from the charge trapping on the Ge surface between the Ge nanowire channel and the back-gate dielectric, the region that is not covered by the Al_2O_3 capping layer.

3. Conclusion and Discussion for Future Study

In summary, Ge nanowire heterostructures with atomically sharp interfaces have been demonstrated by the solid-state reaction between a single-crystalline Ge nanowire and Ni contact pads via a facile rapid thermal annealing process in a temperature range of $400\text{--}500^\circ\text{C}$. The crystallographic epitaxial relationships in the formation of the $\text{Ni}_2\text{Ge}/\text{Ge}/\text{Ni}_2\text{Ge}$ nanowire heterostructure were determined

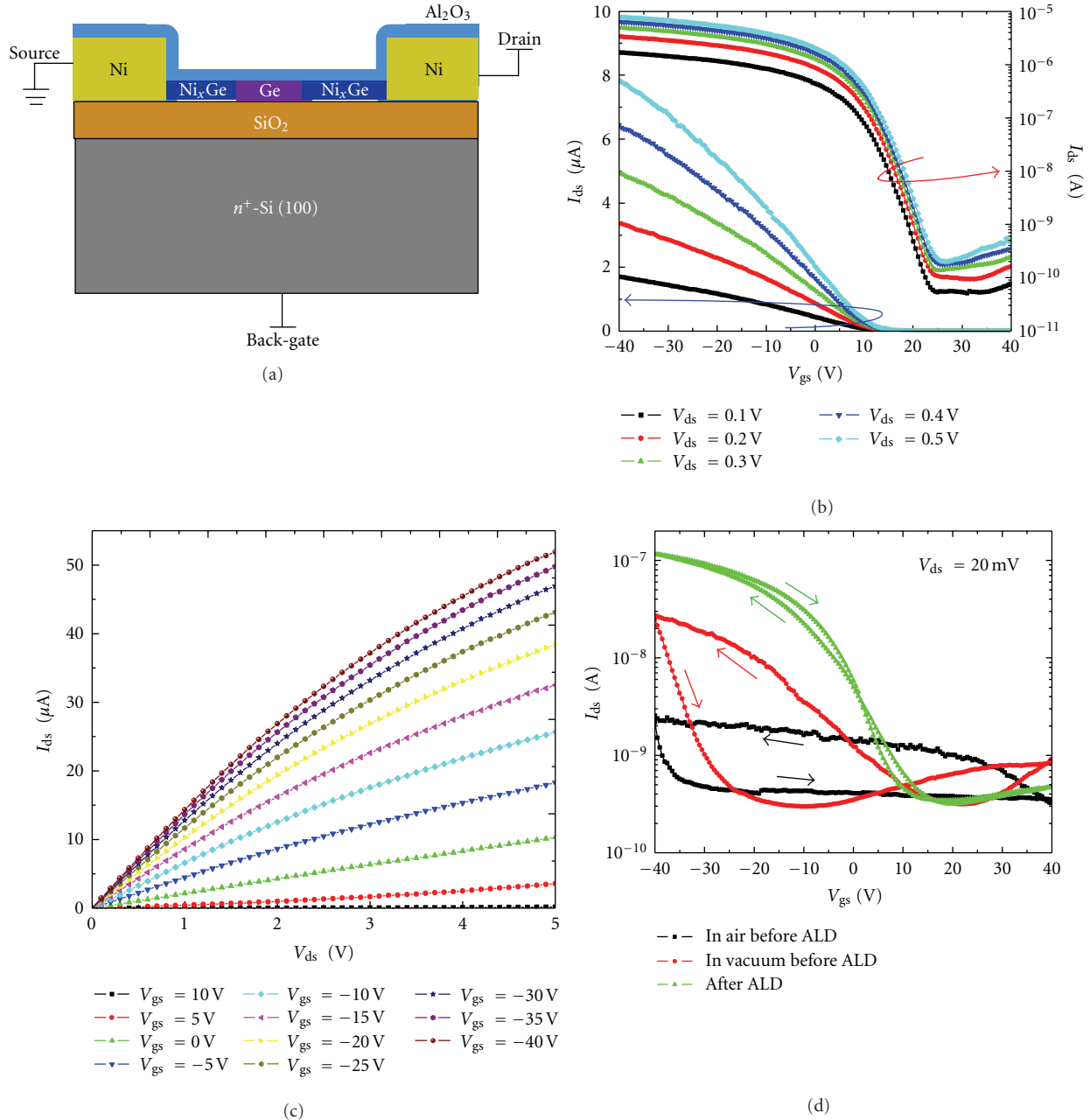


FIGURE 10: Electrical characteristics of Ge nanowire back-gate FETs (with Al₂O₃ capping during annealing) at 300 K. (a) Schematic illustration of a Ge nanowire back-gate FET. (b) I_{ds} - V_{gs} curves of the back-gate Ge nanowire transistor after RTA, showing a p-type MOSFET behavior. (c) I_{ds} - V_{ds} curves of the back-gate Ge nanowire transistor after RTA. (d) Dual sweepings of the gate bias V_{gs} between +40 V to -40 V showing different sizes of hysteresis under various conditions. The arrows indicate the sweeping directions. The hysteresis was significantly reduced after Al₂O₃ passivation. A small hysteresis was still observed after ALD, which may be attributed to the charge trapping on the Ge surface between the Ge nanowire channel and the back-gate dielectric, the region that is not covered by the Al₂O₃ capping layer. Reproduced from [14].

to be Ge[01 $\bar{1}$]/Ni₂Ge[0 $\bar{1}$ 1] and Ge(1 $\bar{1}$ $\bar{1}$)/Ni₂Ge(100). Back-gate FETs were fabricated using the formed Ni₂Ge region as source/drain contacts to the Ge nanowire channel. The electrical measurement shows an on/off ratio over 10³ and a field-effect hole mobility of about 65.4 cm²/Vs, which are superior to reported values for SFLS-synthesized Ge nanowires.

More importantly, the effect of oxide confinement on the formation of the Ge nanowire heterostructure was studied by capping the Ge nanowire device with a layer of Al₂O₃ before the annealing process. In contrast to the single germanide phase in the Ni₂Ge/Ge/Ni₂Ge nanowire heterostructure, a segment of high-quality epitaxial NiGe was then formed between Ni₂Ge and Ge. The crystallographic epitaxial

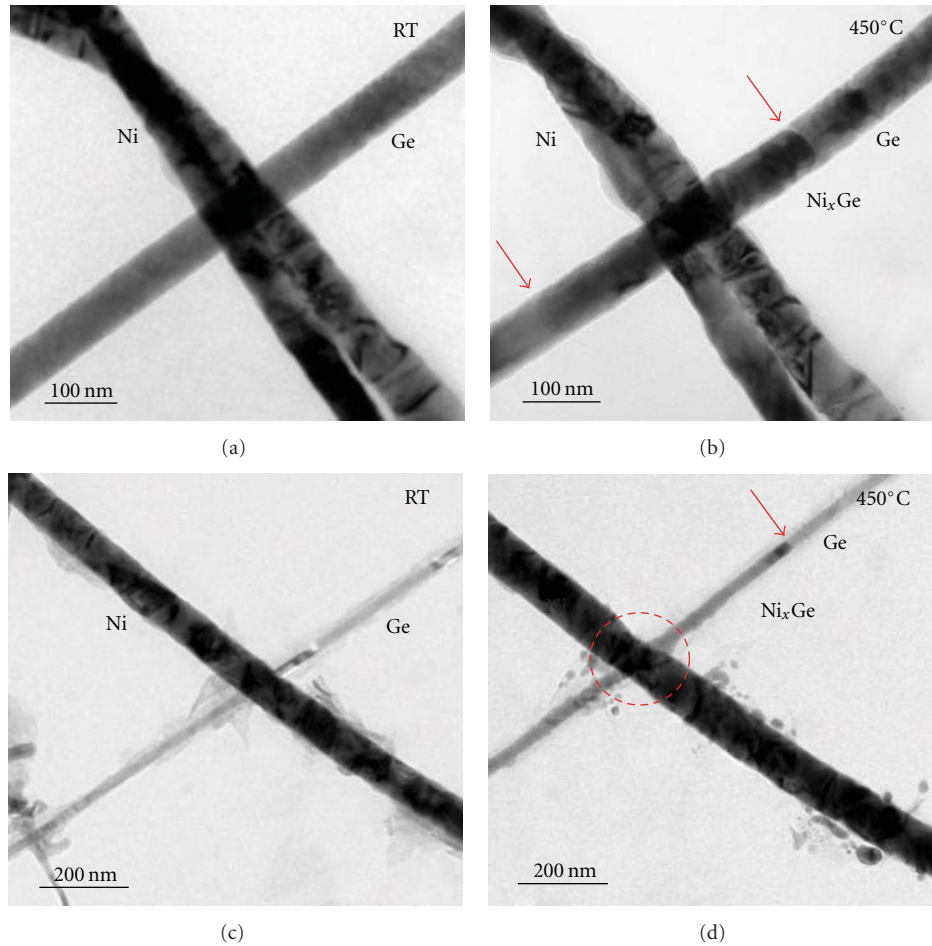


FIGURE 11: (a) TEM image of a Ge nanowire in point-contact with two Ni nanowires on the TEM grid at room temperature. (b) TEM image showing the diffusion of Ni into the Ge nanowire upon 450°C annealing. The red arrows indicate the growth tip of the Ni_xGe nanowire. (c) TEM image of another Ge nanowire in point contact with a Ni nanowire on the TEM grid at room temperature. (d) TEM image showing the diffusion of Ni into the Ge nanowire upon 450°C annealing. The red circle highlights the consumption of Ni in the formation of the Ni_xGe nanowire upon annealing. Also, the segregation of Ni_xGe nanoparticles was not observed in the Ni-Ge nanowire point-contact system upon annealing.

relationships were determined to be $\text{Ge}[01\bar{1}]/\text{NiGe}[010]$ and $\text{Ge}(1\bar{1}\bar{1})/\text{NiGe}(001)$ for the Ge/NiGe interface and $\text{Ni}_2\text{Ge}[100]/\text{NiGe}[010]$ and $\text{Ni}_2\text{Ge}(011)/\text{NiGe}(001)$ for the $\text{Ni}_2\text{Ge}/\text{NiGe}$ interface, respectively. Similarly, back-gate FETs were fabricated on the formed $\text{Ni}_2\text{Ge}/\text{NiGe}/\text{Ge}/\text{NiGe}/\text{Ni}_2\text{Ge}$ nanowire heterostructure, and the electrical measurements reveal a high-performance p-type behavior, showing a high on/off ratio of 10^5 and a field-effect hole mobility of about $210 \text{ cm}^2/\text{Vs}$. Moreover, the Al_2O_3 capping was found to passivate the Ge nanowire surface as well as to provide an appreciable confinement during the growth of germanide and changes its composition to maintain the high-quality epitaxial relationships.

For further understanding the growth kinetics of Ge nanowire heterostructures, a more detailed study is required [8, 9, 34–36]. For instance, the size of the metal diffusion (contact) source may affect the formation of Ge nanowire heterostructure, especially the segregation of nanoparticles.

In this paper, the metal source was defined with EBL and e-beam evaporation, in which the size of planar Ni contacts (typically in the μm range) is much larger than the diameter of Ge nanowires (typically below 100 nm) [13]. On the other hand, in some other studies of Si nanowire heterostructures, another extensively-studied diffusion source was metal nanowires or dots (refer to Table 1), which led to a point-contact rather than a planar contact to the Si nanowire [8, 9, 37, 38]. Similarly, we have also studied the formation of Ge nanowire heterostructures through the point contact reaction between a Ge nanowire and a Ni nanowire. Figure 11(a) shows the TEM image of a Ge nanowire in point contact with two Ni nanowires on the TEM grid at room temperature. The Ni nanowires were prepared by the electrochemical deposition, and the diameter was typically 50–100 nm which depends on the size of the anodic aluminum oxide (AAO) template. Figure 11(b) shows the TEM image, similarly illustrating the diffusion

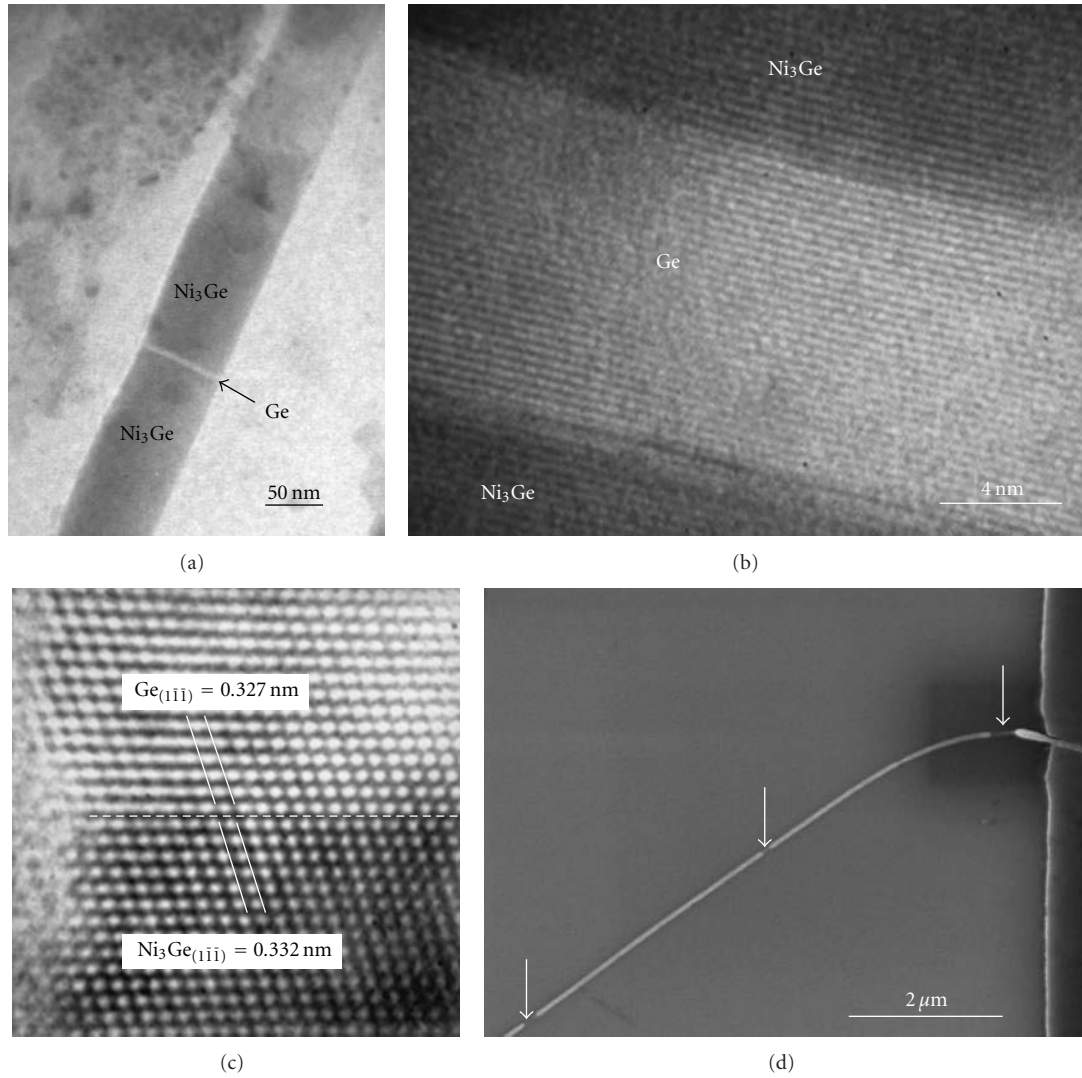


FIGURE 12: (a) TEM image of a fragmented Ni₃Ge nanowire on the TEM grid upon 650°C annealing. (b) HRTEM image of the Ni₃Ge/Ge/Ni₃Ge nanowire heterostructure showing a clean and sharp interface. (c) Lattice-resolved HRTEM image of the Ni₃Ge/Ge interface. The measured lattice mismatch was only 1.5% at the Ni₃Ge(111)/Ge(111) interface. As a result, the twisted growth mode, which was observed in both Ni₂Ge/Ge/Ni₂Ge and Ni₂Ge/NiGe/Ge/NiGe/Ni₂Ge nanowire heterostructures to accommodate the large lattice mismatch, did not occur in this Ni₃Ge/Ge/Ni₃Ge nanowire heterostructure. (d) SEM image showing a broken Ge nanowire upon 650°C RTA due to a low melting pointing of the Ge nanowire. Reproduced from [13].

of Ni into the Ge nanowire upon 450°C annealing. The red arrows indicate the growth tip of the Ni_xGe nanowire. It is worth noting that the growth of the Ni_xGe nanowire started from the point-contact region, similar to the planar contact case [13]. However, this is different from the case of the NiSi/Si/NiSi nanowire heterostructure formed via the point-contact reaction between a Si nanowire and a Ni nanowire, in which the growth of NiSi actually started from both ends of the Si nanowire instead of the point-contact region [8]. Further kinetics study is needed to understand the different phenomena in Ge and Si nanowire heterostructures. Figure 11(c) TEM image of another Ge nanowire in point-contact with a Ni nanowire at room temperature. Figure 11(d) shows the TEM image illustrating the diffusion

of Ni into the Ge nanowire upon 450°C annealing. Clear consumption of Ni in the formation of the Ni_xGe nanowire upon annealing was observed, as highlighted by the red circle. Moreover, it is surprising that the segregation of Ni_xGe nanoparticles was not observed in the Ni-Ge nanowire point-contact system upon annealing [13]. We believe that the much smaller Ni flux through such point contact compared with the planar contact may play an important role in preventing the segregation of nanoparticles. Therefore, the difference of various metal contacts in the formation of Ge nanowire heterostructures requires further study.

For the device applications, we have demonstrated in this study that the formed germanides with atomically sharp interface to Ge can be used as a good electrical contact.

Indeed, Lin et al. [11] have successfully detected the electrical spin injection into a Si nanowire from the ferromagnetic MnSi contact in the formed MnSi/Si/MnSi nanowire heterostructure. However, the signal can be observed only at relatively low temperature, since MnSi has a low Curie temperature of about 30 K. On the other hand, there are many germanides, such as Mn_5Ge_3 and Ni_3Ge , which exhibit room-temperature ferromagnetism [20, 21], and thus offer great advantages over silicides for promising applications in room-temperature spintronics, including spin injection, transport and detection.

In fact, a room-temperature ferromagnetic germanide phase, Ni_3Ge [20], was developed at high reaction temperature, in which a high-concentration Ni vapor from a large-area Ni contact pattern surrounded the Ge NWs to form a fragmented Ni_3Ge nanowire. Figure 12(a) shows the TEM image of the formed $\text{Ni}_3\text{Ge}/\text{Ge}/\text{Ni}_3\text{Ge}$ nanowire heterostructure on the TEM grid upon 650°C annealing. Figure 12(b) illustrates the HRTEM image of the Ge nanowire heterostructure with a clean and sharp interface between Ni_3Ge and Ge. The Ge region was controlled down to as small as 12 nm. The strained short Ge region in the $\text{Ni}_3\text{Ge}/\text{Ge}/\text{Ni}_3\text{Ge}$ nanowire heterostructure is promising for high-performance FETs and spintronics applications [11, 39]. Figure 12(c) shows the lattice-resolved TEM image of the Ni_3Ge -Ge interface, and the formed germanide was identified to be single-crystalline Ni_3Ge with a face-centered cubic (FCC) lattice structure (Fd3m, space group 227 and JCPDS no. 65-7680) and a lattice constant of $a = 0.574$ nm. Although a slight volume expansion was still observed, the Ni_3Ge lattice was well fit with the Ge lattice, due to their same lattice structure and a very small lattice mismatch of only 1.5% (the lattice constant of Ge is $a = 0.568$ nm). It is worth mentioning that the twisted growth mode, which was observed in both $\text{Ni}_2\text{Ge}/\text{Ge}/\text{Ni}_2\text{Ge}$ and $\text{Ni}_2\text{Ge}/\text{NiGe}/\text{Ge}/\text{NiGe}/\text{Ni}_2\text{Ge}$ nanowire heterostructures to accommodate the large lattice mismatch, did not occur in this $\text{Ni}_3\text{Ge}/\text{Ge}/\text{Ni}_3\text{Ge}$ nanowire heterostructure due to such a small lattice mismatch. However, as mentioned above, the melting point of Ge nanowires is significantly reduced from that of bulk Ge [29]. As a result, Ge nanowires were easily broken at high temperature, as shown in Figure 12(d). Therefore, a ferromagnetic germanide remains undeveloped at a relatively low temperature in order to study the spin transport in Ge nanowire.

Acknowledgments

This work was in part supported by Western Institution of Nanoelectronics (WIN) and Focus Center on Functional Engineered Nano Architectonics (FENA). The authors also acknowledged the support from National Science Council through Grant no. NSC 98-2221-E-007-104-MY3. J. Tang and C. Y. Wang contributed equally to the paper.

References

- [1] D. Wang, Q. Wang, A. Javey et al., "Germanium nanowire field-effect transistors with SiO_2 and high- κ HfO_2 gate dielectrics," *Applied Physics Letters*, vol. 83, no. 12, pp. 2432–2434, 2003.
- [2] M. I. Van Der Meulen, N. Petkov, M. A. Morris et al., "Single crystalline $\text{Ge}_{1-x}\text{Mn}_x$ nanowires as building blocks for nanoelectronics," *Nano Letters*, vol. 9, no. 1, pp. 50–56, 2009.
- [3] Y. Huang, X. Duan, Y. Cui, L. J. Lauhon, K. H. Kim, and C. M. Lieber, "Logic gates and computation from assembled nanowire building blocks," *Science*, vol. 294, no. 5545, pp. 1313–1317, 2001.
- [4] C. Thelander, H. A. Nilsson, L. E. Jensen, and L. Samuelson, "Nanowire single-electron memory," *Nano Letters*, vol. 5, no. 4, pp. 635–638, 2005.
- [5] Y. Cui, Q. Wei, H. Park, and C. M. Lieber, "Nanowire nanosensors for highly sensitive and selective detection of biological and chemical species," *Science*, vol. 293, no. 5533, pp. 1289–1292, 2001.
- [6] Y. Wu, J. Xiang, C. Yang, W. Lu, and C. M. Lieber, "Single-crystal metallic nanowires and metal/semiconductor nanowire heterostructures," *Nature*, vol. 430, no. 6995, pp. 61–65, 2004.
- [7] W. M. Weber, L. Geelhaar, A. P. Graham et al., "Silicon nanowire transistors with intruded nickel-suicide contacts," *Nano Letters*, vol. 6, no. 12, pp. 2660–2666, 2006.
- [8] K. C. Lu, W. W. Wu, H. W. Wu et al., "In situ control of atomic-scale Si layer with huge strain in the nanoheterostructure $\text{NiSi}/\text{Si}/\text{NiSi}$ through point contact reaction," *Nano Letters*, vol. 7, no. 8, pp. 2389–2394, 2007.
- [9] Y. C. Chou, W. W. Wu, S. L. Cheng et al., "In-situ TEM Observation of repeating events of nucleation in epitaxial growth of nano CoSi_2 in nanowires of Si," *Nano Letters*, vol. 8, no. 8, pp. 2194–2199, 2008.
- [10] Y. C. Lin, K. C. Lu, W. W. Wu et al., "Single crystalline PtSi nanowires, PtSi/Si/PtSi nanowire heterostructures, and nanodevices," *Nano Letters*, vol. 8, no. 3, pp. 913–918, 2008.
- [11] Y. C. Lin, Y. Chen, A. Shailos, and Y. Huang, "Detection of spin polarized carrier in silicon nanowire with single crystal MnSi as magnetic contacts," *Nano Letters*, vol. 10, no. 6, pp. 2281–2287, 2010.
- [12] Y. Zhou, M. Ogawa, X. Han, and K. L. Wang, "Alleviation of Fermi-level pinning effect on metal/germanium interface by insertion of an ultrathin aluminum oxide," *Applied Physics Letters*, vol. 93, no. 20, Article ID 202105, 2008.
- [13] J. Tang, C. Y. Wang, F. Xiu et al., "Single-crystalline $\text{Ni}_2\text{Ge}/\text{Ge}/\text{Ni}_2\text{Ge}$ nanowire heterostructure transistors," *Nanotechnology*, vol. 21, no. 50, Article ID 505704, 2010.
- [14] J. Tang, C. Y. Wang, F. Xiu et al., "Oxide-confined formation of Ge nanowire heterostructure for high-performance transistors," *ACS Nano*, vol. 5, no. 7, pp. 6008–6015, 2011.
- [15] N. S. Dellas, S. Minassian, J. M. Redwing, and S. E. Mohny, "Formation of nickel germanide contacts to Ge nanowires," *Applied Physics Letters*, vol. 97, no. 26, Article ID 263116, 2010.
- [16] T. Burchhart, A. Lugstein, Y. J. Hyun, G. Hochleitner, and E. Bertagnolli, "Atomic scale alignment of copper-germanide contacts for ge nanowire metal oxide field effect transistors," *Nano Letters*, vol. 9, no. 11, pp. 3739–3742, 2009.
- [17] T. Burchhart, C. Zeiner, Y. J. Hyun, A. Lugstein, G. Hochleitner, and E. Bertagnolli, "High performance Ω -gated Ge nanowire MOSFET with quasi-metallic source/drain contacts," *Nanotechnology*, vol. 21, no. 43, Article ID 435704, 2010.
- [18] T. Burchhart, A. Lugstein, C. Zeiner, Y. J. Hyun, G. Hochleitner, and E. Bertagnolli, "Nanowire-metal heterostructures for

- high performance MOSFETs,” *Elektrotechnik und Informationstechnik*, vol. 127, no. 6, pp. 171–175, 2010.
- [19] K. Yamane, K. Hamaya, Y. Ando et al., “Effect of atomically controlled interfaces on Fermi-level pinning at metal/Ge interfaces,” *Applied Physics Letters*, vol. 96, no. 16, Article ID 162104, 2010.
- [20] T. Izumi, M. Taniguchi, S. Kumai, and A. Sato, “Ferromagnetic properties of cyclically deformed Fe_3Ge and Ni_3Ge ,” *Philosophical Magazine*, vol. 84, no. 36, pp. 3883–3895, 2004.
- [21] M. Jamet, A. Barski, T. Devillers et al., “High-curie-temperature ferromagnetism in self-organized $\text{Ge}_{1-x}\text{Mn}_x$ nanocolumns,” *Nature Materials*, vol. 5, no. 8, pp. 653–659, 2006.
- [22] H. Y. Tuan and B. A. Korgel, “Importance of solvent-mediated phenylsilane decomposition kinetics for high-yield solution-phase silicon nanowire synthesis,” *Chemistry of Materials*, vol. 20, no. 4, pp. 1239–1241, 2008.
- [23] T. Hanrath and B. A. Korgel, “Supercritical fluid-liquid-solid (SFLS) synthesis of Si and Ge nanowires seeded by colloidal metal nanocrystals,” *Advanced Materials*, vol. 15, no. 5, pp. 437–440, 2003.
- [24] Y. L. Chueh, C. N. Boswell, C. W. Yuan et al., “Nanoscale structural engineering via phase segregation: Au-Ge system,” *Nano Letters*, vol. 10, no. 2, pp. 393–397, 2010.
- [25] A. D. Schricker, S. V. Joshi, T. Hanrath, S. K. Banerjee, and B. A. Korgel, “Temperature dependence of the field effect mobility of solution-grown germanium nanowires,” *Journal of Physical Chemistry B*, vol. 110, no. 13, pp. 6816–6823, 2006.
- [26] T. Hanrath and B. A. Korgel, “Influence of surface states on electron transport through intrinsic Ge nanowires,” *Journal of Physical Chemistry B*, vol. 109, no. 12, pp. 5518–5524, 2005.
- [27] S. Zhang, E. R. Hemesath, D. E. Perea, E. Wijaya, J. L. Lensch-Falk, and L. J. Lauhon, “Relative influence of surface states and bulk impurities on the electrical properties of Ge nanowires,” *Nano Letters*, vol. 9, no. 9, pp. 3268–3274, 2009.
- [28] Y. F. Hsieh, L. J. Chen, E. D. Marshall, and S. S. Lau, “Partial epitaxial growth of Ni_2Ge and NiGe on $\text{Ge}(1\ 1\ 1)$,” *Thin Solid Films*, vol. 162, pp. 287–294, 1988.
- [29] Y. Wu and P. Yang, “Melting and welding semiconductor nanowires in nanotubes,” *Advanced Materials*, vol. 13, no. 7, pp. 520–523, 2001.
- [30] Y. C. Lin, Y. Chen, D. Xu, and Y. Huang, “Growth of nickel silicides in Si and Si/SiO_x core/shell nanowires,” *Nano Letters*, vol. 10, no. 11, pp. 4721–4726, 2010.
- [31] Y. Zhou, W. Han, Y. Wang et al., “Investigating the origin of Fermi level pinning in Ge Schottky junctions using epitaxially grown ultrathin MgO films,” *Applied Physics Letters*, vol. 96, no. 10, Article ID 102103, 2010.
- [32] S. Ramo, J. R. Whinnery, and T. V. Duzer, *Fields and Waves in Communication Electronics*, John Wiley & Sons, New York, NY, USA, 3rd edition, 1994.
- [33] D. Wang, Y. L. Chang, Q. Wang et al., “Surface chemistry and electrical properties of germanium nanowires,” *Journal of the American Chemical Society*, vol. 126, no. 37, pp. 11602–11611, 2004.
- [34] Y. C. Chou, W. W. Wu, L. J. Chen, and K. N. Tu, “Homogeneous nucleation of epitaxial CoSi_2 and NiSi in Si nanowires,” *Nano Letters*, vol. 9, no. 6, pp. 2337–2342, 2009.
- [35] L. J. Chen and W. W. Wu, “In situ TEM investigation of dynamical changes of nanostructures,” *Materials Science and Engineering R*, vol. 70, no. 3–6, pp. 303–319, 2010.
- [36] Y. C. Chou, W. W. Wu, C. Y. Lee, C. Y. Liu, L. J. Chen, and K. N. Tu, “Heterogeneous and homogeneous nucleation of epitaxial NiSi_2 in $[1\ 1\ 0]$ Si nanowires,” *Journal of Physical Chemistry C*, vol. 115, no. 2, pp. 397–401, 2011.
- [37] K. C. Lu, K. N. Tu, W. W. Wu, L. J. Chen, B. Y. Yoo, and N. V. Myung, “Point contact reactions between Ni and Si nanowires and reactive epitaxial growth of axial nano-NiSi/Si,” *Applied Physics Letters*, vol. 90, no. 25, Article ID 253111, 2007.
- [38] W. W. Wu, K. C. Lu, C. W. Wang et al., “Growth of multiple metal/semiconductor nanoheterostructures through point and line contact reactions,” *Nano Letters*, vol. 10, no. 10, pp. 3984–3989, 2010.
- [39] W. W. Wu, K. C. Lu, K. N. Chen et al., “Controlled large strain of Ni silicide/Si/Ni silicide nanowire heterostructures and their electron transport properties,” *Applied Physics Letters*, vol. 97, no. 20, Article ID 203110, 2010.

Research Article

Thermal Effect on Structure of Silver in Ion-Exchanged Soda-Lime Glasses and Aluminum-Doped Zinc Oxide Films

Paul W. Wang,¹ Yanfeng Jiang,² Jin-Cherng Hsu,³ Yu-Yun Chen,⁴
Yung-Hsing Lin,⁴ and Huang-Lu Chen⁴

¹Department of Physics, Bradley University, 1501 W. Bradley Avenue, IL 61625, USA

²Department of Microelectronics, North China University of Technology, 5 Jinyuanzhuang Road, Shijingshan District, Beijing 100144, China

³Department of Physics, Fu-Jen Catholic University, 510 Chung-Cheng Road, Hsin-Chuang 242, Taiwan

⁴Graduate Institute of Applied Science and Engineering, Fu Jen Catholic University, 510 Chung-Cheng Road, Hsin-Chuang 242, Taiwan

Correspondence should be addressed to Paul W. Wang, pwang@bradley.edu

Received 6 April 2011; Revised 20 June 2011; Accepted 26 June 2011

Academic Editor: Joseph Lai

Copyright © 2011 Paul W. Wang et al. This is an open access article distributed under the Creative Commons Attribution License, which permits unrestricted use, distribution, and reproduction in any medium, provided the original work is properly cited.

Heat treatment is commonly used during device processing in order to achieve specific functionalities of the devices. How a series of heat treatment applies to accomplish this goal can be found in the literature. However, specific properties of the devices after the treatment are more emphasized than the details of the structural modifications in the industrial applications. In this paper, it is intended to illustrate the fundamental changes in the structure due to heat treatment which result in the desired physical properties of the devices. Two study cases, Ag ion-exchanged soda-lime glasses and aluminum doped ZnO (AZO) films, were illustrated. The changes in chemical states, the structural modification during and after heat treatment are explored. By understanding how the metallic Ag formed and accumulated during annealing, an optimum heat treatment to grow the proper size and density of silver quantum dots in the films are possible. Post annealing effect on the AZO films shows that the crystallinity, the peak positions shifts, and grain sizes were changed after annealing. Both illustrated cases indicate thermally induced changes in chemical state, the stress release, and rearrangement of atoms in materials during and after annealing.

1. Introduction

Heat treatment is commonly used to change the properties of metals, such as to soften or harden, to relieve the internal stress and to modify the grain structures [1]. Heat treatment is also widely applied to semiconductor and optoelectronic devices. For example, in order to activate the electrical properties of ultralow energy ion implanted donors and acceptors in silicon, recrystallize the damaged silicon crystal caused by ion implantation [2], and to maintain the shallow dopant depth profile similar to as-implanted profile, a subsequent rapid thermal annealing, at high ramp rate (400°C/s), short time (<1 s), and high temperature (>1000°C) annealing is required [3]. The other example is that heat treatment is used to form the quantum dots/nanocrystals after metal ions implanted in MgO, SiO₂ and Si [4–6]. Moreover, the size and density of the quantum dots in the film were closely

correlated to the annealing temperatures [7]. Even though there are so many reports of heat treatment on different materials, the specific properties of the devices after the treatments are more emphasized than the consequence of the structural modifications in the industrial applications.

Chemical states of metal atoms in optical materials play an important role in optical properties since they control the polarizability of electrons in the metal-ligand matrix under light exposure and therefore, the refractive indices of materials are greatly affected by them. They also indicate how the metal atoms form different bonds to its neighboring atoms [8]. As a result, in this paper, the structural modifications, that is, chemical states of Ag in Ag ion-exchanged soda-lime glasses and the structure of AZO films were investigated by X-ray Photoelectron Spectroscopy (XPS) and X-ray Diffractometer (XRD) during and after the heat treatment.

2. Experiment

2.1. Silver in Ion-Exchanged Soda-Lime Glasses. Silver ion-exchanged soda-lime glasses were prepared by using commercially available soda-lime glasses (72.6% SiO₂, 15.4% Na₂O, 6.3% CaO, 3.87% MgO, 1.63% Al₂O₃, and 0.2% Fe₂O₃) submerged into a molten AgNO₃ salt at 450°C for 45 min. Samples were examined by the Perkin-Elmer PHI model 560 system for XPS analyses. The X-ray was Mg K α line (1253.6 eV), produced by 15 KV electron impact on a magnesium anode at a power level of 300 W and was used as an excitation source. The pass energy was set at 25 eV to provide a 0.5 eV resolution. The heat treatment of the ion-exchanged glass sample was carried out by using a button heater underneath the metal plate on which the sample was mounted. The sample was heated in 50°C increments up to 450°C, and the photoelectrons were collected by a double-pass cylindrical mirror energy analyzer at various sample temperatures. The time that the sample was held at each temperature was 30 min which allowed the collection of XPS data. In order to separate the metallic state from an Ag3d XPS peak, a pure metal silver foil with native oxide was studied before and after 2.8-keV argon ion sputtering for 1 h by XPS. Once the spectra of the metallic silver and oxidized silver from sputtering study had been obtained, the curve fitting technique was applied to resolve the metallic and the oxidized state of Ag in Ag3d spectra. The peak position in the XPS spectrum is the binding energy of the emitted photoelectron which represents a certain chemical state. The relative surface concentration of the chemical state of that element was calculated from the integrated area of XPS peak with the atomic sensitivity factor taken into account. The calibration of the binding energy due to surface charging even after the surface was neutralized by a low energy electron flood gun was done, similar to other researchers [9], by assuming the binding energy of adventitious carbon 1s photoelectrons located at 284.6 eV.

2.2. Aluminum-Doped Zinc Oxide Films. The apparatus of the ion beam sputtering deposition (IBSD) system included an ion source used to produce an energetic ion beam for sputtering metal materials off from target and then to deposit the metal oxide onto a substrate in oxygen ambience. The ion source of this system was made by Veeco Inc. equipped with 3 cm diameter molybdenum grids. The details of the IBSD setup was previously published [10]. The high purity 99.99% zinc and aluminum metal targets with the same sizes of 12 cm \times 10 cm \times 1 cm were mounted side by side on a water-cooled copper block as shown in our previous publication [11]. The incident angle between ion beam and the normal of target surface was 45°.

Prior to mounting the substrates and pumping down the system, the 1.3 cm \times 1.3 cm B270 glass substrates were cleaned by alcohol in an ultrasonic cleaner and blown dry by nitrogen gas. The chamber was cryogenically pumped down to a base pressure of 6×10^{-6} Torr. Then the targets were cleaned *in situ* by the ion beam with a shutter to cover the substrate for 30 mins. The ion-beam voltage was kept at 1000 V with the ion-beam current at 20 mA during deposition. Argon was fed

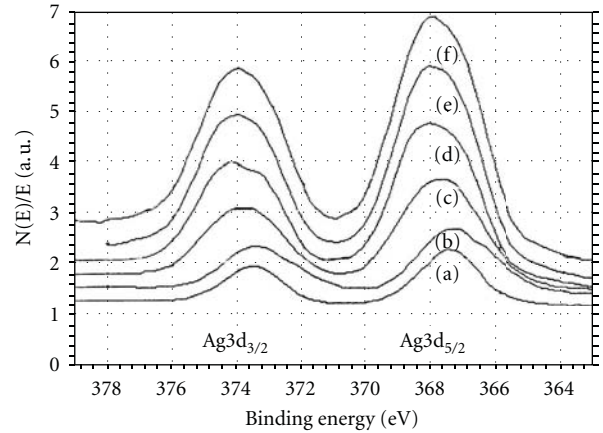


FIGURE 1: The *in situ* XPS spectra of Ag3d_{3/2} and Ag3d_{5/2} from ion-exchanged glass at various sample temperatures: (a) 20°C, (b) 100°C, (c) 200°C, (d) 300°C, (e) 400°C, and (f) 450°C.

into the ion source as a working gas and oxygen was fed into the chamber at a partial pressure of 1.2×10^{-4} Torr which was examined by our previous study of deposition ZnO film [12]. The total pressure of the chamber was maintained at 2.4×10^{-4} Torr. The AZO thin films were deposited onto B270 glass substrates at room temperature.

By adjusting the positions of two targets with respect to the Ar ion beam, the relative concentrations of Al and Zn in the films were controlled by the sputtered area ratio of the Al to Zn target. The as-deposited AZO films were annealed in air at 100, 200, 300, and 400°C, respectively. An X-ray diffraction (XRD) apparatus (Rigaku Multiflex) with a Cu K α line (1.54055 Å) was used to examine the structure of the films after annealing. The d-spacing between adjacent crystalline planes, grain sizes in the film, and the stress in the films was deduced from the diffraction angles and the full width at half maximum (FWHM) of the diffraction peak.

3. Results and Discussion

3.1. Silver in Ion-Exchanged Soda-Lime Glasses. A series of *in situ* XPS spectra under heating were shown in Figure 1(a)–1(f) where each XPS scanned the binding energy range of the photoelectron from 379 down to 363 eV at the sample temperature range from 20 to 450°C. The origin of the core level photoelectron of the element was labeled at each peak position. Not only do the binding energies of the silver peaks continuously shift, but also the line shapes of the peak change as the heating temperature increases.

In order to investigate the chemical states of silver during heating, a pure silver foil with native oxide on it was studied by ion sputtering and the XPS. The XPS spectrum of silver with silver oxide was shown in Figure 2(a) where the oxidized silver was found. Only metallic silver was seen in the XPS spectrum after 1 h of 2.8 keV argon ion sputtering shown in Figure 2(b). The binding energies and the FWHMs of oxidized silver, and metallic silver of Ag3d_{5/2} and 3d_{3/2} peaks are listed in Table 1. The FWHMs of Ag3d_{3/2} and 3d_{5/2} peaks

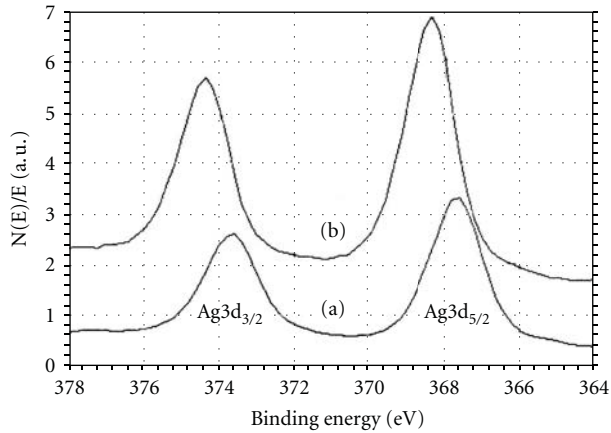


FIGURE 2: The XPS spectra of $\text{Ag}3d_{3/2}$ and $\text{Ag}3d_{5/2}$ from pure silver with native oxide (a) before sputtering and (b) after 1 h of argon ion sputtering.

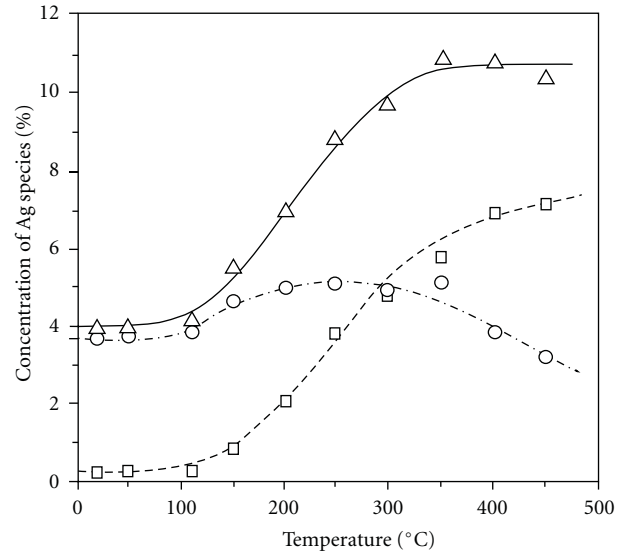
TABLE 1: The variations of FWHM and binding energy shifts of metallic silver and oxidized silver of $\text{Ag}3d_{3/2}$ and $\text{Ag}3d_{5/2}$.

States	Peak	FWHM (eV)	Binding energy (eV)
Oxidized	$3d_{3/2}$	1.62	373.61
Oxidized	$3d_{5/2}$	1.68	367.61
Metallic	$3d_{3/2}$	1.51	374.32
Metallic	$3d_{5/2}$	1.55	368.32

of metallic silver are 1.51 eV and 1.55 eV, and those of $\text{Ag}3d_{3/2}$ and $3d_{5/2}$ peaks of oxidized silver are 1.62 and 1.68 eV. It is clear that the line width of metallic silver is smaller than that of oxidized silver, and the binding energy of metallic silver is approximately 0.6 eV higher than that of oxidized silver which is consistent with the results in the literature [13]. By comparing the data listed in Table 1 and Figure 1, it is clearly seen that the metallic silver on the surface gradually increases and becomes the dominant state during the heat treatment. In other words, more Ag–O bonds break and more metallic silver is formed on the surface during the heat treatment.

The metallic, Ag^0 , and oxidized silver, Ag^+ , components in the $\text{Ag}3d$ spectra shown in Figure 1, are decomposed by using a best Gaussian curve fitting program. The two chemical states of silver, Ag^0 and Ag^+ , obtained from sputtering results in Table 1 were used as a guide to fit the spectra. The relative Ag concentrations including total, oxidized, and the metallic Ag during heating were calculated and plotted in Figure 3. A three-step growth of total Ag on the surface is clearly seen. Under 100°C the growth rate is low, then the Ag grows rapidly until 350°C , and finally it slows down. The oxidized Ag increases a little before 250°C and then decreases till 450°C , while the accumulation of metallic Ag shows a similar three-step pattern as the total Ag does.

It is clearly shown in Figure 1 that silver inside the ion-exchanged sample diffuses towards the surface during the heat treatment. Two chemical states of silver, Ag^0 and Ag^+ , were resolved by comparing the line shapes of the $\text{Ag}3d$



- Metallic Ag (%)
- Oxidized Ag (%)
- △ Total Ag (%)

FIGURE 3: The concentration changes of total, metallic, and oxidized Ag on surface at different sample temperatures. A three-step diffusion process was observed.

signals at various sample temperatures to the $\text{Ag}3d$ spectra obtained from the sputtering of a pure silver metal. The growth of the higher binding energy component of the $\text{Ag}3d$ signal indicates that the metallic silver is formed during heating.

The accumulation of silver on the surface was produced by Ag–O bond breaking during heating. This bond breaking in ion-exchanged sample results from the difference in Gibbs free energies of pure silver, silver oxide and SiO_2 . Even though the Gibbs free energy of silver oxide ($-2.68 \text{ kcal mol}^{-1}$ at 25°C) is lower than that of pure silver (0 kcal mol^{-1} at 25°C) and higher than that of SiO_2 ($\sim -200 \text{ kcal mol}^{-1}$ at 25°C), the dissociation of oxygen from Ag–O bonds to form Si–O and Ag–Ag bonds still results in a net loss in the system energy [14]. Combining this energy loss and the thermal relaxation of the surface stress introduced by the size difference between Ag^+ and Na^+ (the ratio of ionic radii, $r_{\text{Ag}^+}/r_{\text{Na}^+}$, is 1.29) [15, 16] during the ion-exchange process, surface diffusion, and accumulation of metallic silver are clear. That is to say that the Ag–O bond breaking and the Ag–Ag and Si–O bond formation are thermodynamically favorable. Thus, the oxidized silver inside the glass network diffuses to the surface and then precipitates in order to maintain the system at a minimum energy state. Since a slight amount of metallic silver on the surface after the ion-exchange process and before heat treatment was observed, these metallic silvers can serve as nuclei for the precipitation.

The new Si–O bond formation on the surface was confirmed by the line shape changes and the positive binding energy shifts of O1s and Si2p XPS peaks which were described and discussed elsewhere [17]. These metallic silver

clusters in ion-exchanged glass were also found by Fourier transform IR spectroscopy [18].

The oxidized silver is involved in the diffusion process through the same diffusion mechanism as sodium inside alkali oxide glasses [19]. Only a few oxidized silvers have enough energy to move towards the incompletely relaxed surface at low temperature; hence, little metallic silvers are seen. Once the temperature is high enough (above 100°C), many Ag–O bonds are broken as the result of a more relaxed surface and consequently, more Ag⁰ is precipitated. It is seen that the metallic silver is dominant product of the diffusion at sample temperature above 300°C. As more metallic silver and oxidized silver accumulate on the surface, either a repulsive potential must be generated which retards further diffusion or no more room for the silver to accommodate on the sample surface. This explains not only why the oxidized silver starts decreasing at 250°C but also the enrichment of total silver apparently slows down at temperature above 350°C.

3.2. Aluminum-Doped Zinc Oxide Films. Figure 4 shows the crystalline orientations of the as-deposited AZO film and films after annealed at 100, 200, 300, and 400°C observed *ex situ* by XRD. Even though a small (100) and big (002) peaks were observed between 26° and 40° as shown in Figure 4(a), only the obvious changes in (002) peak caused by the annealing were reported here. The changes of (002) peak measured by XRD *in situ* during annealing at specific temperatures were published previously [11]. It was seen that the diffraction angles changed as a function of annealing temperature in Figure 4. The double diffraction angle, 34.18°, was found in the as-deposited film; not much change in the double diffraction angles after 100, 200, and 300°C annealing which were 34.14°; 34.16°; and 34.16°, respectively. However, a big shift to 34.42° was observed in the film after 400°C annealing. The corresponding d-spacing, lattice constant, between two adjacent (002) crystalline planes was calculated by using the Bragg diffraction equation. The d-spacing in the film after being annealed at different temperatures was listed in Table 2.

The other feature in Figure 4(b) was that the intensity of the peak varied as a function of annealing temperature, very intense peak in as-deposited film, about the same but lower peak height seen in the films after annealed at 100, 200, and 300°C, and the lowest peak height after film annealed at 400°C. These peak heights as a function of annealing temperature were different when the XRD spectra were measured *in situ* at specific annealing temperatures reported previously [11] in which the peak intensity grew slowly when the annealing temperature was below 250°C but grew rapidly after 250°C. Since the intensity of the XRD peak indicates the quality of the crystallinity, a good quality of crystallinity in as-deposited film was seen, but the quality is getting worse after annealing. Energy provided by annealing activates the rearrangement of the atoms in the lattice which results in the changes of crystallinity. A significant amount of smaller Al³⁺ ions (74–104 pm radius [20]) substitute bigger Zn²⁺ ions (74–104 pm radius [20]) after 400°C annealing may result in the change in local strain, the reduction of the lattice constant, and the change of the crystalline quality.

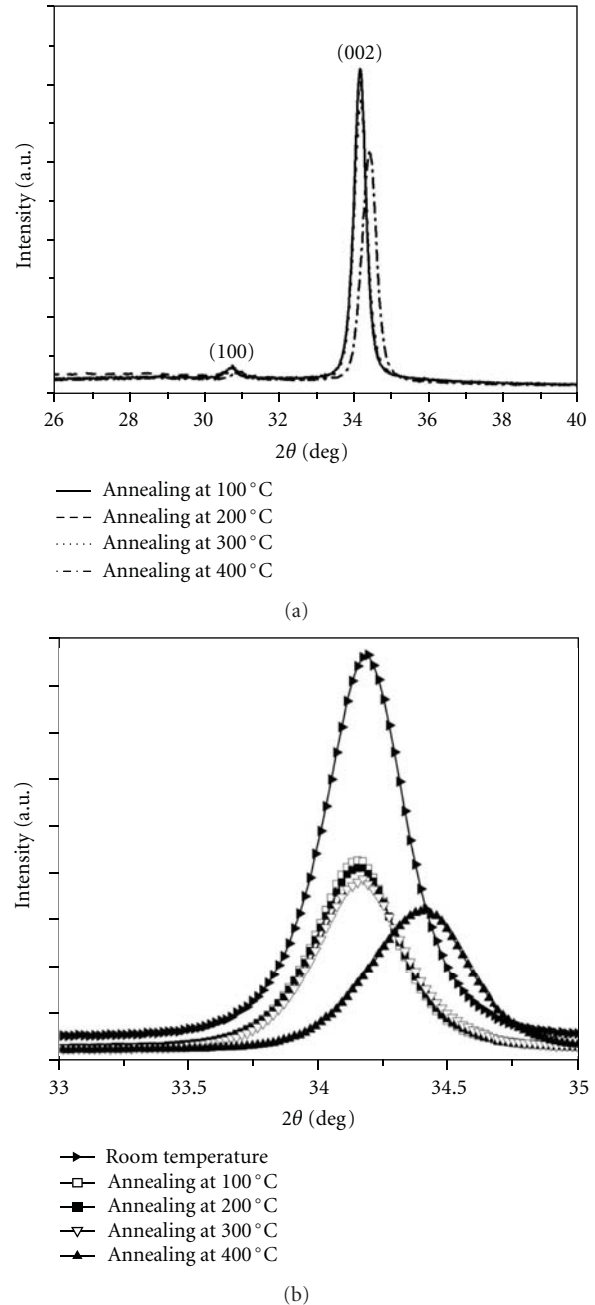


FIGURE 4: The XRD spectra of AZO films before and after annealing at various temperatures. (a) One small (100) and one big (002) peaks were observed in a range of 26° to 40° and (b) detailed variation of (002) peak as a function of annealing temperature.

From the analyses of the XRD peak shapes in Figure 4(b), the grain sizes along (002) orientation can be calculated by using the FWHM of the peak and the Scherer's formula. Both the FWHMs and the grain sizes were plotted in Figure 5 in which the higher the annealing temperature, the smaller the grain size was detected, that is, the smaller the grain size, the worse the quality of the crystallinity. The growth of the grain was expected after annealing but the opposite was observed. When the XRD spectra measured *in situ* at 400°C

TABLE 2: The d-spacing between (002) planes in AZO films under different conditions.

Film condition	2θ (°)	d-spacing (Å)
As-deposited at room temperature	34.18	2.621
After 100°C annealing and cooling down to room temperature	34.14	2.624
After 200°C annealing and cooling down to room temperature	34.16	2.623
After 300°C annealing and cooling down to room temperature	34.16	2.623
After 400°C annealing and cooling down to room temperature	34.42	2.603

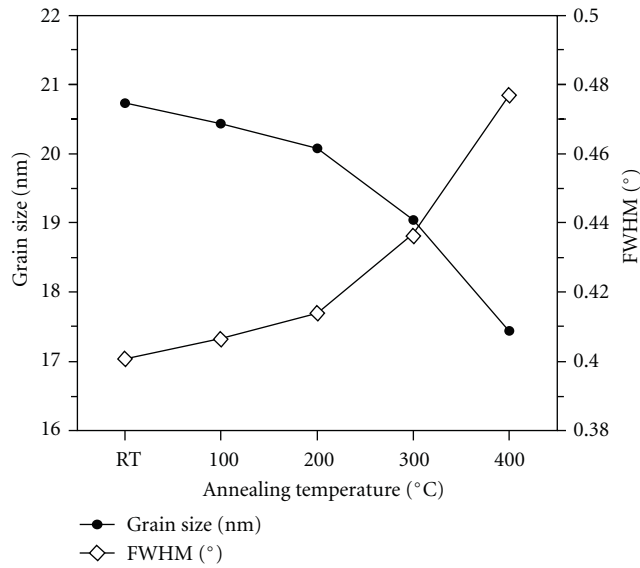


FIGURE 5: The grain sizes and FWHMs of the AZO films before and after annealing at different temperatures.

the replacement of Zn^{2+} by Al^{3+} occurred, and the increase of the grain size was observed in previous study [11]. However, when the spectra were collected *ex situ* after annealing at 400°C and cooling down to room temperature, the stress was greatly released as shown below. Cracks of the film were observed visually which resulted in the decrease of the grain size in the film. The thermally activated replacement of Zn^{2+} by Al^{3+} ions still remained in the film hence the reduction of the d-spacing was still detected.

The thermal energy may enhance or reduce the stress in the film which influences the rearrangement of the atoms in the film during the annealing. It is important to calculate the stress in the film after annealing. A biaxial strain model [21] was applied to calculate the stress in the films. The strain in the *c*-axis direction determined by XRD is $\epsilon = (C_{\text{film}} - C_0)/C_0$, where C_0 is the unstrained lattice parameter from the ZnO powder, and C_{film} is the lattice constant of the film obtained from XRD spectra. The stress σ_{film} parallel to

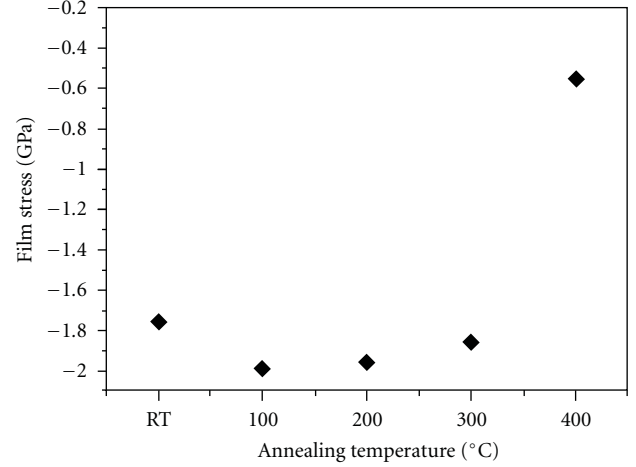


FIGURE 6: The compressive stress in the AZO film before and after annealing at different temperatures.

the film surface can be calculated by using the following formula, which is valid for the hexagonal lattice [22]:

$$\sigma_{\text{film}} = \frac{2c_{13}^2 - c_{33}(c_{11} + c_{12})}{2c_{13}} \times \frac{C_{\text{film}} - C_0}{C_0}. \quad (1)$$

For elastic constants c_{ij} , data of single ZnO crystalline have been used: $c_{11} = 208.8$, $c_{12} = 119.7$, $c_{13} = 104.2$, $c_{33} = 213.8$ GPa. The final equation of the film stress derived from XRD is deduced

$$\sigma_{\text{film}} = -233 \cdot \epsilon (\text{GPa}). \quad (2)$$

The negative sign in above equation indicates that the stress in the film is compressive stress. The compressive stress determined from the above formula as a function of the annealing temperature is shown in Figure 6. It was found that the stress increases little after 100°C annealing and then decreases little after 200 and 300°C annealing, but there are a huge decrease in stress after 400°C annealing and cooling down to room temperature. From the calculation, there is about 1.8 Gpa compressive stress in the film after the deposition at room temperature by IBSD method. This compressive stress in the film was mainly caused by the kinetic energy loss of sputtered species, the film's structure, and the surface energy difference between the film and glass substrate.

Recent study of glass substrate temperature during sputtering deposition of aluminum by Sebag et al. [23] found that the substrate temperature rose in a range of 2 to 7°C during *ca.* 100 s time interval at the beginning of the deposition. Since the temperature risen was so low, there is no thermal effect on the deposited film fabricated by the IBSD method. The sputtered species with an energy ranged typically from a few eV to tens eV lost their energies from the momentum transfer process but no thermal annealing involved during the film growth on the substrate using IBSD method. A good quality of crystallinity in as-deposited film may attribute to this high compressive stress. The change

of compressive stress in the film after the annealing results from thermally activated replacement of bigger Zn^{2+} ions by smaller Al^{3+} ions and the formation and interaction of defects, vacancies, and interstitials. Once the compressive stress was greatly released after the 400°C annealing, the grain shrunk significantly due to the cracks of the film, that is, bigger grains were cut into small pieces. It was found that the resistivity and energy band-gaps of the AZO films are correlated well to the film structure [24].

4. Conclusion

Two case studies of Ag in ion-exchanged glasses and Al-doped ZnO films during and after heat treatment clearly demonstrate the thermal effect on the structural changes in both materials. The XPS and XRD were used to monitor the *in situ* and *ex situ* structural modifications of the Ag in ion-exchanged layer and AZO films. Two chemical states of Ag resulted from the reduction of the total Gibbs energy and the stress relaxation were found during annealing. By understanding how the metallic Ag formed and accumulated during annealing, an optimum heat treatment to grow the proper size and density of silver quantum dots in the films is possible. Postannealing effect on the AZO films shows that the crystallinity of the film decreases as the annealing temperature increases while the peak position shifts toward to higher diffraction angle, and grain size decreases dramatically after 400°C annealing due to cracks in the film. All the observed property changes can be explained by the thermally activated Zn^{2+} ions replacement by Al^{3+} ions and the compressive stress in the film.

Acknowledgment

Paul W. Wang acknowledges the support from a special emphasis research grant of Bradley University.

References

- [1] J. L. Smith, G. M. Russel, and S. C. Bhatia, *Heat Treatment of Metals*, Alkem, Singapore, 2009.
- [2] A. H. Al-Bayati, K. G. Orrman-Rossiter, J. A. van den Berg, and D. G. Armour, "Composition and structure of the native Si oxide by high depth resolution medium energy ion scattering," *Surface Science*, vol. 241, no. 1-2, pp. 91-102, 1991.
- [3] A. J. Murrell, E. J. H. Collart, M. A. Foad, and D. Jennings, "Process Interactions between Low-energy Ion Implantation and Rapid-thermal Annealing for Optimized Ultrashallow Junction Formation," *Journal of Vacuum Science and Technology*, pp. 462-467, 2000.
- [4] A. Ueda, R. Mu, Y. S. Tung et al., "Interaction of F_n-centers with gold nanocrystals produced by gold ion implantation in MgO single crystals," *Nuclear Instruments and Methods in Physics Research B*, vol. 141, no. 1-4, pp. 261-267, 1998.
- [5] J. P. Zhao, Y. Meng, D. X. Huang, W. K. Chu, and J. W. Rabalais, "Sn quantum dots embedded in Si O₂ formed by low energy ion implantation," *Journal of Vacuum Science and Technology B*, vol. 25, no. 3, pp. 796-800, 2007.
- [6] A. Portavoce, R. Hull, M. C. Reuter, and F. M. Ross, "Nanometer-scale control of single quantum dot nucleation through focused ion-beam implantation," *Physical Review B*, vol. 76, no. 23, Article ID 235301, 2007.
- [7] L. Chen, Z. Q. Chen, C. Liu, and Q. Fu, "Effect of annealing temperature on density of ZnO quantum dots," *Solid State Communications*, vol. 137, no. 10, pp. 561-565, 2006.
- [8] K. Fukumi, A. Chayahara, N. Kitamura et al., "Chemical state and refractive index of Mg-ion-implanted silica glass," *Japanese Journal of Applied Physics*, vol. 41, no. 12, pp. 7447-7452, 2002.
- [9] G. M. Renlund, S. Prochazka, and R. H. Doremus, "Silicon oxycarbide glasses: part II. Structure and properties," *Journal of Materials Research*, vol. 6, pp. 2723-2734, 1991.
- [10] J.-C. Hsu, P. W. Wang, and C.-C. Lee, "X-ray photoelectron spectroscopy study of thin TiO₂ films cosputtered with Al," *Applied Optics*, vol. 45, no. 18, pp. 4303-4309, 2006.
- [11] Y.-Y. Chen, J.-C. Hsu, P. W. Wang, Y.-W. Pai, C.-Y. Wu, and Y.-H. Lin, "Dependence of resistivity on structure and composition of AZO films fabricated by ion beam co-sputtering deposition," *Applied Surface Science*, vol. 257, no. 8, pp. 3446-3450, 2011.
- [12] C. T. Chang, J. C. Hsu, P. W. Wang, and Y. H. Lin, "ZnO thin films deposited with various oxygen partial pressures by ion beam sputtering at room temperature," in *Proceedings of the International Conference on Optics and Photonics in Taiwan (OPT '08)*, National Chiao Tung University, Taiwan Optical Engineering Society, Taipei, Taiwan, 2008, Fri-P1-044.
- [13] J. S. Hammond, S. W. Gaarenstroom, and N. Winograd, "X-ray photoelectron spectroscopic studies of cadmium- and silver-oxygen surfaces," *Analytical Chemistry*, vol. 47, no. 13, pp. 2193-2199, 1975.
- [14] D. R. Lide, *CRC Handbook of Chemistry and Physics*, CRC press, Boca Raton, Fla, USA, 1991.
- [15] S. S. Kistler, "Stresses in glass produced by nonuniform exchange of monovalent ions," *Journal of the American Ceramic Society*, vol. 45, no. 2, pp. 59-68, 1962.
- [16] R. C. West and M. J. Astle, *CRC Handbook of Chemistry and Physics*, CRC Press, Boca Raton, Fla, USA, 1981.
- [17] P. W. Wang, "Thermal Stability of Silver in Ion Exchanged Soda Lime Glasses," *Journal of Vacuum Science and Technology*, vol. A14, pp. 465-470, 1996.
- [18] N. A. Sharaf, R. A. Condrate, and A. A. Ahmed, "FTIR spectral/structural investigation of the ion exchange/thermal treatment of silver ions into a silicate glass," *Materials Letters*, vol. 11, no. 3-4, pp. 115-118, 1991.
- [19] J. R. Johnson, R. H. Bristow, and H. H. Blau, "Diffusion of Ions in Some Simple Glasses," *Journal of the American Ceramic Society*, vol. 34, pp. 165-172, 1951.
- [20] J. E. Huheey, *Inorganic Chemistry: Principles of Structure and Reactivity*, Harper Collins, New York, NY, USA, 1983.
- [21] A. Segmuller, M. Murakami, and R. Roscoberg, *Analytical Techniques for Thin Films*, Academic Press, Boston, Mass, USA, 1988.
- [22] R. Cebulla, R. Wendt, and K. Ellmer, "Al-doped zinc oxide films deposited by simultaneous rf and dc excitation of a magnetron plasma: relationships between plasma parameters and structural and electrical film properties," *Journal of Applied Physics*, vol. 83, no. 2, pp. 1087-1095, 1998.
- [23] J. Sebag, J. Andrew, D. Neill, and M. Warner, "Substrate temperature and strain during sputter deposition of aluminum on cast borosilicate glass in a Gemini Observatory coating chamber," *Applied Optics*, vol. 49, no. 24, pp. 4610-4620, 2010.

- [24] Y.-Y. Chen, J.-C. Hsu, C.-Y. Lee, and P. W. Wang, "Post-annealing Properties of Aluminum Doped Zinc Oxide Films Fabricated by Ion Beam Co-sputtering," in *Proceedings of the 11th International Symposium on Sputtering and Plasma*, Kyoto, Japan, July 2011.

Research Article

The Effects of Different Types of Fly Ash on the Compressive Strength Properties of Briquettes

Özlem Çelik Sola,¹ Murat Yayla,² Barış Sayın,³ and Cengiz Duran Atış⁴

¹ Civil Engineering Department, Engineering Faculty, Istanbul University, Avcılar Campus, Avcılar, Istanbul, Turkey

² Yapi İnşaat Ltd. Co., Istanbul, Turkey

³ Building and Technical Office, Istanbul University, Beyazıt Campus, Istanbul, Turkey

⁴ Civil Engineering Department, Engineering and Architecture Faculty, Abdullah Gul University, Kayseri, Turkey

Correspondence should be addressed to Özlem Çelik Sola, celik@istanbul.edu.tr

Received 10 May 2011; Accepted 9 July 2011

Academic Editor: Kin Ho Lo

Copyright © 2011 Özlem Çelik Sola et al. This is an open access article distributed under the Creative Commons Attribution License, which permits unrestricted use, distribution, and reproduction in any medium, provided the original work is properly cited.

The aim of this study is to evaluate the effect of the different types of fly ash on the compressive strength properties of sintered briquettes. Thermal gravimetric (TG) analysis was carried out. The chemical composition and physical properties of the materials used were determined. Particle size distribution and microstructure elemental analyses of the materials used were carried out by a particle size analyzer (Mastersizer) and a scanning electron microscope (SEM-EDS). Following the characterization of the materials, briquettes were prepared by sintering at different temperatures. Compressive strength test results of the briquette samples indicated that briquettes with a compressive strength value of 47.45 N/mm² can be produced. The results obtained exceed the Turkish standard (TS EN 771-1) requirements (9.8–23.54 N/mm²). SEM-EDS results showed that briquette samples made with Tunçbilek (T) fly ash had a higher percentage of the glassy phase than the other briquette samples. Due to this microstructure, it results in higher compressive strength value.

1. Introduction

As an industrial waste, fly ash presents some environmental and storage problems; however, it has been used widely as an excellent mineral additive in the construction industry [1, 2]. The use of fly ash prevents environmental pollution, and it contributes to a reduced need for natural resources. Fly ash is available in different types, such as C and F. The F type has a low Ca content, and its content of SiO₂ + Fe₂O₃ + Al₂O₃ is greater than 70 (ASTM C 618) [3]. There are many studies investigating fly ash and its use as an additive in cement mortars [4, 5]. Fly ash is also used as an additive in the production of briquettes [6–11]. This study presents comprehensive details about the utilization of different types of fly ash that were collected from different thermal power plants (Çayırhan, Orhaneli, Seyitömer, and Tunçbilek) in Turkey and that were used to produce briquettes that have high compressive strength values.

2. Materials and Methods

2.1. Properties of Materials Used

2.1.1. Soil. The soil was obtained from the Boyabat Brick Factory in Turkey. Its specific surface area was 0.7502 m²/g, and its chemical properties are given in Table 1. It had a high SiO₂ content (51.21%).

2.1.2. Fly Ash. Four samples of fly ash were collected from the Çayırhan (C), Orhaneli (OE), Seyitömer (SO), and Tunçbilek (T) thermal power plants in Turkey, which are recycling materials for evaluation as additive materials in the building sector. Their specific surface areas are 0.5957, 0.8731, 0.4420, and 1.2769 m²/g, respectively. The chemical analysis results of the fly ashes are given in Table 1. According to ASTM 618, the SiO₂ + Al₂O₃ + Fe₂O₃ values indicated that

TABLE 1: The chemical composition (%w/w) of the materials used.

Constituents (%)	Soil	C	OE	SO	T
SiO ₂	51.21	44.05	43.18	53.32	58.36
Al ₂ O ₃	12.59	11.57	19.36	20.16	22.17
Fe ₂ O ₃	2.66	8.81	7.71	10.50	7.09
CaO	7.04	14.19	17.84	4.40	2.61
MgO	3.31	4.97	2.80	4.50	2.46
K ₂ O	1.70	1.80	1.64	2.98	2.27
Na ₂ O	1.52	3.59	0.36	0.51	0.71
SO ₃	5.57	10.34	2.53	1.04	0.34
KK	12.00	1.39	4.00	1.65	3.35
F CaO	0.07	0.14	0.31	—	0.01
Cl ⁻	0.0085	—	—	—	—

TABLE 2: Content of the soil sample.

Content	%w/w
Gravel	0.0
Sand	24.1
Silt	63.4
Clay	12.5

the fly ash sample obtained from the (C) thermal power plant should be classified as type C and the (OE), (SO), and (T) fly ash samples should be classified as type F.

2.1.3. Experimental Program. In order to prepare the briquette specimens from the materials, characterization experiments were carried out. A physical analysis of the soil was performed to determine the percentage of sand and gravel present. In addition to the physical analysis, a hydrometer analysis was applied to the mass of the soil that passed through sieve No. 200 in order to separate the silt and clay materials. Tests of the consistency limits of the soil—the plastic limit, the liquid limit, and the plasticity index (PI)—were conducted. In order to determine the thermal behavior of the soil, a TG analysis was carried out with a TGA-50. The particle size distribution of the materials was measured by the Mastersizer-x technique (Malvern, MS-X 1995 model). In order to describe the microstructure and to conduct an elemental analysis of the materials and briquettes, the SEM-EDS technique (JSM-5910LV, EDS Model: Oxford-Inca-7274) was used. The compressive strength results were explained by using the results obtained from these analyses.

2.1.4. Preparation and Testing of Briquettes. Following the characterization tests, different mixtures were prepared from fly ash samples. Fly ash was added to the soil in ratios of 5% and 10%. Each mixture was treated with 6% water to provide sufficient plasticity. At the end of this procedure, the mixtures were squeezed at 200 kgf/cm², and the samples were molded

TABLE 3: Test of consistency limits of the soil sample.

Limits	%
Liquid	37.5
Plastic	23.4
Plasticity index	14.1

TABLE 4: Granulometric data for the materials used in experiments and their size fractions.

Materials	Percentages % of particles with diameter		
	$d_{(0.10)}$ (μm)	$d_{(0.50)}$ (μm)	$d_{(0.90)}$ (μm)
S	2.83	17.44	73.41
C	3.70	27.23	129.95
OE	3.43	21.18	77.71
SO	6.16	29.76	96.86
T	1.99	13.76	52.39

for sintering. Before sintering, the moisture in the mixtures was evaporated in an oven at 105°C. The remolded mixtures had dimensions of 3.6 × 3.6 cm², and they were sintered at 850, 900, and 950°C in the laboratory oven. After the oven had reached the required temperature, the briquettes were removed from the oven. The briquettes produced with this process were tested for compressive strength according to the Turkish standards (TS EN 771-1) [12].

3. Results and Discussion

3.1. Characterization of the Materials

3.1.1. Hydrometer Analysis. A hydrometer analysis was carried out to obtain the soil content, which was found to be 24.1% sand, 63.4% silt, and 12.5% clay. The findings are listed in Table 2. The results of the tests of the consistency limits of the soil are given in Table 3: a 37.5% liquid limit, a 23.4% plastic limit, and a 14.1% plasticity index. From the test results, it can be concluded that the soil is suitable for brick production according to the American Association of State Highway and Transportation Officials (AASHTO).

3.1.2. Particle Size Distribution. The Mastersizer-x technique was used for measuring the particle size distribution. Granulometric data for the S showed that the $d_{(90)}$ and $d_{(50)}$ values were 73.41 and 17.44 μm . Granulometric data for the size fractions of the C, OE, SO, and T fly ash is displayed in Table 4; the $d_{(90)}$ and $d_{(50)}$ values were 129.95 and 27.23, 77.71, and 21.18, 96.86, and 29.76 and 52.39 and 13.76 μm , respectively. The particle size ranged from 3 μm to well over 129 μm for the materials. It can be observed that there are significant differences in the particle size distributions of the two samples of C and T for $d_{(90)}$: 129.95 and 52.39 μm , respectively. It can also be observed from the granulometric data that T was the finest fly ash.

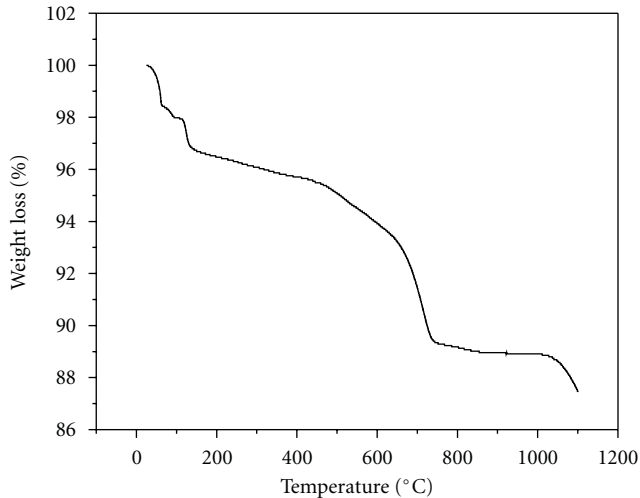


FIGURE 1: TG analysis of the soil sample.

3.1.3. Thermogravimetric (TG) Analysis. In order to obtain the thermal behavior of the soil, a TG analysis was carried out. A 13% weight loss was found. The moisture and water loss of the soil were 4% up to 200°C. Decomposition started and the water loss of the soil increased to 7% between 200 and 800°C. Figure 1 shows that above 800°C, decomposition continued, but the curve is not very sharp. Therefore, the temperature range from 850 to 950°C was chosen for sintering.

3.1.4. Morphological and Elemental Analyses. Morphological and elemental analyses were conducted using SEM-EDS. Figure 2 shows that fly ash samples are spherical in shape, whereas the soil sample is amorphous. The T fly ash sample has a finer particle size than the C fly ash sample, and the elemental analysis shows that the C fly ash sample has more Ca content than the T fly ash sample (Table 3). The C fly ash is C type, and the T fly ash is F type [5]. In addition to the morphological analyses performed to obtain an elemental analysis of the materials, four points (P) were chosen on the SEM photographs, and they were analyzed. The analysis results are shown in Table 5.

3.2. Compressive Strength Values of the Produced Briquettes

3.2.1. Mixing Ratios and Compressive Strength Values of the Produced Briquettes. After the sintering process, compressive strength tests of the briquettes were performed according to the Turkish standard (TS EN 771-1). It was concluded that briquettes with a compressive strength value of 47.45 N/mm² can be produced at 950°C. This result was obtained from the briquette that was prepared with 5% T fly ash. This is the best compressive strength result obtained for the samples that were prepared. This compressive strength result is a very high value; the Turkish standard (TS EN 771-1) only requires 9.8–23.54 N/mm². When the briquettes made with T fly ash were compared with the others, the compressive strength of the T briquettes was higher than that of the others at the

same temperatures. The compressive strength results for the briquettes are shown in Table 6. The compressive strength of the briquettes changed with the different types of fly ash.

3.2.2. SEM-EDS Analysis of the Briquettes after the Compressive Strength Tests. After the compressive strength tests, morphological and elemental analyses were applied to the samples by using SEM-EDS. There are three groups of mixtures. The first group included mixtures with 5% fly ash, the second group included those with 10% fly ash, and the third group included mixtures with 20% fly ash. Samples were chosen from the first group (b, e) and the third group (l). The samples b and e have 5% fly ash; they contain different types of fly ash, and l includes two samples with 10% fly ash, with different types of fly ashes (C and OE). No samples were chosen from the second group because their compressive strength results were similar to those of the first group. The selected samples have the best mechanical strengths in their respective groups.

It can be observed in Figure 3 that there are distinct differences between sample e and the others. Primarily, a quartz (SiO₂) phase was formed, and this can be seen in Figure 3. This is comparable with point 1 of Table 7. There are different phases shown in Figure 3. These phases are anhydrite (CaSO₄) in trace ratios, gehlenite (2CaO·Al₂O₃·SiO₂), potassium aluminum silicate (K₂O·Al₂O₃·4SiO₂), hematite (Fe₂O₃), and aluminum silicate (3Al₂O₃·2SiO₂). Here, the phases that affect the compressive strength properties are quartz, gehlenite, and potassium aluminum silicate. These phases are all proportional in Table 7.

4. Conclusions

The following conclusions can be drawn from the experimental results.

- (i) Briquettes can be manufactured with different types of fly ash.
- (ii) The briquettes sintered at 950°C had better compressive strength results than those sintered at 900 and 850°C.
- (iii) When the amount of fly ash added was increased from 5% to 10%, the compressive strength decreased, but the compressive strength of all of the briquettes was higher than 9.8 N/mm².
- (iv) The briquette created with 5% T fly ash had better mechanical strength than did those prepared using other materials. The mechanical strength of this briquette was very high (47.45 N/mm²), and when compared with the standard value (9.8–23.54 N/mm²), it is remarkable. Therefore, stronger construction could be designed with these briquettes.
- (v) Fly ash not only provides better mechanical strength for building materials but also contributes to decreasing environmental pollution, production costs, and the use of natural resources.

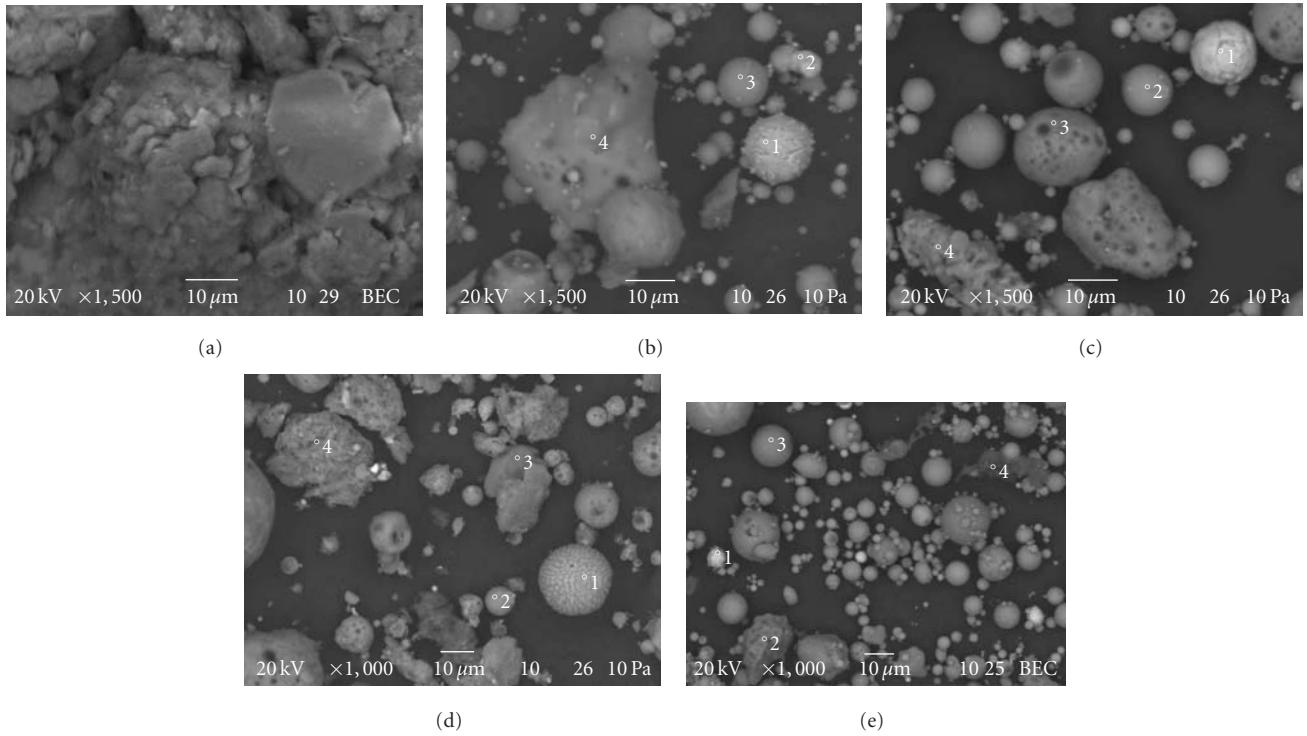


FIGURE 2: SEM micrographs of fly ashes (a) Soil $\times 1500$ (b) C $\times 1500$ (c) OE $\times 1500$ (d) SO $\times 1000$ (e) T $\times 1000$.

TABLE 5: SEM-EDS elemental analyses of materials.

Elemental analysis													
C	O	Na	Mg	Al	Si	P	S	K	Ca	Ti	Fe	Total	
S													
P1	54.44	0.85	2.72	8.41	18.43		2.54	2.00	4.63	0.45	5.52	100	
C													
P1	13.15	37.14		1.65	3.10		0.55		1.69		42.73	100	
P2	8.92	40.93		3.30	2.13		1.34		7.56		31.87	100	
P3	12.64	49.21	0.85	6.43	5.94		0.59		9.04	1.17	1.56	100	
P4	13.23	47.94		5.04	2.63	13.28	0.78	0.65	0.34	11.52	0.64	3.95	100
OE													
P1	15.32	35.68			2.99	2.87			1.34		41.81	100	
P2		51.95		2.01	11.36	18.78		1.30	9.54		5.06	100	
P3	25.25	43.82	0.68	0.61	11.98	13.72		0.81	1.64		1.49	100	
P4	17.76	49.20		0.61	2.37	2.17		0.57	26.40		0.92	100	
SO													
P1	21.88	37.14		1.44	3.43	10.66		0.78	1.32		23.34	100	
P2	18.73	47.96		2.01	7.95	15.30		1.72	3.38		2.95	100	
P3	15.70	53.95		0.74	2.76	24.03		0.73	0.43		1.67	100	
P4	15.08	50.62		0.77	10.37	20.25		1.29			1.60	100	
T													
P1	8.05	34.88			2.05	2.49			0.65		51.88	100	
P2	16.32	50.96			0.84	31.89						100	
P3		52.17	3.08		10.37	31.35		1.79			1.25	100	
P4	74.46	22.39			1.15	2.00						100	

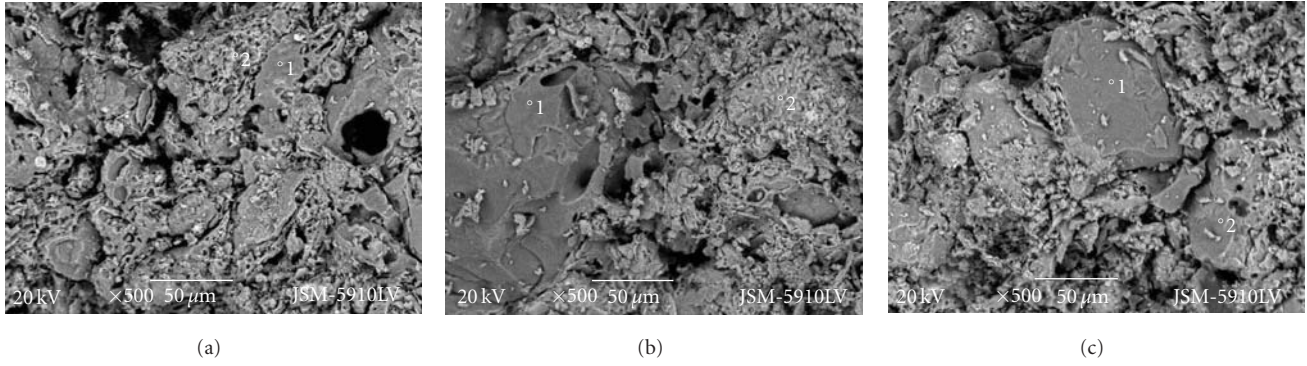


FIGURE 3: SEM micrographs of briquettes (a) b x 500 (b) e x 500 (c) l x 500.

TABLE 6: Mixing ratios of the materials and average compressive strength values of briquettes.

Sample code	Mixing ratios	Compressive strength values (N/mm ²)		
		850°C	900°C	950°C
b	95% S + 5% C	30.8	38.6	41.4
c	95% S + 5% OE	30.8	38.7	40.7
d	95% S + 5% SO	26.7	32.7	34.4
e	95% S + 5% TB	35.0	44.8	47.5
g	90% S + 10% C	14.9	29.2	36.8
h	90% S + 10% OE	22.5	27.9	31.2
i	90% S + 10% SO	11.8	26.5	31.0
j	90% S + 10% T	33.4	42.8	43.9
l	80% S + 10% C + 10% OE	15.5	31.7	38.2
m	80% S + 10% SO + 10% T	17.2	25.0	27.1

TABLE 7: SEM-EDS elemental analyses of briquettes (wt%).

		Elemental analysis										
C	O	Na	Mg	Al	Si	P	S	K	Ca	Ti	Fe	Total
b												
P1	50.91	3.36		8.72	30.11			6.90				100
P2	49.92	1.70	3.53	8.57	21.10			1.14	8.68		5.36	100
e												
P1	56.58				43.42							100
P2	40.13	1.44	1.99	4.96	17.09		1.95	1.03	16.86		14.55	100
l												
P1	49.40				50.60							100
P2	45.73	2.21	1.35	8.96	31.67			7.22	1.19		1.68	100
P3	50.71		2.83	8.15	20.67				10.15		7.50	100

- (vi) The compressive strength results of the briquettes changed with the fly ash properties.
- (vii) It was proven that all of the fly ash samples used in the experiments were suitable for use in briquette production.

Acknowledgments

The authors would like to thank Istanbul Asphalt Factories Head of Production Zafer Sola for helping. This work

was supported by the Scientific Research Projects Coordination Unit of Istanbul University, Project number UDP-4547/13112009.

References

[1] F. Tutunlu and U. Atalay, "Utilization of fly ash in manufacturing of building bricks," in *International Ash Utilization Symposium*, Center for Applied Energy Research, Salt Lake City, Utah, USA, 2001.

- [2] O. Ozdemir, B. Erhan, and M. S. Celik, "Separation of pozzolanic material from lignitic fly ash of Tuncbilek power station," in *International Ash Utilization Symposium*, Center for Applied Energy Research, Salt Lake City, Utah, USA, 2001.
- [3] ASTM standard, ASTM C 618, "Fly ash for use as mineral admixture in Portland cement concrete".
- [4] Ö. Çelik, E. Damcı, and S. Pişkin, "Characterization of fly ash and its effects on the compressive strength properties of Portland cement," *Indian Journal of Engineering & Materials Sciences*, vol. 15, no. 5, pp. 433–440, 2008.
- [5] O. Celik, *Utilization of Industrial Wastes in Building Sectors*, Ph.D. thesis, Yıldız Technical University, 2004.
- [6] L. Xu, W. Guo, T. Wang, and N. Yang, "Study on fired bricks with replacing clay by fly ash in high volume ratio," *Construction and Building Materials*, vol. 19, no. 3, pp. 243–247, 2005.
- [7] M. Dondi, G. Ercolani, G. Guarini, and M. Raimondo, "Orimulsión fly ash in clay bricks—part 1: composition and thermal behaviour of ash," *Journal of the European Ceramic Society*, vol. 22, no. 11, pp. 1729–1735, 2002.
- [8] M. Dondi, G. Guarini, M. Raimondo, and I. Venturi, "Orimulsión fly ash in clay bricks—part 2: technological behaviour of clay/ash mixtures," *Journal of the European Ceramic Society*, vol. 22, no. 11, pp. 1737–1747, 2002.
- [9] Z. Haiying, Z. Youcai, and Q. Jingyu, "Utilization of municipal solid waste incineration (MSWI) fly ash in ceramic brick: product characterization and environmental toxicity," *Waste Management*, vol. 31, no. 2, pp. 331–341, 2011.
- [10] T. Takegawa, "Manufacture of bricks from fly ashes," *Fuel and Energy Abstracts*, 37-3, Chapter 96/03074, 1996.
- [11] G. Cultrone and E. Sebastián, "Fly ash addition in clayey materials to improve the quality of solid bricks," *Construction and Building Materials*, vol. 23, no. 2, pp. 1178–1184, 2009.
- [12] Turkish Standards EN 771-1, "Specification for masonry units-part 1: clay masonry units," Turkish Standards Institute, Ankara, Turkey, 2005.

Research Article

Crystallization Behavior and Microstructural Analysis of Strontium Rich $(\text{Pb}_x\text{Sr}_{1-x})\text{TiO}_3$ Glass Ceramics in Presence of La_2O_3

C. R. Gautam,¹ Devendra Kumar,² and Om Parkash²

¹Department of Physics, University of Lucknow, Lucknow 226007, India

²Department of Ceramic Engineering, Institute of Technology, Banaras Hindu University, Varanasi 221005, India

Correspondence should be addressed to C. R. Gautam, gautam_ceramic@yahoo.com

Received 11 April 2011; Accepted 21 June 2011

Academic Editor: Joseph Lai

Copyright © 2011 C. R. Gautam et al. This is an open access article distributed under the Creative Commons Attribution License, which permits unrestricted use, distribution, and reproduction in any medium, provided the original work is properly cited.

Crystallization and microstructural behavior of various strontium-rich glass ceramics in the system $65[(\text{Pb}_x\text{Sr}_{1-x})\text{TiO}_3]-24[2\text{SiO}_2\cdot\text{B}_2\text{O}_3]-5[\text{BaO}]-5[\text{K}_2\text{O}]-1[\text{La}_2\text{O}_3]$ ($0.0 \leq x \leq 0.4$) with addition of 1% La_2O_3 have been investigated. The addition of La_2O_3 has been found to play an important role in crystallization of perovskite $(\text{Pb,Sr})\text{TiO}_3$ as a solid solution phase. Also, it causes a change in the surface morphology of the fined crystallites of the major phase. Differential thermal analysis (DTA) shows only one exothermic crystallization peak, which shifts towards higher temperature with increasing amount of strontium oxide. Glasses were subjected to various heat treatment schedules for the crystallization. Very good crystallization of strontium-rich glass compositions is observed. X-ray diffraction studies confirm that cubic perovskite lead strontium titanate crystallizes as major phase. Lattice parameter decreases with increasing strontium content similar to lead strontium titanate ceramics. Uniform and interconnected crystallites are dispersed in glassy matrix.

1. Introduction

Strontium titanate has a cubic structure above -163°C where it transforms to a paraelectric phase. There is no dielectric anomaly at -163°C , but a strong elastic anomaly is observed [1]. The dielectric constant follows Curie-Weiss law below room temperature. Strontium titanate is a prototype ceramic with perovskite structure and is of much technological importance. Applications of strontium titanate glass ceramics for a long time have been limited to cryogenic temperature sensors and include a capacitance thermometer, a dielectric bolometer, and capacitive energy storage dielectrics [2]. The materials studied by Stookey [3] were essentially different from the group of glass ceramic materials discovered by King and Stookey [4]. In the later type of materials a relatively unstable glass was devitrified by the addition of a nucleating agent. They found that by dissolving TiO_2 in such a glass a situation could be created in which, in a certain temperature range, the material was supersaturated in TiO_2 , giving rise to crystallization of rutile. In some cases, TiO_2

did not crystallize as such, but combined with one of the modifying ions of the base glass to precipitate as a titanate, for example, crystallization of SrTiO_3 with perovskite structure. The crystallization and microstructural behavior of glass ceramic with perovskite titanate phases, SrTiO_3 [5–14] have been investigated. Thakur et al. [15] investigated the crystallization, microstructure and dielectric behavior of SrTiO_3 glass ceramic. SrTiO_3 could be crystallized as the major phase by addition of an appropriate concentration of K_2O and selected heat treatment schedules. In these glass ceramics addition of La_2O_3 enhances the crystallization of strontium titanate phase and increases the dielectric constant enormously. Recently Sahu et al. [16] explored the substitution of strontium for lead in lead titanate precipitated in borosilicate glass with suitable choice of composition and heat treatment schedule. The investigation on the phase development and microstructural characteristics of the glass ceramic in the system $[\text{SrOTiO}_2]-[2\text{SiO}_2\text{B}_2\text{O}_3]-[\text{K}_2\text{O}-\text{BaO}]$ showed that the solid solution of SrTiO_3 with

PbTiO₃ phases can be crystallized in borosilicate glasses [17].

The present paper reports our results of investigations carried out to crystallize perovskite lead strontium titanate/perovskite strontium titanate solid solution phase in a borosilicate glassy matrix in presence of La₂O₃. The donor doped La₂O₃ was chosen as an additive because it strongly affects the crystallization behavior and dielectric properties of the perovskite glass ceramic systems 65[(Pb_xSr_{1-x})TiO₃]-24[2SiO₂·B₂O₃]-5[BaO]-5[K₂O]-1[La₂O₃].

2. Experimental Procedure

The nomenclature, preparation, and characterization methods of glass and glass ceramic samples are described elaborately in part I of this paper entitled “Crystallization Behavior and Microstructural Analysis of Lead-Rich (Pb_xSr_{1-x})TiO₃ Glass Ceramics Containing 1 mole % La₂O₃”. A brief description is presented here. Sr-rich glass compositions in the system 65[(Pb_xSr_{1-x})OTiO₂]-24[2SiO₂·B₂O₃]-5[K₂O]-5[BaO]-1[La₂O₃] with varying lead-to-strontium ratios ($0.0 \leq x \leq 0.40$) have been prepared by melt quench method by melting the glass in the temperature range 1210–1330°C and annealing at 400°C for three hours in another furnace. All the glasses were characterized by DTA to determine glass transition and the crystallization temperatures (Table 1). On the basis of DTA results, various glass ceramic samples were prepared by heat treating the glasses in the temperature range 820–890°C. The different heat treatment schedules and nomenclature of glass ceramic samples are listed in Table 2. The nomenclature of various glasses and glass ceramic samples in the system is reported earlier [18]. The nomenclature of glass ceramic samples includes the code of their parent glass composition followed by heat treatment temperature then by letter “T” and “S” for 3 and 6 hours heat treatment, respectively. X-ray diffraction patterns were recorded using a Rigaku X-ray diffractometer using Cu K α radiation. X-ray diffraction patterns were compared with standard d-values from JCPDS files for different constituting phases. The glass ceramic samples were ground and polished successively using SiC powders and diamond paste (1 μ m). The polished glass ceramic samples were etched for 1 minute with etchant (30% HNO₃ + 20% HF). Gold coatings were applied to the etched surface of various glass ceramic samples by the sputtering method in order to study the morphology of the different crystalline phases present by scanning electron microscopy (SEM).

3. Results

3.1. Differential Thermal Analysis (DTA). DTA patterns of various glass samples 4PL5B, 3PL5B, 2PL5B, 1PL5B, and STL5B are given in Figures 1 and 2.

All glasses show only a single exothermic peak in their DTA patterns. A shift in the base line is observed in the DTA plot, which depends on the composition of the glass. This shift in the base line shows a change in the specific heat of the glass, which is attributed to the glass transition temperature,

TABLE 1: Glass transition temperature, DTA peaks of various glass samples in system [(Pb_xSr_{1-x})·TiO₃]-[2SiO₂·B₂O₃]-[BaO·K₂O]-[La₂O₃].

Compositions (x)	Glass code	T _g (°C)	DTA Peaks T _c (°C)
0.4	4PL5B	600	820
0.3	3PL5B	635	871
0.2	2PL5B	635	865
0.1	1PL5B	660	878
0.0	STL5B	660	890

T_g. Glass transition and exothermic crystallization peak temperatures T_c, for different glass samples are listed in Table 1. The crystallization peaks are differing with respect to their broadness and symmetry. The peak temperature increasing with increases the strontium content.

3.2. X-Ray Diffraction Analyses and Crystallization Behavior. On the basis of DTA results, various glass ceramic samples were prepared by heat treating the glasses in the temperature range 820–890°C for 3- and 6- hour heat treatment schedule. The different heat treatment schedules and nomenclature of glass ceramic samples are listed in Table 2. X-ray diffraction (XRD) patterns for various glass ceramic samples crystallized at different temperatures for 3 hours are shown in Figures 3 and 4, respectively. These glass ceramic samples show the formation of perovskite phase in major amount along with rutile (R) and/or strontium borate (SB) as minor phase. Minor rutile (R) phase is present in glass ceramic sample with $0.1 \leq x \leq 0.4$. SB phase appears only in the lead-free STL5B890T glass ceramic sample. Figure 5 shows XRD patterns for the glass ceramic samples 4PL5B820S 3PL5B871S and 2PL5B865. Perovskite lead strontium titanate crystallizes as the major phase. It is also observed that the secondary phase of rutile (trace amount) is also present in these glass ceramic samples. Figure 6 shows the XRD pattern for the glass ceramic samples 2PL5B878S and STL5B890S, respectively. These are strontium-rich compositions and major phase of perovskite strontium titanate with traces of rutile (TiO₂) and strontium borate (Sr₂B₂O₅) as secondary crystalline phases.

Excellent crystallization is observed in 4PL5B820S and STL5B890S glass ceramic samples. Both glass samples crystallize for six-hour heat treatment schedule. The excellent crystallization is attributed to the sufficient nucleation and growth for six-hour heat treatment schedule. It is too difficult to crystallize major phase of perovskite strontium titanate in glassy matrix. La₂O₃ plays an important role in crystallization of the glass samples and therefore acts as a nucleating agent. Heat treatment schedules, glass ceramic codes, and crystalline phases of different strontium rich glass ceramic samples are shown in Table 2.

The lattice parameters are much closer to standard lattice parameters [19]. The observed crystal structure is cubic, similar to SrTiO₃, over the entire composition range ($0.0 \leq x \leq 0.4$). Density of the glass and glass ceramic samples was determined by using Archimedes principle [20]. Density

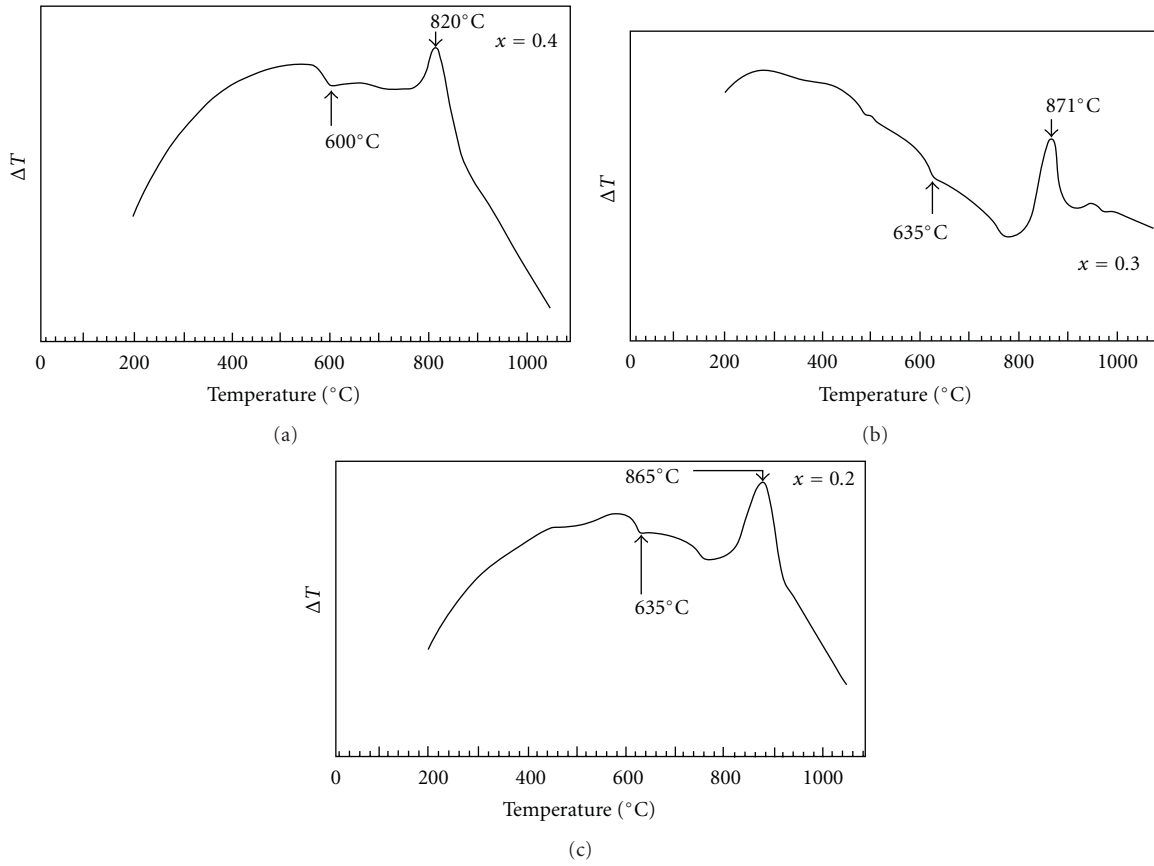


FIGURE 1: DTA patterns of glasses (a) 4PL5B, $x = 0.4$, (b) 3PL5B, $x = 0.3$, and (c) 2PL5B, $x = 0.2$.

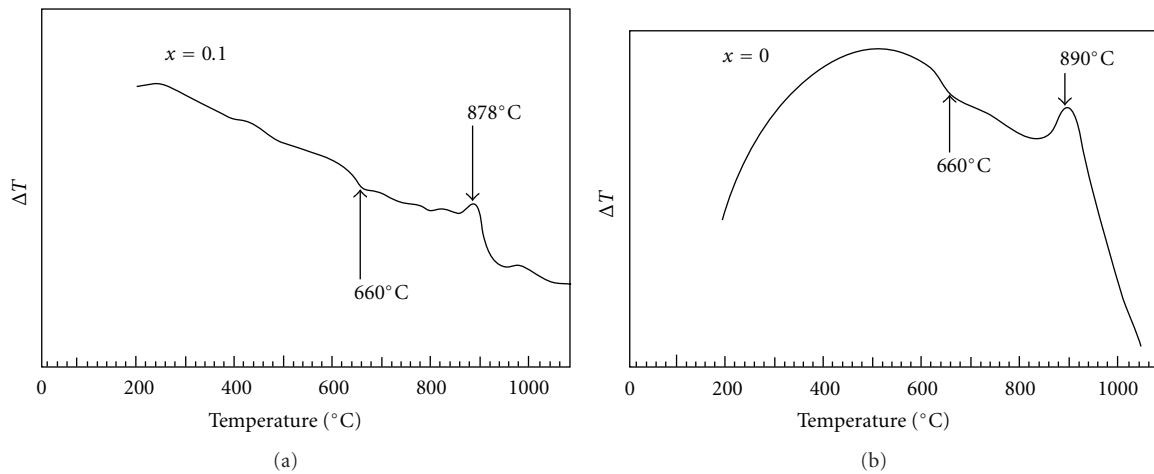


FIGURE 2: DTA pattern of glasses (a) 1PL5B, $x = 0.1$, and (b) STL5B, $x = 0.0$.

of the glass ceramic samples was determined using distilled water as the liquid medium.

The following weights were taken and used in the density calculations:

W_1 is the weight of empty specific gravity bottle (gram); W_2 is the weight of specific gravity bottle with sample (gram); W_3 is the weight of specific gravity bottle with

sample and distilled water (gram); W_4 is the weight of specific gravity bottle with distilled water (gram).

$$\text{Density} = \frac{W_2 - W_1}{W_4 - W_1 - (W_3 - W_2)} \quad (1)$$

3.3. *Surface Morphological Analysis.* Figures 7(a), 7(b), and 7(c) illustrate the scanning electron micrographs for glass

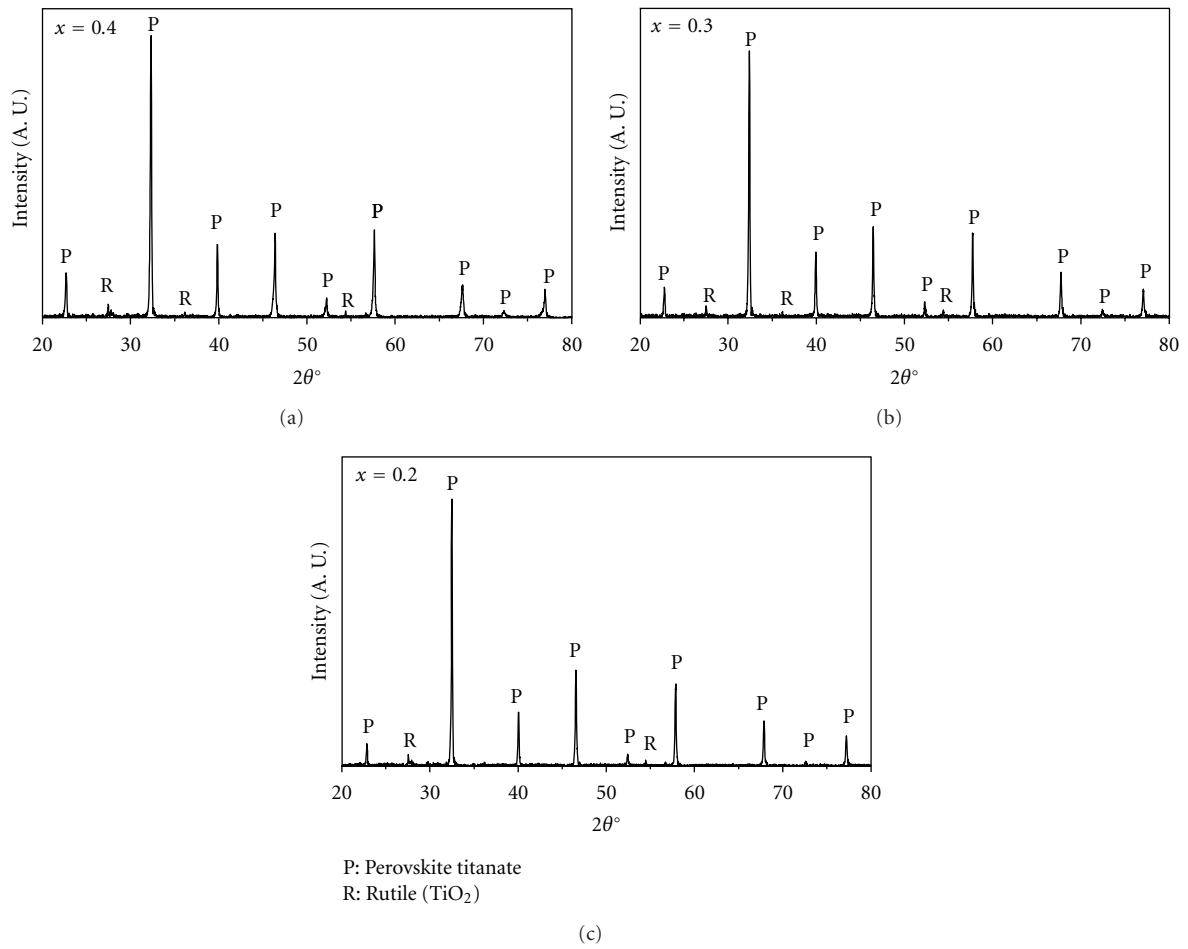


FIGURE 3: X-ray diffraction patterns of glass ceramic samples (a) 4PL5B820S (b) 3PL5B871T and (c) 2PL5B865T.

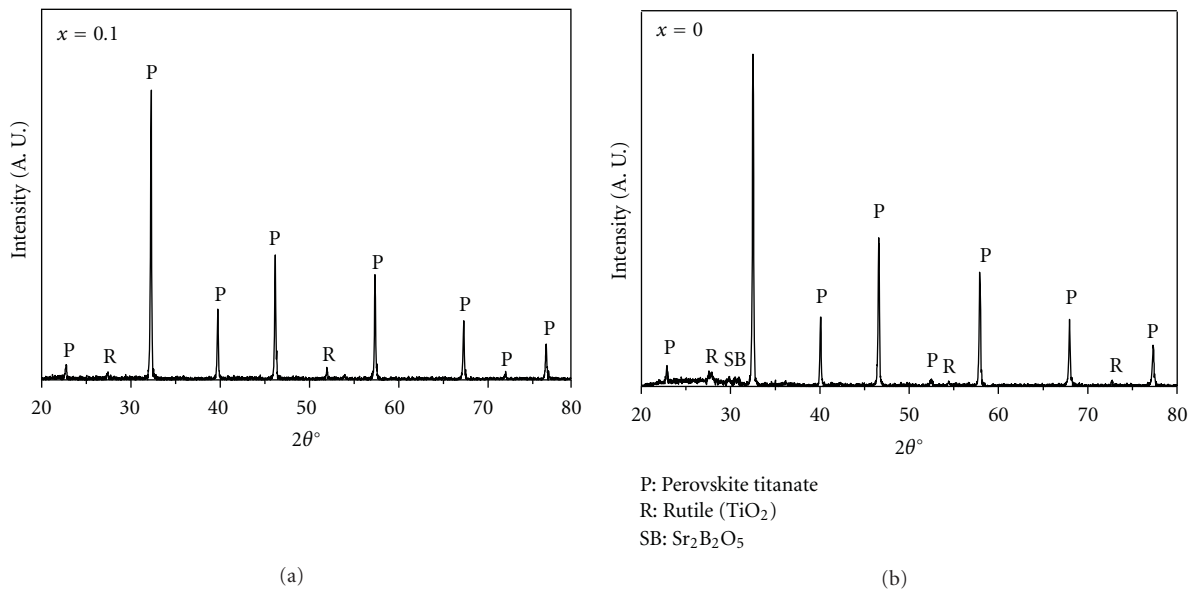


FIGURE 4: X-ray diffraction patterns of different glass ceramic samples (a) 1PL5B878T and (b) STL5B890T.

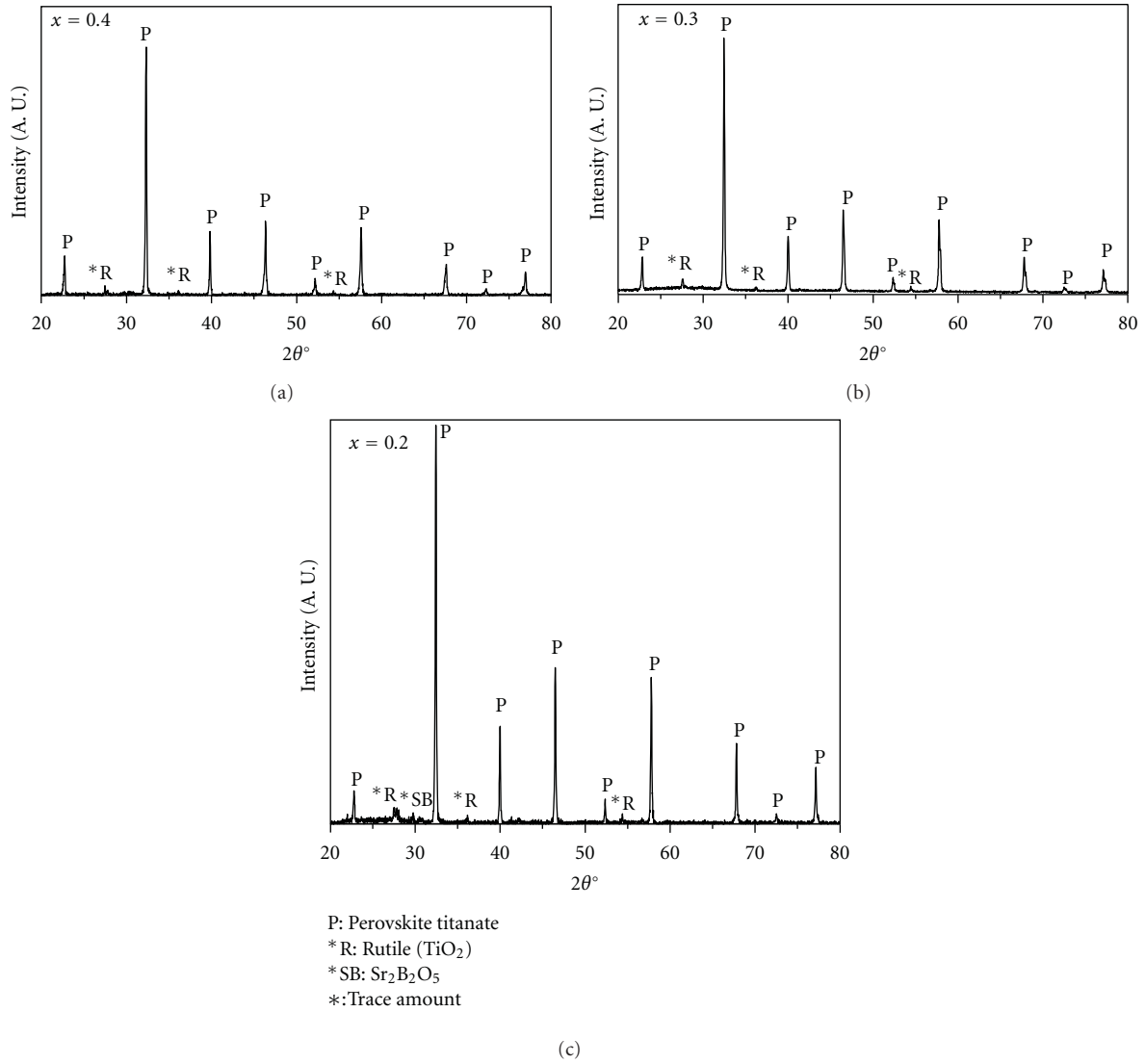


FIGURE 5: X-ray diffraction patterns of glass ceramic samples (a) 4PL5B820S, (b) 3PL5B871S, and (c) 2PL5B870S.

TABLE 2: Heat treatment schedules, glass ceramic codes, and crystalline phases of different strontium rich glass ceramic samples in the system $[(\text{Pb}_x\text{Sr}_{1-x})\text{O} \cdot \text{TiO}_2] - [2\text{SiO}_2 \cdot \text{B}_2\text{O}_3] - [\text{K}_2\text{O}] - [\text{BaO}] - \text{La}_2\text{O}_3$.

Glass code	Glass ceramic code	Heat treatment schedules			Crystalline phases
		Heating rate (°C/min)	Holding temp (°C)	Holding time (hrs)	
4PL5B	4PL5B820T	5	840	3	P + R
	4PL5B820S	5	840	6	P
3PL5B	3PL5B871T	5	871	3	P + R
	3PL5B871S	5	871	6	P + R*
2PL5B	2PL5B870T	5	870	3	P + R + SB*
	2PL5B870S	5	870	6	P + R* + SB*
1PL5B	1PL5B878T	5	878	3	P + R
	1PL5B878S	5	878	6	P + R*
STL5B	STL5B890T	5	890	3	P + R* + SB*
	STL5B890S	5	890	6	P + R*

P: perovskite titanate, PT: PbTi_3O_7 , R: rutile (TiO₂), SB: strontium Borate. (Sr₂B₂O₅), *: trace amount.

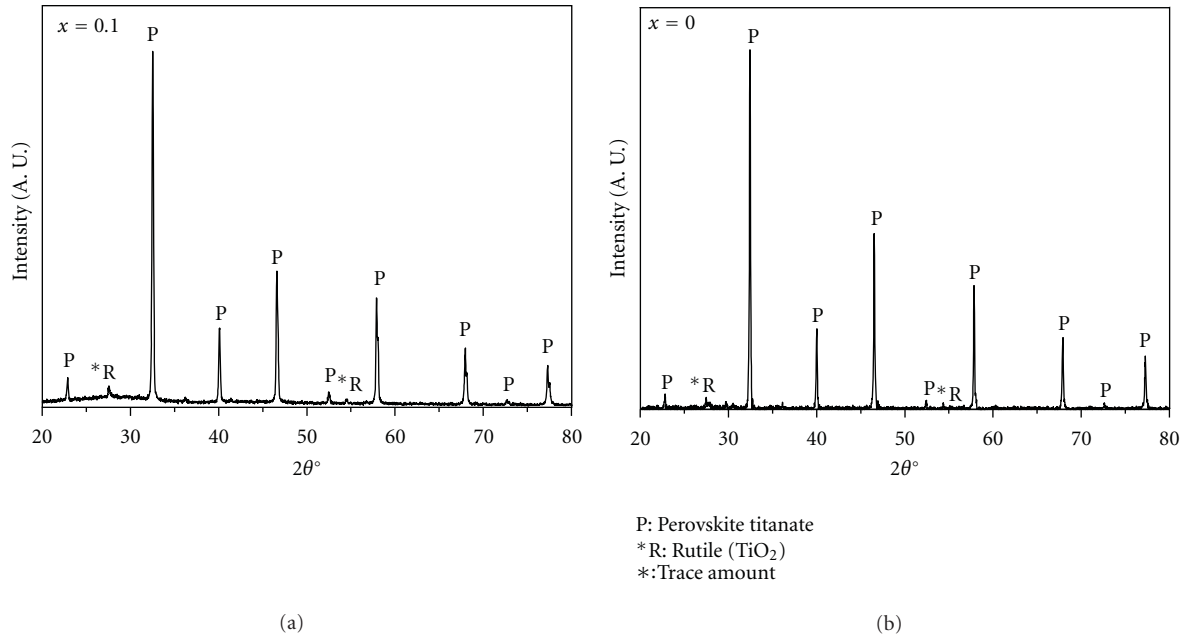


FIGURE 6: X-ray diffraction patterns of glass ceramic samples (a) 1PL5B878S and (b) STL5B890S.

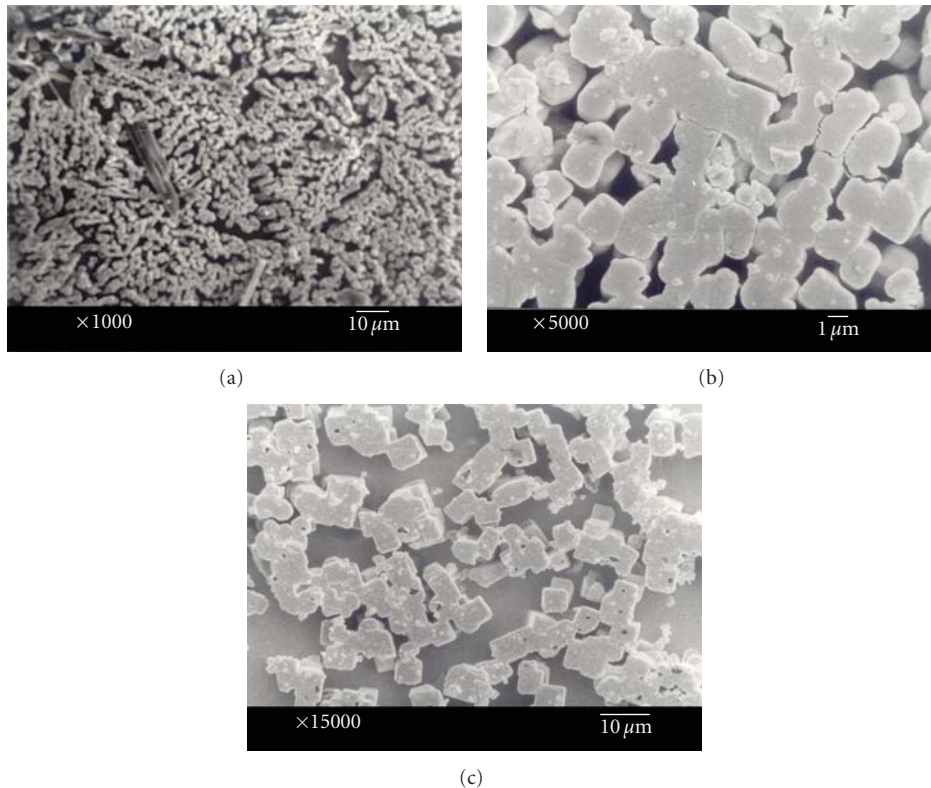


FIGURE 7: Scanning electron micrographs of glass ceramic samples (a) 4PL5B840T, (b) 3PL5B871T, and (c) 1PL5B878T.

ceramic samples (4PL5B840T, 3PL5B871T, and 1PL5B878T) obtained by crystallizing the glass samples 4PL5B, 3PL5B, and 1PL5B for 3 hours, respectively. Glass ceramic sample 4PL5B840T shows random growth of the crystallites of perovskite titanate as major phase, which are interconnected with one another. The secondary phase formation of the

rutile is also which is represented by the dark needle-like shapes in the micrographs. This secondary phase is also confirmed by XRD analysis.

Scanning electron micrographs of the glass ceramic sample 3PL5B871T are shown in Figure 7(b). The micrograph of this glass ceramic sample shows that the crystallites

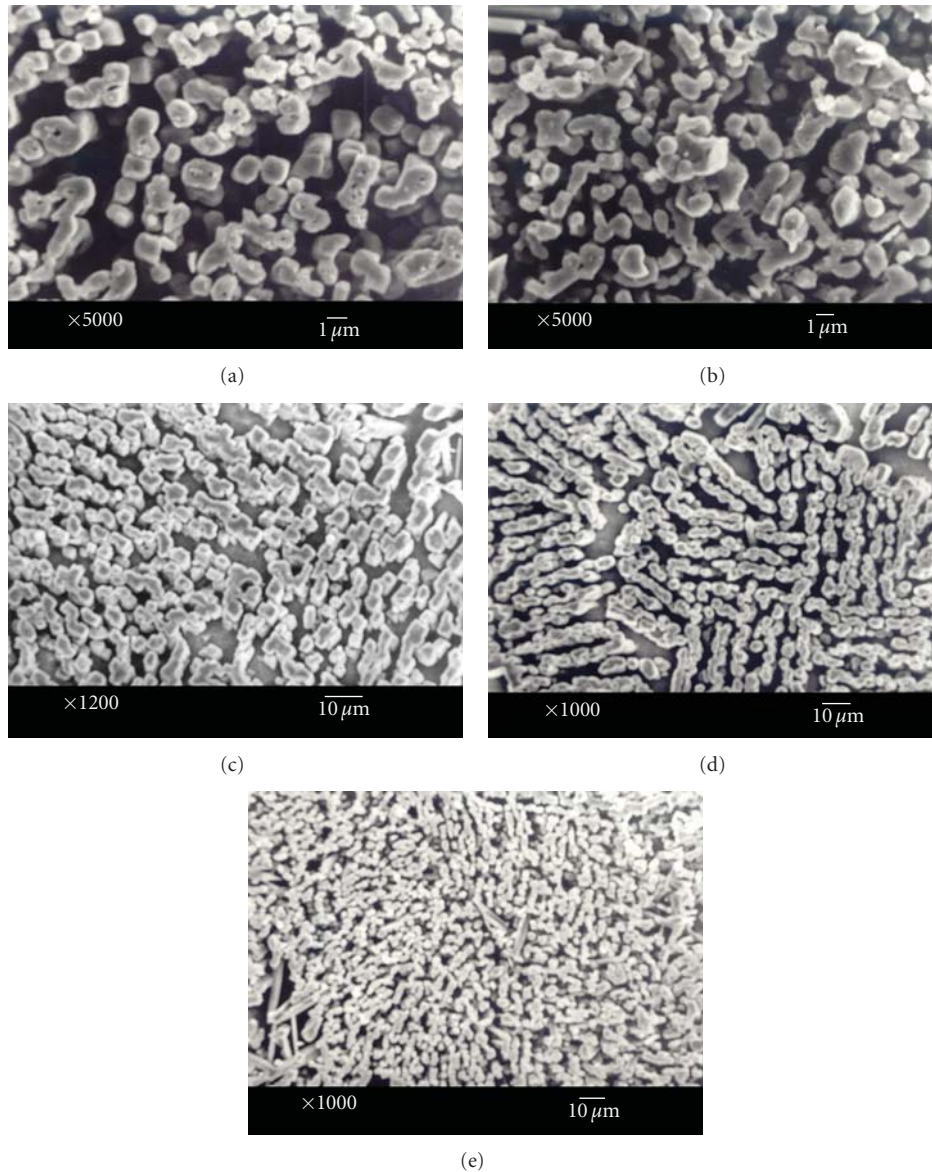


FIGURE 8: Scanning electron micrographs of glass ceramic samples (a) 4PL5B840S, (b) 3PL5B871S, (c) 2PL5B870S, (d) 1PL5B878S, and (e) STL5B890S.

are fully developed in the glassy matrix. These crystallites are interconnected and randomly oriented in the glassy phase. The scanning electron microstructure of glass ceramic sample 1PL5B878T crystallized at 878°C for 3 hours is shown in Figure 7(c). This glass ceramic sample shows the square shape crystallites of the perovskite titanate phase, which are randomly distributed, in the residual glassy network. It is also observed that the large amount of residual glass remaining after crystallization is due to smaller soaking time. Figure 8 shows the scanning electron micrographs of the different glass ceramic samples 4PL5B840S, 3PL5B871S, 2PL5B870S, 1PL5B878S, and STL5B890S, respectively. All these glass ceramic samples are obtained by the crystallization of their respective glasses for 6-hour soaking time. The crystallization of 4PL5B840S is similar to the crystallization

of glass ceramic sample 3PL5B871S. It is also observed that the morphology of the crystallites of 4PL5B840S and 3PL5B871S was found to be the same. Only a small change is marked in secondary phase of rutile. Figure 8(c) shows the scanning electron micrograph for the glass ceramic sample 2PL5B870S, which is obtained by crystallization at 870°C for 6 hours corresponding to the exothermic peak in the DTA plot. Crystallite sizes of the order of a micron are formed which are uniformly distributed in the glassy matrix. Some of crystallites are aligned towards the right side and the rest are aligned towards the left side. Figure 8(e) depicts the scanning electron micrograph of the glass ceramic sample STL5B890S crystallized at 890°C for 6 hours. Well-interconnected crystallites of SrTiO₃ are randomly distributed in the glassy network. Needle-like fine

TABLE 3: Density of glass and glass ceramic, crystal structure, lattice parameters, and axial ratio of major crystalline phase in different strontium-rich glass ceramic samples in the system $[(\text{Pb}_x\text{Sr}_{1-x})\text{O} \cdot \text{TiO}_2] - [2\text{SiO}_2 \cdot \text{B}_2\text{O}_3] - [\text{K}_2\text{O}] - [\text{BaO}] - \text{La}_2\text{O}_3$.

Glass code	Density (gm/cc)	Glass ceramic	Density (gm/cc)	Crystal structure	Lattice parameters, a (Å)	(PbSr)TiO ₃ ceramic*, a (Å)
4PL5B	3.827	4PL5B820T	3.856	Cubic	3.915 ± 0.006	3.927
		4PL5B820S	4.109	Cubic	3.913 ± 0.002	
3PL5B	3.635	3PL5B871T	4.208	Cubic	3.911 ± 0.000	3.943
		3PL5B871S	3.256	Cubic	3.902 ± 0.003	
2PL5B	3.507	2PL5B870T	3.961	Cubic	3.899 ± 0.001	3.880
		2PL5B870S	3.671	Cubic	3.904 ± 0.005	
1PL5B	3.384	1PL5B878T	3.857	Cubic	3.904 ± 0.001	3.880
		1PL5B878S	3.426	Cubic	3.895 ± 0.002	
STL5B	3.212	STL5B890T	3.261	Cubic	3.897 ± 0.000	3.904
		STL5B890S	3.386	Cubic	3.901 ± 0.000	

* Reference [19].

The glass codes, density of glass and glass ceramics, crystal structure and lattice parameters are shown in Table 3.

crystallites present in trace amount are of rutile phase, which is confirmed by XRD studies. The crystallization temperature for this glass was found to the maximum among all the glass compositions because of the absence of lead in this composition. The excellent crystallization was observed for this glass ceramic sample.

4. Discussion

The XRD data of the major perovskite phase in different glass ceramic samples for the Sr-rich glass ceramic compositions $x \leq 0.4$ were indexed on the basis of a cubic unit cell similar to SrTiO₃. Values of lattice parameters “c” and “a” for perovskite phase in strontium-rich glass ceramic samples was determined from software “CEL” and are given in Table 3. Density of the glass and glass ceramic samples were determined using Archimedes principle [20, 21]. It is observed that the density of glasses systematically decreases with increasing the concentration of SrO (Table 3). Density of various glass samples lies between 3.212 and 3.287 gm/cc. It found to be larger for the glass sample 4PL5B while it is less for glass sample STL5B. Sahu [22] has reported that the strontium-rich glass ceramic samples without doping of La₂O₃ show that the phase separation is smaller and rate of crystallization is higher during heat treatment. Hence, high cooling rate is required during the quenching of the melt to get bulk transparent glasses. This might be one of the reasons for the difficulty of glass forming of these compositions. In the intermediate compositions, that is, when the Pb²⁺/Sr²⁺ ratio is 1 or nearly one, glass-in-glass phase separation takes place during the early stage of crystallization treatment. This also makes the glass formation easy with a relatively low cooling rate. But after doping the La₂O₃ in the strontium-rich glass ceramic samples the morphology of the crystallites is very dense and directionally distributed in the glassy matrix. The doping of La₂O₃ enhances the crystallization and retards the minor phase in these glass ceramic samples. Therefore, a very high value of dielectric constant and low loss are observed in these glass ceramic samples [18].

5. Conclusions

Very good transparent and bulky glasses were prepared in the strontium rich compositions. DTA patterns of strontium-rich glass samples show only a single exothermic peak. The addition of lanthanum oxide promotes the crystallization of major phase and retards the crystallization of minor phases. Therefore, very good crystallization is observed in these glass ceramic samples. X-ray diffraction patterns of strontium-rich glass ceramic compositions show presence of strontium titanate or perovskite lead strontium titanate as major phase with some secondary phase of rutile and strontium borate. Directional morphology of the perovskite fine crystallite growth was seen in the micrographs for these glass ceramic samples. XRD data of the major perovskite phase in strontium-rich glass ceramic samples show that the structure of crystalline phase is cubic, similar to SrTiO₃, for $x \leq 0.4$.

Acknowledgments

The authors are deeply grateful to Defence Research Organization (India) for the financial support. Professor D. Pandey SMST, IT BHU., Varanasi, India, is also thanked for providing the XRD facilities.

References

- [1] H. E. Weaver, “Dielectric properties of single crystals of SrTiO₃ at low temperatures,” *Journal of Physics and Chemistry of Solids*, vol. 11, pp. 245–274, 1959.
- [2] W. N. Lawless, “Three application areas for strontium titanate glass-ceramics,” *Ferroelectrics*, vol. 3, pp. 287–293, 1972.
- [3] S. D. Stookey, “Method of making ceramics and product thereof,” United States Patent 2920971, 829, *British Patent*, 447, 1960.
- [4] C. B. King and S. D. Stookey, “United States Patent,” 2960801, 1960.
- [5] W. N. Lawless, “Cryogenic Engg. Cont. Boulder,” *Advances in Cryogenic Engineering*, Boulder, Colo, USA, 1970.

- [6] W. N. Lawless, "Capacitance thermometry characteristics of titanate glass-ceramics at low temperature," *Advances in Cryogenic Engineering*, vol. 16, pp. 261–267, 1971.
- [7] W. N. Lawless, "A low temperature glass-ceramic capacitance thermometer," *Review of Scientific Instruments*, vol. 42, pp. 561–566, 1972.
- [8] W. N. Lawless, *Private communication*, 1981.
- [9] S. L. Swartz, A. S. Bhalla, L. E. Cross, and W. N. Lawless, "Strontium titanate (SrTiO_3) glass ceramics part I. Crystallization and microstructure," *Journal of Materials Science*, vol. 23, pp. 3997–4003, 1988.
- [10] S. L. Swartz, A. S. Bhalla, L. E. Cross, and W. N. Lawless, "SrTiO₃ glass ceramics part II. Dielectric properties," *Journal of Materials Science*, vol. 23, no. 11, pp. 4004–4012, 1988.
- [11] R. K. Mandal, C. Durga Prasad, Om Parkash, and D. Kumar, "Dielectric behaviour of glasses and glass ceramics in the system BaO-PbO-TiO₂-B₂O₃-SiO₂," *Bulletin of Materials Science*, vol. 9, no. 4, pp. 255–262, 1987.
- [12] O. P. Thakur, D. Kumar, Om Parkash, and L. Pandey, "Dielectric and microstructural behaviour of strontium titanate borosilicate glass ceramic system," *Bulletin of Materials Science*, vol. 18, no. 5, pp. 577–585, 1995.
- [13] O. P. Thakur, D. Kumar, and Om Parkash, "Crystallization microstructure development and dielectric behavior of glass ceramics in the system [(SrO.TiO₂)-[2SiO₂.B₂O₃]-La₂O₃]," *Journal of Materials Science*, vol. 37, no. 12, pp. 2597–2606, 2002.
- [14] S. L. Swartz, E. Breval, and A. S. Bhalla, "Effect of nucleation on the crystallization and dielectric properties of strontium titanate glass-ceramics," *The American Ceramic Society Bulletin*, vol. 67, no. 4, pp. 763–770, 1988.
- [15] O. P. Thakur, D. Kumar, Om Parkash, and L. Pandey, "Effect of K₂O addition on crystallization and microstructural behavior of strontium titanate borosilicate glass ceramic system," *Materials Letters*, vol. 23, pp. 253–260, 1995.
- [16] A. K. Sahu, D. Kumar, and O. Parkash, "Crystallisation of lead strontium titanate perovskite phase in [(Pb_{1-x}Sr_x)O.TiO₂]-[2SiO₂.B₂O₃]-[K₂O] glass ceramics," *The British Ceramic Transactions*, vol. 102, no. 4, pp. 139–147, 2003.
- [17] A. K. Sahu, D. Kumar, O. Parkash, and C. Prakash, "Effect of K₂O/BaO ratio on crystallization, microstructure and dielectric properties of strontium titanate borosilicate glass ceramics," *Ceramics International*, vol. 30, no. 3, pp. 477–483, 2004.
- [18] D. Kumar, C. R. Gautam, and O. Parkash, "Preparation and dielectric characterization of ferroelectric (Pb_xSr_{1-x})TiO₃ glass ceramics doped with La₂O₃," *Applied Physics Letters*, vol. 89, no. 11, pp. 112908–112911, 2006.
- [19] S. Subrahmanyam and E. Goo, "Nucleation of the ferroelectric phase in the (Pb_xSr_{1-x})TiO₃ system," *Acta Materialia*, vol. 46, no. 3, pp. 817–822, 1998.
- [20] V. A. Hiremath, S. K. Date, and S. M. Kulkarni, "A new combustion route to γ -Fe₂O₃ synthesis," *Bulletin of Materials Science*, vol. 24, no. 6, pp. 617–621, 2001.
- [21] C. R. Gautam, D. Kumar, and Om Parkash, "Dielectric and impedance spectroscopic studies of (Sr_{1-x}Pb_x)TiO₃ glass ceramics with addition of Nb₂O₅," *Bulletin of Material Science*. In press.
- [22] A. K. Sahu, *Preparation microstructure and dielectric properties of lead strontium titanate borosilicate glass ceramic system*, Ph.D. thesis, Institute of Technology, Banaras Hindu University, India, 2002.

Research Article

Crystallization Behavior and Microstructural Analysis of Lead-Rich ($\text{Pb}_x\text{Sr}_{1-x}$) TiO_3 Glass Ceramics Containing 1 mole % La_2O_3

C. R. Gautam,^{1,2} Devendra Kumar,^{1,2} and Om Parkash^{1,2}

¹Department of Physics, University of Lucknow, Lucknow 226007, India

²Department of Ceramic Engineering, Institute of Technology, Banaras Hindu University, Varanasi 221005, India

Correspondence should be addressed to C. R. Gautam, gautam_ceramic@yahoo.com

Received 1 March 2011; Accepted 15 June 2011

Academic Editor: Joseph Lai

Copyright © 2011 C. R. Gautam et al. This is an open access article distributed under the Creative Commons Attribution License, which permits unrestricted use, distribution, and reproduction in any medium, provided the original work is properly cited.

Solid solution of perovskite Pb,SrTiO_3 in Pb-rich composition can be crystallized in borosilicate glassy matrix. The addition of rare earth and transition metal oxides is known to influence the crystallization behavior and surface morphology of perovskite crystallites in glassy matrix. In the present paper, the glasses in the lead-rich system $64[(\text{Pb}_x\text{Sr}_{1-x})\cdot\text{TiO}_3]-25[2\text{SiO}_2\cdot\text{B}_2\text{O}_3]-5[\text{K}_2\text{O}]-5[\text{BaO}]$ ($1 \leq x \leq 0.5$) with the addition of 1 mol % La_2O_3 were prepared to study its effect on their crystallization behavior. Differential thermal analysis (DTA) patterns show one or more exothermic crystallization sharp peaks, which shift towards higher temperature with increasing concentration of SrO. The glasses were subjected to various heat-treatment schedules for crystallization. X-ray diffraction analysis of these glass ceramic samples shows that major crystalline phase of the entire glass ceramic sample with $x \geq 0.5$ was found to have tetragonal structure similar to PbTiO_3 ceramic, and addition of La_2O_3 enhances the crystallization of the perovskite phase and retards the crystallization of minor phases.

1. Introduction

Glass ceramics are an important class of materials that have been commercially quite successful. The pore-free polycrystalline materials are produced by the controlled crystallization of glass and composed of randomly oriented crystals with some residual glass [1]. Crystallization is accomplished by subjecting the glasses to a carefully regulated heat treatment schedule, which results in the nucleation and growth of crystal phases within the glass samples [2]. Extensive studies have been reported on the crystallization and dielectric behavior of ferroelectric glass ceramics, specifically PbTiO_3 and NaNbO_3 [3]. These studies show that both the parent glass composition and heat treatment schedule determine the crystalline phase constitution, microstructure, and dielectric properties of respective glass ceramics. Bergeron and Russell investigated the growth of PbTiO_3 from $\text{PbO-B}_2\text{O}_3\text{-TiO}_2$ glasses and found that the crystallization proceeded mainly from the surface [4]. The crystallization and microstructural behavior of glass ceramic with perovskite titanate phases,

such as PbTiO_3 [5–11] and SrTiO_3 [12–15], have been investigated. Limited work has been carried on the lead strontium titanate borosilicate glass-ceramic system, despite its wide applications. Thakur et al. [16] investigated the crystallization, microstructure, and dielectric behavior of SrTiO_3 glass ceramic with different oxide additions. They could crystallize SrTiO_3 as a major phase in borosilicate glass ceramic system with addition of proper concentration of alkali oxide K_2O and selected heat treatment schedules. It was also reported that the addition of La_2O_3 enhances the crystallization of strontium titanate [17]. Later on Sahu et al. [18, 19] explored the possibility of substitution of strontium for lead in the system $[(\text{Pb}_{1-x}\text{Sr}_x)\text{O}\cdot\text{TiO}_2]-[2\text{SiO}_2\cdot\text{B}_2\text{O}_3]-[\text{K}_2\text{O}]-[\text{BaO}]$ for crystallization of solid solution perovskite phase. The phase development, microstructural analysis, and dielectric behavior of the glass ceramics indicated that both the glass composition and heat-treatment schedules determine the crystalline phase constitution. Solid solution of PbTiO_3 and SrTiO_3 phases could be crystallized in borosilicate glasses [20–23].

TABLE 1: Glass transition temperature, density of glass, and DTA peaks of various glass samples in the system $[(\text{Pb}_x\text{Sr}_{1-x})\text{O}\cdot\text{TiO}_2] - [2\text{SiO}_2\cdot\text{B}_2\text{O}_3] - [\text{BaO}\cdot\text{K}_2\text{O}] - [\text{La}_2\text{O}_3]$.

Compositions (x)	Glass code	Density (gm/cc)	T_g	DTA Peaks ($^{\circ}\text{C}$)		
				T_{e1}	T_{e2}	T_{e3}
1.0	PTL5B	5.655	510	—	620	700
0.9	9PL5B	4.485	540	597	635	695
0.8	8PL5B	4.357	570	—	—	726
0.7	7PL5B	4.125	575	—	686	739
0.6	6PL5B	3.965	575	—	—	730
0.5	5PL5B	3.912	600	—	—	806

TABLE 2: Heat treatment schedules, glass ceramic codes, and crystalline phases of different lead-rich glass ceramic samples in the system $[(\text{Pb}_x\text{Sr}_{1-x})\text{O}\cdot\text{TiO}_2] - [2\text{SiO}_2\cdot\text{B}_2\text{O}_3] - [\text{BaO}\cdot\text{K}_2\text{O}] - [\text{La}_2\text{O}_3]$.

Glass code	Glass ceramic code	Heat treatment schedules			Crystalline phases
		Heating rate ($^{\circ}\text{C}/\text{min}$)	Holding time (hrs)	Holding temp ($^{\circ}\text{C}$)	
PTL5B	PTL5B700T	5	3	700	P + PT
	PTL5B700S	5	6	700	P + PT
9PL5B	9PL5B597T	5	3	597	P + PT
	9PL5B635T	5	3	635	P + PT
	9PL5B700T	5	3	700	P + PT*
	9PL5B700S	5	6	700	P + Pb
8PL5B	8PL5B726T	5	3	726	P + R
	8PL5B726S	5	6	726	P + R*
7PL5B	7PL5B686T	5	3	686	P + R* + PT
	7PL5B739T	5	3	739	P
	7PL5B739S	5	6	739	P + PT
6PL5B	6PL5B730T	5	3	730	P + R
	6PL5B730S	5	6	730	P + U*
5PL5B	5PL5B806T	5	3	806	P + R
	5PL5B806S	5	6	806	P + R*

P: Perovskite titanate, PT: PbTi_3O_7 , R: Rutile (TiO_2), Pb: Pb_2O_4 , *Trace amount.

A brief report on crystallization and dielectric behavior of lead strontium titanate borosilicate glass ceramics with addition of La_2O_3 was reported [21]. In the present paper, a detailed study has been made to understand the crystallization behavior and microstructural morphology in the lead-rich glass ceramic samples in the system $64[(\text{Pb}_x\text{Sr}_{1-x})\text{TiO}_3] - 25[2\text{SiO}_2\text{B}_2\text{O}_3] - 5[\text{K}_2\text{O}] - 5[\text{BaO}]$ with addition of 1% La_2O_3 . The crystallization and surface morphology of strontium-rich compositions are given in the second paper ‘‘Crystallization behavior and surface morphology of strontium rich $(\text{Pb}_x\text{Sr}_{1-x})\text{TiO}_3$ glass ceramics in presence of La_2O_3 -II.’’

2. Experimental Procedure

Glasses in the system $64[(\text{Pb}_x\text{Sr}_{1-x})\text{TiO}_3] - 25[2\text{SiO}_2\cdot\text{B}_2\text{O}_3] - 5[\text{K}_2\text{O}] - 5[\text{BaO}] - 1[\text{La}_2\text{O}_3]$ with varying lead to strontium ratio ($1 \leq x \leq 0.5$) have been prepared by melt-quench method. The highly pure chemicals powder of PbO , SrCO_3 , TiO_2 , SiO_2 , H_3BO_3 , BaCO_3 , K_2CO_3 , and La_2O_3 was mixed in a mortar using acetone as a grinding medium. The dry powders were melted in the temperature range 1120 – 1240°C in an electrically heated furnace. The melt was poured into

an aluminium mould, pressed by a thick aluminium plate, and immediately annealed at temperature 400°C for three hours in another furnace. All the glasses were characterized by differential thermal analysis (DTA) to determine glass transition and the crystallization temperatures (Table 1). Differential thermal analysis was done on the powdered glass samples at a heating rate of $10^{\circ}\text{C}/\text{min}$. On the basis of DTA results, various glass ceramic samples were prepared by heat treating the glasses in the temperature range 600 – 806°C . The different heat-treatment schedules and nomenclature of glass ceramic samples are listed in the Table 2. The glasses were heat treated by heating them at a heating rate of $5^{\circ}\text{C}/\text{min}$ to the desired temperature and holding them for 3 or 6 hours. The samples were then cooled to room temperature at a cooling rate of $10^{\circ}\text{C}/\text{min}$. Three-hour heat treatment was given to all glasses at their respective DTA peaks, whereas six-hour heat treatment was given to all glasses at their DTA corresponding to major crystalline perovskite phase. The nomenclature of glass ceramic samples includes the code of their parent glass composition followed by heat-treatment temperature and followed by a letter ‘‘T’’ and ‘‘S’’ for 3 and 6 hours heat treatment, respectively. X-ray diffraction patterns

were recorded using a Rigaku X-ray diffractometer using Cu $K\alpha$ radiation. X-ray diffraction patterns were compared with standard d -values from JCPDS files for different constituting phases. Gold coatings were applied by the sputtering method to the etched surfaces of various glass ceramic samples intended for scanning electron microscopy (SEM) in order to study the morphology of different crystalline phases.

3. Results

3.1. Differential Thermal Analysis (DTA). DTA curves for these glasses with different (Pb) lead to strontium (Sr) ratio ($x = 1.0$ to 0.5) are shown in Figures 1 and 2. DTA patterns of different glasses show one or more exothermic peaks. These exothermic peaks represent the temperature at which the rate of crystallization of different phases is maximum. All glasses show a shift in the base line at a temperature, depending on the composition, in the temperature range of 510–600°C. This shift in the base line shows a change in the specific heat of the glass, which is attributed to the glass transition temperature, T_g . Glass transition temperatures of different glass samples are given in Table 1. The glass transition temperature has been found to increase with the increasing concentration of SrO. This may be due to increase in the viscosity of the melt.

DTA pattern of the glass PTL5B with no strontium shows two exothermic peaks at 620 and 700°C (Figure 1(a)). The peak at 700°C represents the crystallization of the major perovskite lead titanate, (P), $PbTiO_3$ phase in the glass ceramic. The peak at 620°C represents the crystallization of the minor $PbTi_3O_7$ (PT). This is confirmed by powder X-ray diffraction (XRD) studies. The peak corresponding to crystallization of major perovskite phase is present in DTA patterns of all the glasses. Two DTA peaks are also observed for the glass 7PL5B.

Three DTA peaks are observed for the glass 9PL5B. All other glasses show a single exothermic peak in their DTA patterns. The temperature of peaks T_{c1} , T_{c2} , and T_{c3} for different glasses in this system with PbO to SrO ratio and 1% La_2O_3 is given in Table 1.

3.2. X-Ray Diffraction Analysis and Crystallization Behavior. X-ray diffraction (XRD) patterns for various glass ceramic samples crystallized at different temperatures for 3 hours are shown in Figure 3. All the peaks in respective XRD patterns were matched with JCPDS of various compounds data for constituent oxides. X-ray diffraction pattern for the glass ceramic samples PTL5B700T ($x = 1.00$) is shown in Table 2.

In Figure 3(a), it is observed from the XRD pattern that $PbTiO_3$ (P) is the major crystalline phase and $PbTi_3O_7$ (PT) is the secondary phase in this glass ceramic sample. Figures 3(b) and 3(c) show the XRD patterns of glass ceramic samples 9PL5B695T and 8PL5B726T with heat treatment at different temperatures. XRD patterns of glass ceramic sample 9PL5B695T show the presence of tetragonal perovskite phase as major phase and $PbTi_3O_7$ as a minor phase. When the glass is heat treated at lower temperature, the amount of minor $PbTi_3O_7$ phase is more in comparison to the glass

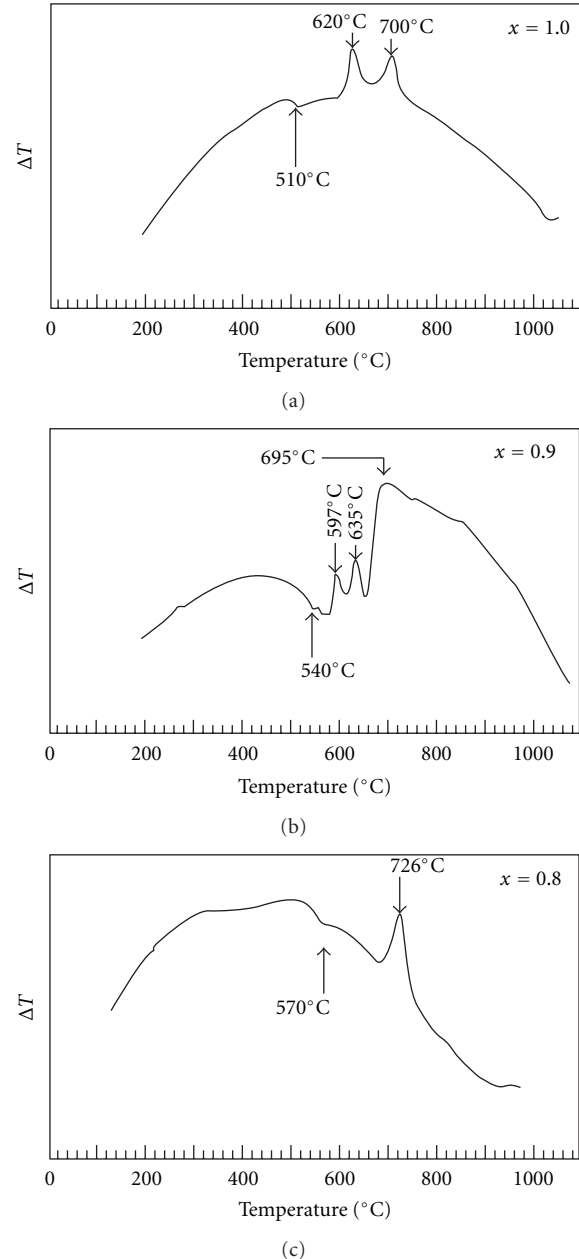


FIGURE 1: DTA pattern of glasses: (a) PTL5B, $x = 1.0$, (b) 9PL5B, $x = 0.9$, and (c) 8PL5B, $x = 0.8$.

ceramic sample obtained by heat treating at 695°C. This is indicated by the relative intensity of XRD lines of P and PT phases. This shows that the DTA peaks at lower temperatures correspond to crystallization of minor phase, while the peak T_{c3} at 695°C corresponds to crystallization of perovskite phase.

The XRD data of the major phase of these glass ceramic samples were indexed on the basis of tetragonal unit cell similar to lead titanate. The lattice parameters (s) for the major crystalline phases in the glass ceramic system were obtained by using software CEL. The structure, lattice parameters (c , a), tetragonality, c/a , for the crystalline phase are given in Table 3. The glass ceramic samples obtained by

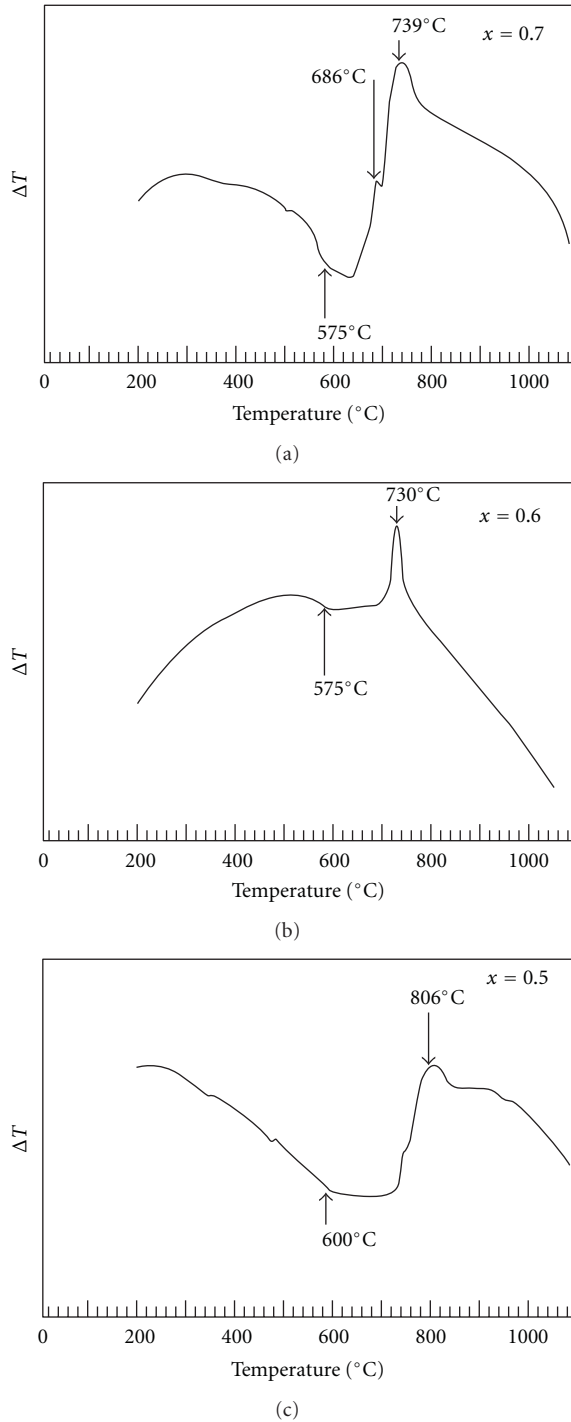


FIGURE 2: DTA pattern of glasses: (a) 7PL5B, $x = 0.7$, (b) 6PL5B, $x = 0.6$, and (c) 5PL5B, $x = 0.5$.

heat-treating glasses with $x = 1.0$ and 0.9 were found to show similar crystallization behavior (Figure 3). They differ only in terms of minor phase and value of lattice parameters. XRD patterns for glass ceramic samples 9PL5B597T; 9PL5B635T; 9PL5B695T are shown in Figure 4. The XRD patterns for these glass ceramic samples show the formation of perovskite as a major phase. Large amount of PT and small amount of rutile (R) are also present. The amount of secondary

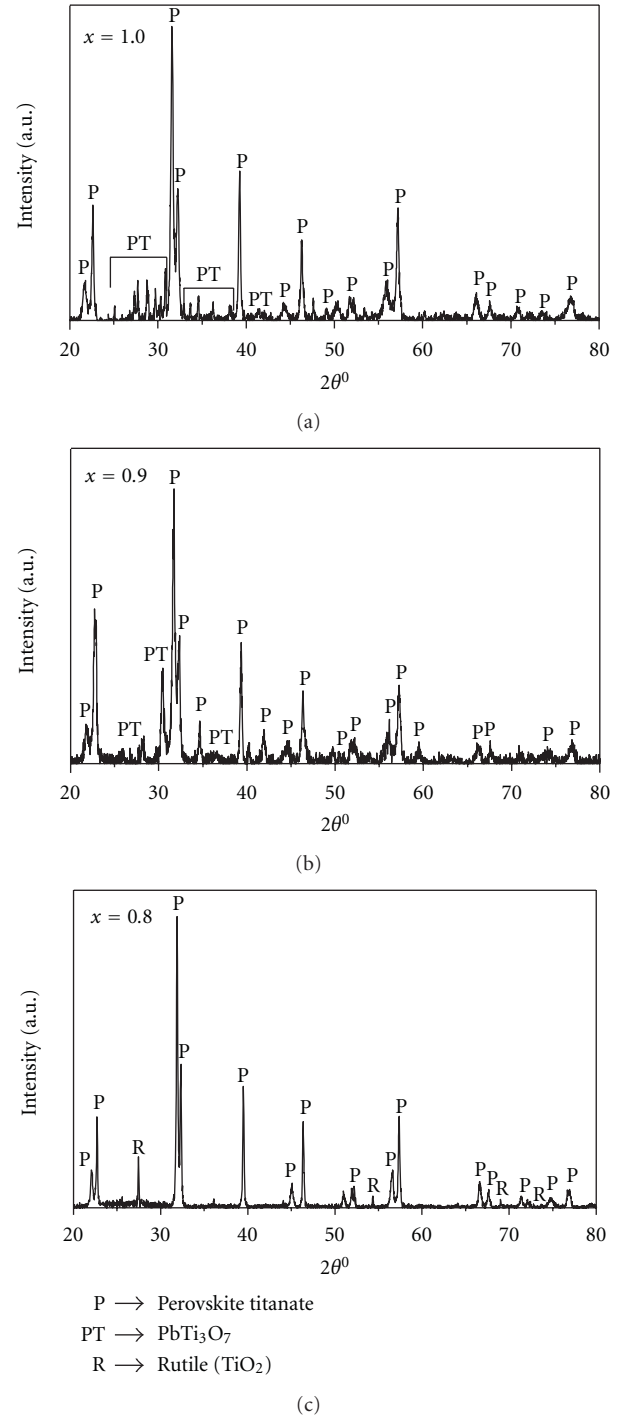
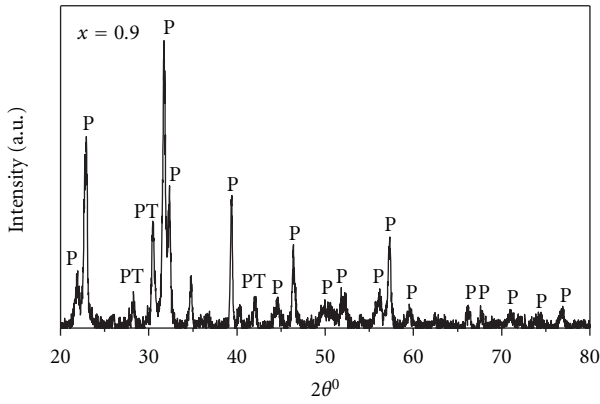
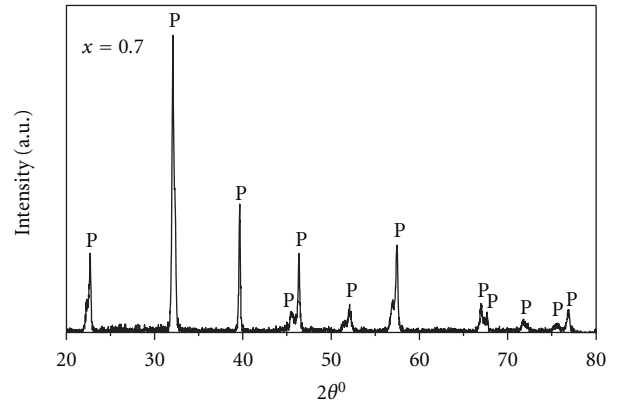


FIGURE 3: X-ray diffraction patterns of different glass ceramic samples: (a) PTL5B700T, (b) 9PL5B695T, and (c) 8PL5B726T.

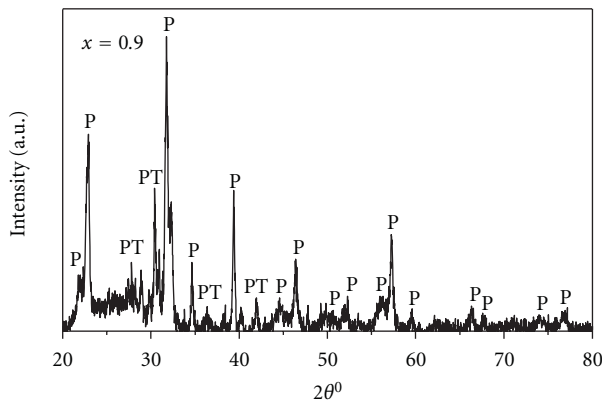
phase of PbTi_3O_7 for $x = 0.9$ obtained by heat treatment at higher temperature is found to be less in comparison to the composition with $x = 1.0$. The glass with $x = 0.7$ was heat treated for 3 and 6 hours at 686°C and 739°C to study the effect of the crystallization temperature and soaking time on the microstructure and dielectric behavior of the resulting glass ceramic samples. Perovskite titanate was found to be major phase with secondary PbTi_3O_7 and trace amount of



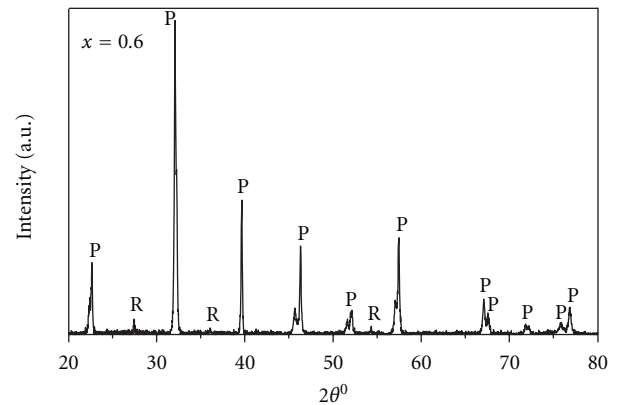
(a)



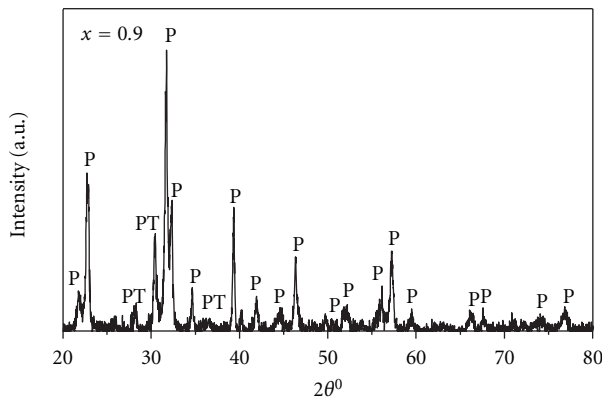
(a)



(b)

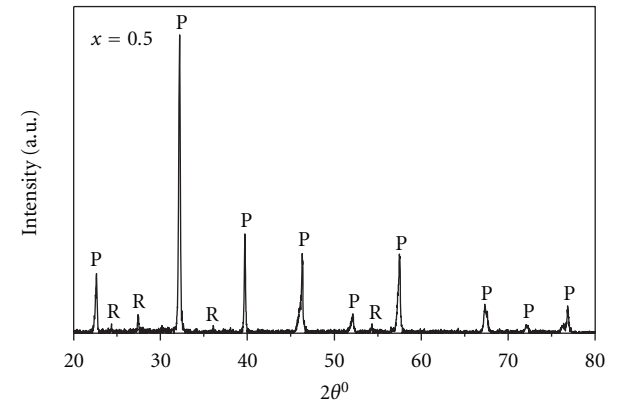


(b)



(c)

P → Perovskite titanate
PT → PbTi₃O₇



(c)

P → Perovskite titanate
PT → PbTi₃O₇
R → TiO₂

FIGURE 4: X-ray diffraction patterns of different glass ceramic samples: (a) 9PL5B597T, (b) 9PL5B635T, and (c) 9PL5B695T.

FIGURE 5: X-ray diffraction patterns of different glass ceramic samples: (a) 7PL5B739T, (b) 6PL5B730T, and (c) 5PL5B806T.

rutile phase. But for glass ceramic obtained by heat-treating at 739°C for 3 hours, the presence of secondary phases of PbTi₃O₇ and rutile (TiO₂) was not observed. Figure 5 shows the XRD patterns for the glass ceramic samples 6PL5B730T and 5PL5B806T. Perovskite titanate (P) was found as a major phase and rutile (R) as a minor phase. They contain the same phases but only differ in the tetragonality.

XRD patterns for glass ceramic samples PTL5B700S, 9PL5B700S, and 8PL5B726S crystallized at 700°C and 726°C for 6 hours, respectively, are shown in Figure 6. Glass ceramic sample PTL5B700S has the phase constitution similar to PTL5B700T that is obtained by heat treating the glass for 3 hours.

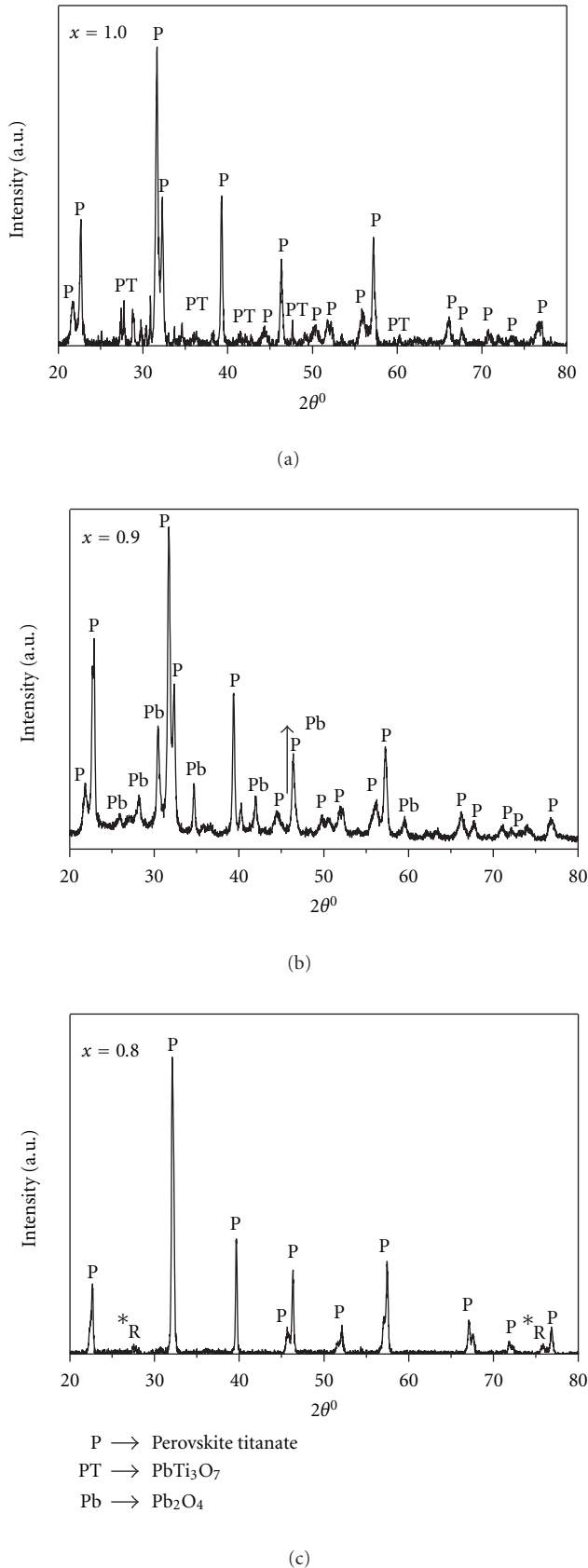


FIGURE 6: X-ray diffraction patterns of different glass ceramic samples: (a) PTL5B700S, (b) 9PL5B700S, and (c) 8PL5B726S. *: Trace amount of Rutile (TiO_2) phase.

For the glass ceramic sample 9PL5B700S, a change is observed in the crystalline phase in comparison to 9PL5B700T. This change is in the form of secondary phases, PbTi_3O_7 (PT) and Pb_2O_4 (Pb). For sample heat treated at 700°C for 3 hours, the secondary phase is PbTi_3O_7 whereas for 6 hrs of heat treatment, the secondary phase is Pb_2O_4 . Figure 6(c) depicts the XRD pattern of glass ceramic sample 8PL5B726S. This shows the presence of perovskite titanate as the major phase. A little amount of TiO_2 (rutile) phase is also present. This glass ceramic sample shows better amount of perovskite phase in comparison to 3-hour heat treatment schedules. Figure 7(a) shows the XRD pattern for the glass ceramic sample 7PL5B739S. This sample contains PbTi_3O_7 as minor phase along with perovskite as major phase.

Figures 7(b) and 7(c) show XRD patterns for the glass ceramic samples 6PL5B730S and 5PL5B806S. Perovskite lead strontium titanate is crystallized as the major phase. It is also observed that the secondary phase of rutile (trace amount) is also present in these glass ceramic samples except for the glass ceramic sample 6PL5B730S. In 6PL5B700S glass ceramic sample, an unidentified phase is observed in small amount in place of rutile phase.

Comparison of XRD data of these glass ceramic samples with standard data from JCPDS files for different possible phases of constituent oxides indicates that although the major phase is lead titanate or lead strontium titanate, solid solution perovskite and many minor phases form in significant proportion. The parent glasses for lead rich glass ceramic samples also show many exothermic peaks in their respective DTA plots. Since these glass ceramic samples are rich in lead, minor phases PbTi_3O_7 and Pb borate form. As the strontium content increases in the glass ceramic sample, the exothermic peaks corresponding to the crystallization of minor phases are suppressed. It results in the crystallization of lead strontium titanate perovskite phase predominantly. XRD patterns of these glass ceramic samples indicate the presence of the other minor phases only in trace amount. In strontium-rich compositions, rutile is mostly present in trace amount. Glass ceramic samples for all glasses were also prepared with 6 hours holding time at their respective crystallization temperatures for the major phase. XRD patterns of these glass ceramic samples with the XRD patterns of the respective glass ceramic samples, which were crystallized for 3 hours, were compared. It is found that XRD peaks of the major phase are well developed and sharp for samples obtained by heating for 6 hours. The peak intensity of minor phase/s decreases. In a few cases, there is a change in the nature of the minor phase. In case of glass ceramic samples 9PL5B695T, the minor phase is PbTi_3O_7 (PT), whereas in glass ceramic samples, the minor phase present is PbB_2O_4 . The crystallization rate of PbB_2O_4 may be slower than that of PbTi_3O_7 and hence PbB_2O_4 minor appears on longer heat treatment.

3.3. Surface Morphology. The surface morphology of all glass ceramic samples shows fine crystallites of perovskite major phase of lead titanate and lead strontium titanate. Qualitative inspection of all these micrographs revealed that the relative

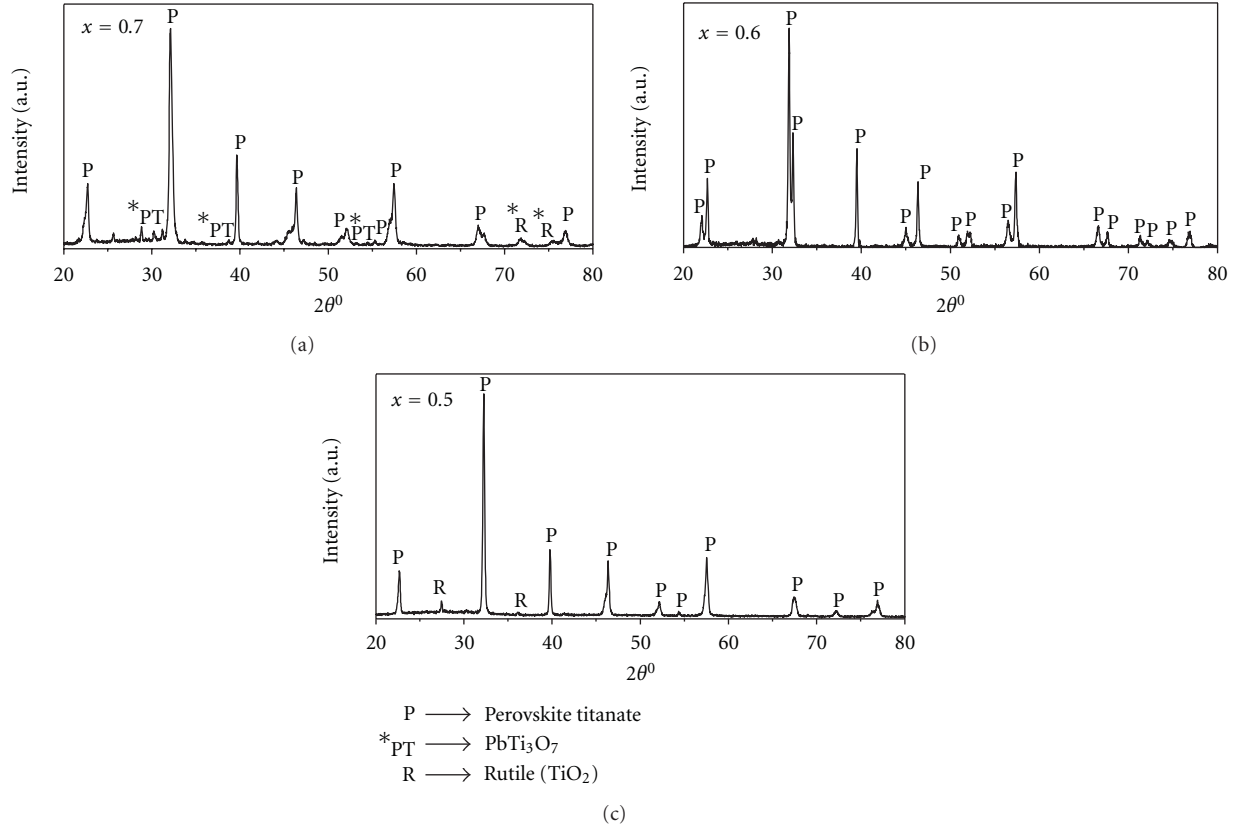


FIGURE 7: X-ray diffraction patterns of different glass ceramic samples: (a) 7PL5B739S, (b) 6PL5B730S, and (c) 5PL5B806S.

TABLE 3: Crystal structure, lattice parameters, and axial ratio of major crystalline phase in different lead-rich glass ceramic samples.

Glass ceramics	Crystal structure	Lattice parameters		Axial ratio (c/a)	(Pb,Sr)/TiO ₃ ceramic*		
		c (Å)	a (Å)		c (Å)	a (Å)	c/a
PTL5B700T	Tetragonal	4.117 ± 0.005	3.916 ± 0.005	1.051			
PTL5B700S	Tetragonal	4.125 ± 0.005	3.906 ± 0.005	1.056	4.138	3.892	1.063
9PL5B700T	Tetragonal	4.080 ± 0.002	3.910 ± 0.002	1.043			
9PL5B700S	Tetragonal	4.079 ± 0.005	3.909 ± 0.005	1.043	4.004	3.837	1.043
8PL5B726T	Tetragonal	4.019 ± 0.001	3.916 ± 0.001	1.026			
8PL5B726S	Tetragonal	4.163 ± 0.007	3.910 ± 0.007	1.064	3.983	3.864	1.030
7PL5B739T	Tetragonal	3.974 ± 0.001	3.921 ± 0.001	1.013			
7P5B739S	Tetragonal	3.977 ± 0.002	3.922 ± 0.002	1.014	3.984	3.903	1.020
6PL5B730T	Tetragonal	3.967 ± 0.001	3.916 ± 0.001	1.013			
6PL5B730S	Tetragonal	4.024 ± 0.001	3.915 ± 0.001	1.027	3.947	3.882	1.016
5PL5B806T	Tetragonal	3.932 ± 0.002	3.927 ± 0.002	1.001			
5PL5B806S	Tetragonal	3.938 ± 0.001	3.918 ± 0.001	1.005	3.960	3.896	1.016

* Reference [20].

content of residual glass phase was little or not significant. The coexistence of coarse and ne perovskite particles has also been observed and reported in similar lead titanate glass ceramics [18, 24]. Scanning electron micrographs of the various glass ceramic samples heat treated for 3 and 6 hours are shown in Figures 8 and 9. Figure 8 shows scanning electron micrographs of glass ceramic samples PTL5B700T, 9PL5B695T, 8PL5B726T, 7PL5B739T, and 5PL5B806T. The

glass ceramic sample PTL5B700T is found to be composed of interconnected fine crystallites of lead titanate (PbTiO₃), which are dispersed in the glassy matrix (Figure 8(a)). XRD studies confirm that the fine crystallites are of PbTiO₃, which is the major crystalline phase. In general, the white region in the microstructure represents the major crystalline phase/secondary phase, while the black region depicts the residual glass in all scanning electron micrographs. For the

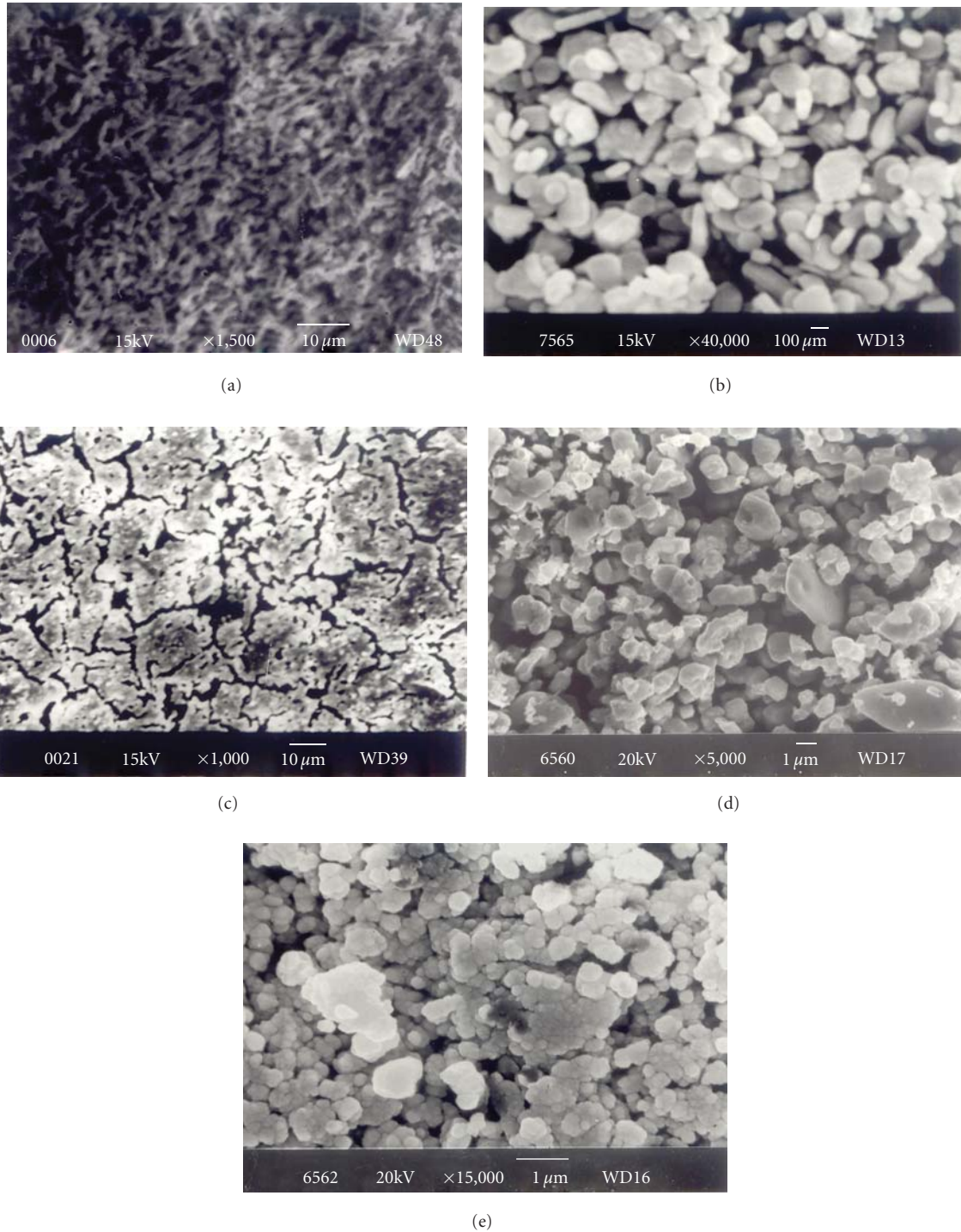


FIGURE 8: Scanning electron micrographs of glass ceramic samples: (a) PTL5B700T, (b) 9PL5B695T, (c) 8PL5B726T, (d) 7PL5B739T, and (e) 5PL5B806T.

glass ceramic sample PTL5B700S, there is a change in the morphology of the crystallites of the major phase, PbTiO_3 , (Figure 9(a)). These crystallites are found to have round shape and are agglomerated. The size of the crystallites is higher in comparison to that for 3-hour of heat-treated glass ceramic sample. Figure 8(b) shows the scanning electron micrograph of the glass ceramic sample 9PL5B700T. The

crystallites size is in the submicron range. The volume fraction of the residual glass is small. Some smaller whitish grains represent the secondary phase of PbTi_3O_7 . Figures 8(c) and 9(b) are the scanning electron micrographs for the glass ceramic samples 8PL5B726T and 8PL5B726S, respectively. The glass ceramic sample 8PL5B726T shows dispersion of the major perovskite phase in the glassy matrix. As the

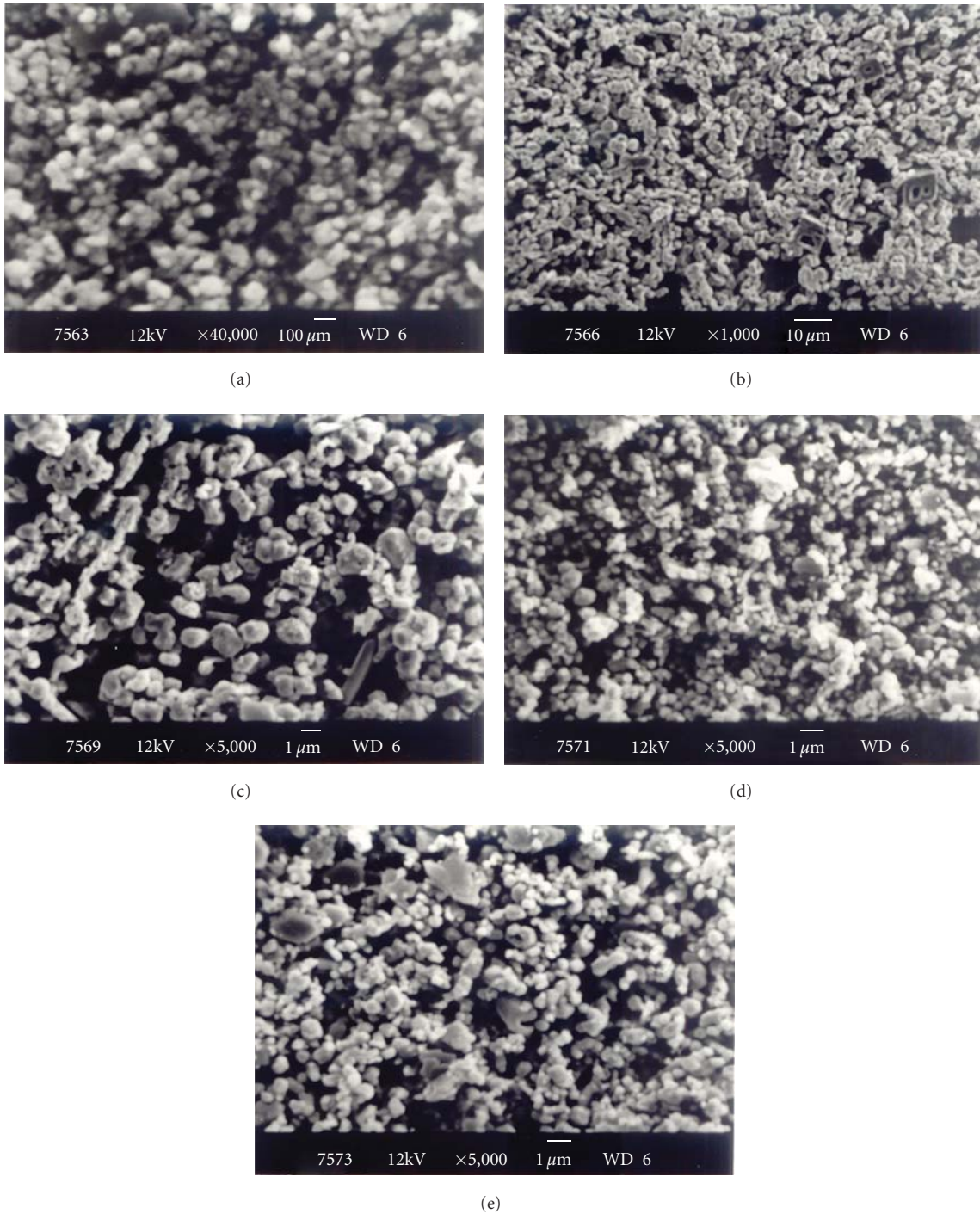


FIGURE 9: Scanning electron micrographs of glass ceramic samples: (a) PTL5B700S, (b) 8PL5B726S, (c) 7PL5B739S, (d) 6PL5B730S, and (e) 5PL5B806S.

crystallization time is increased from 3 to 6 hours, well-separated crystallites of major phase are formed as shown in Figure 9(b).

It is confirmed from the study of XRD and SEM that the 6-hour heat-treatment schedule is not suitable for the crystallization of glass sample 7PL5B ($x = 0.7$). The scanning electron micrograph of glass ceramic sample 6PL5B730S shown in Figure 9(d) shows crystallization of submicrometer

grains of perovskite phase. The shiny white region represents the trace amount of the unidentified phase.

Figures 8(e) and 9(e) show the scanning electron micrographs of chemically etched surfaces of glass ceramic samples 5PL5B806T and 5PL5B806S, which are obtained by the crystallization of the glass 5PL5B at 806°C for 3 and 6 hours of heat treatment schedule. The large amounts of rutile (TiO_2) are crystallized on the upper side of the perovskite

titanate major phase, while for the 6-hour heat-treated glass ceramic sample 5PL5B806S, the trace amount of rutile is distributed inside the glassy matrix.

4. Discussion

There is a shift in different XRD peaks positions of major perovskite phase with changing lead to strontium ratio in the compositions of the base glasses. The position of XRD peaks for various glass ceramic samples shifts systematically with composition, x or Pb/Sr ratio. The lattice parameters “ c ” and “ a ” and the axial ratio (c/a) of the perovskite phase continuously decrease as the concentration of SrO increases in the glass. In general, XRD patterns of the glass ceramic samples rich in lead with $x = 1.0$ to 0.5 indicate the formation of tetragonal crystals similar to lead titanate. The shift in the XRD peak positions and hence the resulting changes in the lattice parameters from that of undoped PbTiO_3 ceramics could be due to two factors: (i) formation of PbTiO_3 solid solution with SrTiO_3 (ii) and strain due to crystal clamping. Since both of these effects may have been present, the crystal phase developed in these compositions cannot be identified unambiguously through room temperature XRD techniques. Some other characterization techniques have to be adopted to confirm the composition of crystallites.

5. Conclusions

Differential thermal analysis (DTA) patterns show more than one peak in the lead-rich glass compositions. These peaks are sharp. Doping of La_2O_3 affects the crystallization behavior and dielectric properties of the glass ceramic samples. The addition of La_2O_3 promotes the crystallization of major phase and retards the crystallization of minor phases. X-rays diffraction patterns of lead-rich glass ceramic samples show that the major phase of PbTiO_3 or perovskite $(\text{Pb,Sr})\text{TiO}_3$ and a trace amount of pyrochlore phase of PbTi_3O_7 . Crystalline phase of all the glass ceramic sample of glasses with $x \leq 0.5$ was found to have tetragonal structure. Surface morphology of the fined crystalline phase is observed uniform and well interconnected in residual glassy matrix.

Acknowledgments

The authors are highly grateful to Dr. Chandra Prakash and Dr. O. P. Thakur of the Electroceramic Division, Solid State Physics Laboratory, Delhi (India) for providing access to the gold coating facility for the glass ceramic samples. Financial support from Defence Research and Development Organization (India) is gratefully acknowledged.

References

- [1] M. W. Barsoum, *Fundamental of Ceramics*, McGraw-Hill, Singapore, 1997.
- [2] P. W. Mc Millan, *Glass Ceramics*, Academic Press, London, UK, 2nd edition, 1974.
- [3] T. Kokubo and M. Tashiro, “Dielectric properties of fine-grained PbTiO_3 crystals precipitated in a glass,” *Journal of Non-Crystalline Solids*, vol. 13, no. 2, pp. 328–340, 1974.
- [4] C. G. Bergeron and C. K. Russell, “Nucleation and growth of lead titanate from a glass,” *Journal of the American Ceramic Society*, vol. 48, no. 3, pp. 115–118, 1965.
- [5] D. G. Grossman and J. O. Isard, “Lead Titanate glass-ceramics,” *Journal of the American Ceramic Society*, vol. 52, pp. 230–241, 1969.
- [6] D. G. Grossman and J. O. Isard, “Crystal clamping in PbTiO_3 glass-ceramics,” *Journal of Materials Science*, vol. 4, no. 12, pp. 1059–1063, 1969.
- [7] S. M. Lynch and J. E. Shelby, “Crystal clamping in lead titanate glass-ceramics,” *Journal of the American Ceramic Society*, vol. 67, no. 6, pp. 424–427, 1984.
- [8] W. Mianxue and Z. Peinan, “Piezoelectricity, pyroelectricity and ferroelectricity in glass ceramics based on PbTiO_3 ,” *Journal of Non-Crystalline Solids*, vol. 84, no. 1–3, pp. 344–351, 1986.
- [9] J. J. Shyu and Y. S. Yang, “Crystallization of a $\text{PbO-BaO-TiO}_2\text{-Al}_2\text{O}_3\text{-SiO}_2$ glass,” *Journal of the American Ceramic Society*, vol. 78, no. 6, pp. 1463–1468, 1995.
- [10] W. N. Lawless, “Thermometer equations for low-temperature glass-ceramic capacitance thermometers,” *Cryogenics*, vol. 42, pp. 561–566, 1972.
- [11] W. N. Lawless, “Three application areas for strontium titanate glass-ceramics,” *Ferroelectrics*, vol. 3, pp. 287–293, 1971.
- [12] W. N. Lawless, “Some low-temperature properties and applications of SrTiO_3 crystallized from glass,” *Ferroelectrics*, vol. 7, pp. 379–381, 1974.
- [13] S. L. Swartz, E. Breval, and A. S. Bhalla, “Effect of nucleation on the crystallization and dielectric properties of strontium titanate glass-ceramics,” *American Ceramic Society Bulletin*, vol. 67, no. 4, pp. 763–770, 1988.
- [14] S. L. Swartz, E. Breval, C. A. Randall, and B. H. Fox, “Strontium Titanate (SrTiO_3) glass ceramics—part I: crystallization and Microstructure,” *Journal of Materials Science*, vol. 23, no. 11, pp. 3997–4003, 1988.
- [15] S. L. Swartz, A. S. Bhalla, L. E. Cross, and W. N. Lawless, “Strontium Titanate (SrTiO_3) glass ceramics—part II: dielectric properties,” *Journal of Materials Science*, vol. 23, pp. 4004–4012, 1988.
- [16] O. P. Thakur, D. Kumar, O. Parkash, and L. Pandey, “Effect of K_2O addition on crystallization and microstructural behavior of strontium Titanate borosilicate glass ceramic system,” *Journal of Materials Letters*, vol. 23, pp. 253–260, 1995.
- [17] O. P. Thakur, *Crystallization, microstructure and dielectric behavior of strontium Titanate borosilicate glass ceramics with some additives*, Ph.D. thesis, Banaras Hindu University, Varanasi, India, 1998.
- [18] A. K. Sahu, D. Kumar, and O. Parkash, “Crystallisation of lead strontium titanate perovskite phase in $[(\text{Pb}_{1-x}\text{Sr}_x)\text{O} \cdot \text{TiO}_2] - [2\text{SiO}_2 \cdot \text{B}_2\text{O}_3] - [\text{K}_2\text{O}]$ glass ceramics,” *British Ceramic Transactions*, vol. 102, no. 4, pp. 139–147, 2003.
- [19] A. K. Sahu, D. Kumar, and O. Parkash, “Lead-strontium titanate glass ceramics: I—crystallization and microstructure,” *Journal of Materials Science*, vol. 41, no. 7, pp. 2075–2085, 2006.
- [20] S. Subrahmanyam and E. Goo, “Nucleation of the ferroelectric phase in the $(\text{Pb}_x\text{Sr}_{1-x})\text{TiO}_3$ system,” *Acta Materialia*, vol. 46, no. 3, pp. 817–822, 1998.
- [21] A. K. Sahu, D. Kumar, O. Parkash, O. P. Thakur, and C. Prakash, “Effect of $\text{K}_2\text{O/BaO}$ ratio on crystallization, microstructure and dielectric properties of strontium titanate borosilicate glass ceramics,” *Ceramics International*, vol. 30, no. 3, pp. 477–483, 2004.

- [22] D. Kumar, C. R. Gautam, and O. Parkash, "Preparation and dielectric characterization of ferroelectric $(\text{Pb}_x\text{Sr}_{1-x})\text{TiO}_3$ glass ceramics doped with La_2O_3 ," *Applied Physics Letters*, vol. 89, no. 11, pp. 112908–112910, 2006.
- [23] W. Liu, C. H. Mao, G. X. Dong, and J. Du, "Effects of PbO and SrO contents on crystallization and dielectric properties of $\text{PbO-SrO-Na}_2\text{O-Nb}_2\text{O}_5\text{-SiO}_2$ glass-ceramics system," *Ceramics International*, vol. 35, no. 3, pp. 1261–1265, 2009.
- [24] A. Bahramia, Z. Ali Nematia, P. Alizadehb, and M. Bolandia, "Crystallization and electrical properties of $[(\text{Pb}_{1-x}\text{Sr}_x)\cdot\text{TiO}_3]\text{-}[(2\text{SiO}_2\cdot\text{B}_2\text{O}_3)]\text{-}[\text{K}_2\text{O}]$ glass-ceramics," *Journal of Materials Processing Technology*, vol. 206, pp. 126–131, 2008.

Research Article

Powder Characterization and Electrochemical Properties of $\text{LiNi}_{0.5}\text{Mn}_{1.5}\text{O}_4$ Cathode Materials Produced by Large Spray Pyrolysis Using Flame Combustion

Shinsuke Akao, Motofumi Yamada, Takayuki Kodera, Kenichi Myoujin, and Takashi Ogihara

Graduate School of Fiber Amenity Engineering, University of Fukui, 9-1 Bunkyo 3, Fukui-shi, Fukui 910-8507, Japan

Correspondence should be addressed to Takashi Ogihara, ogihara@matse.u-fukui.ac.jp

Received 2 April 2011; Accepted 7 June 2011

Academic Editor: Joseph Lai

Copyright © 2011 Shinsuke Akao et al. This is an open access article distributed under the Creative Commons Attribution License, which permits unrestricted use, distribution, and reproduction in any medium, provided the original work is properly cited.

$\text{LiNi}_{0.5}\text{Mn}_{1.5}\text{O}_4$ cathode materials were produced by spray pyrolysis apparatus using the flame combustion. SEM revealed that as-prepared powders had spherical morphology with porous microstructure which had an average diameter of about $2\ \mu\text{m}$ with broad size distribution. After the calcination, $\text{LiNi}_{0.5}\text{Mn}_{1.5}\text{O}_4$ powders with polygonal morphology and narrow particle size distribution were obtained. XRD showed that $\text{LiNi}_{0.5}\text{Mn}_{1.5}\text{O}_4$ was well crystallized after the calcination at 900°C . Rechargeable measurement of $\text{LiNi}_{0.5}\text{Mn}_{1.5}\text{O}_4$ cathode showed that the long plateau was observed at $4.7\ \text{V}$ in discharge curve of $\text{LiNi}_{0.5}\text{Mn}_{1.5}\text{O}_4$ cathode and its discharge capacity was $145\ \text{mAh/g}$ at $1\ \text{C}$. The capacity retention of $\text{LiNi}_{0.5}\text{Mn}_{1.5}\text{O}_4$ cathode were 95% at $1\ \text{C}$ after 100 cycles. The discharge capacity and capacity retention of $\text{LiNi}_{0.5}\text{Mn}_{1.5}\text{O}_4$ cathode were $125\ \text{mAh/g}$ and 88% at $20\ \text{C}$. $\text{LiNi}_{0.5}\text{Mn}_{1.5}\text{O}_4$ cathode exhibited also stable cycle performance at 50°C .

1. Introduction

Lithium ion batteries have been extensively used as energy storage devices for portable electronics. Recently, these are well noted as the power sources for the vehicles such as EV and HEV [1]. Both layered type LiCoO_2 and spinel type LiMn_2O_4 is the most important cathode materials because of their high operating voltage at $4\ \text{V}$ [2, 3]. LiCoO_2 have been mostly used as cathode material of commercial lithium ion batteries. However, LiCoO_2 has a problem related to capacity fading due to the instability in rechargeable cycles. Cobalt is also expensive and its resource is not sufficient. Furthermore, the thermal stability is very low in the rechargeable process. Therefore, LiCoO_2 cathode material is not suitable as a lithium ion battery for EV and HEV. On the other hand, LiMn_2O_4 cathode material is suitable due to their advantages such as low cost, abundance, nontoxicity, and thermally stable [4]. It was known that Ni-substitute lithium manganese oxide spinel ($\text{LiNi}_{0.5}\text{Mn}_{1.5}\text{O}_4$) was exhibited rechargeable behavior at about $5\ \text{V}$ [5–7].

$\text{LiNi}_{0.5}\text{Mn}_{1.5}\text{O}_4$ has attracted significant attention as a cathode material with high energy density. It was important

to control the chemical composition to obtain homogeneous $\text{LiNi}_{0.5}\text{Mn}_{1.5}\text{O}_4$ powders. So far, $\text{LiNi}_{0.5}\text{Mn}_{1.5}\text{O}_4$ powders have been prepared via the solution techniques such as coprecipitation [8, 9], spray drying [10], sol-gel [11, 12], polymer gel [13] and chemical wet process [14]. $\text{LiNi}_{0.5}\text{Mn}_{1.5}\text{O}_4$ powders have been also prepared via the improved solid state reaction [15–18] and molten salt reaction [19, 20].

We have noted spray pyrolysis in order to prepare a homogeneous $\text{LiNi}_{0.5}\text{Mn}_{1.5}\text{O}_4$ powder. It was well known that the spray pyrolysis was an effective process for the rapid synthesis of homogeneous multicomponent oxide powders [21]. We have tried to synthesize various type cathode materials for lithium ion battery by spray pyrolysis [22–24]. The rechargeable capacity and cycle performance of lithium ion battery were improved by using the cathode materials for lithium ion battery derived from spray pyrolysis. Park and Sun [25] have reported that homogeneous $\text{LiNi}_{0.5}\text{Mn}_{1.5}\text{O}_4$ powders can be obtained by ultrasonic spray pyrolysis. However, spray pyrolysis has not been applied as an industrial process because it is difficult to homogeneously pyrolyze the mist of inorganic salts in the electrical furnace that the scale-up was done. The difference of pyrolysis temperature

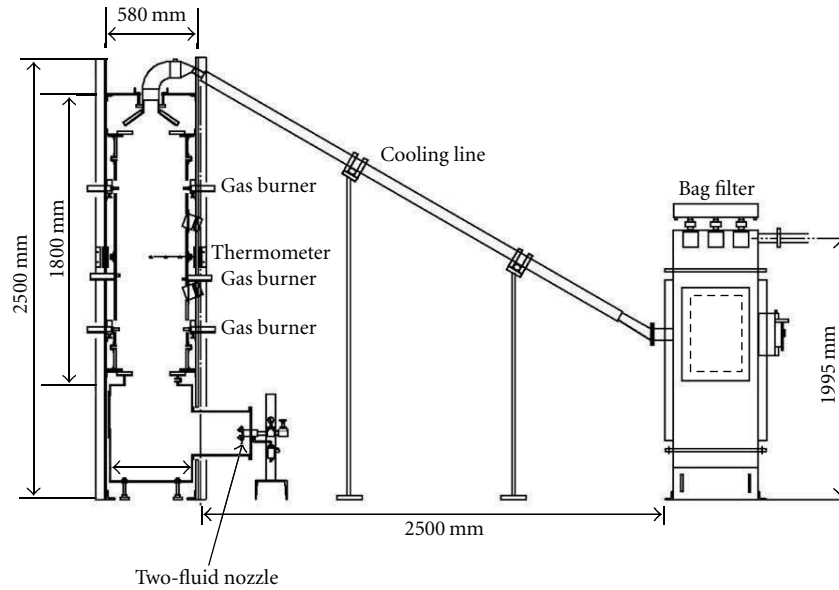


FIGURE 1: Schematic diagram of flame spray pyrolysis apparatus.

inside and outside of the electrical furnace increases with increasing the dimension of electrical furnace. So far, we have also offered the two types of spray pyrolysis apparatuses by using gas burner to produce cathode materials [26, 27]. The advantage of these apparatuses is that it is possible to pyrolyze a large amount of mist during the short time compared with that of electrical furnace. The spray pyrolysis using the flame combustion has also the high effect of energy saving compared with that using the heating of conventional electric furnace. In this work, we modified the flame combustion type spray pyrolysis apparatus [26] in which the mist flowed from the bottom to the top and then tried to produce $\text{LiNi}_{0.5}\text{Mn}_{1.5}\text{O}_4$ powders. In this paper, the powder characterization and electrochemical properties of the $\text{LiNi}_{0.5}\text{Mn}_{1.5}\text{O}_4$ powders produced by large spray pyrolysis apparatus using the flame combustion were described.

2. Experimental

2.1. Powder Preparation. LiNO_3 , $\text{Mn}(\text{NO}_3)_2 \cdot 6\text{H}_2\text{O}$, and $\text{Ni}(\text{NO}_3)_2 \cdot 6\text{H}_2\text{O}$ were used as starting reagents. They were weighted out to attain the molar ratio of metal component (Li:Mn:Ni) of 2:3:1 and were dissolved in distilled water to prepare the starting solution. The concentration of the starting solution was 1 mol/dm^3 . Figure 1 shows schematic diagram of flame spray pyrolysis apparatus used in this work. The apparatus is a prototype developed in order to verify the industrial production of cathode materials by the spray pyrolysis. This consisted of a two-fluid nozzle atomizer (the diameter of nozzle was $10 \mu\text{m}$), a furnace ($1800 \text{ mm} \times 580 \text{ mm}$) with six gas burners, a cooling line, and a bag filter. In comparison with the spray pyrolysis apparatus developed in a past study [26], the scale-up of the furnace was done. The flame combustion was generated using the liquefied petroleum gas and then the temperature of it was maintained

at 500°C . The mist of the starting solution was continuously generated by two-fluid nozzle atomizer with the flow rate of $10 \text{ dm}^3/\text{h}$. The mist was introduced to the furnace by using the air carrier gas and pyrolyzed in the furnace at 500°C . The temperature in the furnace was monitored by the thermometer using Pt thermocouple. The thermometer was set in the centre of the furnace. The cooling line was naturally cooled by the radiation of heat using air. The potential of powders production increased up to 5 kg/day compared with the spray pyrolysis apparatus (3 kg/day) developed in a past. Both as-prepared $\text{LiNi}_{0.5}\text{Mn}_{1.5}\text{O}_4$ powders and outgas were cooled less than 100°C by a cooling line before the powder collection in the bag filter because the temperature of outgas was more than 200°C . $\text{LiNi}_{0.5}\text{Mn}_{1.5}\text{O}_4$ powders were continuously produced for 5 h at the rate of 200 g/h . As-prepared $\text{LiNi}_{0.5}\text{Mn}_{1.5}\text{O}_4$ powders were calcined from 700°C to 1000°C for 2 h under the air atmosphere.

2.2. Characterization of Powders. The crystal phases of $\text{LiNi}_{0.5}\text{Mn}_{1.5}\text{O}_4$ powders were identified with powder X-Ray Diffraction (XRD-6100, Shimadzu). The particle morphology, microstructure, and state of aggregation of $\text{LiNi}_{0.5}\text{Mn}_{1.5}\text{O}_4$ powders were observed with a scanning electron microscope (SEM, JSM-6390, JEOL). The chemical component of $\text{LiNi}_{0.5}\text{Mn}_{1.5}\text{O}_4$ powders was determined by induced coupled plasma analysis (ICP, SII, SPS-7800). Specific surface area of $\text{LiNi}_{0.5}\text{Mn}_{1.5}\text{O}_4$ powders was measured by BET method (SSA, BEL Japan, BELSORP-miniII). The particle density of $\text{LiNi}_{0.5}\text{Mn}_{1.5}\text{O}_4$ powders was determined with the pycnometer (Pycnomatic, Thermoelectron) using He gas.

2.3. Electrochemical Measurement. Cathode was prepared using 80 wt% $\text{LiNi}_{0.5}\text{Mn}_{1.5}\text{O}_4$ powders, 10 wt% acetylene black as a conductive agent, and 10 wt% polyvinylidene fluoride resin as a binder. They were homogeneously mixed

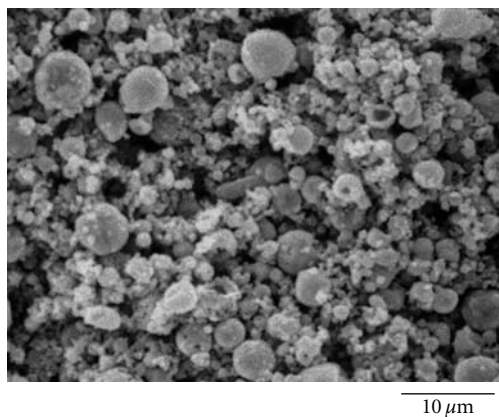


FIGURE 2: SEM photograph of as-prepared $\text{LiNi}_{0.5}\text{Mn}_{1.5}\text{O}_4$ powders.

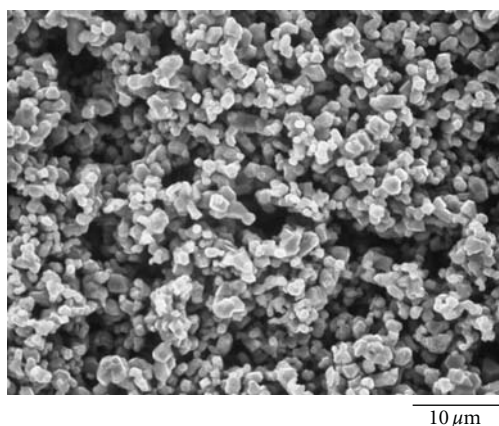


FIGURE 3: SEM photograph of $\text{LiNi}_{0.5}\text{Mn}_{1.5}\text{O}_4$ powders calcined at 800°C .

with *N*-methyl-2-pyrrolidone. They were dried at 120°C for 24 h in a vacuum oven. Metal lithium sheet was used as the anode. Microporous polypropylene membrane was used as a separator. 1 mol/dm^3 LiPF_6 in ethylene carbonate/diethyl carbonate (EC:DEC = 1:1 in volume ratio) was used as the electrolyte. The coin type cell (CR2032) was assembled in a glove box filled with an argon gas. The rechargeable capacity and cycle stability of $\text{LiNi}_{0.5}\text{Mn}_{1.5}\text{O}_4$ cathode were measured by the rechargeable tester (BTS2004H, Hosen) from 3.5 V to 4.9 V at the rechargeable rate from 1 C to 20 C. The cycle stability of $\text{LiNi}_{0.5}\text{Mn}_{1.5}\text{O}_4$ cathode was also measured at 50°C .

3. Results and Discussion

3.1. Particle Characterization of $\text{LiNi}_{0.5}\text{Mn}_{1.5}\text{O}_4$ Powders. $\text{LiNi}_{0.5}\text{Mn}_{1.5}\text{O}_4$ powders were continuously produced at rate of 200 g/h. Figure 2 shows an SEM image of $\text{LiNi}_{0.5}\text{Mn}_{1.5}\text{O}_4$ powders obtained after 5 h. SEM image revealed that as-prepared $\text{LiNi}_{0.5}\text{Mn}_{1.5}\text{O}_4$ particles had spherical morphology with broad particle size distribution. The average particle size and geometrical standard deviation (σ_g) of them were $1.68\ \mu\text{m}$ and 1.34, respectively. The follow particles or spheroidal particles were also observed in Figure 2. This

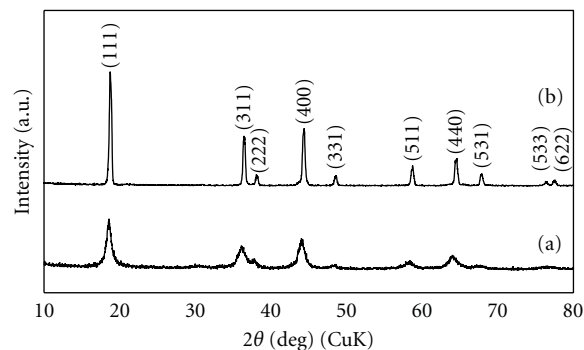


FIGURE 4: XRD patterns of $\text{LiNi}_{0.5}\text{Mn}_{1.5}\text{O}_4$ powders, (a) as-prepared, (b) calcined at 800°C .

result suggested that the large mist derived from two-fluid nozzle atomizer with about nozzle size of $10\ \mu\text{m}$ led to large particle size and broad size distribution of $\text{LiNi}_{0.5}\text{Mn}_{1.5}\text{O}_4$ powders. Specific surface area and particle density of as-prepared $\text{LiNi}_{0.5}\text{Mn}_{1.5}\text{O}_4$ powders were $24.6\ \text{m}^2/\text{g}$ and $3.32\ \text{g}/\text{cm}^3$, respectively. These results suggested that $\text{LiNi}_{0.5}\text{Mn}_{1.5}\text{O}_4$ particles obtained had the porous microstructure which was consisted of primary particles.

Figure 3 shows the particle morphology of $\text{LiNi}_{0.5}\text{Mn}_{1.5}\text{O}_4$ powders calcined at 900°C for 2 h. When as-prepared $\text{LiNi}_{0.5}\text{Mn}_{1.5}\text{O}_4$ powders were calcined at 900°C , the primary particles were sintered to form uniform polygonal morphology. The average particle size and σ_g of them were $1.01\ \mu\text{m}$ and 1.3, respectively. It was found that the particle size and size distribution became small and narrow. Specific surface area of $\text{LiNi}_{0.5}\text{Mn}_{1.5}\text{O}_4$ powders decreased to $1.03\ \text{m}^2/\text{g}$. The particle density of them increased to $4.17\ \text{g}/\text{m}^3$ due to the sintering of the primary particles. This led to the improvement for the dispersibility of $\text{LiNi}_{0.5}\text{Mn}_{1.5}\text{O}_4$ powders in *N*-methyl-2-pyrrolidone solvent, so that the homogeneous slurry of them was obtained for the preparation of cathode.

Figure 4 shows XRD patterns of as-prepared $\text{LiNi}_{0.5}\text{Mn}_{1.5}\text{O}_4$ powders and $\text{LiNi}_{0.5}\text{Mn}_{1.5}\text{O}_4$ powders calcined at 900°C for 2 h. XRD revealed that the crystallinity of as-prepared powders was low, but that was well crystallized by the calcination at 900°C . It was seemed that these diffraction patterns of $\text{LiNi}_{0.5}\text{Mn}_{1.5}\text{O}_4$ powders were identified with a cubic spinel structure with $\text{Fd}3\text{m}$ of space group. The diffraction patterns of impurities except for spinel phase were not observed. From ICP analysis of $\text{LiNi}_{0.5}\text{Mn}_{1.5}\text{O}_4$ powders calcined at 900°C , the molar ratio of $\text{LiNi}_{0.5}\text{Mn}_{1.5}\text{O}_4$ powders was 1.0:0.49:1.49 and showed good agreement with that of starting solution. This suggested that Li^+ ion, Ni^{2+} ion and Mn^{4+} ion were uniformly mixed at molecular level in each mist which was played a role as a microreactor.

3.2. Electrochemical Properties of $\text{LiNi}_{0.5}\text{Mn}_{1.5}\text{O}_4$ Cathode. Figure 5 shows the charge and discharge curves of $\text{LiNi}_{0.5}\text{Mn}_{1.5}\text{O}_4$ cathode at discharge rate indicated. The plateau was observed at around 4.7 V in discharge curves of them. This was attributed to $\text{Ni}^{2+}/\text{Ni}^{4+}$ redox couple [28].

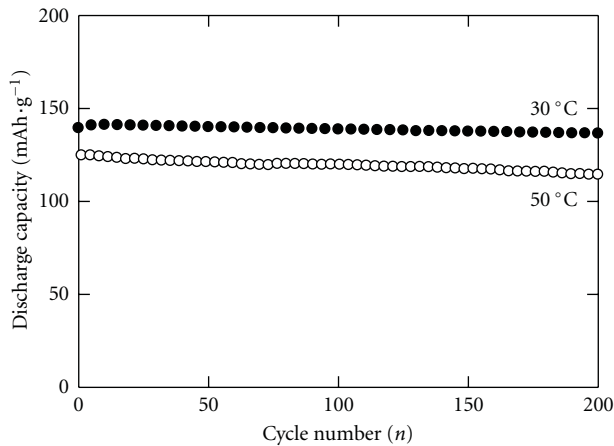


FIGURE 9: Relation between discharge capacity and cycle number at 30°C and 50°C.

and 10 C. 140 mAh/g of discharge capacity was maintained at 1 C. The discharge capacity of $\text{LiNi}_{0.5}\text{Mn}_{1.5}\text{O}_4$ cathode decreased to 130 mAh/g at 10 C. $\text{LiNi}_{0.5}\text{Mn}_{1.5}\text{O}_4$ cathode had also good stability for the alternate cycle test at the higher and lower dischargeable rate. This suggested that the spinel structure of $\text{LiNi}_{0.5}\text{Mn}_{1.5}\text{O}_4$ was also stable for intercalation of Li^+ ion at the high and low rechargeable rate. This suggests that $\text{LiNi}_{0.5}\text{Mn}_{1.5}\text{O}_4$ spinel structure may lead to the high cycle stability for the volume change during the rapid intercalation of lithium ion.

Figure 9 shows the cycle performance of $\text{LiNi}_{0.5}\text{Mn}_{1.5}\text{O}_4$ cathode at 30°C and 50°C. The cycle test was examined at 1 C for 200 cycles. The discharge capacity of $\text{LiNi}_{0.5}\text{Mn}_{1.5}\text{O}_4$ cathode at 30°C was 135 mAh/g after 200 cycles. The capacity retention of it was 95%. The discharge capacity of $\text{LiNi}_{0.5}\text{Mn}_{1.5}\text{O}_4$ cathode at 50°C was 115 mAh/g after 200 cycles. The capacity retention of it was 91%. It was found that the cycle performance at 50°C was also stable as well as that at room temperature.

4. Conclusions

$\text{LiNi}_{0.5}\text{Mn}_{1.5}\text{O}_4$ cathode materials were successfully produced by spray pyrolysis apparatus using the flame combustion. As-prepared $\text{LiNi}_{0.5}\text{Mn}_{1.5}\text{O}_4$ powders had spherical morphology with porous microstructure which had an average diameter of $1.68\ \mu\text{m}$ with broad size distribution. After the calcination, $\text{LiNi}_{0.5}\text{Mn}_{1.5}\text{O}_4$ powders with polygonal morphology and narrow particle size distribution were obtained. $\text{LiNi}_{0.5}\text{Mn}_{1.5}\text{O}_4$ powders were well crystallized after the calcination at 900°C and the chemical composition was in good agreement with that of starting solution. Rechargeable measurement of $\text{LiNi}_{0.5}\text{Mn}_{1.5}\text{O}_4$ cathode showed that the plateau was observed at 4.7 V in discharge curve of $\text{LiNi}_{0.5}\text{Mn}_{1.5}\text{O}_4$ cathode and its discharge capacity was 146 mAh/g at 1 C. The capacity retention of $\text{LiNi}_{0.5}\text{Mn}_{1.5}\text{O}_4$ cathode was 95% at 1 C after 100 cycles. The discharge capacity and capacity retention of $\text{LiNi}_{0.5}\text{Mn}_{1.5}\text{O}_4$ cathode was 125 mAh/g and 88% at 20 C. $\text{LiNi}_{0.5}\text{Mn}_{1.5}\text{O}_4$ cathode exhibited stable cycle performance at 50°C.

References

- [1] E. Karden, S. Ploumen, B. Fricke, T. Miller, and K. Snyder, "Energy storage devices for future hybrid electric vehicles," *Journal of Power Sources*, vol. 168, no. 1, pp. 2–11, 2007.
- [2] K. Mizushima, P. C. Jones, P. J. Wiseman, and J. B. Goodenough, " Li_xCoO_2 ($0 < x \leq 1$): a new cathode material for batteries of high energy density," *Materials Research Bulletin*, vol. 15, no. 6, pp. 783–789, 1980.
- [3] D. Guyomard and J. M. Tarascon, "The carbon/ $\text{Li}_{1+x}\text{Mn}_2\text{O}_4$ system," *Solid State Ionics*, vol. 69, no. 3-4, pp. 222–237, 1994.
- [4] Z. Pegeng, F. Huiqing, F. Yunfei, L. Zhuo, and D. Yongli, "Synthesis and electrochemical properties of sol-gel derived LiMn_2O_4 cathode for lithium-ion batteries," *Rare Metals*, vol. 25, no. 6, pp. 100–104, 2006.
- [5] B. Markovsky, Y. Talyosoff, G. Salitra, D. Aurbach, H. J. Kim, and S. Choi, "Cycling and storage performance at elevated temperatures of $\text{LiNi}_{0.5}\text{Mn}_{1.5}\text{O}_4$ positive electrodes for advanced 5 V Li-ion batteries," *Electrochemistry Communications*, vol. 6, no. 8, pp. 821–826, 2004.
- [6] Y. Idemoto, H. Sekine, K. Ui, and N. Koura, "Physical property, crystal structure and electrode performance depend on synthetic condition of $\text{LiNi}_{0.5}\text{Mn}_{1.5}\text{O}_4$ as cathode materials for 5 V class lithium secondary battery," *Electrochemistry*, vol. 72, no. 8, pp. 564–568, 2004.
- [7] Y. Idemoto, Y. Tsunoda, and N. Koura, "Thermodynamic stability and cathode performance of $\text{LiMn}_{2-x}\text{Ni}_x\text{O}_4$ as an active material for Li secondary battery," *Electrochemistry*, vol. 72, no. 8, pp. 557–563, 2004.
- [8] Y. Fan, J. Wang, X. Ye, and J. Zhang, "Physical properties and electrochemical performance of $\text{LiNi}_{0.5}\text{Mn}_{1.5}\text{O}_4$ cathode material prepared by a coprecipitation method," *Materials Chemistry and Physics*, vol. 103, no. 1, pp. 19–23, 2007.
- [9] X. Fang, N. Ding, X. Y. Feng, Y. Lu, and C. H. Chen, "Study of $\text{LiNi}_{0.5}\text{Mn}_{1.5}\text{O}_4$ synthesized via a chloride-ammonia coprecipitation method: electrochemical performance, diffusion coefficient and capacity loss mechanism," *Electrochimica Acta*, vol. 54, no. 28, pp. 7471–7475, 2009.
- [10] D. Li, A. Ito, K. Kobayakawa, H. Noguchi, and Y. Sato, "Electrochemical characteristics of $\text{LiNi}_{0.5}\text{Mn}_{1.5}\text{O}_4$ prepared by spray drying and post-annealing," *Electrochimica Acta*, vol. 52, no. 5, pp. 1919–1924, 2007.
- [11] Y. S. Lee, Y. K. Sun, S. Ota, T. Miyashita, and M. Yoshio, "Preparation and characterization of nano-crystalline $\text{LiNi}_{0.5}\text{Mn}_{1.5}\text{O}_4$ for 5 V cathode material by composite carbonate process," *Electrochemistry Communications*, vol. 4, no. 12, pp. 989–994, 2002.
- [12] T. Yang, K. Sun, Z. Lei, N. Zhang, and Y. Lang, "The influence of holding time on the performance of $\text{LiNi}_{0.5}\text{Mn}_{1.5}\text{O}_4$ cathode for lithium ion battery," *Journal of Alloys and Compounds*, vol. 502, no. 1, pp. 215–219, 2010.
- [13] H. Y. Xu, S. Xie, N. Ding, B. L. Liu, Y. Shang, and C. H. Chen, "Improvement of electrochemical properties of $\text{LiNi}_{0.5}\text{Mn}_{1.5}\text{O}_4$ spinel prepared by radiated polymer gel method," *Electrochimica Acta*, vol. 51, no. 21, pp. 4352–4357, 2006.
- [14] G. Q. Liu, Y. J. Wang, Q. Lu, W. Li, and C. Hui, "Synthesis and electrochemical performance of $\text{LiNi}_{0.5}\text{Mn}_{1.5}\text{O}_4$ spinel compound," *Electrochimica Acta*, vol. 50, pp. 1956–1968, 2005.
- [15] H. S. Fang, Z. X. Wang, X. H. Li, H. J. Guo, and W. J. Peng, "Low temperature synthesis of $\text{LiNi}_{0.5}\text{Mn}_{1.5}\text{O}_4$ spinel," *Materials Letters*, vol. 60, no. 9-10, pp. 1273–1275, 2006.
- [16] H. S. Fang, Z. X. Wang, X. H. Li, H. J. Guo, and W. J. Peng, "Exploration of high capacity $\text{LiNi}_{0.5}\text{Mn}_{1.5}\text{O}_4$ synthesized by

- solid-state reaction,” *Journal of Power Sources*, vol. 153, no. 1, pp. 174–176, 2006.
- [17] H. Wu, C. V. Rao, and B. Rambabu, “Electrochemical performance of $\text{LiNi}_{0.5}\text{Mn}_{1.5}\text{O}_4$ prepared by improved solid state method as cathode in hybrid supercapacitor,” *Materials Chemistry and Physics*, vol. 116, no. 2-3, pp. 532–535, 2009.
- [18] X. Fang, Y. Lu, N. Ding, X. Y. Feng, C. Liu, and C. H. Chen, “Electrochemical properties of nano- and micro-sized $\text{LiNi}_{0.5}\text{Mn}_{1.5}\text{O}_4$ synthesized via thermal decomposition of a ternary eutectic Li-Ni-Mn acetate,” *Electrochimica Acta*, vol. 55, no. 3, pp. 832–837, 2010.
- [19] L. Wen, Q. Lu, and G. Xu, “Molten salt synthesis of spherical $\text{LiNi}_{0.5}\text{Mn}_{1.5}\text{O}_4$ cathode materials,” *Electrochimica Acta*, vol. 51, no. 21, pp. 4388–4392, 2006.
- [20] J. H. Kim, S. T. Myung, and Y. K. Sun, “Molten salt synthesis of $\text{LiNi}_{0.5}\text{Mn}_{1.5}\text{O}_4$ spinel for 5 V class cathode material of Li-ion secondary battery,” *Electrochimica Acta*, vol. 49, no. 2, pp. 219–227, 2004.
- [21] G. L. Messing, S. C. Zhang, and G. V. Jayanthi, “Ceramic powder synthesis by spray pyrolysis,” *Journal of the American Ceramic Society*, vol. 76, no. 11, pp. 2707–2726, 1993.
- [22] T. Ogihara, H. Aikiyo, N. Ogata et al., “Particle morphology and battery properties of lithium manganate synthesized by ultrasonic spray pyrolysis,” *Advanced Powder Technology*, vol. 13, no. 4, pp. 437–445, 2002.
- [23] I. Mukoyama, T. Kodera, N. Ogata, and T. Ogihara, “Synthesis and lithium battery properties of $\text{LiM}(\text{M}=\text{Fe}, \text{Al}, \text{Mg})_x\text{Mn}_{2-x}\text{O}_4$ powders by spray pyrolysis,” *Key Engineering Materials*, vol. 301, pp. 167–170, 2006.
- [24] T. Ogihara, T. Kodera, K. Myoujin, and S. Motohira, “Preparation and electrochemical properties of cathode materials for lithium ion battery by aerosol process,” *Materials Science and Engineering B*, vol. 161, pp. 109–114, 2009.
- [25] S. H. Park and Y. K. Sun, “Synthesis and electrochemical properties of 5 V spinel $\text{LiNi}_{0.5}\text{Mn}_{1.5}\text{O}_4$ cathode materials prepared by ultrasonic spray pyrolysis method,” *Electrochimica Acta*, vol. 50, no. 2-3, pp. 431–434, 2004.
- [26] K. Myoujin, T. Ogihara, N. Ogata et al., “Synthesis of non-stoichiometric lithium manganate fine powders by internal combustion-type spray pyrolysis using gas burner,” *Advanced Powder Technology*, vol. 15, no. 4, pp. 397–403, 2004.
- [27] M. Yamada, B. Dongying, T. Kodera, K. Myoujin, and T. Ogihara, “Mass production of cathode materials for lithium ion battery by flame type spray pyrolysis,” *Journal of the Ceramic Society of Japan*, vol. 117, no. 1369, pp. 1017–1020, 2009.
- [28] J. H. Kim, S. T. Myung, and Y. K. Sun, “Molten salt synthesis of $\text{LiNi}_{0.5}\text{Mn}_{1.5}\text{O}_4$ spinel for 5 V class cathode material of Li-ion secondary battery,” *Electrochimica Acta*, vol. 49, no. 2, pp. 219–227, 2004.
- [29] M. Akklalouch, J. M. Amarilla, R. M. Rojas, I. Saadoune, and J. M. Rojo, “Sub-micrometric $\text{LiCr}_{0.2}\text{Ni}_{0.4}\text{Mn}_{1.4}\text{O}_4$ spinel as 5 V-cathode material exhibiting huge rate capability at 25 and 55°C,” *Electrochemistry Communications*, vol. 12, no. 4, pp. 548–552, 2010.

Research Article

Low-Temperature Strengths and Ductility of Various Tungsten Sheets

Yutaka Hiraoka¹ and Hiroaki Kurishita²

¹Department of Applied Physics, Okayama University of Science, 1-1 Ridai-cho, Okayama 700-0005, Japan

²International Research Center for Nuclear Materials Science, IMR, Tohoku University, Ibaraki, Oarai 311-1313, Japan

Correspondence should be addressed to Yutaka Hiraoka, hiraoka@dap.ous.ac.jp

Received 18 March 2011; Accepted 6 June 2011

Academic Editor: Kin Ho Lo

Copyright © 2011 Y. Hiraoka and H. Kurishita. This is an open access article distributed under the Creative Commons Attribution License, which permits unrestricted use, distribution, and reproduction in any medium, provided the original work is properly cited.

We used three kinds of tungsten sheets in this study. First, we examined microstructure such as grain size distribution using an optical microscope. Secondly, we carried out three-point bend tests at temperatures between about 290 and 500 K. Then, we examined fracture surface of a failed specimen using a scanning electron microscope. Lastly, by analyzing all these results, we evaluated apparent intergranular and transgranular fracture strengths and discussed strengths and ductility of tungsten. Additionally, we compared mechanical properties of tungsten with those of molybdenum.

1. Introduction

Generally, pure molybdenum after recrystallization indicates a certain amount of ductility at room temperature. In contrast, pure tungsten after recrystallization does not deform plastically near room temperature, since its ductile-to-brittle transition temperature is much above 400 K [1]. Such brittleness of tungsten is principally attributed to high hardness which leads to high yield strength and difficulty of plastic deformation. However, detailed discussion on such difference in the strengths and ductility between tungsten and molybdenum has not been carried out until now.

Materials used in this study are pure tungsten, K-doped tungsten, and La-doped tungsten. All these materials are subjected to recrystallization treatments in various conditions. First, we examined microstructure such as average grain size and size distribution of the specimen after recrystallization using an optical microscope (OM). Secondly, we carried out three-point bend tests at temperatures between about 290 K and 500 K and obtained yield and maximum strengths. From the temperature dependences of the yield and the maximum strengths, we evaluated two parameters (critical stress and critical temperature) [2, 3]. Lastly, we carried out fracture surface observation of a failed specimen by a scanning electron microscope (SEM). Analyzing these experimental data,

we estimated apparent intergranular and/or transgranular fracture strengths. Furthermore, we compared and discussed difference in the mechanical properties between tungsten and molybdenum.

2. Experimental Procedures

Three kinds of tungsten sheets were used in this study. One is pure tungsten sheet (designated as “W” in the text). The others are K-doped tungsten sheet (K: about 50 mass ppm, designated as “KDW” in the text) and La-doped tungsten sheet (La₂O₃: about 1 mass%, designated as “LDW” in the text). Thickness of these sheets is about 1 mm. The materials are produced by powder metallurgy, sintered, hot-rolled, and stress relieved. Typical grain structure of these materials is a fibrous structure. Before the following measurements, the materials were subjected to recrystallization treatments in various conditions. Pure tungsten sheet was heated at 1773 K for 3.6 ks or at 2073 K for 3.6 ks in a vacuum of less than 10⁻⁵ torr. Two doped tungsten sheets were heated at 2073 K for 3.6 ks in vacuum. In the test, heat treatments at 1773 K for 3.6 ks and at 2073 K for 3.6 ks were designated as “r1” and “r2,” respectively. For example, K-doped tungsten after recrystallization at 2073 K for 3.6 ks is designated as “KDW(r2).”

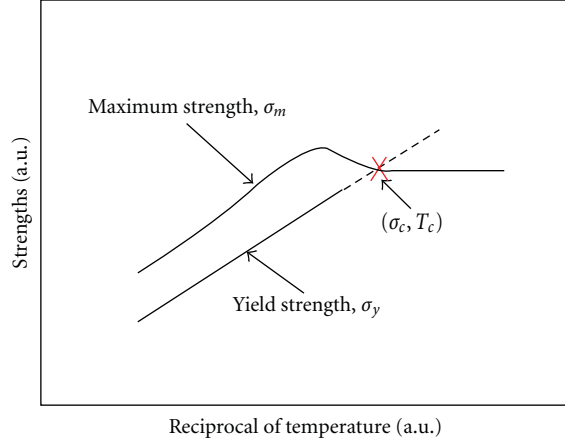


FIGURE 1: Definition of critical stress and critical temperature.

We examined microstructure of the material using OM. Grain shape is approximately equiaxial. Thereby we measured grain size in the direction parallel to the final rolling direction and determined average grain size and its distribution.

We evaluated mechanical properties of the material by three-point bend tests. We carried out the tests at a strain rate of $2 \times 10^{-4} \text{ s}^{-1}$ at a temperature between about 290 K and 500 K. We obtained yield strength (σ_y) and maximum strength (σ_m) using the following:

$$\begin{aligned}\sigma_y &= \frac{3aF_y}{wt^2}, \\ \sigma_m &= \frac{3aF_m}{wt^2}.\end{aligned}\quad (1)$$

F_y and F_m are the load at the yield point and maximum load point, respectively. $2a$ ($= 16 \text{ mm}$) is the support span. w and t are the specimen width and thickness, respectively. In this study, typical specimen width and thickness were 4 mm and 1 mm, respectively. Here, we automatically converted the bend strength (σ_{bt}) to the tensile strength (σ_{tt}) using the following equation. This equation was experimentally obtained [4]:

$$\sigma_{tt} = \frac{\sigma_{bt}}{1.74}.\quad (2)$$

From temperature dependence of the yield and maximum strengths, we estimated two parameters (critical stress, σ_c and critical temperature, T_c) [2, 3]. These parameters are derived as schematically shown in Figure 1. Critical stress is a stress which is necessary to generate and propagate microcracks alternatively along the grain boundaries or in the matrix. This stress corresponds to apparent intergranular fracture strength of a polycrystalline material. Critical temperature, on the other hand, is an expression of ductile-to-brittle transition temperature (DBTT), and reciprocal of this temperature corresponds to low-temperature ductility. Higher value of $(1/T_c)$ means the material is more “ductile” and even at a lower temperature.

We determined fracture mode as follows. We observed the fracture surface of a specimen which failed in a brittle

manner at about 290 K using SEM. In this study, we represent the fracture mode by a parameter, PIF-value. PIF-value is a percent intergranular fracture value and is defined as a ratio of intergranular fracture area to total fracture area. For example, a high PIF-value means grain boundaries of the material are generally very weak. For molybdenum with an average grain size of 20–25 μm , critical stress (σ_c) and fracture mode (PIF-value) demonstrate the following relationship [2, 3]:

$$\text{PIF-value} = 0.2(k - \sigma_c).\quad (3)$$

Here, the constant k corresponds to apparent transgranular fracture strength, since the value of k at PIF-value = 0 means a stress which is necessary to propagate microcracks only in the matrix.

3. Results

3.1. Grain Size and Its Distribution. Grain size distribution of the material is shown in Figures 2(a) (W(r1)), 2(b) (W(r2)), 2(c) (KDW(r2)), and 2(d) (LDW(r2)). Average grain size is also indicated in the figure. Grain size distributions of W(r1) and KDW(r2) are similar. Average grain sizes of these materials are almost the same, and their distributions were relatively narrow. Grain size distributions of W(r2) and LDW(r2) are generally different from W(r1) and KDW(r2). The former materials indicate much larger grain size and much wider size distribution than the latter. At first, these results suggest that grain coarsening occurred after heating at a higher temperature in case of pure tungsten. Secondly, K-doping and La-doping suppressed grain coarsening to a certain extent.

3.2. Strengths and Ductility. Temperature dependences of the strengths are shown in Figure 3 (yield strength) and Figure 4 (maximum strength).

Yield strength of pure tungsten significantly depends on the heating condition. Yield strength of W(r2) which was heated at 2073 K is generally much lower than that of W(r1) which was heated at 1773 K. Yield strength of KDW(r2) is approximately the same as that of W(r1). Yield strength of LDW(r2) is slightly lower than that of W(r1) and/or KDW(r2), but higher than that of W(r2).

Maximum strength of pure tungsten also significantly depends on the heating condition. Maximum strength of W(r2) is generally much lower than that of W(r1). Maximum strengths of KDW(r2) and LDW(r2) are ranging between W(r1) and W(r2), although strength of KDW(r2) is higher than that of LDW(r2).

Critical stress and critical temperature are summarized in Table 1. We obtained these parameters in a manner as already shown in Figure 1. First, critical stress approximately corresponds to the maximum strength. Critical stress of W(r1) is much higher than that of W(r2). Critical stresses of KDW(r2) and LDW(r2) are ranging between W(r1) and W(r2), although stress of KDW(r2) is higher than that of LDW(r2). Critical temperature, on the other hand, does not necessarily follow the critical stress or the maximum strength. Difference in the critical temperature

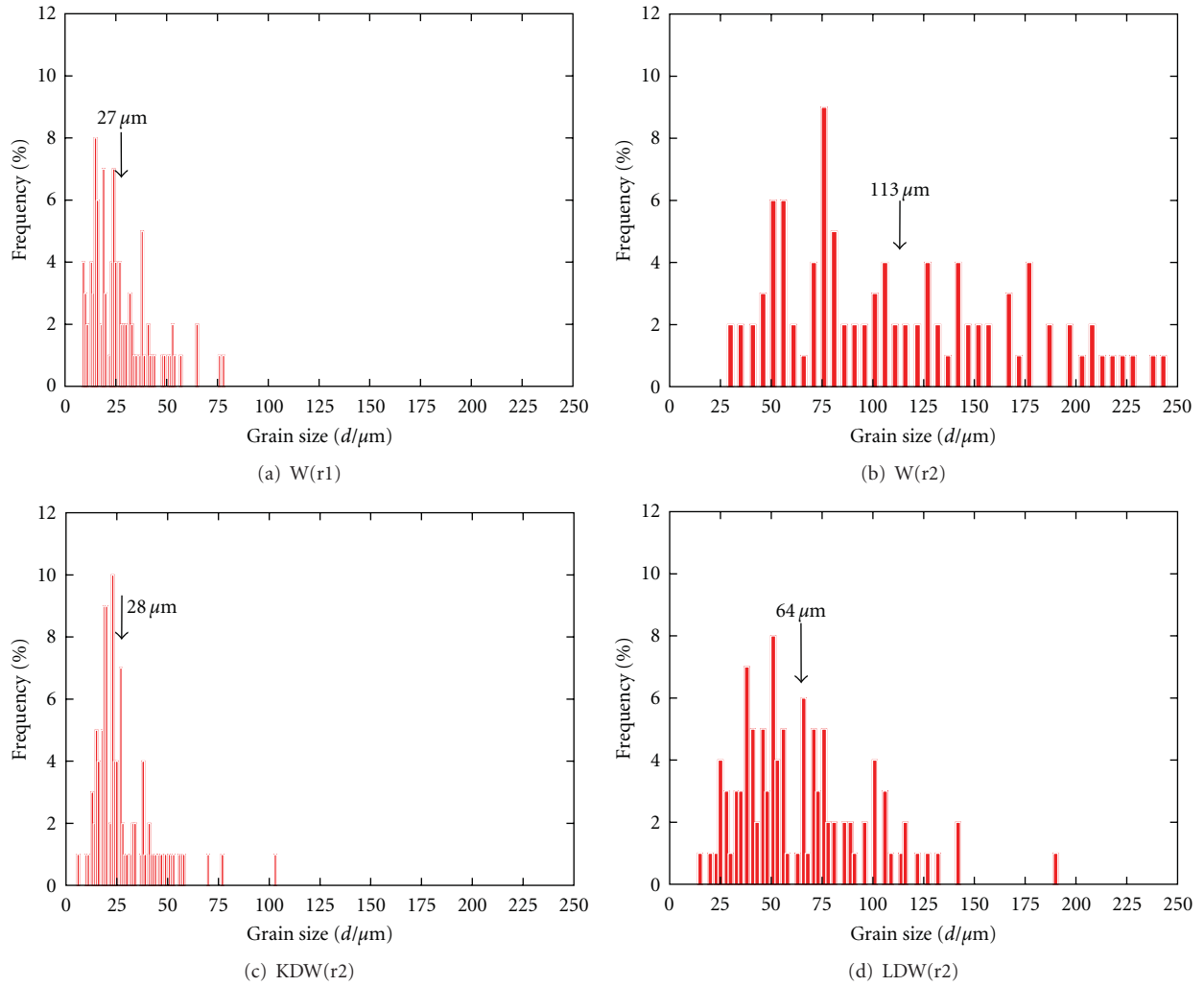


FIGURE 2: Grain size distributions for various materials.

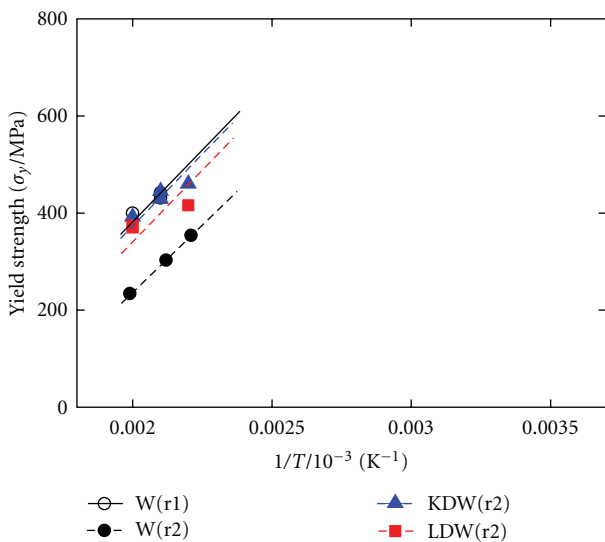


FIGURE 3: Plots of yield strength against test temperature for various materials.

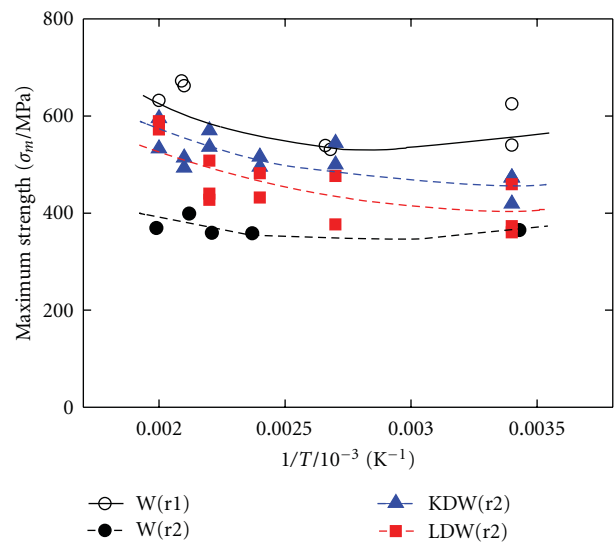


FIGURE 4: Plots of maximum strength against test temperature for various materials.

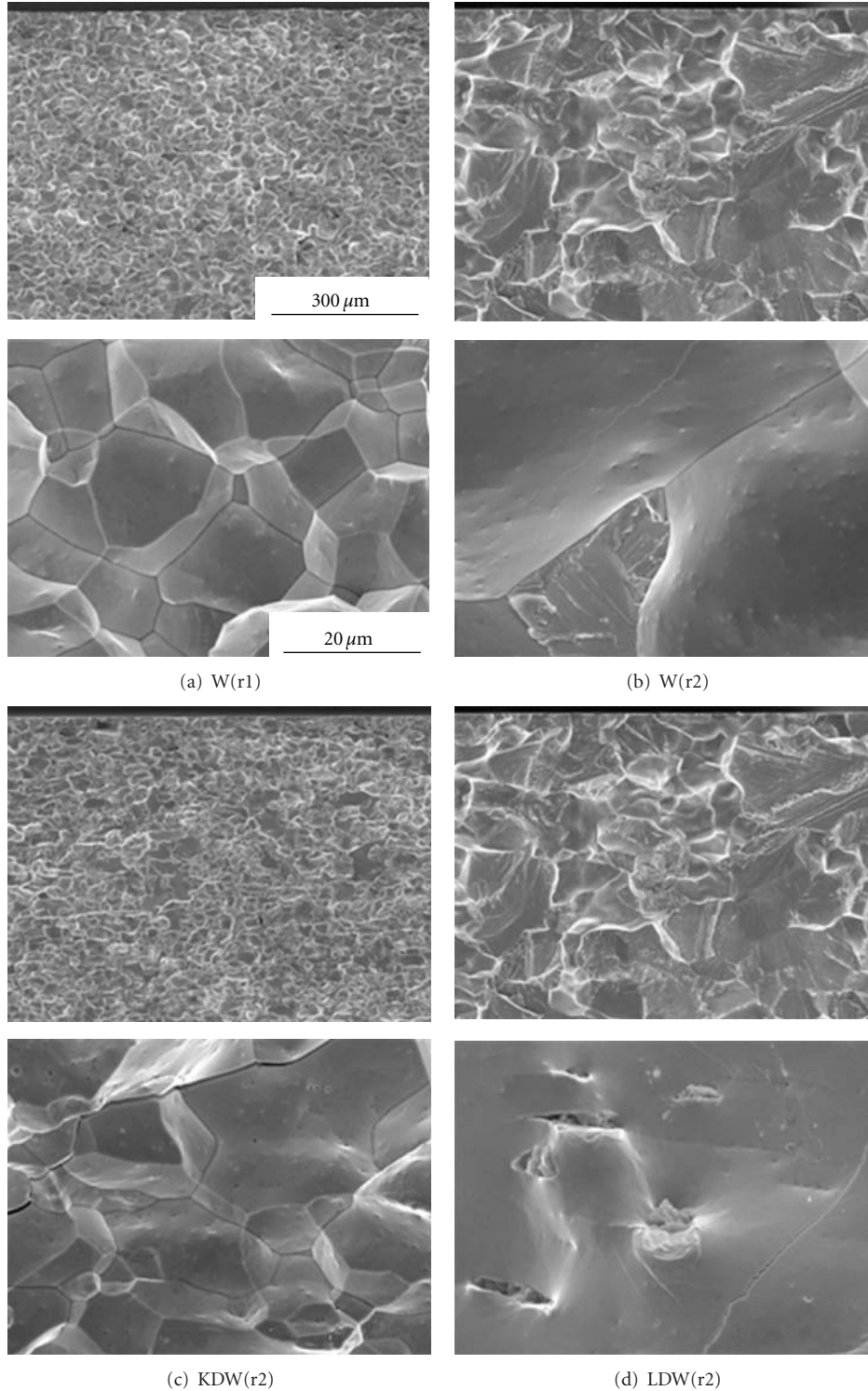


FIGURE 5: Typical fracture surfaces of various materials.

among materials is considerably little in contrast to that in the critical stress. This result is well interpreted, since the critical temperature is determined not only by the maximum strength (critical stress) but by the yield strength. In contrast, the critical stress is determined almost only by the maximum strength [2, 3].

3.3. Fracture Mode. Typical fracture modes of various tungsten are shown in Figures 5(a)(W(r1)), 5(b)(W(r2)), 5(c)(KDW(r2)), and 5(d)(LDW(r2)). Fracture modes of W(r1) and KDW(r2) are principally intergranular fracture. On the other hand, fracture modes of W(r2) and LDW(r2) are mixture of intergranular and transgranular fracture.

TABLE 1: Summaries of critical stress, critical temperature, and PIF-value for various materials.

Materials	Critical stress	Critical temperature	PIF-value (%)
	σ_c /MPa	T_c /K	
W(r1)	585	430	85
W(r2)	370	450	60
KDW(r2)	530	440	93
LDW(r2)	475	450	57

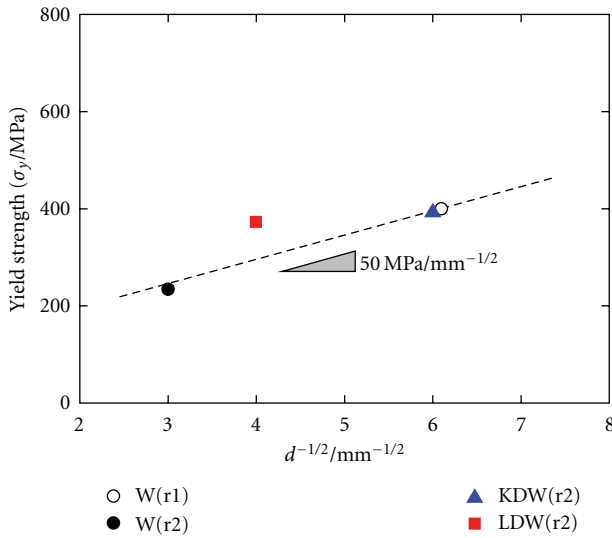


FIGURE 6: Grain size dependence of yield strength for various materials.

By a high-magnification SEM observation, intergranular fracture surfaces of W(r1) and W(r2) are relatively clean, except for a number of very small pores. General aspect of the intergranular fracture surfaces of KDW(r2) is similar to W(r1) and W(r2). On the other hand, some coarse inclusions are recognized on the intergranular fracture surfaces of LDW(r2). Considering the heating temperature of 2073 K, it is supposed that these inclusions are La_2O_3 particles.

Using fracture surface photographs, we determined PIF-value. Average values are summarized also in Table 1. PIF-values of W(r1) and KDW(r2) are as high as about 90% similar to pure molybdenum after recrystallization [5]. On the other hand, PIF-values of W(r2) and LDW(r2) are medium (about 60%).

4. Discussion

4.1. Grain Size Dependence of Yield Strength and Critical Stress. It is well known that strength of a material is significantly affected by the microstructure such as grain size. For example, Hall-Petch relationship stands between the yield strength and the grain size [6]. Thereby we discussed grain size dependence of the yield strength and critical stress in this session.

In Figure 6, yield strength obtained at about 500 K is plotted against the reciprocal of square root of grain size (d). In this study, average grain size was used as the grain

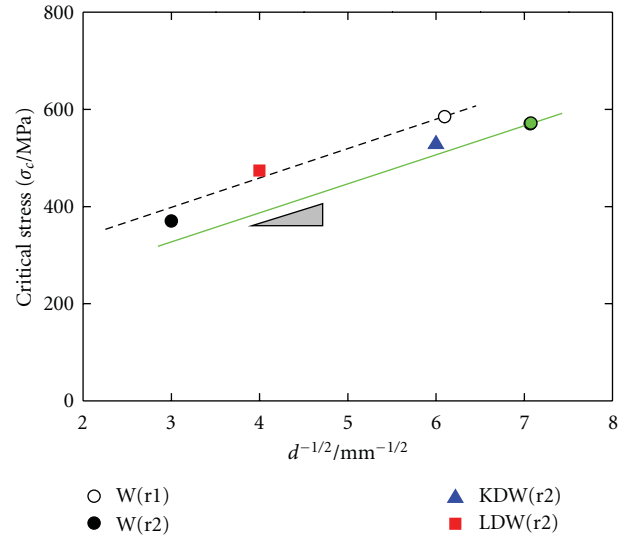


FIGURE 7: Grain size dependence of critical stress for various materials.

size. Dotted line in the figure indicates a linear relationship between the yield strength at 500 K and the reciprocal of grain size that was reported by Yih and Wang [7]. Data of various tungsten are well consistent with the linear relationship, although data of LDW(r2) is slightly higher. The latter result might be attributed to the dispersion of inclusions as shown in Figure 5(d).

In Figure 7, critical stress is plotted against the reciprocal of square root of grain size. In this study, the critical stress corresponds to the fracture strength of a material at a relatively low temperature. There is no data concerning the contribution of grain size to the critical stress or to the fracture strength in tungsten. Therefore, we applied the results obtained for molybdenum with grain size of 20–25 μm (green solid line) [8]. It is obvious that data for tungsten qualitatively agree with the relationship for molybdenum.

4.2. Relationship between Critical Stress and Fracture Mode.

In Figure 8, PIF-value is plotted against critical stress. Data obtained for molybdenum with grain size of 20–25 μm [5] is also plotted in the figure for reference. In addition, the green line having a slope of 0.2 represents linear relationship between the critical stress and the fracture mode for molybdenum [5, 8].

It is interesting that data of W(r1) and KDW(r2) approximately agree with the green line obtained for molybdenum. It is noted that all these materials have grain sizes almost as large as 20–25 μm . Present result suggests, at first, that relationship between the PIF-value and the critical stress is applicable not only to molybdenum but also to tungsten. Secondly, intergranular fracture strength of KDW(r2) is slightly lower than that of W(r1) with their transgranular fracture strengths being equivalent with each other.

Data of W(r2) and LDW(r2) deviate left hand from the linear relationship. This result might be attributed to the contribution of grain size to the intergranular and transgranular fracture strength (the constant, k in (3)), although

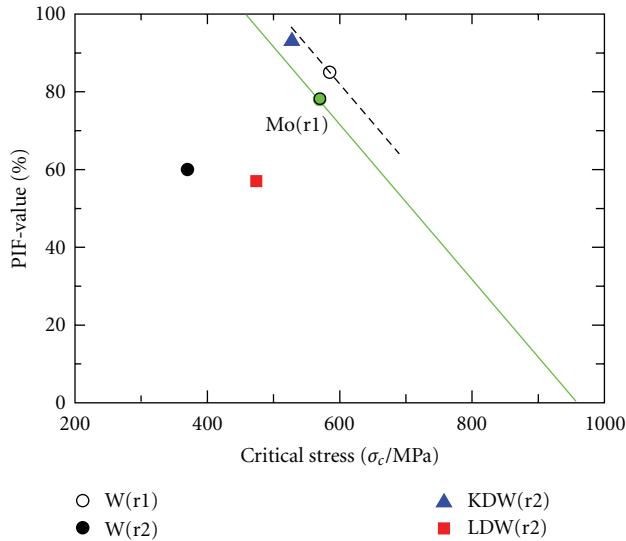


FIGURE 8: Plots of PIF-value against critical stress for various materials.

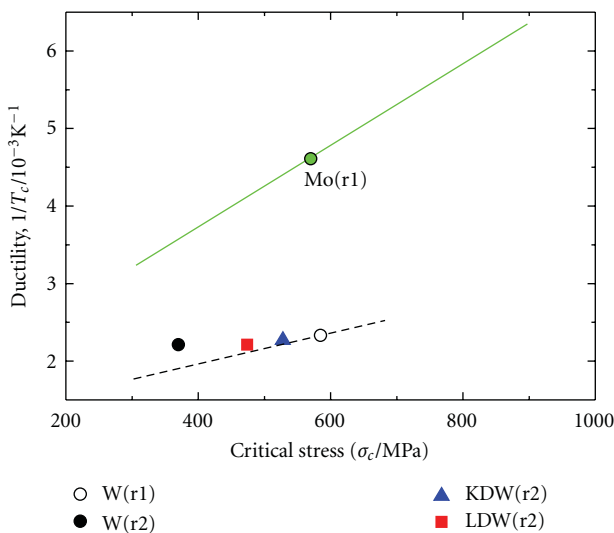


FIGURE 9: Plots of ductility ($1/T_c$) against critical stress for various materials.

contribution of grain size on the transgranular fracture strength for tungsten has not been reported yet. Grain coarsening concurrently induces lowering of transgranular fracture strength as well as lowering of intergranular fracture strength. As a result, PIF-value is almost unchanged.

4.3. Plots of Critical Stress and Reciprocal of Critical Temperature. As already mentioned, the critical stress corresponds to the apparent intergranular fracture strength. On the other hand, the critical temperature is an expression of ductile-to-brittle transition temperature (DBTT), and the reciprocal of critical temperature is a measure of ductility [2].

In Figure 9, reciprocal of critical temperature (ductility) is plotted against critical stress. Data obtained for molybdenum [5] is also plotted in the figure for comparison. At first, it is obvious that ductility of tungsten

is generally much lower than that of molybdenum. This result is principally interpreted by the difference of yield strength between molybdenum and tungsten. It is known that yield strength of tungsten is much higher than that of molybdenum at a given temperature with the grain size being equivalent. The straight line in the figure indicates the temperature dependence of the yield strength. Secondly, intergranular fracture strength of tungsten is almost equivalent with that of molybdenum if the grain size is the same.

5. Summaries of Results

- (1) Yield strength of tungsten principally depends on the microstructure such as grain size. Yield strength of tungsten at a given temperature is much higher than that of molybdenum.
- (2) Critical stress of tungsten depends not only on the grain size but also on the intergranular fracture strength. Critical stress of tungsten is almost equivalent with that of molybdenum if the grain size is the same.
- (3) Low-temperature ductility of tungsten is determined both by the yield strength and the maximum strength (critical stress). As a result, ductility of tungsten is generally much lower than that of molybdenum.

Acknowledgment

The authors greatly appreciate Dr. Tomohiro Takida and A.L.M.T. Corp for supplying pure tungsten and doped tungsten materials.

References

- [1] 8: Tungsten, in *Behavior and Properties of Refractory Metals*, T. E. Tietz and J. W. Wilson, Eds., pp. 274–330, University of Tokyo Press, Tokyo, Japan, 1965.
- [2] Y. Hiraoka, S. Yoshimura, and K. Takebe, “Effects of complex additions of Re or Ti with C on the strength and ductility of recrystallized molybdenum,” *International Journal of Refractory Metals and Hard Materials*, vol. 12, no. 5, pp. 261–268, 1993.
- [3] S. Yoshimura, Y. Hiraoka, and K. Takebe, “Effect of Ti in solution on ductile-brittle transition characteristics of powder-metallurgy molybdenum alloys,” *Journal of the Japan Institute of Metals*, vol. 58, no. 7, pp. 734–739, 1994 (Japanese).
- [4] T. Hoshika, S. Yoshimura, and Y. Hiraoka, “Evaluation of low-temperature fracture characteristics of molybdenum by means of tensile tests and bend tests,” in *Proceedings of the 14th intergranular Plansee Sem*, pp. 1018–1025, Tirol, Austria, 1997.
- [5] T. Kadokura, Y. Hiraoka, Y. Yamamoto, and K. Okamoto, “Change of mechanical property and fracture mode of molybdenum by carbon addition,” *Materials Transactions*, vol. 51, no. 7, pp. 1296–1301, 2010.
- [6] N. J. Petch, “The cleavage strength of polycrystals,” *The Journal of the Iron and Steel Institute*, vol. 173, pp. 25–27, 1953.

- [7] S. W. H. Yih and C. T. Wang, *Tungsten- Sources, Metallurgy, Properties, and Applications*, Plenum, New York, NY, USA, 1977.
- [8] Y. Hiraoka, "Significant effect of carbon content in the low-temperature fracture behavior of molybdenum," *Materials Transactions*, vol. 31, no. 10, pp. 861–864, 1990.

Research Article

Young's Modulus and Coefficient of Linear Thermal Expansion of ZnO Conductive and Transparent Ultra-Thin Films

Naoki Yamamoto, Hisao Makino, and Tetsuya Yamamoto

Research Institute, Kochi University of Technology, Tosayamada-cho, Kochi 782-8502, Japan

Correspondence should be addressed to Naoki Yamamoto, yamamoto.naoki@kochi-tech.ac.jp

Received 29 March 2011; Accepted 17 May 2011

Academic Editor: Kin Ho Lo

Copyright © 2011 Naoki Yamamoto et al. This is an open access article distributed under the Creative Commons Attribution License, which permits unrestricted use, distribution, and reproduction in any medium, provided the original work is properly cited.

A new technique for measuring Young's modulus of an ultra-thin film, with a thickness in the range of about 10 nm, was developed by combining an optical lever technique for measuring the residual stress and X-ray diffraction for measuring the strain in the film. The new technique was applied to analyze the mechanical properties of Ga-doped ZnO (GZO) films, that have become the focus of significant attention as a substitute material for indium-tin-oxide transparent electrodes. Young's modulus of the as-deposited GZO films decreased with thickness; the values for 30 nm and 500 nm thick films were 205 GPa and 117 GPa, respectively. The coefficient of linear thermal expansion of the GZO films was measured using the new technique in combination with *in-situ* residual stress measurement during heat-cycle testing. GZO films with 30–100 nm thickness had a coefficient of linear thermal expansion in the range of $4.3 \times 10^{-6} - 5.6 \times 10^{-6} \text{ } ^\circ\text{C}^{-1}$.

1. Introduction

Optically transparent and conductive ZnO films, such as Ga-doped Zinc oxide (GZO) or Al-doped ZnO films, are attracting attention as alternative electrode materials to indium tin oxide (ITO), with good optical transparency and electrical conductive properties for liquid crystal displays (LCDs), flexible displays, touch-screens, and solar cells. Motivations for the development of ZnO transparent electrodes include (a) the scarcity of indium natural resources and (b) the toxicity of indium. Indium is a rare element and ranks only 61st in abundance in the Earth's crust [1]. Also, in terms of toxicity, recently, indium was suspected to be a cause of pulmonary diseases [2].

ZnO electrodes need to endure against mechanical forces caused by the thermal processing steps during the manufacture of electronic devices such as flat panel displays, flexible displays, touch-screens, and LEDs, and by the expansion or shrinkage of parts caused by thermally severe circumstances (during summer and winter, e.g.) in the case of solar cells. These external forces could enhance the frequency of peeling or cracking in the elements composing the systems, such as transparent electrodes, during the fabrication or operation

of the devices. It is desired that the films used to form such electrodes have mechanically soft properties, because soft materials can absorb external forces and avoid peeling and cracking of the films. To obtain such a film, various mechanical characteristics of the thin film, such as elasticity, plasticity, viscosity, brittleness, yield strength, and adhesiveness, should be evaluated and be analyzed.

In these characteristics, Young's modulus is one of the most important mechanical properties of a film. It is an intrinsic property of the film (material) that relates to the atomic bonding and the crystalline structure.

In this work, a new technique was developed for measuring the mechanical characteristics of an ultra-thin film of a transparent electrode in LCD. Young's moduli and the coefficients of linear thermal expansion of GZO thin films were analyzed using the new technique.

2. Experimental

GZO films were prepared using two deposition methods: (1) conventional magnetron sputtering with dc power (dc MS) or with combined dc power/radiofrequency (rf) sputtering (rf + dc MS), and (2) reactive plasma deposition (RPD) [3].

The concentration of gallium in the deposition source was set to be 3.0–6.0 wt% Ga₂O₃ in order to minimize the GZO film resistivity. The conditions used for preparation of the GZO films are listed in Table 1.

The residual stress in the films was measured by the conventional optical lever method (model: F2300, Flexus Co.), which involved scanning a 633 nm wavelength laser beam of an HeNe laser (CW mode, laser power: 4 mW). A sample was put on the 3 small surface-projections arranged at the positions of the equilateral triangle on the heater plate. The residual stress in the film was measured during heating from 25 to 500°C and then cooling to 25°C. The substrate was deformed by the residual stress in the film. The radius of curvature of the substrate was measured by detecting the reflected laser beam. The residual stress in the film was then obtained by measuring the change in the curvature radius of the substrate before and after forming the film on it, and by using the coefficient of linear thermal expansion and Young's modulus of the substrate.

The crystal structures of the GZO films were analyzed using an X-ray diffractometer (XRD, model: ATX-G Rigaku Co.), a transmission electron microscope (TEM model: H-9000UHR Hitachi High-technologies Co.) and a scanning electron microscope (SEM, model: S-4300 Hitachi High-technologies Co.).

3. Results and Discussion

3.1. Residual Stress in GZO Thin Films

3.1.1. Residual Stress in GZO Films as a Function of Thickness. The crystalline structure of the GZO films was observed using a TEM. Figure 1 shows a cross-sectional TEM image of a 100 nm thick GZO film formed at 180°C by the RPD system. The GZO film has a columnar polycrystalline structure, as shown in the low magnification TEM micrograph in Figure 1(a). The alternating black and white striped layers in the middle magnification micrograph in Figure 1(b) correspond to Zn and O atomic layers in a Wurtzite crystalline structure forming the GZO material. The irregular parts in the image with stacked Zn and O atomic layers can be recognized in the vicinity of the surface of the substrate (region (1) in the lowest magnification micrograph (a)) as shown in Figure 1(b). This irregularity disappeared from a distance of approximately 50 nm from the surface of the substrate. The GZO film had an excellent crystalline structure, similar to a single crystal, as shown in the cross-sectional lattice image in region (2) in Figure 1(a) with distance from the surface of the substrate as shown in Figure 1(c). The boundary position in the cross-sectional lattice image cannot be identified.

Generally, stress increases remarkably at a dispersive location such as a surface or a discontinuity in a material. We forecasted that the residual stress in a GZO film with ca. 50 nm thickness would show an abnormality or irregularity on the dependence of the residual stress as a function of the film thickness. Figure 2 shows the typical residual stress dependence of the GZO film on the thickness. The residual stress of the film was measured at ca. 25°C in air. The films were formed on a (100) Si single crystal substrate (wafer) and

a thermally oxidized silicon dioxide film at 180°C by the RPD system.

All the films formed in this work had compressive stress. It is known that the residual stress in a film depends on the degree of energetic particle bombardment, that is, energy striking the condensing film, during deposition in sputtering or ion-plating with plasma discharge [4–9]. RPD is a kind of ion-plating method. Energy particle bombardment, “atomic peening effect”, introduces compressive stress in a film. The energy is a function of various process parameters such as working pressure, discharge voltage, gas mass, and substrate temperature.

The irregularities in the dependence of the residual compressive stress of the GZO films on the thickness appeared at approximately 60 nm thickness of the films formed on the Si wafer and the SiO₂ layer. This thickness corresponds to a distance of ca. 50 nm from the surface of the substrate, indicating that a boundary between region (1) and region (2) shown in Figure 1(a) exists. This correspondence proved the close connection between the residual stress and the distribution of crystalline irregularities in the film. This indicates that residual stress measurement, one of the available macroscopic evaluation methods, can be used as a monitor of the crystal structure in the nanoscale regime in the film. Figure 3 compares the dependence of the residual stresses on thickness for the GZO films formed by dc MS, rf + dc MS, and RPD. It was found that the region with crystalline irregularities in the vicinity of the interface for the film formed by rf + dc MS was distributed up to a distance of approximately 100 nm from the surface of the substrate. This distance was about twice longer than that for the film formed by RPD.

3.1.2. Hysteresis Behavior of Stress-Temperature Characteristics of GZO Films. The properties of the residual (compressive) stresses in GZO films formed by RPD and magnetron sputtering methods with various thicknesses, shown in Figures 4 and 5, were analyzed using heat-cycle testing. Such testing for GZO films was also discussed in our previous papers [10, 11]. Testing between room temperature and 500°C was carried out twice for each sample. The heating and cooling rates were controlled to about 2.8°C/min. It is considered that these rates realized a thermally quasi-static (thermal equilibrium) situation for the samples. *In-situ* measurements of residual stresses in the films during the heat-cycle testing were carried out. Measurement of the residual stress took less than a few milliseconds at each point in the heat-cycle testing. Each film showed the following common behavior: (a) the compressive residual stress in the film was reduced steeply beginning from 200 to 400°C (the temperature differed among the films formed by dc MS, rf + dc MS, and RPD) when the temperature was increased in the first heating step (step (1)), (b) the residual stress decreased monotonically when the temperature was lowered from 500°C (step (2)), and (c) the dependence of the residual stress on the temperature in each film during the second heat-cycle (steps (3) and (4)) almost coincided with that in step (2). The linear relationship between the residual stress and temperature in steps (2)–(4) indicates that the

TABLE 1: Specifications for the formation of GZO films by dc MS, rf + dc MS, and RPD.

	Magnetron sputtering		RPD
	dc MS	rf + dc MS	
Ga ₂ O ₃ content in ZnO source (wt%)		Ga ₂ O ₃ : 3.0–6.0	Ga ₂ O ₃ : 3.0–5.0
Power (kW)	0.1–2.0	rf: 0.1–1.5 dc: 0.1–1.5 rf/dc = 0.5–2.0	Discharge current: 140–150 (A)
Operation pressure (Pa)	0.1–0.8	0.1–0.8	0.4–0.6
Deposition rate (nm/min)	4–20	4–20	150–170
Operation temperature (°C)	150–350	150–350	150–250

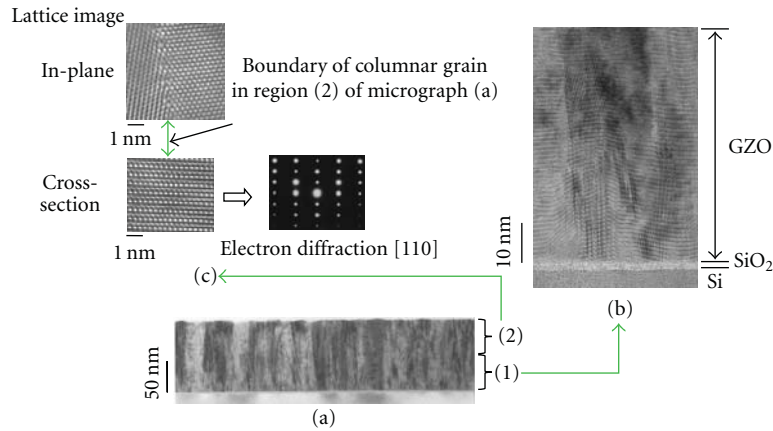


FIGURE 1: (a) Cross-sectional TEM micrograph of a GZO film. (b) Close-up view of a region in the vicinity of the film-substrate interface (region (1) in (a)). The layered structure in a GZO film with a Wurtzite structure, enhanced using Photoshop Elements 3.0 software (Adobe Systems Inc.). (c) Lattice image and electron diffraction pattern observed by TEM in the vicinity of the surface of the film (region (2) in (a)).

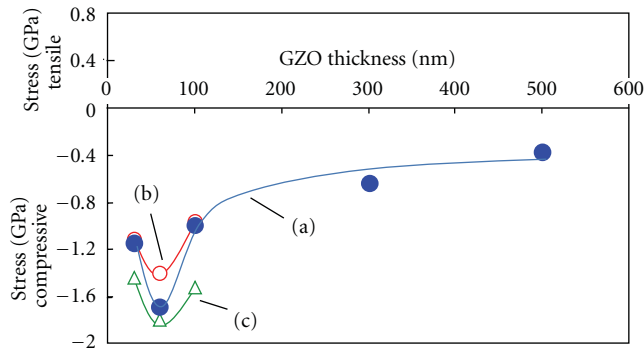


FIGURE 2: Dependence of residual stress in the GZO film formed by the RPD system on the film thickness before heat treatment. The symbols denote measured data. The dots (a) and open (b) circles correspond to the 1st and 2nd experimental series of GZO films respectively, and the triangles (c) show the residual stress in ZnO films without Ga (3rd series). The films in the 1st and 3rd series were formed on Si wafers with thermally oxidized silicon layer films.

major residual stress component in each film was thermal stress. This thermal stress is caused by the difference in the coefficient of linear thermal expansion between the GZO film and the Si substrate. The residual stress behavior in step (1) for the films prepared by RPD and dc MS was

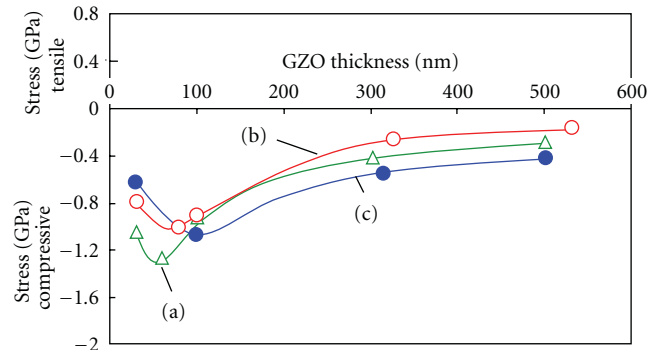


FIGURE 3: Comparison of the dependence of residual stress on film thickness in as-deposited GZO films prepared at 180°C by (a) RPD, (b) dc MS, and (c) rf + dc MS.

closer to that during steps (2)–(4) for comparatively thicker (i.e., 500 nm) GZO films. Thus, the main component of the residual stress in such thick films was thermal stress (intrinsic stress), even before the heat-cycle testing for the as-deposited film. The GZO films approached the ideal crystalline structure with increasing thickness. On the other hand, the residual stress behavior in step (1) in the GZO films prepared by rf + dc MS was obviously not close to that in steps (2)–(4) even in the 500 nm thick films. This

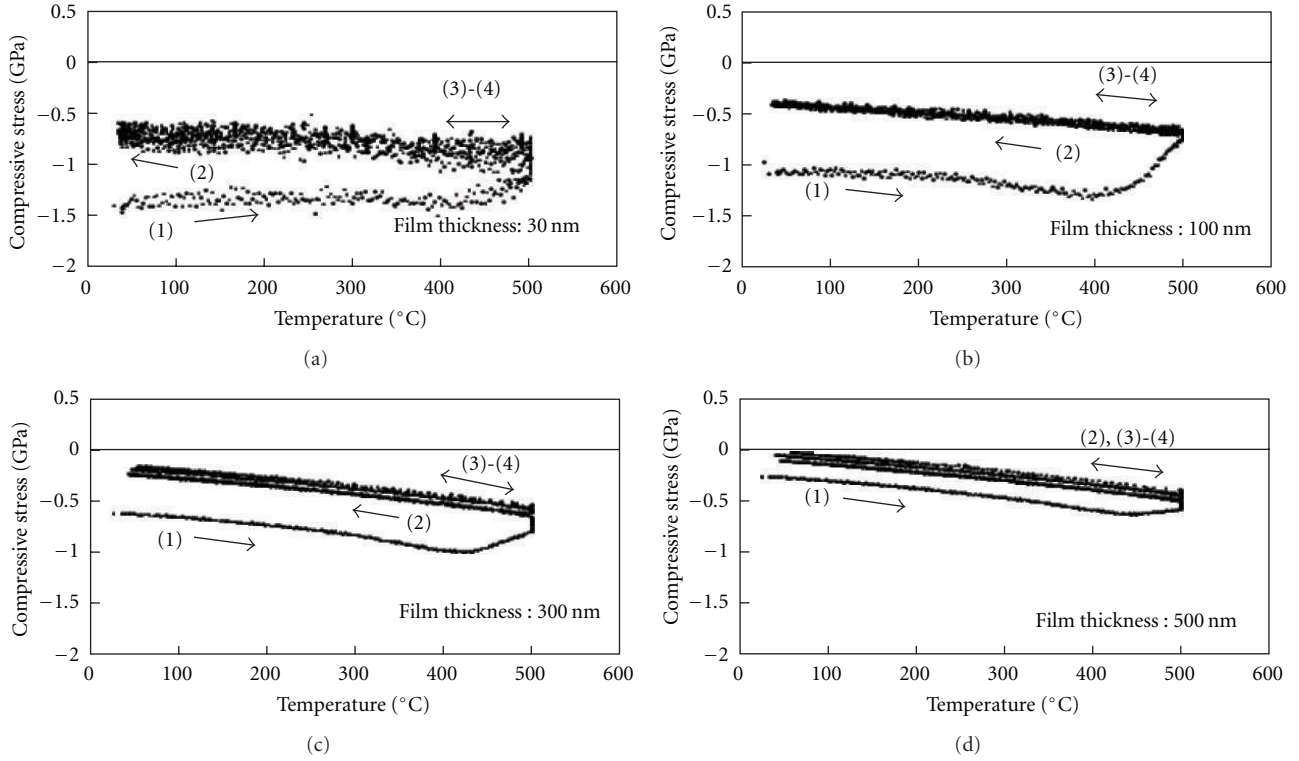


FIGURE 4: Residual stress behavior during heat-cycle testing (room temp: -500°C) in an atmosphere of flowing Ar gas for GZO films formed by the RPD system.

indicates that high strain or irregular crystalline structures exist until a far distance from the substrate surface in the film. This is consistent with the result for the dependence of the residual stress on the thickness in the rf + dc MS film prior to annealing, as mentioned previously in Figure 2. In the case of the film formed by the rf + dc MS, the irregularity, strain or dispersion of the c -axis direction perpendicular to the substrate surface was seen above 500 nm from the interface.

The behavior of the residual stress due to heat treatment can yield the coefficient of thermal expansion value of a film. For obtaining the coefficient, Young's modulus of the GZO thin-film needs to be determined by some measurement technique. Furthermore, the thermal stress in the film has to be derived from the dependence of the residual stress on the temperature. The residual stresses in the GZO films formed by magnetron sputtering as a function of temperature changed in a complicated manner compared with the residual stress in the GZO film formed by RPD during heating in the first cycle (step (1)), as shown in Figures 4 and 5. Hence, we focus on the mechanical properties of the GZO thin film formed by the RPD system in this paper. We propose a new technique for the measuring Young's modulus of ultra-thin films and demonstrate its effectiveness for analyzing mechanical characteristics of a film in the present stage.

3.2. Young's Modulus of GZO Film

3.2.1. Proposed New Technique for Measuring Young's Moduli of Ultra-Thin Films.

Current methods of measuring Young's

modulus that are used widely are destructive techniques that damage the samples. In any case, Young's modulus of ultra-thin films cannot be measured by these methods. We propose a new nondestructive measurement method for Young's modulus that does not damage the sample and is applicable for ultra-thin films with thickness in the range of approximately 10 nm. Furthermore, we discuss the mechanical characteristics of GZO films obtained using the new method.

Young's modulus (E) has been conventionally determined by techniques measuring the distortion caused in a sample by an external applied force (F) using the following formula:

$$E = \left(\frac{F}{A}\right) / \left(\frac{\Delta l}{l}\right), \quad (1)$$

where A is the unit area on the cross-section of the sample perpendicular to the direction of the applied force (load), Δl is the expanded length, and l is the original length of the sample. Various traditional techniques using this relationship have been applied for measuring Young's modulus for a long time. The nanoindentation method [12], as shown in Figure 6, has become the major technique for measuring Young's modulus of thin films. However, the method is not applicable to films thinner than ca. $1\ \mu\text{m}$. The front edge of a Berkovich tip that is usually employed in depth-sensing indentation systems penetrates the film that easily reaches the vicinity of the under-layer such as a substrate. This causes the penetration depth of the tip-loading weight (force) relationship to deviate from the intrinsic curve that should be observed in the film material. Thus, Young's modulus derived

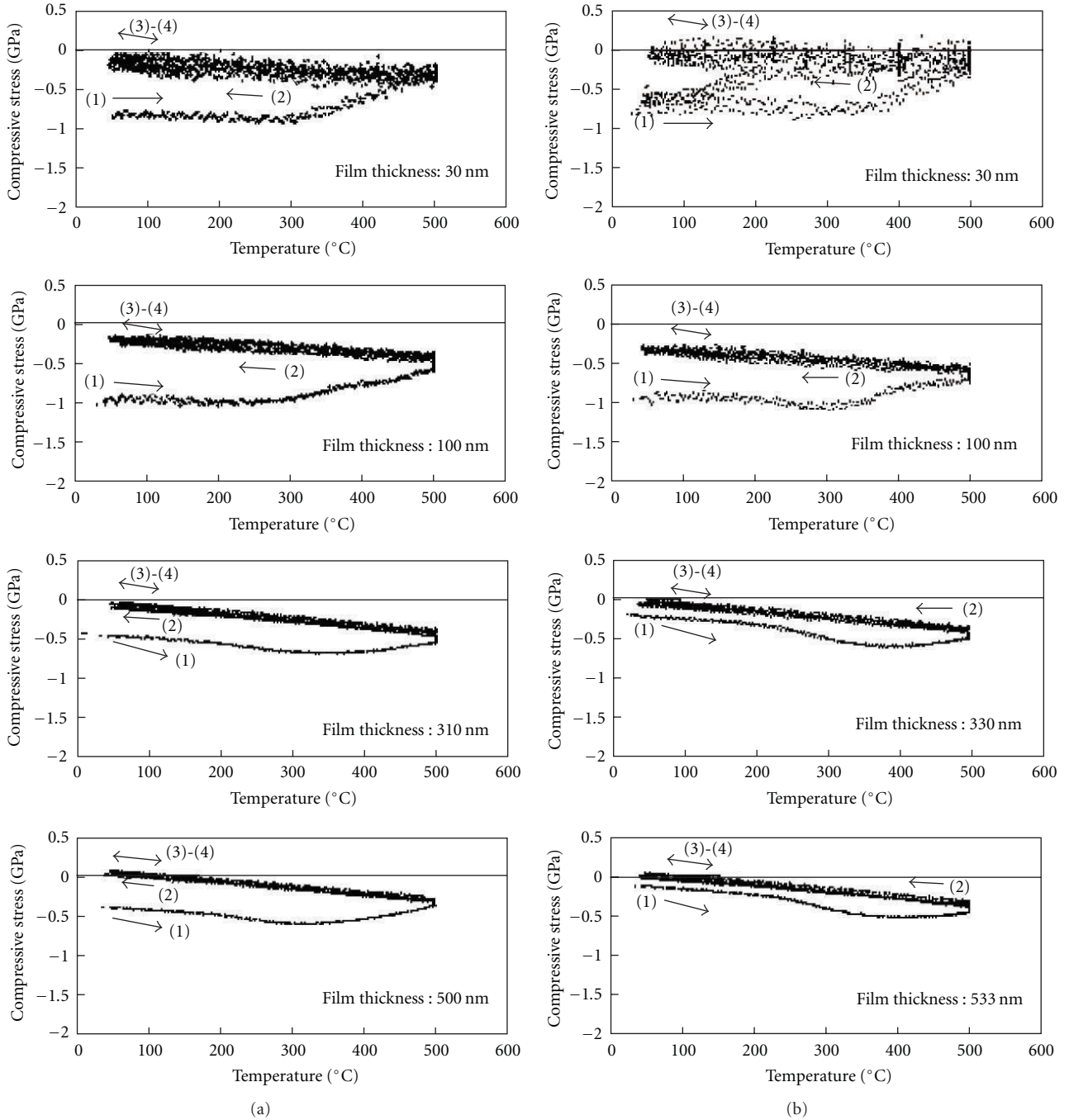


FIGURE 5: Residual stress behavior during heat-cycle testing (room-temperature: -500°C) in an atmosphere of flowing Ar gas for GZO films formed by the magnetron sputtering system. The columns (a) and (b) correspond to changes in the residual stress during heat-cycle testing, respectively.

using such a curve deviates from the intrinsic modulus value of the thin film material.

The new technique developed in this work for measuring Young's modulus is applicable for films thinner than $1\ \mu\text{m}$. The principle of Young's modulus measurement is shown in Figure 7. (F/A) and $(\Delta l/l)$ in formula (1) correspond to the stress (σ) and strain (ϵ), respectively. Thus, formula (1) can be rewritten as

$$E = \frac{\sigma}{\epsilon}. \quad (2)$$

This is the basic equation of Hooke's law indicating that Young's modulus of a material in a thin film form can be determined directly by measuring both stress and strain within the film.

Generally, the residual stress in a film is measured by the optical lever method, the $\sin^2\psi$ method [13] using X-ray diffraction, or the nanoindentation method described previously. The $\sin^2\psi$ method is not suitable for analyzing the residual stress in a thin film with thickness less than a few micrometers.

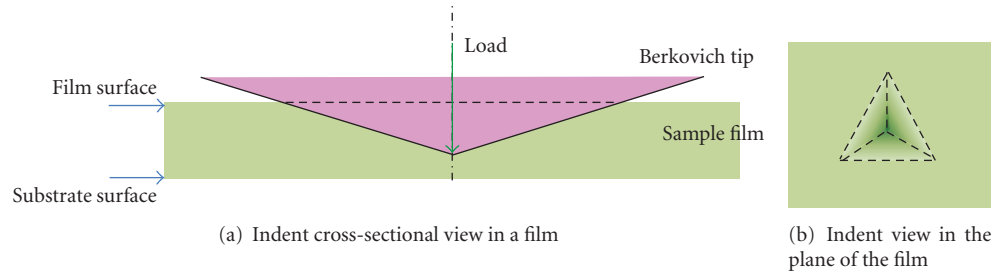


FIGURE 6: Diagram of an indent left by a Berkovich tip in a film.

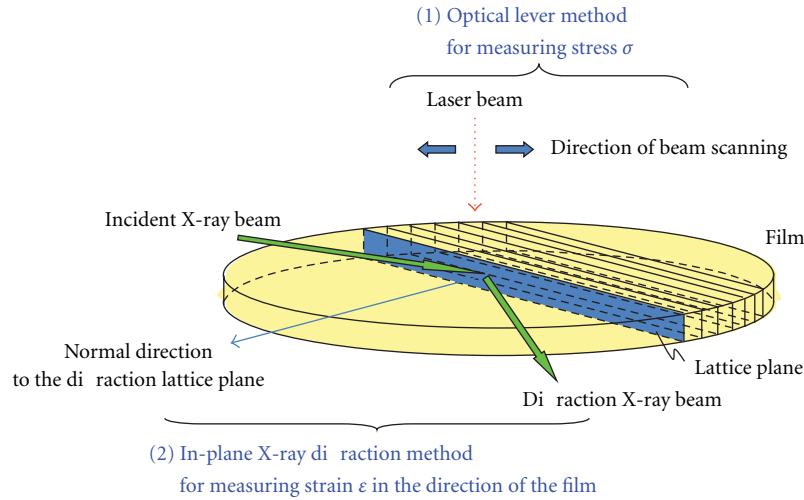


FIGURE 7: Diagram of a nondestructive measurement technique of Young's modulus and coefficient of linear thermal expansion of a polycrystalline film which uses the optical lever technique for measuring the residual stress in conjunction with the in-plane X-ray diffraction technique for measuring strain.

The stress measured by this technique using the optical lever method is the in-plane component of the residual stress in the film. The strain was measured using grazing-incidence wave-dispersive XRD (sometimes referred to as "in-plane X-ray diffraction" [14]). A Cu-K α X-ray (wavelength: 0.154184 nm) beam was irradiated with a low angle of incidence on the surface of the sample. This angle was set to 0.35 degrees with respect to the surface, which is close to the total reflection angle for a ZnO film. The strains and grain sizes along the in-plane direction in each film were obtained by the Williamson-Hall equation (plot) [15], shown hereinafter, using the angles and the full widths at half maxima (FWHMs) of the diffraction X-ray peaks with crystalline indexes of the material of the film:

$$\frac{\sigma \cos \theta}{\lambda} = 2\varepsilon \left(\frac{\sin \theta}{\lambda} \right) + \left(\frac{1}{\delta} \right), \quad (3)$$

where σ is the full width at half maximum (FWHM) of the diffraction X-ray peak, θ is the angle of X-ray diffraction peak, ε is the strain, and δ is the grain size.

Therefore, when $\sigma \cos \theta / \lambda$ (vertical axis: y -axis) as a function of $\sin \theta / \lambda$ (horizontal axis: x -axis) is plotted, the strain is obtained from the slope of the y - x curve and the grain size is determined from the y -intercept.

Our proposed technique for measuring Young's modulus combines the previous two techniques. It has the following special features: (1) It is nondestructive (the sample is not damaged), (2) it is applicable for ultra-thin films with thickness as small as ca. 10 nm, (3) it allows for the value of each layer in a multilayer composite sample to be obtained separately, and (4) it can determine Young's modulus in the direction of a crystalline index. (This is fundamentally possible in the optical lever method; however, it can typically only measure the residual stress in the direction of the plane of the film. It then becomes necessary to introduce a method of enabling vector analysis on the stress.)

3.2.2. Strain and Grain size in GZO Polycrystalline Ultra-Thin Films. The diffraction patterns from GZO films prepared by the RPD system obtained using out-of-plane and in-plane techniques for XRD measurements are shown in Figure 8. Only the (002) and (004) diffraction peaks of ZnO with a Wurtzite crystalline structure in the diffraction data were obtained by the out-of plane XRD technique, as shown in Figure 8(a). According to Figure 8(b), the peaks obtained by the in-plane XRD technique were diffracted from the (xx0) crystalline planes. These results indicate that the GZO polycrystalline films consist of grains with the c -axes of the

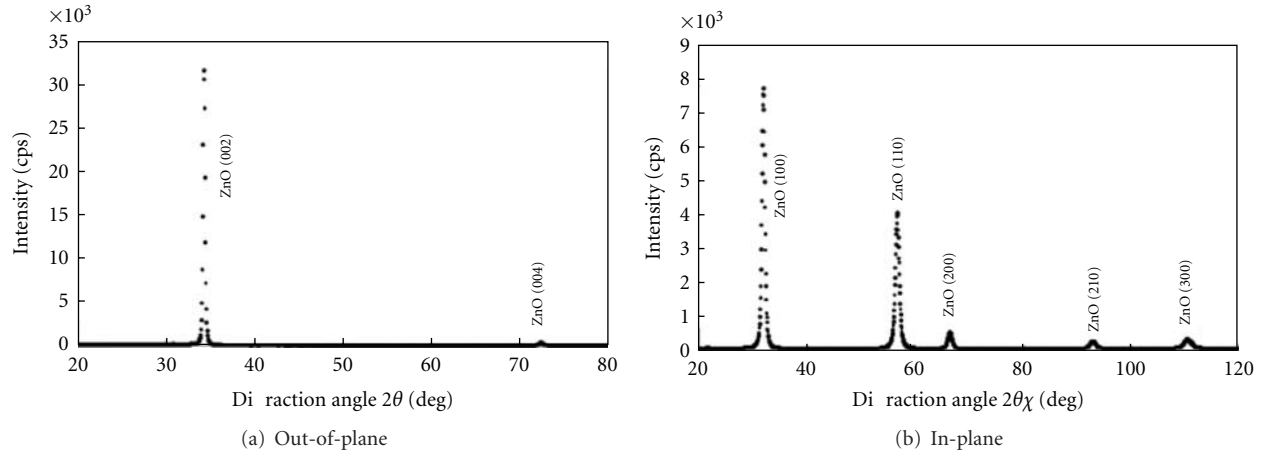


FIGURE 8: Typical XRD profile of a GZO film with 150 nm thickness prepared at 180°C using the RPD system. Profiles (a) and (b) were obtained using out-of-plane and in-plane techniques for XRD measurements, respectively.

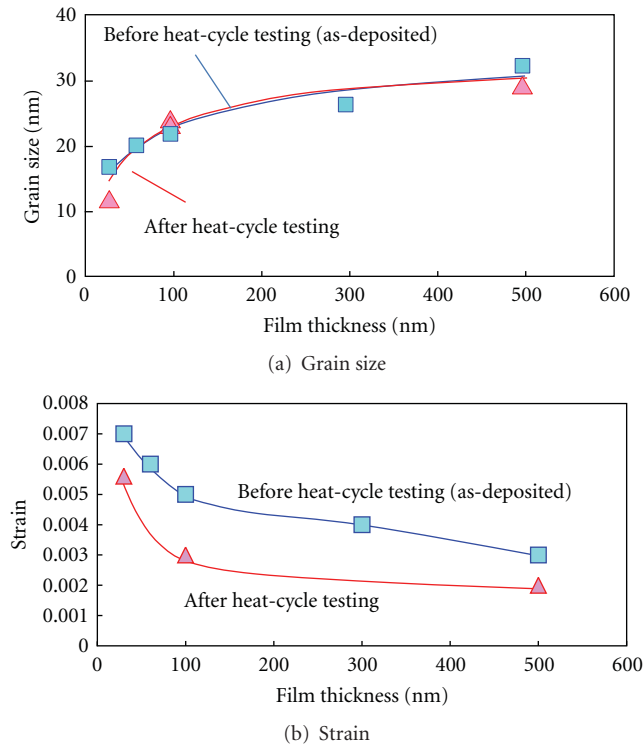


FIGURE 9: Average grain size and strain in the in-plane direction (a -axis of Wurtzite cell) as a function of film thickness.

Wurtzite crystalline cells oriented strictly along the normal direction to the surface of the film.

The strains and grain sizes in polycrystalline GZO films were determined using (3) and the (x00) diffraction peaks in the in-plane XRD patterns, respectively. The obtained strain is the component in the a -axis direction of the Wurtzite crystalline cell of ZnO, that is, in the in-plane direction of the GZO film. Figure 9 shows the dependence of strain and grain size in a GZO film on the film thickness before and after the heat-cycle testing in the range of room temperature to 500°C. The grain size increased monotonically with the

film thickness. On the other hand, the strain decreased with increasing film thickness. These dependencies on the film thickness had good correspondence to cross-sectional TEM micrographs shown previously in Figure 1. That is, region (1) close to the interface of the substrate had smaller grains and higher strains caused because the direction of stacking of alternative Zn and O atomic layers (the direction coincided with that of the c -axis of the Wurtzite crystalline cell) was not corresponding between each crystalline grain. To compare with it, the stacking directions were precisely oriented among grains in region (2) at a far distance from the surface of the substrate as shown in Figure 1. In particular, the dependence of strain on film thickness was consistent with the dependence of the regular stacking of atomic layers on the distance from the interface. The strain characteristics as a function of the GZO thickness in region (1) in Figure 1 had a slope steeper than that in region (2).

We next discuss changes in the grain size and strain in a GZO film caused by the heat-cycle testing between room temperature and 500°C. The heat treatment had little or no effect on grain growth in the in-plane direction (a -axis direction). On the other hand, the strain in the GZO film decreased remarkably by the heat-cycle testing. The reduction rate of strain in the film with ca. 100 nm thickness caused by the heat-cycle testing reached about 50%. On the other hand, strain in a very thin film with ca. 30 nm thickness was reduced only about 20% by the heat treatment. It is estimated that the heat-cycle testing condition was inadequate for releasing high strain caused by highly crystalline irregularities in region (1). It is considered that a large number of crystalline defects were included in the vicinity of the interface with the substrate, such as in region (1) in Figure 1(a).

3.2.3. Young's Modulus of GZO Thin Film. Young's modulus of a GZO thin film was derived by substituting stress and strain into (2) as mentioned in the previous section. Young's modulus of the as-deposited GZO film depended on the film thickness as shown in Figure 10(a). Young's modulus of

an ultra-thin film, such as with 30 nm thickness, was about 205 GPa. The film with 60 nm thickness had a maximum modulus of 300 GPa. This value decreased with increasing thickness of the film and reached a value of about 117 GPa in the comparatively thick GZO film with 500 nm thickness. Generally, Young's modulus shows a correlation with the hardness of a material. The hardness increases with the number of defects in a material. The defects pin atomic layer slip relative to other layers in a crystal due to an external force. Then, Young's modulus in an ultra-thin film or in the interfacial neighborhood with a large number of defects becomes larger than that of a thick film or at a far distance from the surface of a substrate. This dependence shown in Figure 10(a) is consistent with that of the distribution of crystalline irregularities or the dispersion of the stacking direction of atomic layers within each grain shown in Figures 1(a) and 1(b). The dependence of Young's modulus of a GZO thin film on the film thickness after heat-cycle testing between room temperature and 500°C is also shown in Figure 10(b). Young's modulus of the comparatively thicker film with 500 nm thickness was reduced remarkably by about one digit and half from the value before heat-cycle testing. The reason why Young's modulus of the thicker film with relatively fewer defects decreased drastically is not yet clear. In an area away from the interface with the substrate, as shown in Figure 1(c), the Zn and O atomic layers at the polycrystalline grain boundary were smoothly connected. The proportion of the volume of the region where a large number of defects existed in the vicinity of the surface of the substrate in the total volume of the film decreased with the increasing thickness of the film. Then, the value obtained for Young's modulus was affected by the ratio of region (2)/(region (1) + region (2)) as shown in Figure 1. In the case of the 500 nm-thick GZO film, Young's modulus measured by this new technique was almost equal to that of region (2) with small amount of defects, since the volume of the region became one order of magnitude larger than that of region (1) with a large number of defects. At this stage, we can only speculate on the reason for why Young's modulus of the 500 nm thick was reduced significantly by heat-cycle testing. Very small numbers of defects existed at grain boundaries in region (2), which was one of the main factors contributing to the modulus before heat treatment. The positions that the Zn and O atomic layers were connected continuously smoothly at the grain boundaries as shown in region (2) in Figures 1(a) and 1(c) and the positions that they were not connected smoothly in region (1) existed in a film. Then, the crystalline defects occurred at the later positions in the grain boundaries. This small number of defects in region (2) could disappear easily from the grain boundaries by heat treatment. As a result, Young's modulus of thick films, such as with 500 nm thickness, was reduced remarkably by heat treatment. The value was almost comparable with that of a material with low hardness, such as talc or calcium sulfate.

3.3. Coefficient of Linear Thermal Expansion of GZO Films. The thermal stress (σ_T) in a film is derived by the following equation using the temperature (T) dependence of residual stress in the film:

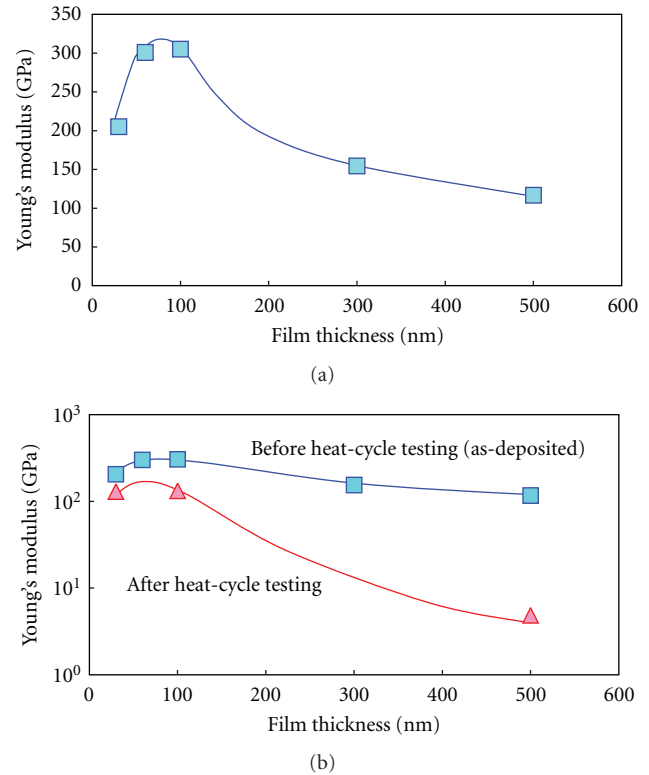


FIGURE 10: Young's modulus in the in-plane direction (a -axis of Wurtzite cell) of the GZO film formed by the RPD system as a function of film thickness. (a) Young's modulus before heat-cycle testing (as-deposited). (b) Reduction in Young's modulus value of the thin film caused by the heat-cycle testing. The same data in (a) is redrawn in (b).

$$\sigma_T = \frac{\Delta\sigma}{\Delta T}. \quad (4)$$

Using the thermal stress (σ_T) and Young's modulus of the film, the coefficient of linear thermal expansion (α_f) of the film can be derived by the following:

$$\alpha_f = \frac{\sigma_T(1 - \nu_f)}{E_f} + \alpha_s. \quad (5)$$

Here, ν_f , E_f , and α_s represent the Poisson's ratio of the film, Young's Modulus of the film, and the coefficient of linear thermal expansion of the substrate, respectively.

The thermal stress and the coefficient of linear thermal expansion of the GZO films formed on the thermally oxidized Si wafer of a single crystal with a (100) crystalline surface were obtained using the stress-temperature characteristics of the GZO film shown in Figure 4 and using (4) or (5). These material properties of the GZO films were derived from the stress-temperature characteristics in the range between room temperature and 250°C taking into account the following factors: (1) Young's moduli of the GZO films derived using the measured residual stresses and strains in the films mentioned in the previous section were values at room temperature, and (2) the highest processing

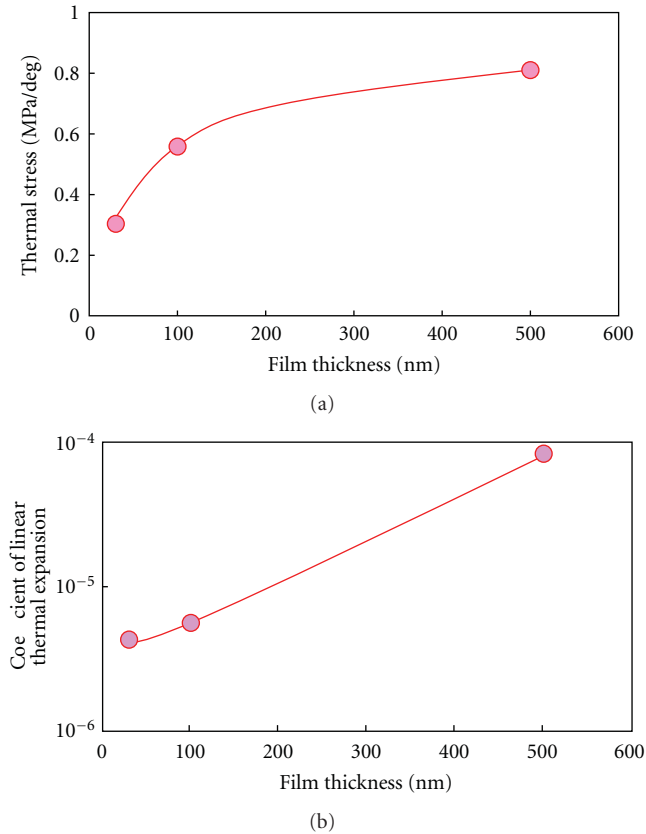


FIGURE 11: Thermal stress and coefficient of linear thermal expansion of GZO films formed by the RPD system as a function of film thickness. (a) Dependence of thermal stress on film thickness, and (b) dependence of the coefficient of linear thermal expansion on film thickness.

temperature for manufacturing LCDs is generally limited to about 250°C since parts such as RGB (Red-Green-Blue) color filters that form LCDs are made of organic materials. As shown in Figure 4, when the samples were heated up in the first cycle step (step (1)), the behavior of the residual stress as a function of the temperature was complicated. Then, the dependence of the residual stress on the temperature on the second heating stage (step (3)) was used for obtaining the thermal stress.

The value of $2.67 \times 10^{-6} \text{ }^{\circ}\text{C}^{-1}$ at around 100°C for the coefficient of linear thermal expansion of Si as function of temperature, reported by Okada and Tokumura [16], was used for α_s in (5). The thermal stress and the coefficient of linear thermal expansion of a GZO film were then determined as shown in Figure 11. The Poisson ratio of a GZO film was tentatively assigned as 0.3, which is the average of the Poisson ratios of ZnO picked as obtained from various reports [17–23], because our technique had not yet reached an applicable level to measure it in this stage. In the case of a Poisson ratio of 0.1 lower or higher than 0.3 (Poisson ratio: 0.2 or 0.4), the coefficient of linear thermal expansion increases or decreases only about 7%.

The coefficients of linear thermal expansion of the GZO films with 30–100 nm thickness coincided with our expectation. On the other hand, the coefficient of linear

thermal expansion of the 500 nm thick film deviated far from our expectation. It is not clear why an abnormal coefficient of linear thermal expansion of the film with 500 nm thickness was obtained. We believe that this likely originated in the excellent continuity of atomic layers at polycrystalline boundaries, similar to a single crystal as shown in Figure 1(c).

4. Summary

We developed a new technique for analyzing the mechanical properties of ultra-thin polycrystalline films. This method for measuring Young's modulus of an ultra-thin film used stress measurement by the optical lever technique together with X-ray diffraction with an X-ray beam incident from an approximately total reflection angle (in-plane XRD technique). This measurement technique is nondestructive and does not cause any damage to a film. Furthermore, the technique can be applied for measuring Young's modulus of ultra-thin films of various polycrystalline materials with 10–30 nm thickness.

In the dependence of the residual stress in the GZO thin films on film thickness, the maximum stress appeared in the film with 50–60 nm thickness. This thickness coincided exactly with the distance from the surface of the substrate, that changes from the region with irregular stacking directions of alternate Zn and O atomic layers among columnar grains to the region consisting of grains with strictly aligned stacking direction. Thus, the residual stress represents information from nanoscale regions in crystalline films.

Young's moduli of the GZO films showed a similar dependence on the film thickness. The maximum modulus reached a value of about 300 GPa. The modulus decreased with increasing thickness. The GZO film with 500 nm thickness had a Young's modulus of 117 GPa. This value of the modulus is reasonable compared to values of 61–125 GPa reported for ZnO films with 2–3 μm thickness measured using the nanoindentation technique [24]. The coefficient of linear thermal expansion of GZO films with 30–100 nm thickness was in the range of 4.3×10^{-6} – $5.6 \times 10^{-6} \text{ }^{\circ}\text{C}^{-1}$. On the other hand, the film with 500 nm thickness had a remarkable high coefficient of $8.3 \times 10^{-5} \text{ }^{\circ}\text{C}^{-1}$. We estimated that this high value was related to the excellent continuity of Zn and O atomic layers in the in-plane direction (the direction of the *a*-axis of the Wurtzite cell of ZnO) between grain boundaries similar to a single crystal. This excellent continuity also had a favorable effect on the low Young's modulus and low residual stress.

The results indicate that the new measurement technique for Young's modulus of ultra-thin films is very useful. The mechanical properties of the GZO films formed by conventional magnetron sputtering are not discussed in this paper. In a future paper, the characteristics of the films will be compared with those of the GZO films prepared by the RPD system. Furthermore, the technique will be applied for developing ZnO transparent conductive films that can resist external mechanical pressures during the manufacture of LCDs and testing long-term reliability of

displays under external conditions of heating at 50–60°C and a high humidity of 90–95%.

Acknowledgments

The authors would like to thank Professor Dr. Y. Yasuda of Center for Interdisciplinary Research, Tohoku University, Dr. T. Yamada of Graduate school of Engineering, Osaka University and Mr. M. Hakata of a former board member of CASIO Computer Co., Ltd., for their encouragement, contributions and suggestions during the author's research on the mechanical properties of ultra-thin films. The authors also thank Dr. K. Takeda, Mr. T. Mine, and Mr. N. Sakuma of the Central Research Laboratory of Hitachi Co. Ltd. for providing access to their analytical facilities, and Dr. K. Inaba of the X-ray Research Laboratory of Rigaku Corporation for valuable advice throughout the course of this work. This work was made possible by a grant for Collaboration of Regional Entities for the Advancement of Technological Excellence from the Japan Science and Technology Agency, and it was supported in part by a grant for the Development of Indium Substitute Materials for a Transparent Conducting Electrode in Rare Metal Substitute Materials Development Project from NEDO (New Energy and Industrial Technology Development Organization).

References

- [1] D. Kempthorne and M. D. Myers, *Mineral Commodity Summaries 2007*, United States Government Printing Office, Washington, DC, USA, 2007.
- [2] S. Homma, A. Miyamoto, S. Sakamoto, K. Kishi, N. Motoi, and K. Yoshimura, "Pulmonary fibrosis in an individual occupationally exposed to inhaled indium-tin oxide," *The European Respiratory Journal*, vol. 25, no. 1, pp. 200–204, 2005.
- [3] T. Yamamoto, T. Yamada, A. Miyake, H. Makino, and N. Yamamoto, "Ga-doped zinc oxide: an attractive potential substitute for ITO, large-area coating, and control of electrical and optical properties on glass and polymer substrates," *Journal of the Society for Information Display*, vol. 16, no. 7, pp. 713–719, 2008.
- [4] R. S. Wagner, A. K. Sinha, T. T. Sheng, H. J. Levinstein, and F. B. Alexander, "Tungsten metallization for LSI applications," *Journal of Vacuum Science and Technology*, vol. 11, pp. 582–590, 1974.
- [5] J. A. Thornton and D. W. Hoffman, "Internal stresses in titanium, nickel, molybdenum, and tantalum films deposited by cylindrical magnetron sputtering," *Journal of Vacuum Science and Technology*, vol. 14, pp. 164–168, 1977.
- [6] D. W. Hoffman and J. A. Thornton, "The compressive stress transition in Al, V, Zr, Nb and W metal films sputtered at low working pressures," *Thin Solid Films*, vol. 45, no. 2, pp. 387–396, 1977.
- [7] H. Windischmann, "Intrinsic stress in sputter-deposited thin films," *Critical Reviews in Solid State and Materials Sciences*, vol. 17, no. 6, pp. 547–596, 1992.
- [8] N. Yamamoto, H. Kume, S. Iwata et al., "Fabrication of highly reliable tungsten gate MOS VLSIs," *Journal of the Electrochemical Society*, vol. 133, no. 2, pp. 401–407, 1986.
- [9] R. E. Cuthrell, D. M. Mattox, C. R. Peeples, P. L. Dreike, and K. P. Lamppa, "Residual stress anisotropy, stress control, and resistivity in post cathode magnetron sputter deposited molybdenum films," *Journal of Vacuum Science and Technology A*, vol. 6, no. 5, pp. 2914–2920, 1988.
- [10] N. Yamamoto, T. Yamada, A. Miyake, H. Makino, S. Kishimoto, and T. Yamamoto, "Relationship between residual stress and crystallographic structure in Ga-doped ZnO film," *Journal of the Electrochemical Society*, vol. 155, no. 9, pp. J221–J225, 2008.
- [11] N. Yamamoto, H. Makino, T. Yamada et al., "Heat resistance of Ga-doped ZnO thin films for application as transparent electrodes in liquid crystal displays," *Journal of the Electrochemical Society*, vol. 157, no. 2, pp. J13–J20, 2010.
- [12] E. B. Tadmor, R. Miller, and R. Phillips, "Nanoindentation and incipient plasticity," *Journal of Materials Research*, vol. 14, no. 6, pp. 2233–2250, 1999.
- [13] P. S. Prevey, "X-ray diffraction residual stress techniques," in *Metals Handbook*, vol. 10, pp. 380–392, American Society for Metals, Metals Park, Ohio, USA, 1986.
- [14] B. K. Tanner, T. P. A. Hase, T. A. Lafford, and M. S. Goorsky, "Grazing incidence in-plane X-ray diffraction, international centre for diffraction data," *Advances in X-Ray Analysis*, vol. 47, pp. 309–314, 2004.
- [15] G. K. Williamson and W. H. Hall, "X-ray line broadening from filed aluminium and wolfram," *Acta Metallurgica*, vol. 1, no. 1, pp. 23–31, 1953.
- [16] Y. Okada and Y. Tokumura, "Precise determination of lattice parameter and thermal expansion coefficient of silicon 300 K–1500 K," *Journal of Applied Physics*, vol. 56, no. 2, pp. 314–320, 1984.
- [17] S. Imai, M. Tokuyama, S. Hirose, G. J. Burger, T. S. J. Lammerink, and J. H. J. Fluitman, "A thin-film piezoelectric impact sensor array fabricated on a Si slider for measuring head-disk interaction," *IEEE Transactions on Magnetics*, vol. 31, no. 6, pp. 3009–3011, 1995.
- [18] H. K. Yoon and Y. S. Yu, "Hardness and elastic modulus of ZnO thin films fabricated by PLD method," *Key Engineering Materials*, vol. 353–358, no. 4, pp. 2966–2969, 2007.
- [19] I. Özgenç, M. A. Gülgün, and M. Özcan, "Self-induced crystallinity in RF magnetron sputtered ZnO thin films," *Key Engineering Materials*, vol. 264–268, pp. 1225–1228, 2004.
- [20] H. C. Jung, H. K. Yoon, and Y. S. Yu, "Mechanical properties and process of ZnO deposited various substrates," *Key Engineering Materials*, vol. 297–300, pp. 533–538, 2005.
- [21] G. Cao and X. Chen, "Size dependence and orientation dependence of elastic properties of ZnO nanofilms," *International Journal of Solids and Structures*, vol. 45, no. 6, pp. 1730–1753, 2008.
- [22] G. Stan, C. V. Ciobanu, P. M. Parthangal, and R. F. Cook, "Diameter-dependent radial and tangential elastic moduli of ZnO nanowires," *Nano Letters*, vol. 7, no. 12, pp. 3691–3697, 2007.
- [23] O. Kappertz, R. Drese, and M. Wuttig, "Correlation between structure, stress and deposition parameters in direct current sputtered zinc oxide films," *Journal of Vacuum Science and Technology A*, vol. 20, no. 6, pp. 2084–2095, 2002.
- [24] T.-H. Fang, W.-J. Chang, and C.-M. Lin, "Nanoindentation characterization of ZnO thin films," *Materials Science and Engineering A*, vol. 452–453, pp. 715–720, 2007.

Research Article

TEM Study of High-Temperature Precipitation of Delta Phase in Inconel 718 Alloy

Moukrane Dehmas,¹ Jacques Lacaze,² Aliou Niang,² and Bernard Viguier²

¹ IJL-SI2M UMR 7198 CNRS-Nancy Université-UPV Metz, École des Mines de Nancy, Parc de Saurupt, CS 14234, 54042 Nancy Cedex, France

² Institut Carnot CIRIMAT, Université de Toulouse, INP-ENSIACET, 4 allée Emile Monso, BP 44362, 31030 Toulouse Cedex 4, France

Correspondence should be addressed to Jacques Lacaze, jacques.lacaze@ensiacet.fr

Received 31 March 2011; Accepted 12 May 2011

Academic Editor: Joseph Lai

Copyright © 2011 Moukrane Dehmas et al. This is an open access article distributed under the Creative Commons Attribution License, which permits unrestricted use, distribution, and reproduction in any medium, provided the original work is properly cited.

Inconel 718 is widely used because of its ability to retain strength at up to 650°C for long periods of time through coherent metastable γ'' Ni₃Nb precipitation associated with a smaller volume fraction of γ' Ni₃Al precipitates. At very long ageing times at service temperature, γ'' decomposes to the stable Ni₃Nb δ phase. This latter phase is also present above the γ'' solvus and is used for grain control during forging of alloy 718. While most works available on δ precipitation have been performed at temperatures below the γ'' solvus, it appeared of interest to also investigate the case where δ phase precipitates directly from the fcc matrix free of γ'' precipitates. This was studied by X-ray diffraction and transmission electron microscopy (TEM). TEM observations confirmed the presence of rotation-ordered domains in δ plates, and some unexpected contrast could be explained by double diffraction due to overlapping phases.

1. Introduction

Alloy 718 is the most widely used material for turbine disks and it is selected for many other applications as a high-strength material for temperatures up to 650°C. This alloy was developed in the 60s when the former Fe-based superalloys evolved towards Ni-based superalloys. Alloy 718 contains both Fe and Ni alloyed with some Al and Ti, though the most important addition is the refractory element Nb. A typical composition of alloy 718 is reported in Table 1. It contains a small amount of carbon as well as very low levels of other species such as Si, Ta, Mn, Cu, S, B, P, and Mg, not listed in Table 1 but generally controlled.

The strength of alloy 718 comes from coherent solid-state precipitates, which are for a small part γ' -Ni₃Al but mostly γ'' -Ni₃Nb precipitates [1–6]. Both of these precipitates are ordered forms of the fcc-Al Ni-rich matrix: L1₂ in the case of γ' and DO₂₂ in the case of γ'' . The solvus of these precipitates is at about 900–920°C as discussed previously [7]. Moreover, γ'' precipitates are metastable while the stable form of Ni₃Nb is the so-called delta phase which is orthorhombic. Forging

of 718 alloy is done at about 980°C slightly below the solvus of the delta phase, in such a way that this phase is sufficiently abundant to be effective in limiting grain growth but not too abundant to avoid significant Nb depletion in the matrix which would affect the subsequent strengthening by γ'' precipitation. This latter precipitation is generally obtained after two successive periods of isothermal ageing at 750°C and 650°C, respectively.

Precipitation of delta phase proceeds through a discontinuous reaction starting at grain boundaries and an intragranular precipitation of thin plates. It has been reported that the former reaction predominates at low temperatures whilst the latter is more characteristic of intermediate temperatures [2], but no systematic and quantitative study has been performed on that aspect. At high temperatures, both types of precipitates may be observed as illustrated in Figure 1.

In fully strengthened material, precipitation of delta has been studied for many years at both low and intermediate temperatures as it corresponds to a dramatic decrease of the mechanical properties of alloy 718. Kirman and Warrington [2] showed that the growth of δ at the expense of γ''

TABLE 1: Specification (wt.%) of alloy 718 [8] and composition of the alloys used in the present study [7, 9].

	Ni	Fe	Cr	Nb	Ti	Al	Mo	C	Co
Specification	50.0–55.0	Balance	17.0–21.0	4.75–5.50	0.75–1.15	0.20–0.80	2.80–3.30	<0.08	—
Alloy 1 [9]	54.4	17.4	17.9	5.4	1.1	0.5	3.0	0.02	0.2
Alloy 2 [7]	53.0	17.1	17.5	5.3	1.1	0.5	3.1	0.12	0.2

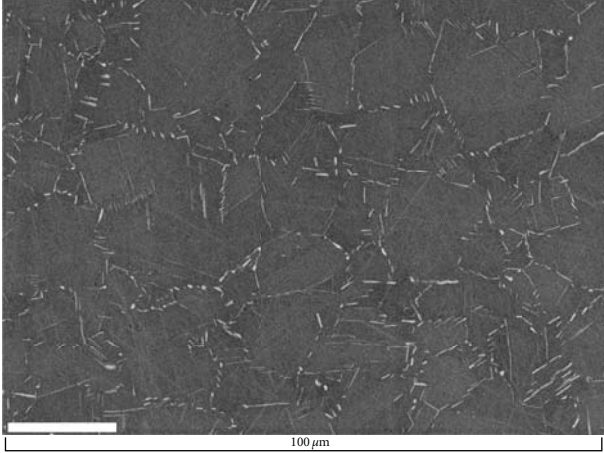


FIGURE 1: SEM micrograph showing mainly cellular (grain boundary) and some intragranular precipitation of delta phase in a sample held for 1 h at 960°C.

precipitates is often associated with the formation of faults within the γ'' . By means of dark field imaging, these authors observed that the faults are illuminated together with the related delta plate, and they concluded that the formation of these faults is the first step in the transformation of metastable to stable Ni_3Nb precipitates. These observations have been repeated more recently by Sundararaman et al. [10]. Further details on the faults appearing in γ'' precipitates have been previously presented by our group [11].

The only report of TEM examination of a material aged at a temperature above the γ'' solvus is due to Sundararaman et al. [10]. In a sample held at 950°C, these authors observed only the presence of delta phase as expected but did not give any details and in particular no diffraction diagram was recorded. The present work was intended to pursue the investigation of the growth conditions of delta phase at high temperature. X-ray diffraction results and TEM observations are reported.

2. Material and Methods

Two Inconel 718 alloys were used in this investigation, supplied, respectively, by Special Metals Corporation (denoted alloy 1 in the following) and by Aubert and Duval (denoted alloy 2). The amounts of the main elements in their composition are listed in Table 1, further details having been given previously [7, 9].

As described previously [9], alloy 1 in the as-received state showed a microstructure very similar to that of a fully strengthened material, that is, some residual delta phase

TABLE 2: Structural parameters for δ phase at 25°C: Pmmn (no. 59) with $a = 5.114 \text{ \AA}$, $b = 4.244 \text{ \AA}$, and $c = 4.538 \text{ \AA}$ [13].

	Wyckoff	x	Y	z	Occupancy
Ni (1)	2a	0	0	0.3182	1
Ni (2)	4f	0.7494	0	0.8414	1
Nb (1)	2b	0	1/2	0.6513	1

precipitates mainly at grain boundaries and a high volume fraction of small γ'' precipitates within the grains. Samples of this material were aged for various times at 960°C or 920°C and then air cooled. Alloy 2 was received in the fully strengthened state and the specimens studied here were aged for 3 h at 960°C.

XRD profiles were all recorded on samples from alloy 1 using a diffractometer with $\text{Cu-K}\alpha$ radiation ($\lambda_{\text{Cu}} = 1.54184 \text{ \AA}$), with the power fixed at 4 kW (40 kV and 100 mA). The instrument was set up for Bragg-Brentano geometry with a line focus and a graphite monochromator in diffracted beam arm. During the scans 2θ ranged between 10 and 100° with an angular step of 0.025° and 30 s counting time at each step. As the volume fraction of the delta phase is low even after heat-treatment, the precipitates were also electrolytically extracted from the heat-treated specimens for X-ray characterization. The solution used to dissolve the matrix consisted of 1 mL ammonium sulfate, 2 mL tartaric acid, and 97 mL water. The current was set at 100 mA/cm² and the time for extraction was 5 to 6 h [12]. From the structural data reported in the literature for the δ phase [13], and listed in Table 2, an initial set of lattice parameters was obtained by least-square refinement using DICVOL software [14]. Then, structure refinement was carried out by Rietveld analysis of the X-ray powder diffraction data with FullProf software [15]. An account of the mathematical procedures implemented in the Rietveld analysis [16] is summarized in the appendix.

For microstructural investigation by TEM, thin foils were prepared by cutting, mechanical thinning down to a thickness of about 50 μm , and jet polishing in a TenuPol-5 at -10°C and a voltage of 22 V. The electrolyte was one part perchloric acid, two parts butylcellosolve, and nine parts methanol. The samples were investigated using either a Philips CM20 or a JEOL 2100F, both operating at an acceleration voltage of 200 kV.

3. Results

3.1. X-Ray Diffraction. Figure 2 shows the whole X-ray diagram recorded on a sample of alloy 1 aged for 1 h at 960°C.

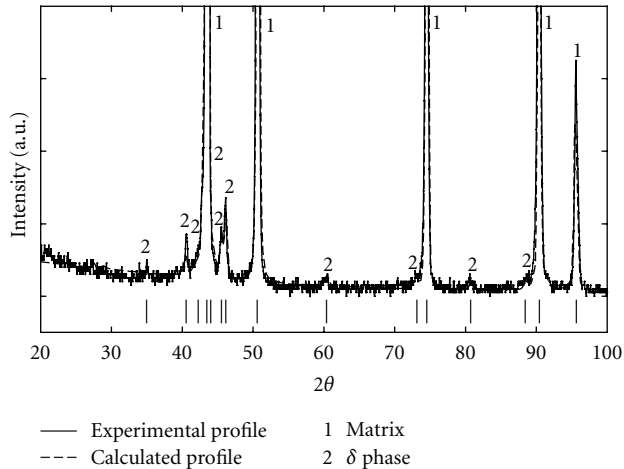


FIGURE 2: Whole experimental X-ray diagram with first indexation of the lines, showing that all the peaks may be attributed to either the fcc matrix or the delta phase.

Through least-squares refinement, the XRD pattern is fully indexed on a cubic lattice (fcc matrix) with unit cell parameter of 3.604 Å and a orthorhombic lattice (δ phase) with unit cell parameters $a = 5.108$ Å, $b = 4.214$ Å, and $c = 4.521$ Å (volume $V = 97.315$ Å³). All peaks in Figure 2 are indexed and there is no evidence of any other phase present, such as γ' or γ'' .

For further exploitation of the X-ray diagrams on bulk samples, the parameters of the delta phase were then evaluated from the X-ray pattern acquired on the extracted precipitates. Figure 3 shows the experimental diagram for 2θ between 39° and 49°, in which the peak at 43.51° is associated to some remains of the matrix and/or the γ'' phase while all other peaks come from the delta phase. To optimally adjust all the delta phase intensities from the initial structural model [13], the atomic positions were refined by Rietveld's method. The refinement was constrained by the space group with its respective Wyckoff's positions as given in Table 2. Then these atom positions were fixed to allow for the refinement of the site occupancies as a function of one of the following conditions:

- (A) Nb site occupancy fixed, the sum of the Ni site occupancies is equal to 1;
- (B) Nb site occupancy fixed, Ni site occupancies are independent;
- (C) the three site occupancies are independent.

Rietveld refinement gave similar results for all three conditions. The X-ray diagram calculated for condition (A) was superimposed on the experimental diagram in Figure 3. The amount of remaining matrix was adjusted so that the height of the calculated peak at 43.51° corresponds to the experimental value. Similarly, the amount of delta phase was fixed so that the height of its most intense peak at 46.11° agrees with the experimental value. It is seen that most of the other peaks of the delta phase are well reproduced by calculation apart from the one at 42.99° which corresponds

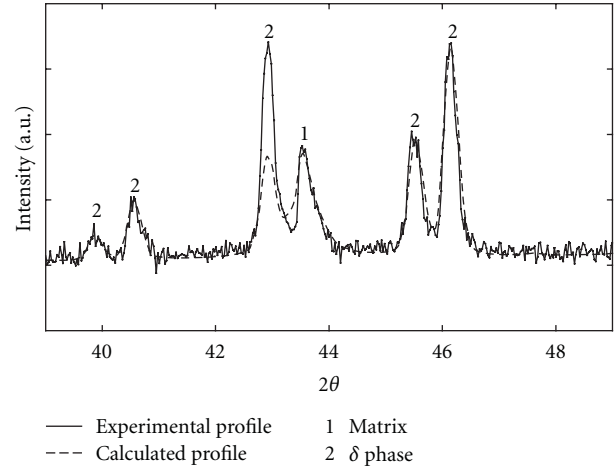


FIGURE 3: Experimental and calculated X-ray diagram corresponding to precipitates extracted from the material. The diagram was calculated after Rietveld refinement according to condition (A).

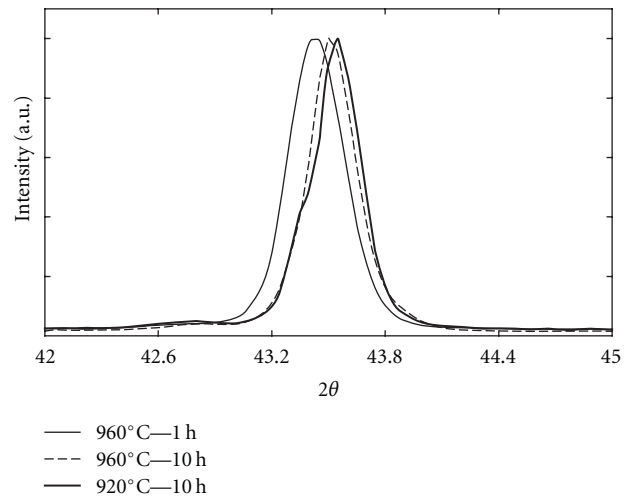


FIGURE 4: XRD pattern showing angular displacement of the (111) matrix peak as function of ageing treatment.

to the close packed (020) plane of delta phase. This is certainly related to the shape of the delta precipitates that are mainly thin discs grown in the (020) plane after heat treating for 1 h at 960°C [9].

XRD profiles were then recorded on samples aged for various times and temperatures, thus showing various amounts of delta phase. It was found that the change of the parameters of the delta phase was not significant while the matrix parameter clearly proved to be affected. This is illustrated in Figure 4 which presents the (111) peak of the matrix for the three samples investigated. A significant shift is seen in the peak position from one sample to another which could certainly be related to alterations of the volume fraction of delta phase as evaluated by image analysis [9]. Rietveld refinement of the X-ray diagrams was also performed to evaluate the volume fraction of delta precipitates in these samples. The structural model for condition (A) obtained

TABLE 3: Volume fraction (%) of delta phase after different ageing treatments obtained by image analysis [9] and by Rietveld refinement.

Ageing conditions	Image analysis [9]	Rietveld Refinement
960°C—1 h	2.3	2.5
960°C—10 h	5.6	6.2
920°C—10 h	7.3	7.8

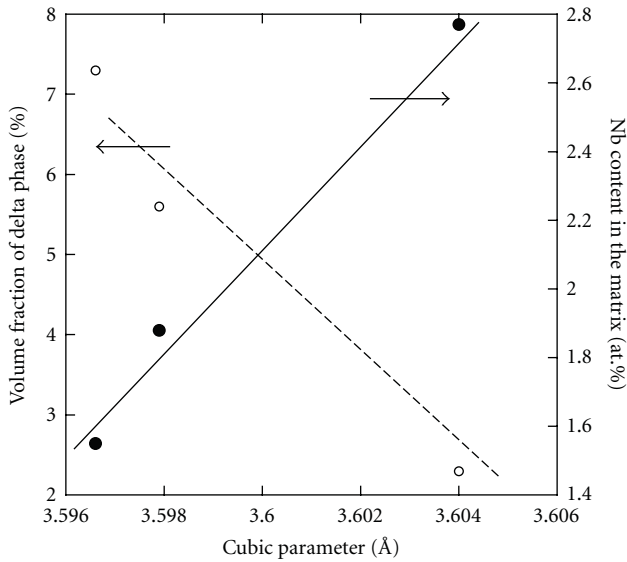


FIGURE 5: Variation of lattice parameter of the matrix versus volume fraction of delta phase and niobium content in the matrix.

from the precipitate extracted from the bulk specimen was used for this purpose. The data obtained are compared in Table 3 to image analysis results and both techniques give values in quite good agreement.

Finally, Figure 5 shows the lattice parameter of the matrix as a function of the volume fraction of delta phase and of the niobium content of the matrix, x_{Nb}^{γ} (at.%), that was evaluated considering that the delta phase is the binary stoichiometric Ni_3Nb phase. It is seen that the lattice parameter of the matrix decreases more or less linearly with increasing volume fraction of delta phase, that is, obeying a Vegard law such as: $a^{\gamma} = 3.587 + 0.0062 \cdot x_{\text{Nb}}^{\gamma}$ (Å). The effect of Nb substitution on the fcc matrix agrees well with the value of $0.007 \text{ \AA} (\text{at.}\%)^{-1}$ estimated from the data assessed by P. Nash and A. Nash for the binary Ni-Nb system [17].

3.2. TEM Observation. It has been shown previously that nucleation of delta phase is difficult in a material free of γ'' precipitates [7]. We therefore investigated the first stage of delta phase growth by TEM. The first TEM observations were performed on a sample of alloy 1 aged for 1 h at 960°C. A typical bright field micrograph showing a plate-like precipitate is shown in Figure 6. Two areas labeled as 1

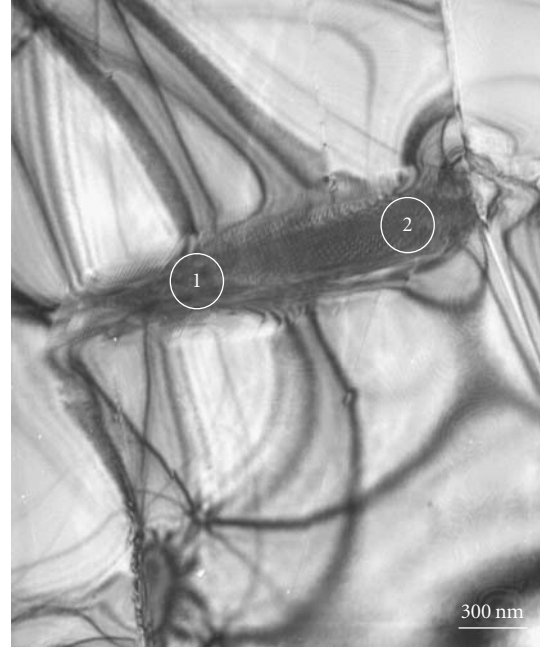


FIGURE 6: Bright field image of a plate-like precipitate with locations 1 and 2 used for recording SAD pattern.

and 2 were selected for electron diffraction and the selected area diffraction (SAD) patterns corresponding to the $[111]_{\gamma}$, $[001]_{\gamma}$ zone axis of the matrix were recorded.

The SAD patterns along the $[111]_{\gamma}$ zone axis obtained on the matrix and on the precipitate in location 1 are shown in Figures 7(a) and 7(b). The pattern in Figure 7(b) was easily indexed as the one corresponding with the $[010]_{\delta}$ zone axis. The orientation relationship between the γ matrix and the δ phase is thus $(111)_{\gamma} // (010)_{\delta}$ and $[\bar{1}01]_{\gamma} // [100]_{\delta}$. This relationship is the same as the one that has been reported after ageing at lower temperatures [18], and simply corresponds to the alignment of compact planes and dense directions in both structures. The SAD pattern obtained with the same conditions in location 2 is presented in Figure 7(c). The additional spots observed in this latter SAD pattern, arise from a mirror image of the pattern in Figure 7(b) with respect to the $(2\bar{2}0)_{\gamma}$ plane. These spots can also be indexed as belonging to a second variant of the δ phase with an orientation relationship to the matrix γ given by $(111)_{\gamma} // (010)_{\delta_2}$ and $[0\bar{1}1]_{\gamma} // [100]_{\delta_2}$. In fact, close observation of the pattern in Figure 7(b) also shows faint dots from this second variant.

A striking figure was obtained when looking at the SAD of the plate along the $[001]_{\gamma}$ zone axis of the matrix. Figure 8(a) shows the pattern recorded on the matrix, Figures 8(b) and 8(c) show those obtained on the plate in locations 1 and 2, respectively. The presence of two variants is again observed in location 2, with one of them being as before the variant showing up in location 1. Astonishingly enough, the pattern in Figure 8(b) is indexed according to the metastable γ'' phase with the usual orientation relationship to the matrix: $(001)_{\gamma} // (100)_{\gamma''}$ and $[010]_{\gamma} // [001]_{\gamma''}$.

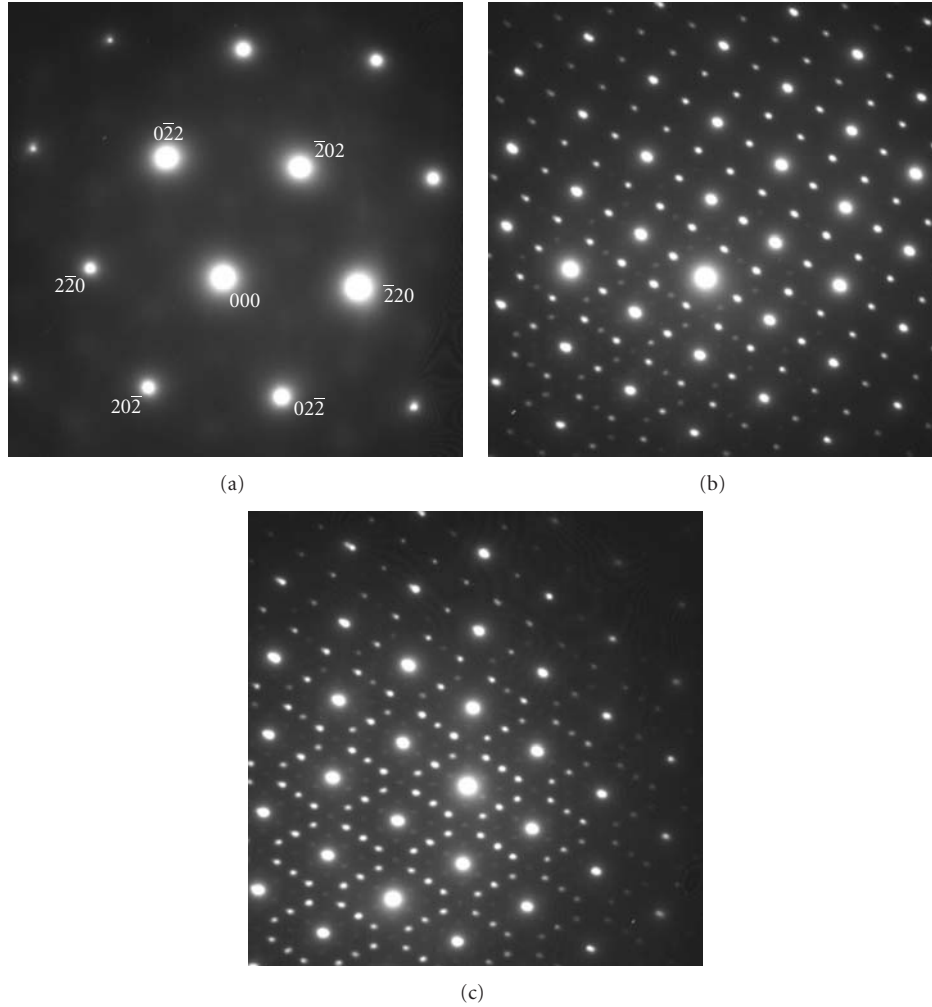


FIGURE 7: Experimental SAD patterns of the matrix (a) and in locations 1 (b) and 2 (c) of the precipitate shown in Figure 6. The patterns were identified as the $[111]_{\gamma}$ zone axis for the matrix (a) and the $[010]_{\delta}$ for the delta plate (b). In location 2, a second variant of the delta phase appears together with that in location 1 (c).

Apparently, this pattern cannot be directly related to the delta phase. In location 2, the pattern is thus apparently the superposition of two variants of the γ'' phase along the $[100]_{\gamma''}$ and $[010]_{\gamma''}$ zone axes, respectively.

Using the CaRIne Crystallography software [19] to simulate the SAD patterns, it was noticed that the reflections of γ'' are superimposed on the δ phase for $[111]_{\gamma}$ and those of δ are superimposed on the γ'' phase for $[010]_{\gamma}$ for both variants. These results suggest that the plate-like precipitate may contain both phases, namely, γ'' and δ . Dark field images with γ'' spots seemed to indicate that this phase surrounds the δ plate. However, these images were not clear and it appeared necessary to resort to high-resolution TEM (HRTEM) to decide whether that precipitation of delta from the gamma matrix involves an intermediate γ'' precipitate even at temperatures where it is not expected to appear.

This second part of the TEM investigation was carried out on a sample of alloy 2 aged for 3 h at 960°C and then quenched. This sample thus contained δ phase that precipitated at the grain boundaries and in the grains, both in

the form of plates. By selecting appropriate areas in the thin foil we successively studied the two phenomena illustrated in the δ plate observed in Figure 6: the existence of different variants of the ordered phases and the concomitant presence of δ and γ'' within the same precipitate.

Figure 9 shows TEM images of a δ platelet lying parallel to the $(111)_{\gamma}$ plane and observed along the $[\bar{1}01]_{\gamma}$ direction. In the low-magnification image, Figure 9(a), different areas can be seen in the platelet, for example, those labeled δ_1 and δ_2 . The borders between these areas are shown with solid lines in Figure 9(a). A closer observation of this boundary is reported in Figure 9(b) showing lattice imaging of the different phases. Examination of these images and the corresponding Fourier transforms (obtained with ImageJ software [20]) indicated that the δ platelet is a coherent precipitate in the γ matrix, with the habit plane $(111)_{\gamma} // (010)_{\delta}$. The Fourier transform patterns showed that the areas labeled δ_1 and δ_2 correspond to different orientations of the orthorhombic phase along $[\bar{1}01]_{\gamma} // [100]_{\delta_1}$ and $[\bar{1}01]_{\gamma} // [102]_{\delta_2}$, respectively. In the δ structure, the $[102]_{\delta}$ axis is rotated $2\pi/3$

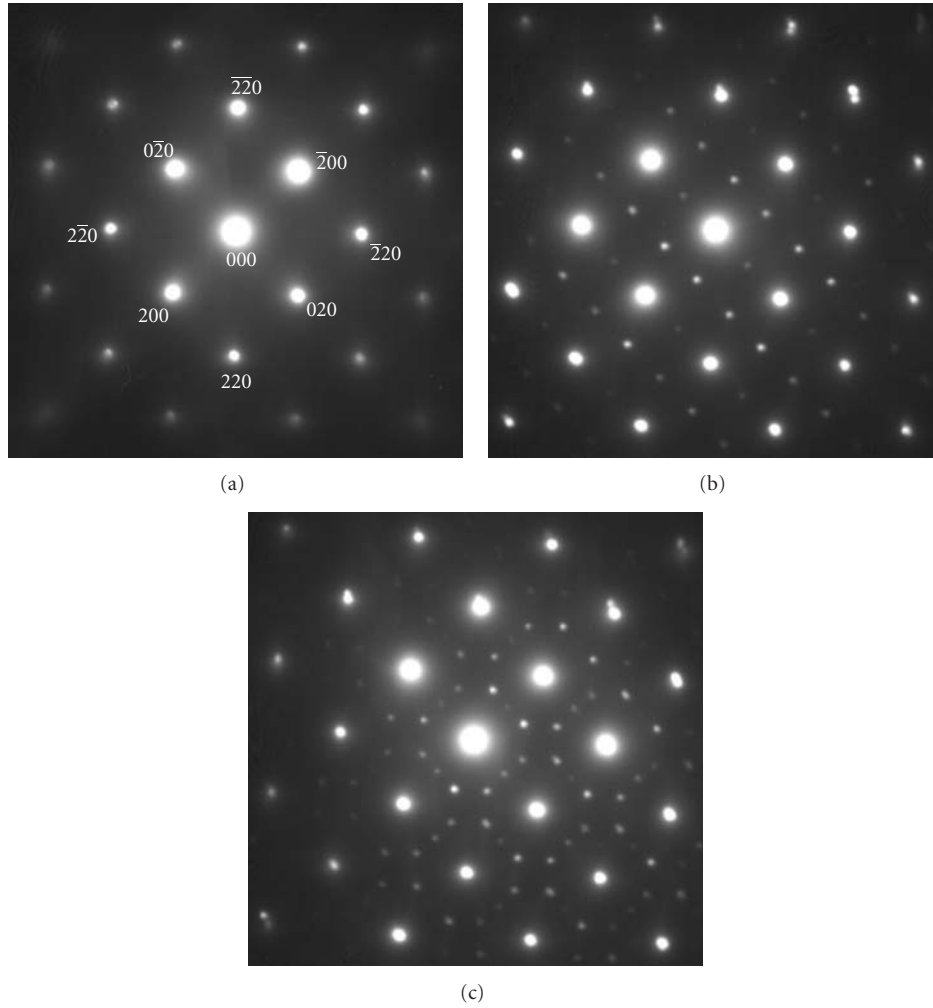


FIGURE 8: Experimental SAD patterns of the matrix (a) and of the precipitate seen Figure 6 in locations 1 (b) and 2 (c). The patterns were identified as the $[001]_{\gamma}$ zone axis for the matrix (a), the $[100]_{\gamma'}$ for location 1, and the $[100]_{\gamma'}$ and $[010]_{\gamma'}$ for location 2.

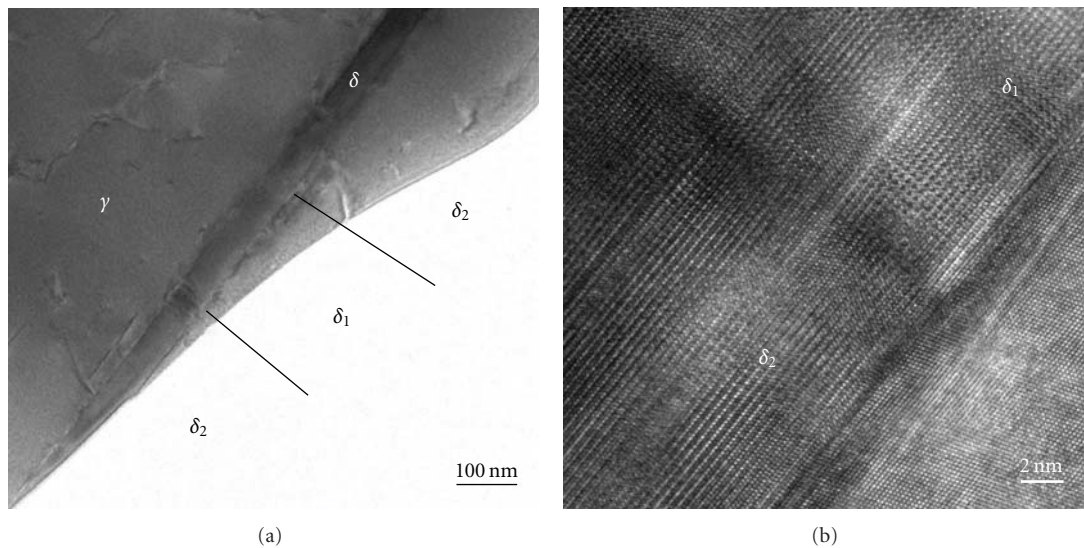


FIGURE 9: TEM observation of a δ platelet in a 718 alloy sample aged 3 h at 960°C . The low-magnification bright field image in (a) shows the extent of different variants of the δ phase, detailed in the HRTEM image of the same sample in (b).

away from $[100]_{\delta}$, so that the latter orientation relationship corresponds to $(111)_{\gamma} // (010)_{\delta 2}$ and $[0\bar{1}1]_{\gamma} // [100]_{\delta 2}$. The two areas observed in Figure 9 thus confirmed the existence of two variants of the δ phase in a given precipitate. Such variants have been previously reported by Zhang et al. [21] and described in terms of orientation twins or antiphase domain structures. Indeed the variants only differ by the orientation of the $[100]_{\delta}$ direction in the $(010)_{\delta}$ plane with respect to different $\langle 110 \rangle_{\gamma}$ directions of the $(111)_{\gamma}$ plane.

Further HRTEM investigation of the same sample showed that the boundary between delta precipitates and the matrix could present unexpected contrast. This is illustrated in Figure 10 that was obtained along the $[\bar{1}01]_{\gamma}$ zone axis of the matrix and shows the extremity of a δ precipitate. The interfaces between precipitate and matrix parallel to $(111)_{\gamma}$ and $(010)_{\delta}$ planes are sharply defined and show ledges. The third interface shows a very different contrast with the occurrence of fringes parallel to the $(111)_{\gamma}$ plane. These fringes repeat every six $(111)_{\gamma}$ planes which recalls the stacking sequence of six compact planes in the γ'' phase ($A_1B_1C_1A_2B_2C_2\dots$ as described by Paulonis et al. [1]). Fourier transforms of the image in the different areas labeled a, b, and c in Figure 10 are shown in Figure 11. The first two correspond, respectively, to the SAD pattern of the matrix along $[\bar{1}01]_{\gamma}$ zone axis and delta phase along $[100]_{\delta}$ zone axis, as shown by the schematic illustration of the indexation in Figure 11.

The third pattern, obtained by the Fourier transformation of the interfacial area c in Figure 10, cannot be indexed as a diffraction pattern of γ'' phase along the various possible directions (either $[110]_{\gamma''}$ or $[201]_{\gamma''}$ type) that would have been compatible with the orientation relation between γ and γ'' . In the corresponding schematic indexation, it is seen that the pattern consists of the superimposition of the two first patterns plus additional points. These points could in fact all be deduced by translations of δ or γ spots by a vector $\pm 1/3(010)_{\delta} = 1/6(111)_{\gamma}$. Such a vector is given for instance by connecting $(\bar{1}\bar{1}\bar{1})_{\gamma}$ and $(0\bar{1}\bar{2})_{\delta}$ as illustrated in Figure 11(c). This corresponds to double diffraction phenomena and leads to the conclusion that the fringes observed are due to the superimposition of γ and δ phases. Such a superimposition and the associated fringes have been reported by Chen et al. [22] in TiAl alloys where the phases involved were the $L1_0$ -gamma and DO_{19} -alpha phases.

This analysis allowed us to reconsider the interpretation of the SAD patterns presented in Figure 8. Indeed the orientation relationship between the matrix γ and the δ_1 phase indicates that the $[001]_{\gamma}$ direction is parallel to the $[\bar{3}\bar{3}\bar{2}]_{\delta_1}$ direction. The corresponding diffraction patterns are shown in Figures 12(a) and 12(b), respectively. The superimposition of these two patterns which is given in Figure 12(c) shows that, when considering double diffraction (e.g., the arrows in Figure 12(c)), all the spots observed in Figure 8(b) could be explained solely by the presence of γ and δ phases. For completeness, we may remark that the diffraction pattern in Figure 8(c) is simply explained in the same way by the mirror symmetry about the $(2\bar{2}0)_{\gamma}$ plane, already noted in Figure 7.

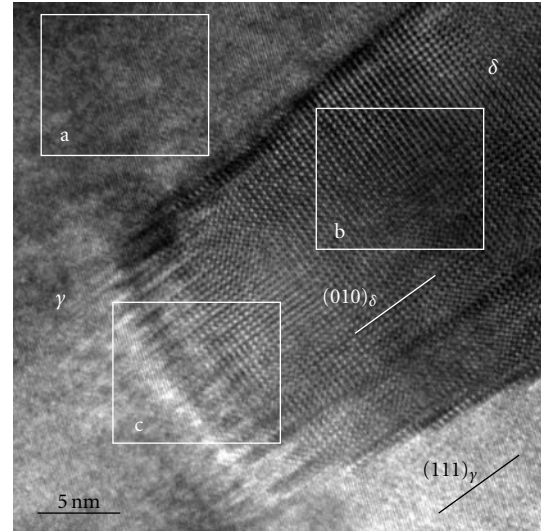


FIGURE 10: HRTEM image taken on a sample held for 3 h at 960°C.

Similar observations were conducted on specimens of the 718 alloy after different heat treatments. When extra spots were observed on SAD patterns they could always be explained by such double diffraction. Accordingly, it may be stated that γ'' was not present on the edges of the delta precipitates as could have been erroneously guessed from the SAD patterns in Figure 8.

4. Conclusion

The precipitation of δ phase at high temperature from a supersaturated matrix (i.e., without γ'' phase) was studied by XRD and TEM. Rietveld refinement proved to be very efficient to study δ precipitation. The volume fraction of δ precipitates was determined and allowed us to calculate the alterations occurring in the γ cell parameter with the amount of dissolved Nb. The results confirm the close correlation between δ precipitate growth kinetics and the evolution of the niobium content in the matrix. Detailed TEM studies of the δ platelets confirmed the existence of antiphase domains related by a $2\pi/3$ rotation around the $[010]_{\delta}$ axis. Some diffraction contrast observed at the edges of delta precipitates could lead to the erroneous conclusion that delta phase grows through the formation of an intermediate γ'' phase. Examination of the Fourier transforms from the images showed that the contrast observed is due to a double diffraction phenomenon occurring when γ and δ phases overlap. The present investigations thus indicate that δ phase may grow directly from the supersaturated γ matrix.

Appendix

Considering the integrated intensity of the peaks to be a function of the refined structural parameters, a least-squares procedure was used to minimize the difference between the observed and simulated powder diffraction patterns. The progress of the minimization was monitored through

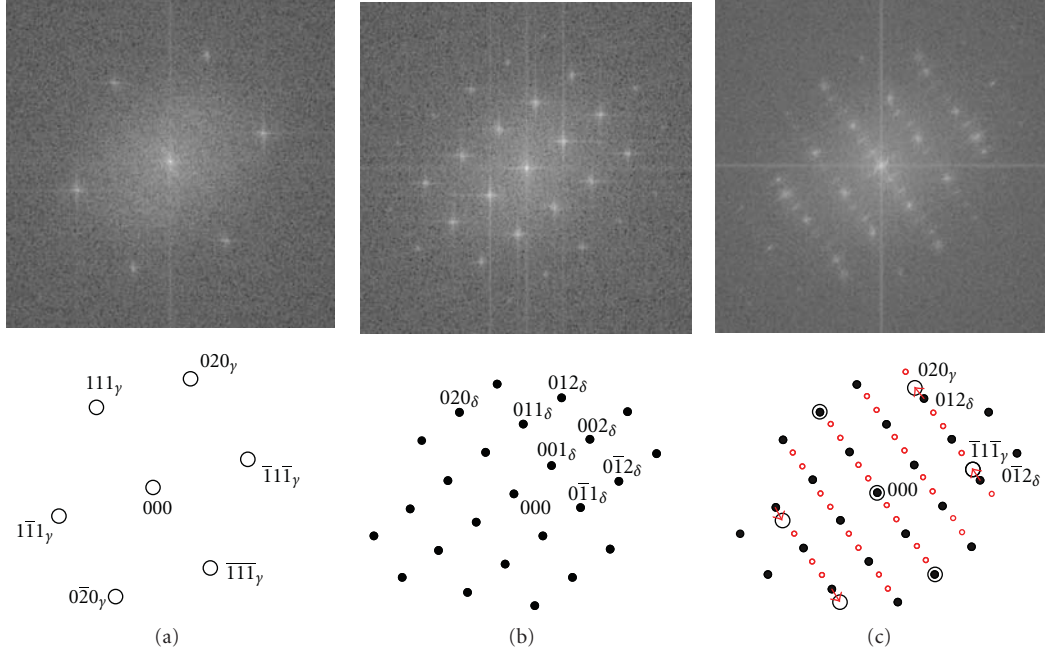


FIGURE 11: Fourier transform of zones a, b, and c in Figure 10 (first row) and their indexing (second row).

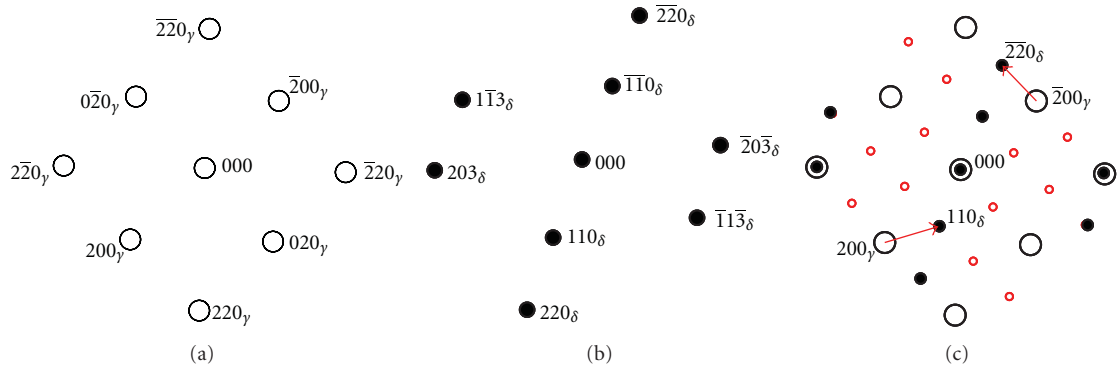


FIGURE 12: Indexing of the SAD pattern shown in Figure 8(b), indicating that the pattern can be obtained by the superimposition of diffraction along $[001]_y$ (a) and $[\bar{3}\bar{3}2]_{\delta_1}$ (b) plus some additional spots arising from double diffraction as shown by the arrows in (c).

the usual reliability parameters, R_{wp} (weighted residual factor) and R_{exp} (expected residual factor) defined as:

$$R_{wp} = \left[\frac{\sum_{2\theta} w_{2\theta} (I_{exp}(2\theta) - I_{calc}(2\theta))^2}{\sum_{2\theta} w_{2\theta} (I_{exp}(2\theta))^2} \right]^{1/2}, \quad (A.1)$$

$$R_{exp} = \left[\frac{N - P}{\sum w_{2\theta} (I_{exp}(2\theta))^2} \right]^{1/2},$$

where $I_{exp}(2\theta)$ and $I_{calc}(2\theta)$ are the experimental and calculated intensities at 2θ angles, $w_{2\theta} = 1/I_{exp}(2\theta)$ are weight factors, N is the number of experimental observations, and

P is the number of refined parameters. Also, we used the so-called goodness of fit (GoF) factor given as

$$GoF = \frac{R_{wp}}{R_{exp}}. \quad (A.2)$$

Refinements were carried out until convergence was reached and the value of the GoF factor became close to 1 (usually, the final GoF varies from 1.1 to 1.3). The parameters that were refined using FullProf are the following:

- (i) background;
- (ii) unit cell parameters;
- (iii) breadth of peaks (a Pearson VII profile function was found to be best suited to fit the experimental peaks);

(iv) scale factors (S_i), which are related to the mass fraction (x_i) of the phase i in the mixture by

$$x_i = \frac{(S_i Z M_i V_i) / t_i}{\sum_i (S_i Z M_i V_i) / t_i}, \quad (\text{A.3})$$

where Z is the number of formula units per unit cell for phase i , M is the mass of the formula unit, V is the unit cell volume, and t is the Brindley coefficient that accounts for microabsorption effects.

Then, the volume fraction (f_i) of phase i can be calculated from the mass fraction as:

$$f_i = \frac{x_i / \rho_i}{\sum_i x_i / \rho_i}, \quad (\text{A.4})$$

where ρ_i is the density of phase i .

Acknowledgment

The authors very much appreciated the possibility of using transmission electron microscopes at CEMES and TEM-SCAN in Toulouse.

References

- [1] D. F. Paulonis, J. M. Oblak, and D. S. Duvall, "Precipitation in nickel-base alloy 718," *Trans. ASM*, vol. 62, no. 3, pp. 611–622, 1969.
- [2] I. Kirman and D. H. Warrington, "The precipitation of Ni₃Nb phases in a Ni-Fe-Cr-Nb alloy," *Metallurgical Transactions*, vol. 1, no. 10, pp. 2667–2675, 1970.
- [3] R. Cozar and A. Pineau, "Morphology of γ' and γ'' precipitates and thermal stability of inconel 718 type alloys," *Metallurgical Transactions*, vol. 4, no. 1, pp. 47–59, 1973.
- [4] J. M. Oblak, D. F. Paulonis, and D. S. Duvall, "Coherency strengthening in Ni base alloys hardened by DO22 γ'' precipitates," *Metallurgical Transactions*, vol. 5, no. 1, pp. 143–153, 1974.
- [5] M. Sundararaman, P. Mukhopadhyay, and S. Banerjee, "Some aspects of the precipitation of metastable intermetallic phases in INCONEL 718," *Metallurgical transactions. A*, vol. 23, no. 7, pp. 2015–2028, 1992.
- [6] C. Slama, C. Servant, and G. Cizeron, "Aging of the Inconel 718 alloy between 500 and 750 °C," *Journal of Materials Research*, vol. 12, no. 9, pp. 2298–2316, 1997.
- [7] A. Niang, B. Viguier, and J. Lacaze, "Some features of anisothermal solid-state transformations in alloy 718," *Materials Characterization*, vol. 61, no. 5, pp. 525–534, 2010.
- [8] L. Yang, K. M. Chang, S. Mannan, and J. D. Barbadillo, "Superalloys 718, 625, 706 and various derivatives," in *Proceedings of the 6th International Symposium on Superalloys 718, 625, 706 and Derivatives*, E. A. Loria, Ed., pp. 353–365, TMS, 1997.
- [9] V. Beaubois, J. Huez, S. Coste, O. Brucelle, and J. Lacaze, "Short term precipitation kinetics of delta phase in strain free Inconel* 718 alloy," *Materials Science and Engineering*, vol. 20, no. 8, pp. 1019–1026, 2004.
- [10] M. Sundararaman, P. Mukhopadhyay, and S. Banerjee, "Precipitation of the δ -Ni₃Nb phase in two nickel base superalloys," *Metallurgical Transactions A*, vol. 19, no. 3, pp. 453–465, 1988.
- [11] A. Niang, J. Huez, J. Lacaze, and B. Viguier, "Characterizing precipitation defects in nickel based 718 alloy," *Materials Science Forum*, vol. 636-637, pp. 517–522, 2010.
- [12] R. B. Li, M. Yao, W. C. Liu, and X. C. He, "Isolation and determination for δ , γ' and γ'' phases in Inconel 718 alloy," *Scripta Materialia*, vol. 46, no. 9, pp. 635–638, 2002.
- [13] T. Fang, S. J. Kennedy, L. Quan, and T. J. Hicks, "The structure and paramagnetism of Ni₃Nb," *Journal of Physics: Condensed Matter*, vol. 4, no. 10, article no. 007, pp. 2405–2414, 1992.
- [14] A. Boultif and D. Loueer, "Indexing of powder diffraction patterns for low-symmetry lattices by the successive dichotomy method," *Journal of Applied Crystallography*, vol. 24, no. 6, pp. 987–993, 1991.
- [15] J. Rodriguez-Carvajal, M. T. Fernandez-Diaz, and J. L. Martinez, "Neutron diffraction study on structural and magnetic properties of La 2NiO₄," *Journal of Physics: Condensed Matter*, vol. 3, no. 19, article no. 002, pp. 3215–3234, 1991.
- [16] H. M. Rietveld, "A profile refinement method for nuclear and magnetic structures," *Journal of Applied Crystallography*, vol. 2, p. 65, 1969.
- [17] P. Nash and A. Nash, "The Nb-Ni (Niobium-Nickel) system," *Bulletin of Alloy Phase Diagrams*, vol. 7, no. 2, pp. 124–130, 1986.
- [18] I. Kirman, "Precipitation in the Fe-Ni-Cr-Nb system," *Journal of the Iron and Steel Institute*, vol. 12, pp. 1612–1618, 1969.
- [19] C. Boudias and D. Monceau, "CaRine Crystallography," (1989–2003), <http://pro.wanadoo.fr/carine.crystallography/>.
- [20] <http://imagej.nih.gov/>.
- [21] J. P. Zhang, H. Q. Ye, K. H. Kuo, and S. Amelinckx, "High-resolution electron microscopy study of the domain structure in Ni/3Nb. II. Orientation and general domains," *Physica Status Solidi (A)*, vol. 93, no. 2, pp. 457–462, 1986.
- [22] C. L. Chen, W. Lu, Y. Y. Cui, L. L. He, and H. Q. Ye, "High-resolution image simulation of overlap structures in TiAl alloy," *Journal of Alloys and Compounds*, vol. 468, no. 1–2, pp. 179–186, 2009.

Research Article

γ' Precipitation and Growth Kinetics in Mechanically Alloyed Ni–Al

QingXin Tang, Shigeharu Ukai, Akinobu Minami, and Shigenari Hayashi

Materials Science and Engineering, Faculty of Engineering, Hokkaido University, N13, W-8, Kita-ku, Sapporo 060-8628, Japan

Correspondence should be addressed to Shigeharu Ukai, s-ukai@eng.hokudai.ac.jp

Received 27 March 2011; Accepted 13 May 2011

Academic Editor: Kin Ho Lo

Copyright © 2011 QingXin Tang et al. This is an open access article distributed under the Creative Commons Attribution License, which permits unrestricted use, distribution, and reproduction in any medium, provided the original work is properly cited.

The precipitation and growth kinetics of γ' precipitates, which are strengthening factors in Ni-base oxide dispersion strengthened (ODS) superalloys, were investigated. The cuboidal-type γ' precipitates are formed in conventional arc-melted Ni–Al alloys, whereas spherical-type precipitates are formed in the mechanically alloyed (MAed) specimens. The morphology is controlled by a lattice misfit between the γ' precipitates and the matrix at the aging temperature of 800°C. The growth kinetics of the γ' precipitates can be followed by Ostwald ripening. The Arrhenius plot yielded a lower activation energy for the solute atom diffusion in MAed specimens, which is attributed to their high dislocation density and nanosized grains.

1. Introduction

In jet engines and gas turbines, where Ni-base superalloys with single crystals are currently used extensively as the materials for blades, disks, and vanes, the inlet temperature exceeds 1600°C. Next-generation Ni-base superalloys are intensively being developed to improve thermal efficiency by increasing inlet temperature; an oxide dispersion strengthened (ODS) type of Ni-base superalloy could be candidate of such alloy. The strength of Ni-base ODS superalloys is affected by both dispersed oxide particles and γ' precipitates with an $L1_2$ ordered structure. The coarsening behavior of γ' precipitates in Ni-base superalloys on being subjected to high temperature has been extensively investigated [1, 2]. Kusabiraki et al. [3] reported that coarsening of γ' precipitates in Inconel X-750 follows Ostwald ripening, according to the Lifshitz-Slyozov-Wagner (LSW) theory [4], which describes that an increase in the radius of γ' precipitates is proportional to $t^{1/3}$ (where t is the time). However, for mechanically alloyed (MAed) Ni-base ODS superalloys, experimental information on γ' precipitate behavior is extremely limited [5]. In this study, the precipitation and growth kinetics of γ' precipitates were investigated for the Ni–15at%Al alloy, Ni–15at%Al–0.6at%Y₂O₃ alloy, and similar MA6000 fabricated by ourselves by mechanical alloying and arc-melting as a reference, focusing on the effects of MA and Y₂O₃ addition.

2. Experimental Procedures

The elemental powders in the size of about 100 μm were provided to make three kinds of target compositions: Ni–15at%Al, Ni–15at%Al–0.6at%Y₂O₃, and similar MA6000 (Ni–15 wt%Cr–1.95 wt%Mo–4.45 wt%Al–2.9 wt%Ti–4 wt%W–1.9 wt%Ta–1 wt%Y₂O₃). These powders were placed in a pot 45 cc in volume together with stearic acid under argon gas atmosphere in a glove box, and they were mechanically alloyed (MAed) by using a planetary-type ball mill (Fritsch P-6). The weight ratio of ball to powder was set to 10:1. The mechanical alloying was processed for 24 h. Subsequently, the MAed powders were sintered by hot-pressing (HP) at 1200°C for 3 h. For comparison, the Ni–15at%Al alloy was fabricated by arc-melting and was then heat-treated at 1200°C for 72 h for forming a solid solution. Here, as-MAed powders are referred to “MA,” the subsequently hot-pressed alloys of MAed powders are referred to “MAHP,” and the arc-melted alloys are referred to “arc.”

In order to measure hardness changes due to γ' precipitation, MAed powders were enclosed in an ampoule under vacuum, and the Vickers hardness test was conducted after annealing at four different durations—3 min, 10 min, 60 min, and 72 h at 800°C. The particle size of the MAed powders was about 50 μm . Hence, the Vickers hardness

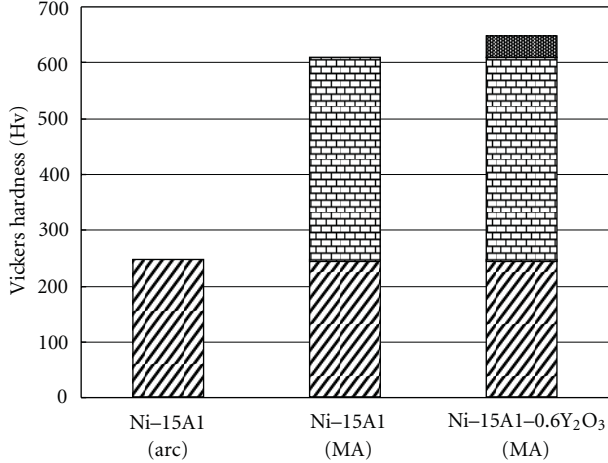


FIGURE 1: Vickers hardness at as-fabricated condition.

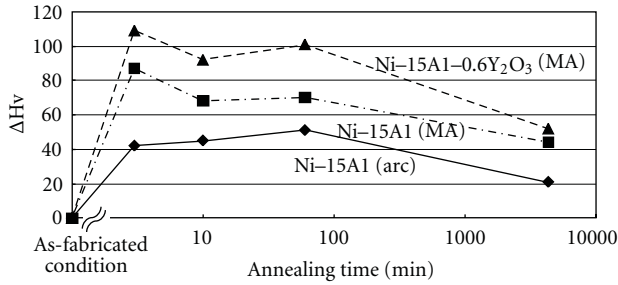


FIGURE 2: Hardness increase ΔH_v during aging at 800°C.

measurement was carried out under lower loading of 100 gf for 5 s and was averaged for 10 times, with the maximum and minimum data points being neglected. For evaluating the growth kinetics of γ' precipitates, their scanning electron microscopy (SEM) observations were carried out after annealing for 24 h, 72 h, and 120 h at 800°C, 850°C, and 900°C.

3. Results and Discussion

3.1. Hardness Increase by γ' Precipitation. Figure 1 shows the results of hardness measurements under as-fabricated conditions of Ni-15at%Al (arc), Ni-15at%Al (MA), and Ni-15at%Al-0.6at%Y₂O₃ (MA). A comparison of the hardness values of the three kinds of alloys showed that mechanical alloying induces a hardness increase by Hv 350, which could be due to the introduction of severe plastic deformation during the alloying process. The addition of 0.6at%Y₂O₃ to Ni-15at%Al (MA) increases the hardness by approximately Hv 40.

The increase in hardness, ΔH_v , from the hardness under the as-fabricated condition, induced by annealing at a temperature of 800°C is shown in Figure 2, where the annealing time is expressed in the logarithmic scale. Dislocation recovery and grain coarsening by annealing induce decrease in hardness. Results of X-ray diffraction analysis confirmed that this hardness increase is attributable

TABLE 1: Dislocation density and grain size of as-fabricated specimens produced by mechanical alloying and arc-melting.

	Dislocation density (1/m ²)	Grain size
Ni-15at%Al (MA)	3.65×10^{16}	91 nm
Ni-15at%Al-0.6at%Y ₂ O ₃ (MA)	5.18×10^{16}	66 nm
Ni-15at%Al (arc)	8.50×10^{13}	3 mm

to γ' precipitation during annealing, as shown in Figure 3, where the low-angle peak corresponds to the γ' precipitates and the high-angle one corresponds to the Ni solid solution in Ni-15at%Al (MA). The maximum ΔH_v becomes Hv 50 for Ni-15at%Al (arc), Hv 90 for Ni-15at%Al (MA), and Hv 110 for Ni-15at%Al-0.6at%Y₂O₃ (MA). These results imply that the process of mechanical alloying leads to the hardness increase because of enhanced precipitation of γ' . With respect to Y₂O₃ behavior, it was found in a previous study that Y₂O₃ particles were dissociated by mechanical alloying, and then, yttrium and oxygen combined and reprecipitated as Y₂O₃ upon annealing at a temperature of around 600°C [6]. On the basis of these findings, it is concluded that Y₂O₃ particles do not directly affect the increase in hardness under the as-fabricated condition, as shown in Figure 1, and during annealing at 800°C, Y₂O₃ particles also precipitate and could affect the hardness increase of Ni-15at%Al-0.6at%Y₂O₃ (MA), as shown in Figure 2.

By X-ray diffraction analyses of the MAed powders and arc-melted alloy before annealing, the grain size (D) and accumulated strain (ϵ) were derived using the diffraction peak angle (θ) and width of the half height (β), according to (1) [7]

$$\beta \frac{\cos \theta}{\lambda} = 2\epsilon \frac{\sin \theta}{\lambda} + \frac{K}{D}, \quad (1)$$

where λ is the wavelength of the incident X-ray (0.154 nm) and K is a constant (0.9). Furthermore, the dislocation density (ρ) can be estimated from accumulated strain (ϵ) using (2) [8]

$$\rho = 14.4 \frac{\epsilon^2}{b^2}, \quad (2)$$

where b is the value of the Burgers vector (0.249 nm) in the Ni solid solution. Table 1 lists the analysis results. It is obvious that mechanical alloying results in extremely fine grains (grain size of the order of nanometers) and an extremely high dislocation density. These values are slightly enhanced by the addition of 0.6 at % Y₂O₃. Specimens produced by arc-melting have a large grain size of 3 mm and lower dislocation density. From the characterization of microstructures under the as-fabricated condition (Table 1), we find that the extremely fine grains and high dislocation density are responsible for the higher hardness in MAed and 0.6 at% Y₂O₃-added alloys.

3.2. γ' Precipitate Morphology. Figure 4 shows the SEM micrographs of Ni-15at%Al (MA) after annealing at 900°C

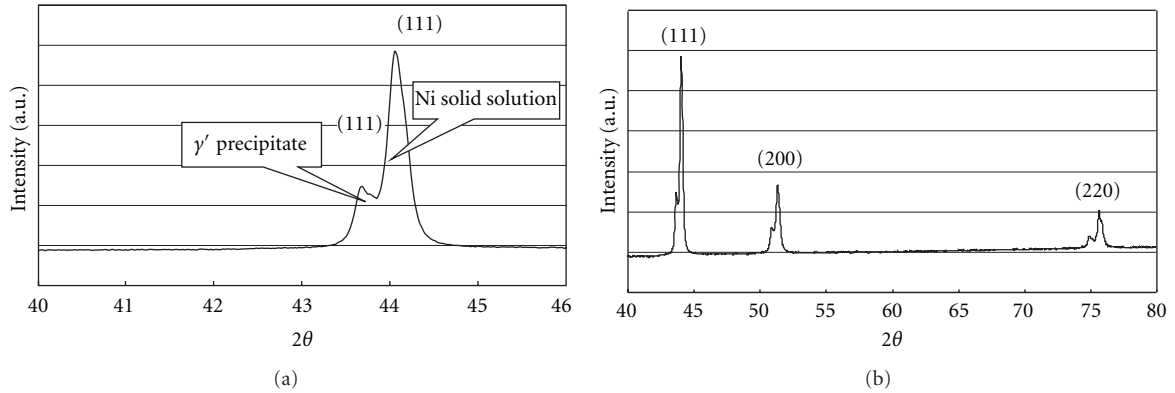


FIGURE 3: Results of X-ray diffraction for Ni-15at%Al (MA) after aging at 800°C.

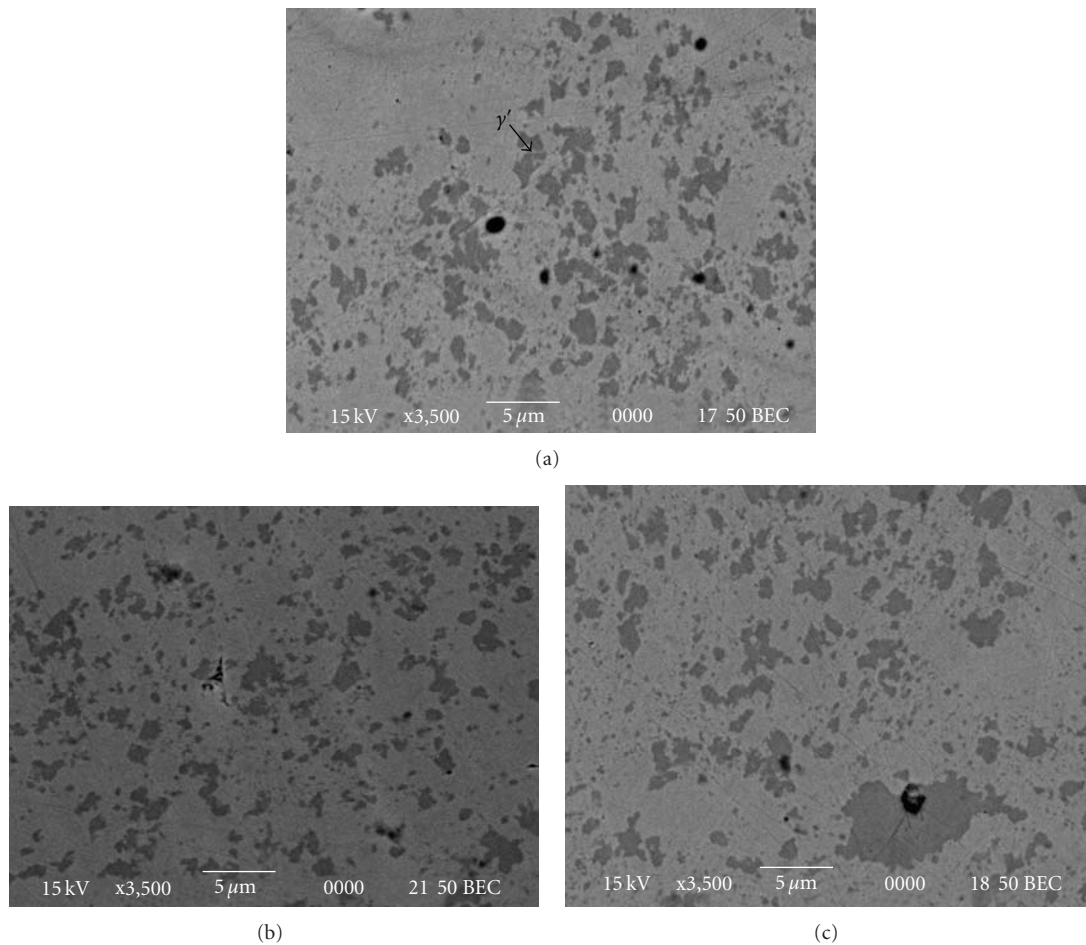


FIGURE 4: SEM micrographs of Ni-15at%Al (MA) after annealing at 900°C for 24 h (a), 72 h (b), and 120 h (c).

for 24 h, 72 h, and 120 h, and Figure 5 shows those of Ni-15at%Al (arc) under the same annealing conditions. The dark region corresponds to the γ' precipitates, which was confirmed by Ni and Al distributions by means of EPMA analyses. As shown in Figure 5, the γ' precipitates in dark region can be observed in regular arrangement along the lattice for arc-melted alloys. It was found that each array

was composed of small cube type of γ' precipitates in a high magnification. A dimension of the cubes is approximately 0.3 μm (cuboidal morphology), and the cubes grow with increasing annealing duration. It is also reported by Ricks et al. [9] that the cube type of the γ' precipitates are developed on the (001) plane and coalescence into the cuboidal arrays. In contrast, the spherical-shaped γ' precipitates are

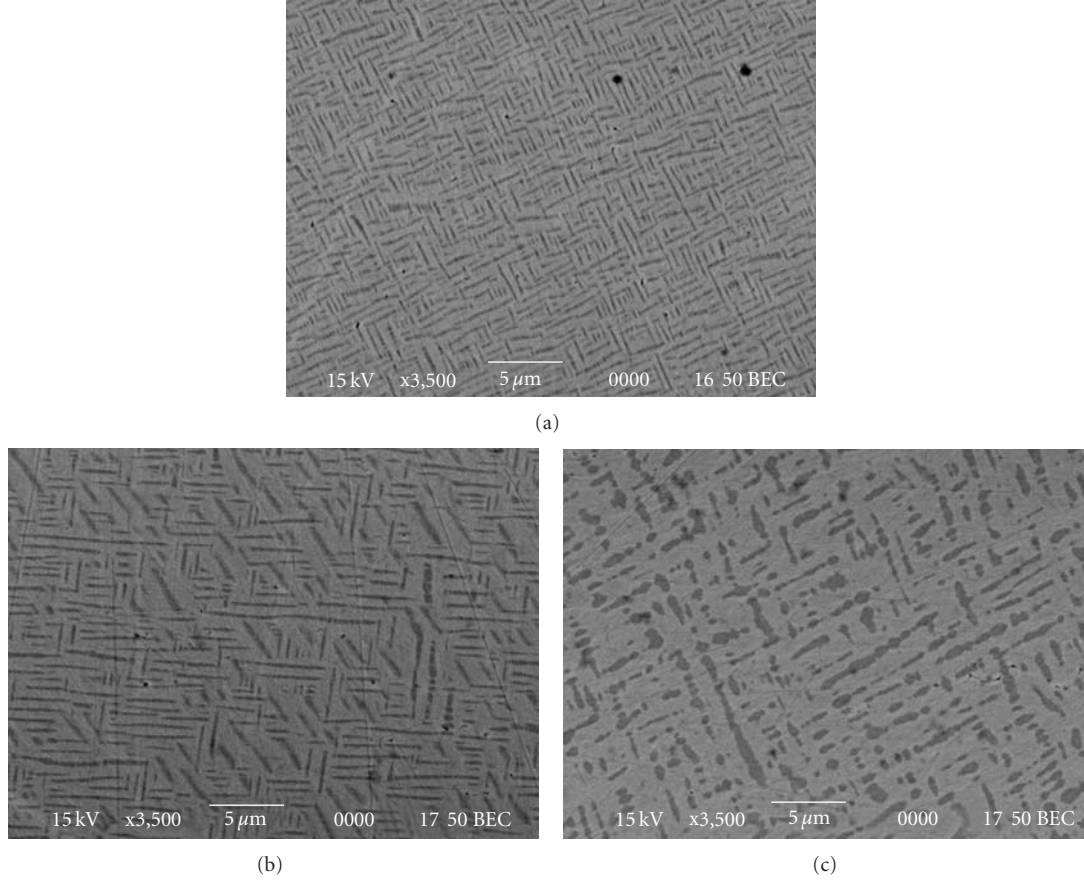


FIGURE 5: SEM micrographs of Ni-15at%Al(arc) after annealing at 900°C for 24 h (a), 72 h (b), and 120 h (c).

heterogeneously distributed in the MAed specimens, where each sphere appears to be an agglomeration of fine spheres in a dimension of approximately $0.2 \mu\text{m}$. Figure 6 shows the distribution of γ' precipitates in the MAHP alloys of Ni-15at%Al, Ni-15at%Al-0.6at%Y₂O₃, and MA6000 after annealing at 900°C for 72 h. The γ' precipitates appear to be slightly arranged along a lattice, rather than spherical-type of agglomeration.

In order to evaluate the various morphologies of the γ' precipitates in MAed and arc-melted alloys, their lattice misfits were evaluated. On the basis of the X-ray diffraction measurements, the lattice constant a is calculated using

$$d = \frac{\lambda}{2 \sin \theta}, \quad (3)$$

$$a = d\sqrt{h^2 + k^2 + l^2},$$

where θ is the diffraction angle, λ is the wavelength of the CuK α characteristic X-ray spectral line of 0.154 nm, and $(h k l)$ is the index of the lattice plane. In the case of Ni-15at%Al (MA), the 2θ values of γ and γ' precipitates are 44.21° and 43.82°, respectively, as shown in Figure 3. The diffracted lattice plane is (111) for both cases. Substituting these values into (3), the lattice constant becomes $a_\gamma = 0.35441$ nm and $a_{\gamma'} = 0.35743$ nm. These lattice constants are at room temperature; the values at 800°C, where γ' precipitation

TABLE 2: Lattice misfit parameters at 800°C measured by X-ray diffraction.

	Lattice misfit (%)
Ni-15at%Al (MA)	0.54
Ni-15at%Al-0.6at%Y ₂ O ₃ (MA)	0.61
Ni-15at%Al (arc)	0.25

occurs, must be calculated. The lattice constants of γ and γ' precipitates at 800°C are estimated to be $a_{\gamma-800} = 0.35928$ nm and $a_{\gamma'-800} = 0.36120$ nm by using thermal expansion coefficients of 1.279×10^{-5} (1/K) for γ and 1.320×10^{-5} (1/K) for γ' precipitates. The lattice misfit δ of Ni-15at%Al (MA) was found to be 0.54% at 800°C when these values were substituted into (4):

$$\delta = \frac{a_{\gamma'} - a_\gamma}{a_\gamma}. \quad (4)$$

The lattice misfit δ of Ni-15at%Al (arc) became 0.25% at 800°C when $2\theta = 43.69^\circ$ for γ and $2\theta = 43.44^\circ$ for γ' precipitates and $a_{\gamma-800} = 0.36333$ nm and $a_{\gamma'-800} = 0.36421$ nm. Similarly, the lattice misfit δ of Ni-15at%Al-0.6at%Y₂O₃ (MA) was found to be 0.61%. These results are listed in Table 2.

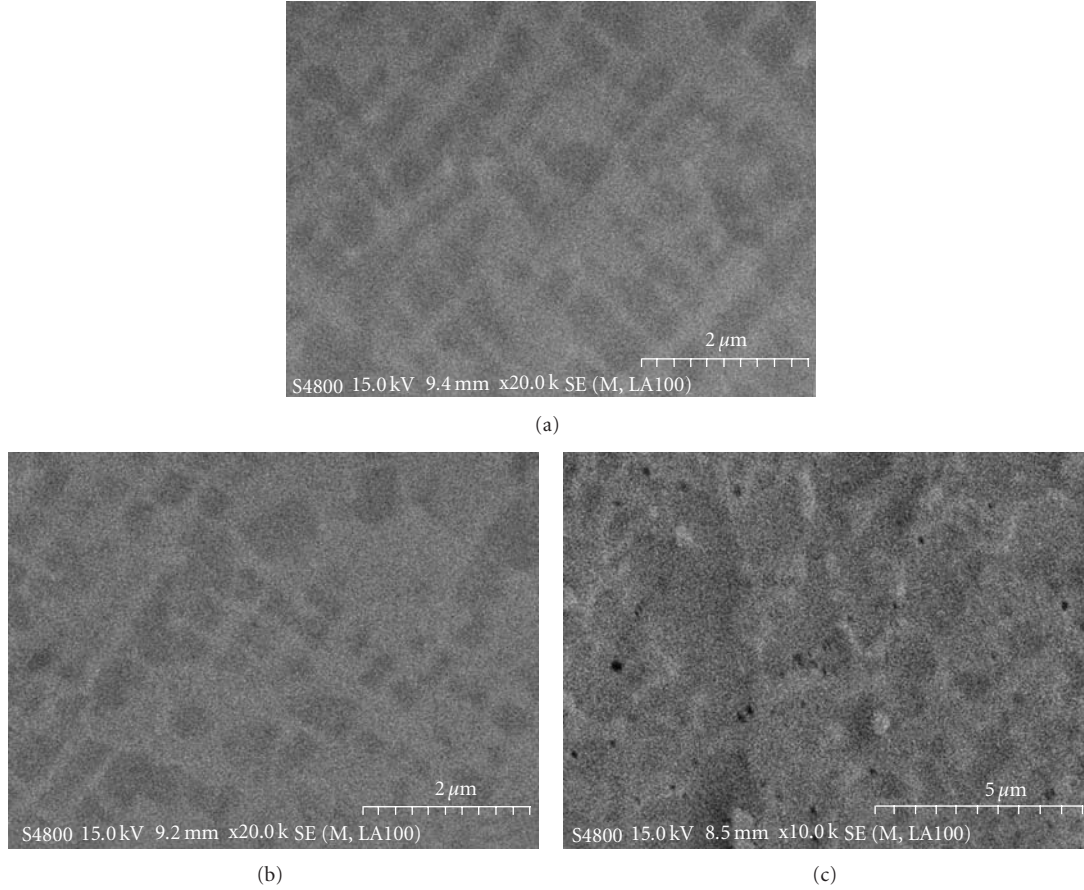


FIGURE 6: SEM micrographs for MAHP specimens after annealing at 900°C for 72 h. Ni-15at%Al (a), Ni-15at%Al-0.6at%Y₂O₃ (b), and MA6000 (c).

TABLE 3: The growth rate constant K' (m³/s) of γ' precipitates at 800°C, 850°C, and 900°C.

	800°C	850°C	900°C
Ni-15at%Al (arc)	4.20×10^{-27}	1.99×10^{-26}	9.22×10^{-26}
Ni-15at%Al (MA)	3.84×10^{-27}	6.84×10^{-27}	2.34×10^{-26}
Ni-15at%Al (MAHP)	3.91×10^{-26}	7.33×10^{-26}	1.23×10^{-25}
Ni-15at%Al-0.6at%Y ₂ O ₃ (MAHP)	7.94×10^{-26}	1.32×10^{-25}	1.81×10^{-25}
MA6000 (MAHP)	3.13×10^{-26}	5.87×10^{-25}	9.86×10^{-25}

If the lattice misfit δ between the γ and γ' precipitates is zero, γ' randomly precipitates in a spherical morphology; however, a slightly positive misfit results in a cuboidal γ' morphology, because preferential growth of the γ' precipitate occurs in the crystalline direction so as to minimize the elastic energy [9]. In addition, it has been reported that increasing the lattice misfit δ by more than 0.5% destroys coherency and leads to spherical precipitates [10]. The results listed in Table 2 are in agreement with the results mentioned above.

3.3. *Growth Kinetics of γ' Precipitates.* Figure 7 shows the sizes of the γ' precipitates for Ni-15at%Al (MA) with

increasing aging time (24 h, 72 h, and 120 h) at 800°C, 850°C, and 900°C. The plot of the average size against the aging time is almost a straight line when the cube of the diameters of the γ' precipitates is considered although their individual sizes vary widely even at the same aging time and same temperature. This could imply that the growth of γ' precipitates is followed by Ostwald ripening, and the LSW relation would be satisfied, which is expressed as [11]

$$\begin{aligned} \bar{d}^3 - \bar{d}_0^3 &= \frac{64\sigma D C_e V_m^2}{9RT} t = K' t, \\ K' &= \frac{64\sigma D_0 C_e V_m^2}{9RT} \exp\left(-\frac{Q}{RT}\right), \end{aligned} \quad (5)$$

where d_0 and d are average particle sizes at the initial time and after aging time t , σ is the interface energy between the γ' precipitate and the matrix, D is the diffusivity of the solute atom, C_e is the solute atom concentration in equilibrium with the γ' precipitate having infinite size, V_m is the molar volume of the γ' precipitate, R is the gas constant, and T is the absolute temperature. K' is the growth rate constant, which is expressed using the activation energy of atomic diffusion, Q . The value of K' at each temperature can be experimentally derived from the slope of the nominal values in Figure 8 although there is wide dispersion in upper and

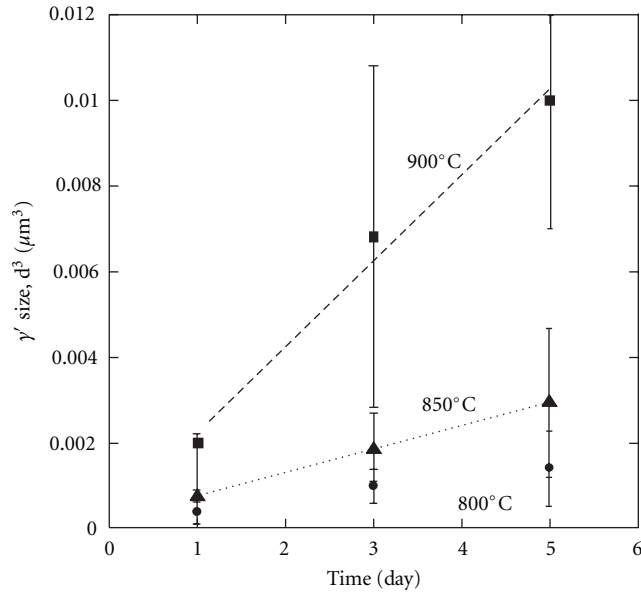


FIGURE 7: Cube of γ' precipitates size versus annealing time at 800°C, 850°C and 900°C for Ni-15at%Al (MA).

TABLE 4: Activation energy Q (kJ/mol) of atomic diffusion derived from growth rate of γ' precipitates.

	Activation energy of atomic diffusion (kJ/mol)
Ni-15at%Al (arc)	303
Ni-15at%Al (MA)	188
Ni-15at%Al (MAHP)	210
Ni-15at%Al-0.6at%Y ₂ O ₃ (MAHP)	186
MA6000 (MAHP)	251

lower limits. Similarly, the values of K' were obtained for Ni-15at%Al (arc), Ni-15at%Al (MA and MAHP), Ni-15at%Al-0.6at%Y₂O₃ (MAHP), and MA6000 (MAHP); these values are listed in Table 3. They are represented by the Arrhenius plot of $\ln(K')$ versus $1/T$. The values of Q estimated from the slope of each line in Figure 8 are 188 kJ/mol for Ni-15at%Al (MA), 303 kJ/mol for Ni-15 at %Al (arc), 210 kJ/mol for Ni-15at%Al (MAHP), 186 kJ/mol for Ni-15at%Al-0.6at%Y₂O₃ (MAHP), and 251 kJ/mol for MA6000 (MAHP). These Q values are summarized in Table 4.

Kusabiraki et al. [3], Castani and Lupinc [12], Ardell and Nicholson [11, 13] pointed out that a growth of the γ' precipitates follows the LSW relation; the activation energy for the γ' growth is reported as 281 kJ/mol [3] and 290 kJ/mol [9] in Inconel X-750 and 269 kJ/mol [11] in Ni-Al. It is also pointed out that this activation energy belongs to that for diffusion of Al in Ni, of which activation energy is reported to be 268 kJ/mol [3]. In this study, similar activation energy of 303 kJ/mol was roughly estimated for the arc-melted alloys. However, MAed specimen is significantly reduced in the activation energy of 188 kJ/mol. This could be due to the high dislocation density and nanosized grains in MA, as shown in Table 1. It is considered that the atomic (Al)

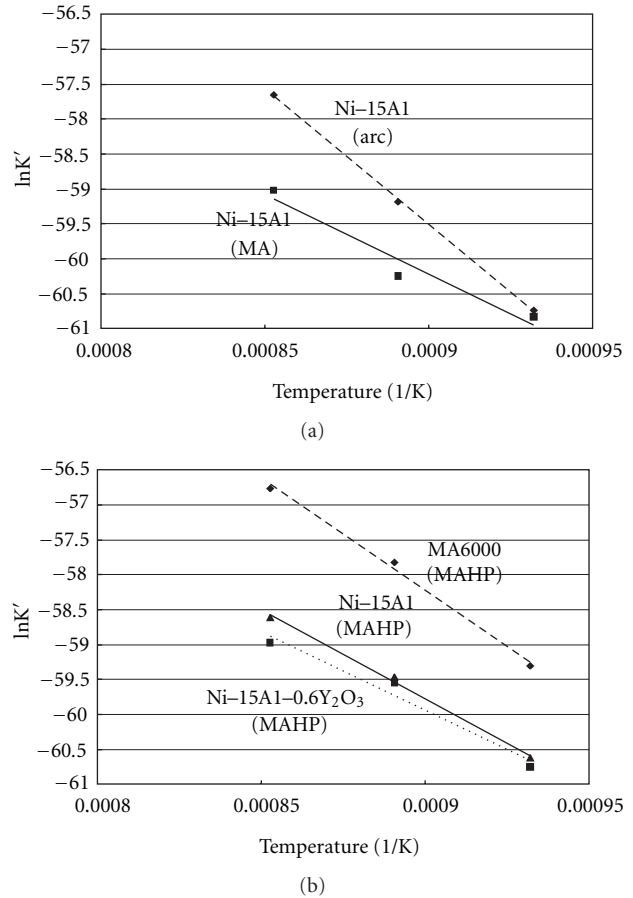


FIGURE 8: The Arrhenius plot for growth rate of γ' precipitates.

diffusion to produce γ' precipitates is adequately enhanced in MAed specimens. The activation energy for MAHP lies between that for MAed and that for arc-melted specimens and could be attributed to dislocation recovery and grain coarsening by hot-pressing at 1200°C for 3 h.

4. Conclusions

The γ' precipitation and growth kinetics in MAed Ni-Al specimens were investigated, and the following results were obtained.

- (1) The morphology of the γ' precipitates is totally different: the morphology is cuboidal in the conventional arc-melted Ni-Al alloys and spherical in the MAed ones. These differences in morphologies are attributed to the different lattice misfits between the γ' precipitates and matrices at the aging temperature of 800°C. The arc-melted specimens have a lower positive value (less than 0.5%) of the lattice misfit δ , causing preferential growth of the γ' precipitate along the crystalline direction, whereas an increased lattice misfit δ (more than 0.5%) in the MAed specimen destroys coherency and leads to isotropic growth in spherical morphology.

The hardness increase induced by the γ' precipitates during aging is accelerated in the MAed specimens.

- (2) The growth kinetics of the γ' precipitates can be expressed by Ostwald ripening. On the basis of the LSW theory, the activation energy for the γ' precipitate growth was derived from the Arrhenius plot: 303 kJ/mol for the arc-melted specimens, 188 kJ/mol for the MAed specimens, 210 kJ/mol for Ni–15at%Al (MAHP), 186 kJ/mol for Ni–15at%Al–0.6at%Y₂O₃ (MAHP), and 251 kJ/mol for the MAHP specimens. The lower activation energy for solute diffusion in the MAed specimen could be attributed to the high dislocation density and nanosized grains.

Acknowledgment

The authors are grateful to Tanikawa Fund Promotion of Thermal Technology for supporting this work.

References

- [1] A. Maheshwari and A. J. Ardell, “Anomalous coarsening behavior of small volume fractions of Ni₃Al precipitates in binary Ni–Al alloys,” *Acta Metallurgica Et Materialia*, vol. 40, no. 10, pp. 2661–2667, 1992.
- [2] A. K. Sinha and J. J. Moore, “Study of precipitation and growth of γ' and dislocation structure in Inconel X-750,” *Metallography*, vol. 19, no. 1, pp. 75–86, 1986.
- [3] K. Kusabiraki, H. Nagahama, L. Wang, and T. Ooka, “Growth of γ' precipitates in nickel-base superalloy,” *Tetsu-To-Hagane*, vol. 75, no. 8, pp. 1354–1361, 1989 (Japanese).
- [4] I. M. Lifshitz and V. V. Slyozov, “The kinetics of precipitation from supersaturated solid solutions,” *Journal of Physics and Chemistry of Solids*, vol. 19, no. 1-2, pp. 35–50, 1961.
- [5] H. O. J. Ryu, S. H. Hong, J. Weber, and J. H. Tundermann, “Effect of elastic interaction energy on coarsening of γ' precipitates in a mechanically alloyed ODS Ni-base superalloy,” *Journal of Materials Science*, vol. 34, no. 2, pp. 329–336, 1999.
- [6] T. Hoshino, S. Ukai, and S. Hayashi, in *Proceedings of the 5th ASM Heat Treatment and Surface Engineering Conference in Europe*, pp. 643–646, 2000.
- [7] W. H. Hall, *The Journal of the Institute of Metals*, vol. 75, p. 1127, 1950.
- [8] G. K. Williamson and R. E. Smallman, “III. Dislocation densities in some annealed and cold-worked metals from measurements on the X-ray debye-scherrer spectrum,” *Philosophical Magazine*, vol. 1, pp. 34–46, 1956.
- [9] R. A. Ricks, A. J. Porter, and R. C. Ecob, “The growth of γ' precipitates in nickel-base superalloys,” *Acta Metallurgica*, vol. 31, no. 1, pp. 43–53, 1983.
- [10] R. C. Reed, *The Super Alloys, Fundamentals and Applications*, Cambridge University Press, Cambridge, UK, 2005.
- [11] A. J. Ardell and R. B. Nicholson, “On the modulated structure of aged Ni–Al alloys. with an Appendix On the elastic interaction between inclusions by J. D. Eshelby Cavendish Laboratory, University of Cambridge, England,” *Acta Metallurgica*, vol. 14, no. 10, pp. 1295–1309, 1966.
- [12] C. Castani and V. Lupinc, “Solution heat treatment, aging and microstructure of inconel X-750,” *Metallurgia Italiana*, vol. 69, no. 7-8, pp. 306–311, 1977.
- [13] A. J. Ardell and R. B. Nicholson, “The coarsening of γ' in Ni–Al alloys,” *Journal of Physics and Chemistry of Solids*, vol. 27, no. 11-12, pp. 1793–1794, 1966.